



ThomX Technical Design Report

A. Variola, J. Haissinski, A. Loulergue, F. Zomer, (eds)

► To cite this version:

A. Variola, J. Haissinski, A. Loulergue, F. Zomer, (eds). ThomX Technical Design Report. 2014, 164 p. <in2p3-00971281>

HAL Id: in2p3-00971281

<http://hal.in2p3.fr/in2p3-00971281>

Submitted on 2 Apr 2014

HAL is a multi-disciplinary open access archive for the deposit and dissemination of scientific research documents, whether they are published or not. The documents may come from teaching and research institutions in France or abroad, or from public or private research centers.

L'archive ouverte pluridisciplinaire **HAL**, est destinée au dépôt et à la diffusion de documents scientifiques de niveau recherche, publiés ou non, émanant des établissements d'enseignement et de recherche français ou étrangers, des laboratoires publics ou privés.

ThomX

LAL / RT 14-21

SOLEIL / SOU-RA-3629

MARS 2014



THOMX TECHNICAL DESIGN REPORT

EDITORS

Alessandro Variola,
Jacques Haissinski,
Alexandre Loulergue,
Fabian Zomer

ThomX

LAL –pub etc etc

EDITORS

Alessandro Variola,
Jacques Haissinski,
Alexandre Louergue,
Fabian Zomer



[THOMX TECHNICAL DESIGN REPORT]

[Tapez le résumé du document ici. Il s'agit généralement d'une courte synthèse du document. Tapez le résumé du document ici. Il s'agit généralement d'une courte synthèse du document.]

INTRODUCTION

1. The ThomX project

The fast performance evolution of laser and particle accelerator systems has opened the way to compact radiation sources based on Compton backscattering (CBS) [1.1]. While CBS-based sources do not compete with the more classical synchrotron sources as far as the photon total flux and beam brightness are concerned, the CBS scheme has several attractive characteristics: it provides the most efficient photon energy boost, so that hard X rays can be produced with a comparatively low energy electron beam resulting in very compact and low cost devices. This is extremely important in view of the integration of such a radiation source in a ‘non-laboratory’ environment, like a hospital or a museum. Another attractive feature of CBS sources resides in the energy versus emission angle correlation. This correlation makes it possible to use a simple setup with a diaphragm to obtain a quasi-monochromatic beam, with a bandwidth on the order of one percent. Moreover the CBS scheme allows the tuning of the photon energy range in several ways: by varying the laser wavelength, the beam energy, or the collision angle. Since the laser polarization is conserved in the electron-photon collision, a CBS-based machine may provide polarized photons.

The ThomX project is taking advantage of the preeminent French technology in accelerator and laser fields. The goal is to design and build a demonstrator with cutting edge performances compared to similar projects either in operation or planned. A flux between 10^{11} - 10^{13} γ/s in the hard X-ray range is expected and the photon energy tunability will provide a Compton edge that can be set between 50 and 90 keV.

This project is a direct outcome of the sustained effort made by several laboratories to achieve a high amplification of laser pulses by stacking them in a passive optical resonator. These studies resulted in a record amplification efficiency in the picosecond regime, obtained in the PLIC experiment [1.2]. They are presently pursued within the MightyLaser program at the ATF accelerator facility at KEK (Tsukuba, Japan) where a vacuum-compatible, four-mirror cavity is installed [1.3].

The ThomX collaboration gathers experts in accelerator physics coming from SOLEIL and LAL, experts in laser systems from CELIA (Bordeaux), in optical resonators from LAL, and in X-ray line instrumentation from the Neel Institute in Grenoble. The ThomX community includes representatives from the medicine field and from the cultural heritage field. The ESRF and INSERM (Grenoble) together with the CNRS C2RMF will design and perform a series of demonstration experiments to check the assets of such a radiation source. Furthermore the ThomX overall characteristics give to this machine a strong industrial potential; the latter will be investigated by an industrial partner, THALES Electron Devices, which will play an active role in the ThomX collaboration.

As a first step in this program, a CDR has been written [1.4]. It describes the basics of the Compton backscattering effect and gives a first estimate of the ThomX performances based on simulations. The main technological solutions are also described in this document. The machine lattice and the entire machine layout are provided, together with the design of the optical resonator and its integration in the collisions region. The main items which need R&D were identified. A global integration plan and a machine cost evaluation were also given.

The present TDR provides a detailed description of all the technical sub-systems, together with the machine integration scheme. It also provides the results of complete beam dynamics simulations which take into account the ring characteristics and all the effects resulting from the collisions between the

electrons stored in the ring and the photons stored in the optical cavity. These simulations lead to precise predictions concerning the X-ray yield. The last part of the TDR deals with the project structure and its management. Finally, the updated cost estimate is presented.

2. Scheme and options

X-ray sources based on Compton backscattering can be designed with various configurations, depending on the main performance goals (average flux, peak flux, brilliance, monochromaticity....). Once this choice is made, one may envisage either a high or a low electron-photon collision frequency. In the first case the electron beam is recirculated in a storage ring or in an ERL in CW mode and continuously interacts with the laser. Another option is to operate directly a high duty cycle or CW super-conducting Linac. Correlatively, the laser system has to provide a high average power in the CW locked mode [1.5]. In this case, to amplify the laser pulse energy, one may envisage the use of a passive optical resonator with a high gain [1.6]. If a high peak instantaneous flux, in single bunch or multi-bunch pulsed mode, is required, the laser system will be a high power laser with a low repetition frequency. Recirculation of the laser beam is possible for a few passages by means of passive or regenerative cavities [1.7]. As far as the accelerator technology is concerned, the warm Linac technology can be made to work in burst mode [1.8]. This allows the production of short, low emittance bunches to increase the source brilliance. Because of the Compton energy-angle correlation, this scheme can also provide an excellent performance as far as monochromaticity is concerned by using a diaphragm which selects a fraction of the X-ray beam.

The ThomX source is designed to maximize the average X-ray flux. Another goal of this project is to provide a compact, reliable, and tunable source which can be operated in hospitals or in museums in a user-friendly way.

These constraints imposed the choice of a high collision rate scheme and of the warm RF technology. Thus the ThomX accelerator system is based on a 50 Hz, warm S band (2998 MHz) linac whose energy is tunable up to 70 MeV, an injection line and a compact electron storage ring whose RF cavity will be warm and will operate at 500 MHz. The ring revolution frequency is 17.8 MHz. The laser is a fully integrated fibre laser which provides a high average energy. Its power is amplified by stacking the pulses in a high gain four-mirror Fabry-Pérot resonator with a 30000 finesse. The laser and the optical cavity repetition frequency is twice the ring revolution frequency, ensuring an electron-photon collision every e^- bunch revolution.

The basic operating scheme of ThomX is illustrated in Fig 1. A 1 nC electron bunch is produced by an RF gun and then accelerated up to the ring injection energy by an S band section. A transport line ensures the bunch transfer from the linac exit to the injection section of the storage ring. After injection, the electron bunch is recirculated for 20 ms in the ring. The ring optics and the RF peak value are such that the beam size is very small (in all directions) at the interaction point (IP).

In parallel, a high power fibre laser produces light pulses of $\sim 1.4 \div 2.8 \mu\text{J}$ energy at $\sim 1.2 \text{ eV}$. These pulses are stacked in a four mirror optical resonator at twice the ring revolution frequency. The expected energy gain per pulse is $10^3 \div 10^4$, corresponding to a beam power of $\sim 70 \div 700 \text{ kW}$ in the optical cavity.

The synchronization system allows a near head-on collision (the crossing angle is two degrees) between the electrons and the laser pulse, every revolution of the electron bunch. These collisions produce hard X rays which are backward emitted in a cone whose angular opening is $\sim 1/\gamma$ (as a result of a relativistic effect).

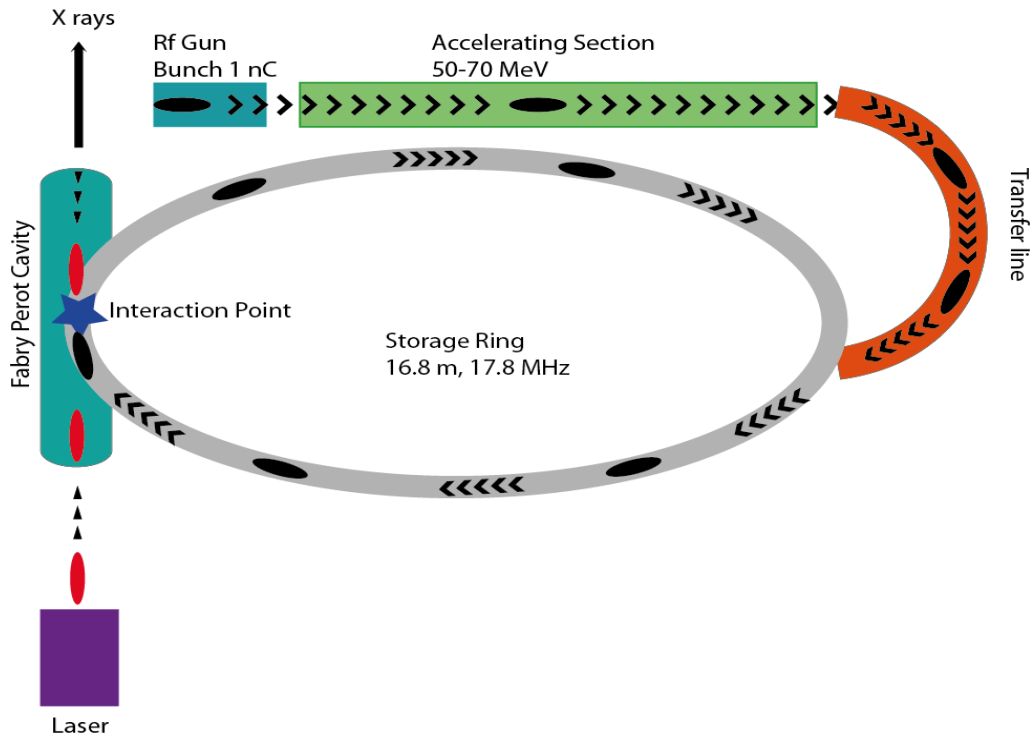


Fig.1. Schematic diagram of the ThomX source.

At the end of a storage period of 20 ms, the electron bunch is extracted from the ring and dumped in a dedicated beam dump to avoid the background noise that would be produced by uncontrolled particle losses. At the same time, a new ‘fresh beam’ is injected in the machine.

3. General layout of the machine

As previously mentioned, the ThomX design takes into account a strong constraint coming from the goal of a small size machine. Nevertheless this design allows for the possible integration of two collision regions [1.9]. Figure 2 shows the general layout of the machine. The linac includes an electron RF photogun (1) followed by a section dedicated to diagnostics (2), the acceleration structure (3), and a quadrupole triplet (4) to allow for a three-gradient measurement in the direct line dump (5) where a diagnostic chamber will be located. The injection line consists of four 45 degree dipoles to steer the beam, four quadrupoles and two chambers (6, 7) for energy spread measurements and beam characterization before injection. The injection is performed by a septum (8) and a fast kicker (9). Another kicker (10) is inserted in the same line to provide, together with the septum, a fast extraction. Once extracted, the beam is transported towards a dedicated beam dump (11).

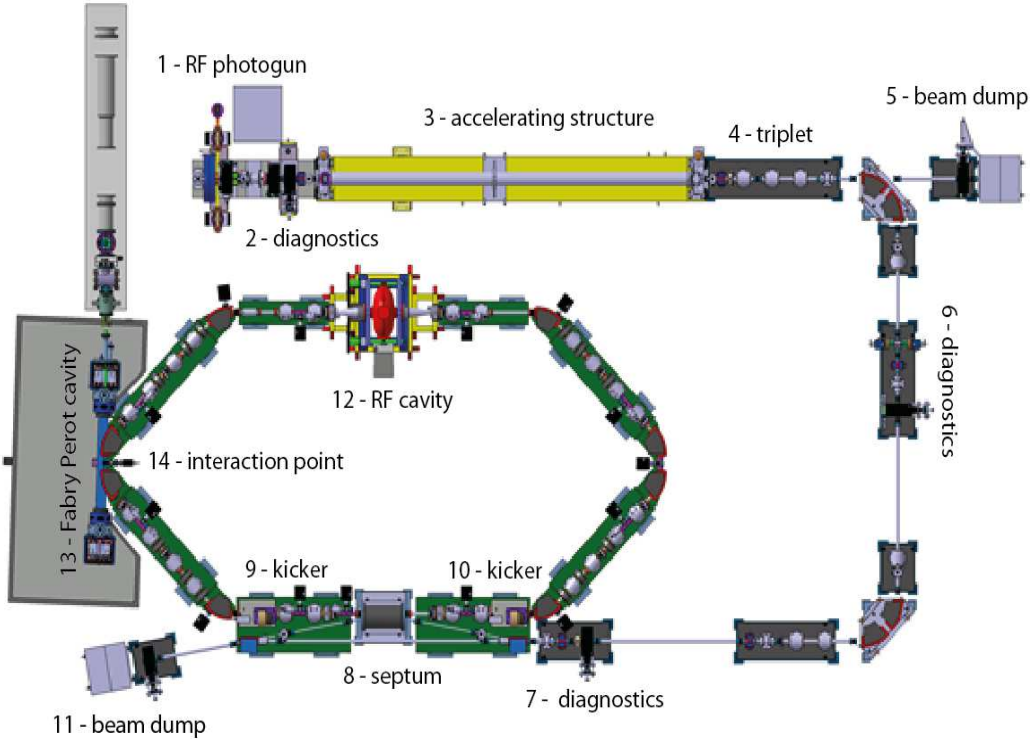


Figure 2. ThomX layout.

The ring design ensures a four-fold symmetry based on a double bend achromat (DBA) optics. It includes 8 dipoles, 24 quadrupoles, and 12 sextupoles for chromatic corrections. The bunch storage time is too short (20 ms) and the beam energy is too low for synchrotron damping to play a role in regard to the Compton back-scattering recoil effect, nor in regard to collective effects such as CSR, IBS and ion instabilities. For this reason, an ‘ELETTRA’ type RF cavity (12) will be used, not to restore energy, but to bunch the electrons and to perform a longitudinal feedback. Transverse position diagnostics and feedback will be provided by a strip-line and by BPMs. A synchrotron radiation chamber will be used for transverse and longitudinal optical diagnostics. The required ultra-vacuum will be maintained by ion pumps distributed along the ring and by two dedicated pumps in the Fabry-Pérot resonator.

In the ring lattice, two of the achromatic lines have been shortened by removing all the quadrupoles (see Fig. 3) so that the Fabry-Pérot cavity (13) can be easily integrated between two dipoles. By minimizing the beta functions, it was possible to locate the collision region (14) in such a short section. Furthermore, this design provides the possibility of implementing a second interaction region in the future.

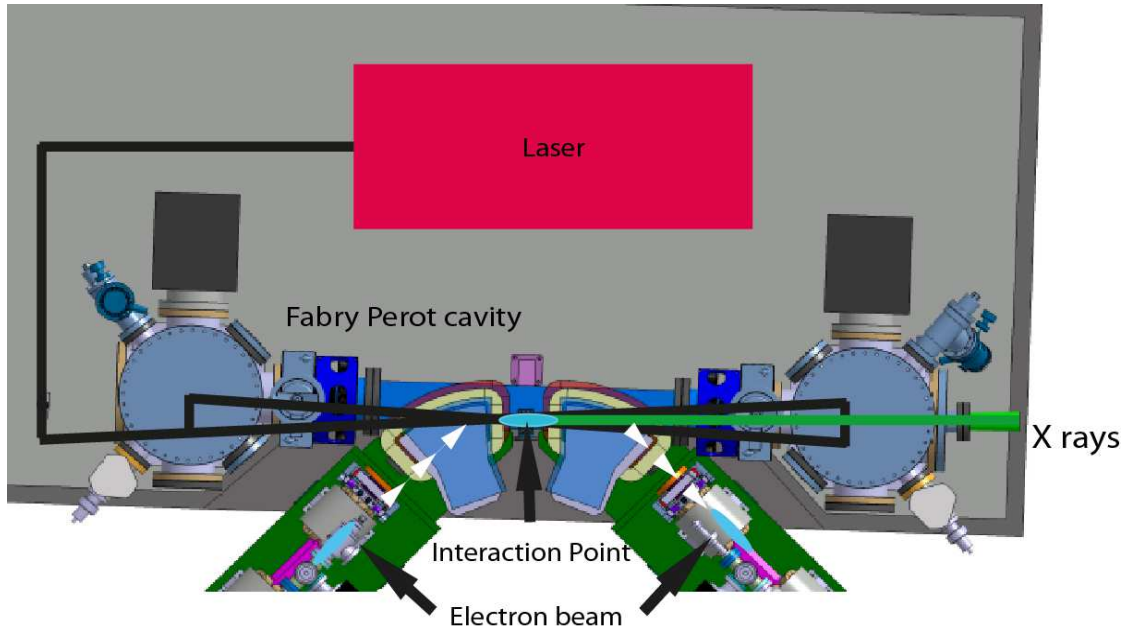


Fig. 3. Layout of the interaction region and of the optical cavity integration.

4. Machine parameters

The ThomX machine is composed of four main systems: the injector, the storage ring, the laser and the Fabry-Pérot resonator. As mentioned previously, we foresee some flexibility in the machine operation so that the X-ray energy can be varied. For this, all four systems are dimensioned to withstand an operating energy up to 70 MeV. Nevertheless, to characterize the machine, a baseline configuration has been chosen at 50 MeV. In Tables 1, 2, 3 and 4, the parameter values which are given below correspond to this baseline configuration.

Table 1.

Injector	
Charge	1 nC
Laser wavelength and pulse energy	266 nm, 100 μ J
Gun Q and Rs	14400, 49 MW/m
Gun accelerating gradient	80 MV/m @ 5 MW
Normalized rms emittance	$4.4 \pi \text{ mm mrad}$
Energy spread	0.4%
Bunch length	4.3%

Table 2.

Ring	
Energy	50 MeV (70 MeV possible)
Circumference	16.8 m
Crossing-Angle (full)	2 degrees
$\beta_{x,y}$ @ IP	0.1 m
$\epsilon_{x,y}$ just after injection	$5 \cdot 10^{-8}$ m
Bunch length just after injection (rms)	4 ps
Bunch length at the end of a 20 ms storage cycle	50 ps (rms)
Beam current	17.84 mA
RF frequency	500 MHz
Transverse/longitudinal damping time	1 s /0.5 s
RF Voltage	300 kV
Revolution frequency	17.84 MHz
σ_x @ IP (just after injection)	70 μ m
Tune x/y	3.17 /1.74
Momentum compaction factor α_c	0.0136
Initial/Final relative energy spread (with IBS and Compton back-scattering)	0.4%/0/6%

Table 3.

Laser and FP cavity	
Laser wavelength	1030 nm
Laser and FP cavity Freq	35.68 MHz
Laser power	50 – 100 W
Laser pulse energy	1.4 – 2.8 μ J
Fabry-Perot pulse energy	28 mJ
Fabry-Perot pulse length (rms)	5 ps
FP cavity finesse/Gain	3000-30000 / 1000- 10000
FP waist	70 μ m
Power circulating in the FP cavity	$\sim 0.07 - 0.7$ MW

Table 4.

Source	
Photon energy cut-off	46 keV (@50 MeV), 90 keV (@ 70 MeV)
Total Flux	10^{11} - 10^{13} photon/s
Bandwidth (with diaphragm)	1 % - 10%
Divergence	10 mrad ($1/\gamma$) without diaphragm @ 50 MeV

5. Summary of the TDR main technical points

After the publication of the CDR much work has been put in simulations, design and technical choices. The goal of this TDR is to provide a reference document in view of the machine construction, as well as a more precise planning and a more precise costing.

The first chapter deals with the machine performances and the tolerances to be met so that the collisions between the electron bunch and the laser pulse do take place in the conditions specified in the CDR. Then the main systems are described and our technical choices are presented. This last section is subdivided as follows:

1. Linac,
2. Beam transfer and injection section, ring,
3. Laser and Fabry-Pérot cavity,
4. X-ray user line.

A special attention is given to the integration of each system and to the global integration of the ThomX machine. The ‘Optical system’ chapter includes a short report on recent results obtained in the laser and Fabry-Pérot cavity R&D program, both in the laboratory and on a beam line at KEK-ATF (Japan).

Special chapters are dedicated to diagnostics, the control of the main systems and their synchronization, safety and radioprotection. The last chapter presents the project management.

Chapter 1. THE THOMX INTERACTION REGION

1.1 Electron beam and laser pulse characteristics in the interaction region

The ThomX injection frequency has been fixed at 50 Hz (20 ms period) by taking into account the Compton scattering recoil effect which continuously deteriorates the beam longitudinal emittance. This effect is all the more important as synchrotron damping is strongly suppressed since the beam energy is low. Because of this lack of damping, the Compton scattering recoil effect and eventual beam instabilities must be controlled by longitudinal and transverse feedback systems.

We stress the fact that, in ThomX, the beam does not reach a permanent state during a storage cycle: its properties are continuously varying. To describe the Compton interaction dynamics, we define a set of *nominal* beam characteristics which are those prevailing just after the injection of a fresh e^- bunch. Simulations have been carried out to characterize the X-rays emitted during a single crossing of the electron bunch and the photon pulse (stored in the optical cavity) as a function of the collision geometric parameters.

These nominal collision parameters are as follows:

Parameter	value	unit
Crossing angle	2	degree
Electrons energy	50	MeV
Electrons energy spread	0.3	%
Number of electrons	$6.25 \cdot 10^9$	
Fabry Perot pulse energy	28	mJ
Repetition rate	17.84	MHz
Laser pulse transverse dimension (rms)	35	μm rms
Electron bunch transverse dimension (rms)	70	μm rms
Laser pulse duration (rms)	5	ps rms
Electron bunch length at injection	4	ps rms

Table 1.1. Nominal collision parameters.

To extend these results to other geometric configurations, one has to take into account the parametric dependence of the Compton collision rate. The X-ray flux is the product of the Compton cross-section and the luminosity. It is proportional to the electron bunch intensity and to the laser pulse power. The geometry dependence is given by the luminosity formula which involves the geometric 6D size and the crossing angle. Assuming Gaussian bunches and neglecting the hourglass effect, the ring luminosity is given by the following expression:

Eq. 1.1

$$L = N_e N_\gamma f \frac{\cos\phi}{2\pi} \frac{1}{\sqrt{\sigma_{ye}^2 + \sigma_{y\gamma}^2} \sqrt{(\sigma_{x\gamma}^2 + \sigma_{xe}^2) \cos^2\phi + (\sigma_{ze}^2 + \sigma_{z\gamma}^2) \sin^2\phi}}$$

where $\sigma_{e,\gamma/x,y,z}$ represent respectively the two transverse dimensions and the longitudinal one of the electron bunch and of the laser pulse, f is the collision frequency, N_e and N_γ are the number of electrons per bunch and photons per pulse, Φ is half the crossing angle.

The X-ray energy cut-off is higher for head-on collisions and for photons which are exactly back-scattered. In this case the photon energy gain is $4\gamma^2$.

This calculation provides a useful reference to assess the efficiency of other configurations, but it remains an approximation since exact results must take into account the beam evolution during a storage cycle and should be obtained from a full revolution by revolution simulation.

1.2 Expected flux and its characteristics

In nominal conditions, the expected flux is $7.8 \cdot 10^{12}$ X-rays/s, whether one uses Eq. 1.1 or the monte-carlo simulation code CAIN. Figure 1.1a shows the energy spectrum of the scattered photons and its cut-off at 45 keV. As shown in Fig. 1.2b, most photons are emitted very close to the interaction region axis, within a small cone with a 2 mrad opening angle. They may be selected by using a small diaphragm. The energy spectrum of the X-rays emitted in a cone of 2.25 mrad opening angle is shown in Fig. 1.2a with a FWHM energy spread of 2.5 keV.

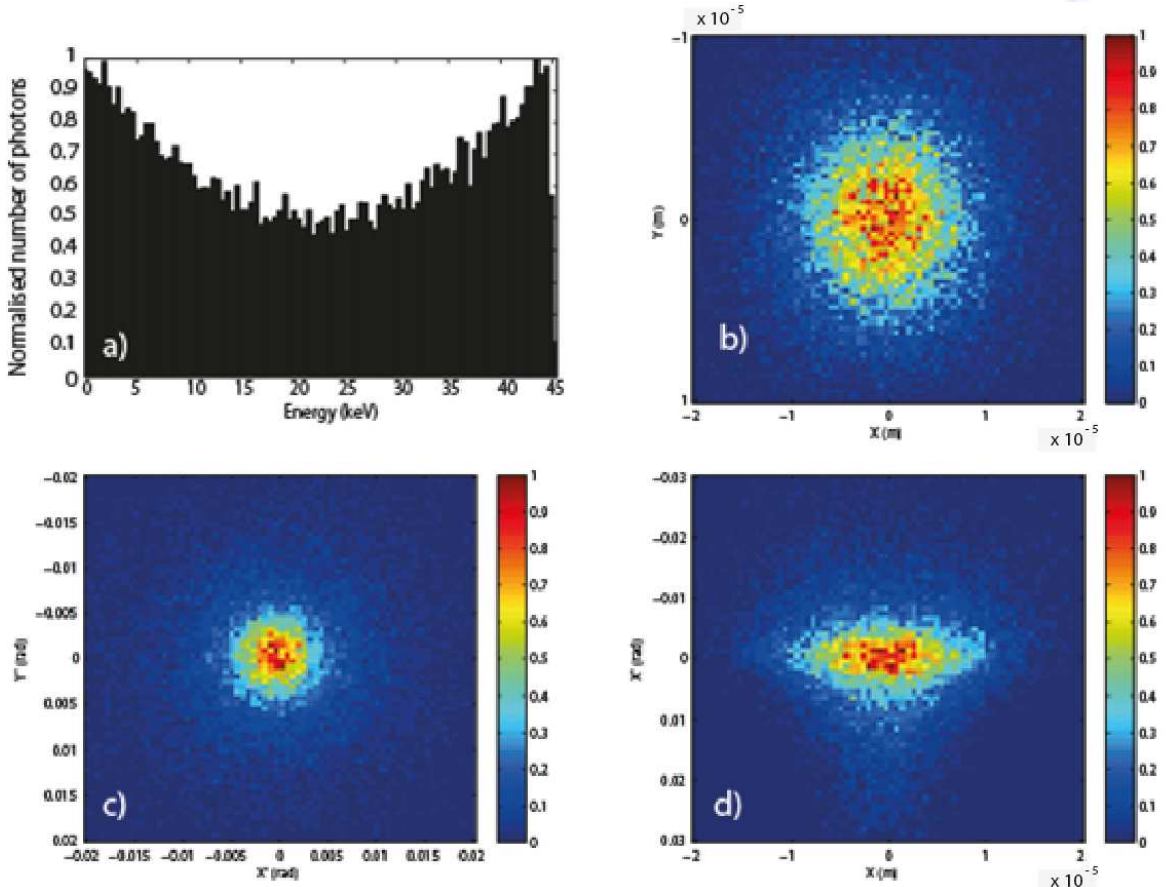


Figure 1.1. Results of simulations performed with CAIN using the parameters listed above. a) Energy spectrum, b) Transverse size of the source, c) Angular emission distribution, d) Horizontal ($x-x'$) phase space of the scattered X-rays.

The spot size at the source is dominated by the electron bunch of $7 \cdot 10^{-5}$ m as illustrated in Fig. 1.1b. The dimensions are assumed to be the same in the horizontal and vertical plane. The *total* divergence of the source is around 15 mrad given by the electron beam energy (*i.e.* the $1/\gamma$ parameter) with an rms size of 4 mrad (Fig. 1.1c). The emittance of the photon source, shown in Fig. 1.1d, is 0.3 mm mrad. The energy-angle correlation and the collimation effect are illustrated in Fig. 1.2. As expected, the high-energy X-ray flux is peaked with a $1/\gamma$ opening angle. The diaphragm which is assumed for this simulation selects emission angles and thus photon energies, resulting in a $\sim 10\%$ monochromatic photon beam.

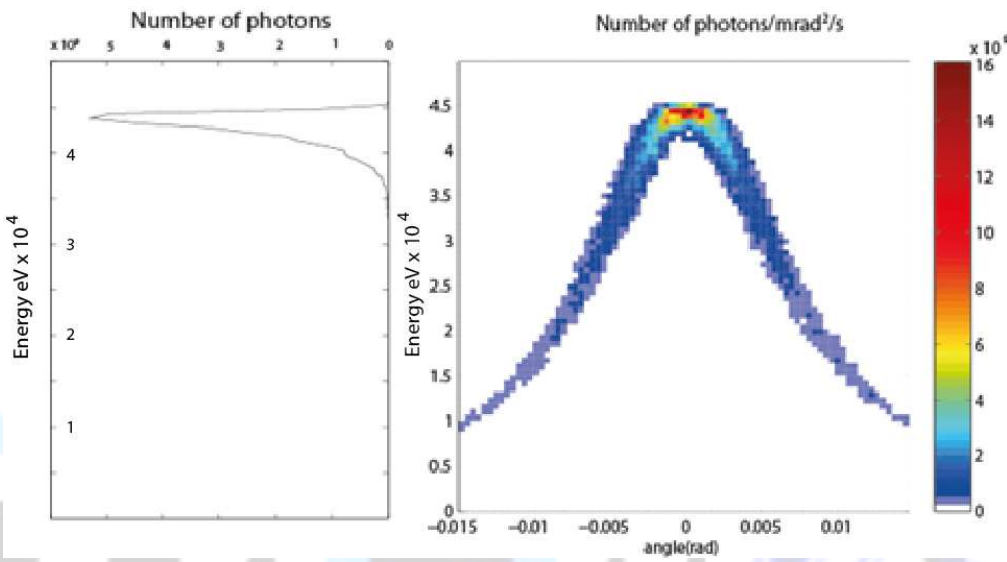


Figure 1.2. Results of simulations performed with CAIN, using the parameters listed above. Left panel: Energy spectrum of photons emitted in a cone with an opening angle of 2.25 mrad. Right panel: Number of photons/mrad²/s versus energy and angle (the color bar indicates the photon number).

1.3 Position stability

To optimize the X-ray flux, a precise transverse alignment must be achieved in the interaction region. It can be performed either by steering the electron beam or by adjusting the optical table position. These procedures will be monitored by means of a double BPM which is integrated in the Fabry-Pérot cavity vacuum chamber, exactly at the interaction point. The resolution of this technique is a few microns. A simulation has been performed to calculate the flux reduction resulting from a possible mismatch between the electron bunch orbit and the laser pulse trajectory. Figure 1.3 shows the number of X-rays produced per bunch crossing and per keV as a function of a *transverse* displacement of the optical cavity axis with respect to the electron orbit, from zero to 140 microns.

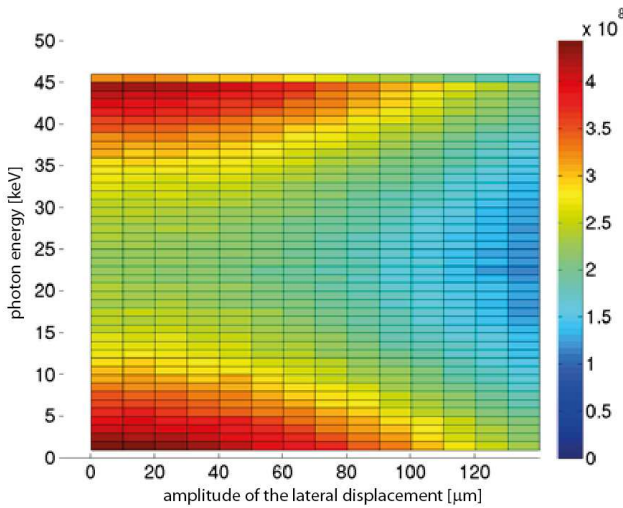


Fig.1.3. Number of back-scattered photons and their energy as a function of a transverse alignment error. This figure clearly shows that the losses entailed by a displacement comparable to the BPM sensitivity are negligible. The color bar indicates the number of X-rays produced at each crossing.

1.4 Timing stability

A precise synchronization between the electron bunch and the laser pulse at the interaction point is another important requirement. A timing mismatch introduces a longitudinal shift between the two bunches at the IP. This can be due to an error in the location of the Fabry-Perot cavity with respect to the e^- storage ring or to a jitter in the synchronization system. Fig 1.4 shows the variation of the X-ray flux as a function of a *longitudinal* displacement.

The flux is not so much reduced as long as the jitter is less than 10 ps. This number fixes the synchronization tolerance and thus the performance of the longitudinal feedback.

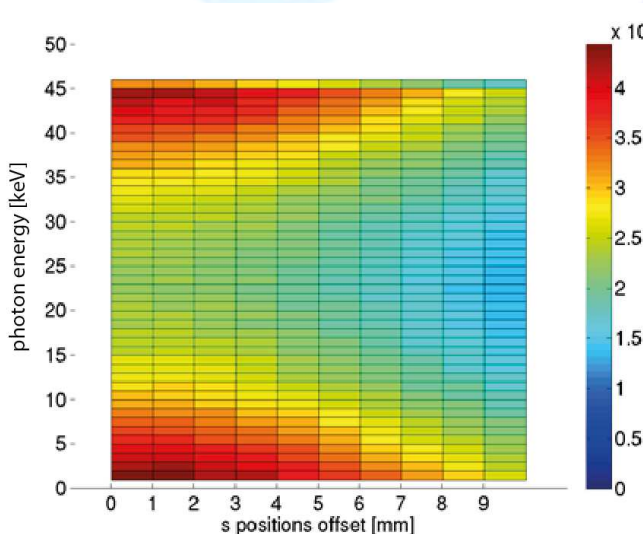
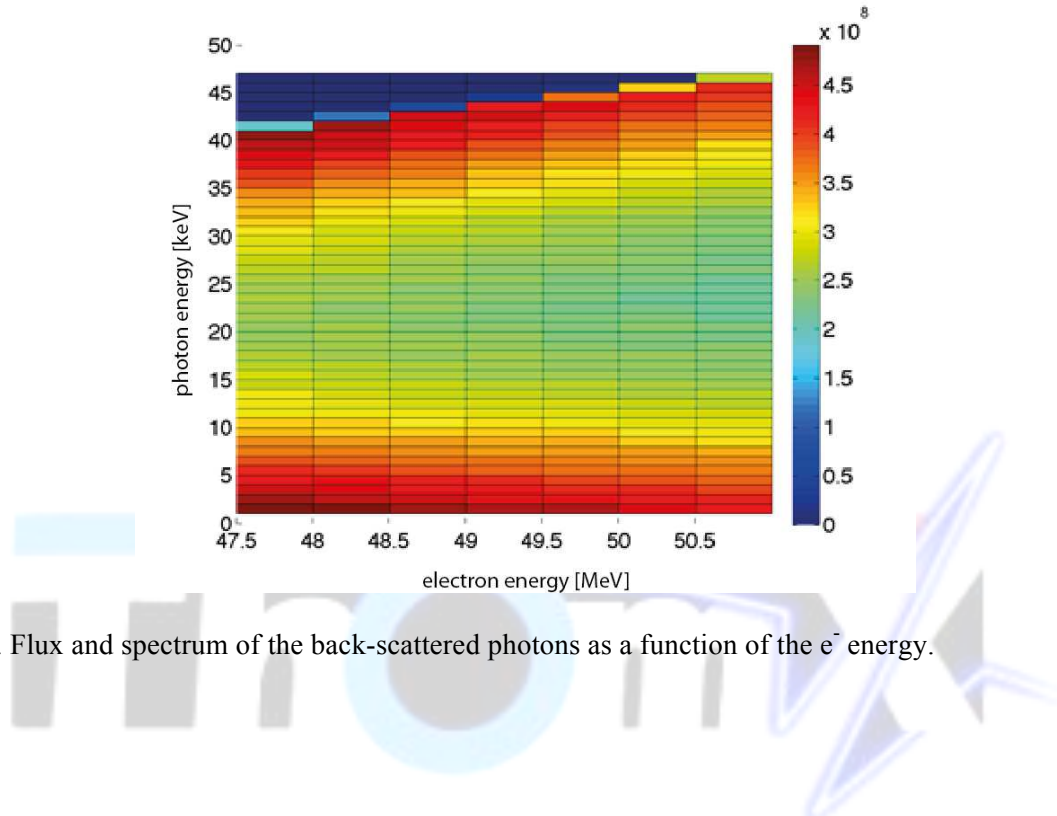


Fig 1.4. Flux and energy spectrum of back-scattered photons as a function of the relative synchronization of the beams (longitudinal displacement).

1.5 Energy stability

The nominal ThomX injection energy is 50 MeV. Phase rotation in the RF source or phase mismatch will generate a jitter in the injection energy. Such a jitter entails synchrotron oscillations which will be damped by the longitudinal feedback. However, before this feedback has stabilized the longitudinal oscillations, the collision conditions will not be nominal. This situation has been simulated; the results are illustrated in Fig.1.5. One can see that it is in the higher part of the X-ray energy spectrum that the loss is more important.



Chapter 2. INJECTOR

The most important components of the linac injector are the electron gun and the acceleration section which brings the beam to the desired energy. Other components are the laser used for the e^- gun, the magnetic elements used to transport the beam, the diagnostics, the vacuum system, the waveguides and the radio-frequency (RF) source. Each component is detailed in the following. First of all, the injector specifications are given since they lead to the choice of some of the linac components.

2.1 Injector specifications

The project goal, namely to produce a high flux of X-rays of energy 50 keV leads to the following specifications for the linac:

Energy	50	MeV
Charge	1	nC
Number of bunches per RF pulse	1	
Emittance (rms, normalised)	<5	mm mrad
Energy spread, rms	<1	%
Bunch length, rms	<5	ps
Average current	50	nA
Repetition frequency	50	Hz

Table 2.1. Nominal linac parameters.

First of all, one notices that the low average current, 50 nA does not justify the use of cold technology (*i.e.* of a superconductor) for the acceleration structure. But there is still a large choice of possibilities for an RF structure operating at room temperature. For economic reasons and because of the long experience accumulated in the field, we have chosen an RF structure operating at 3 GHz. This frequency is a European standard.

Furthermore, the above specifications led us to choose a photo-injector for the electron source since a low emittance beam is required. Again, to minimize risks, we chose to build the same gun as the one we constructed for the CLIC ‘Test Facility 3’ at CERN [2.1]. This gun has been running successfully for 4 years. To increase the current per bunch, we will use a metallic magnesium photocathode which can deliver more than 1 nC with a laser pulse energy of a few tens of a μ J at a wavelength of 260 nm. The gun is made of 2 1/2 copper cells, magnetically coupled to the waveguide. To get 1 nC with an emittance lower than 5 mm.mrad, an accelerating field of 80 MV/m is required, which means an RF power of 5 MW in a 3 μ s pulse. The electron beam energy output by the gun is around 5 MeV.

We will use an industrial laser to extract the electrons from the cathode by photoelectric effect. The main specifications of this laser are the following ones. Wavelength: 260 nm, energy per pulse: 100 μ J, pulse duration: around 5 ps. It must be synchronized with the RF frequency and triggered at 50 Hz. This laser will be installed in an optical hutch located outside the concrete shielding which will enclose the accelerator. Therefore its beam must be transported with dielectric mirrors and lenses over a distance of about 20 meters.

Concerning the acceleration section, SOLEIL, a partner of the project, will lend us a ‘LIL’ section. This section was made by LAL for the pre-injector of LEP at CERN. It has been kept as a spare for the SOLEIL linac. The ThomX project will provide an other section in case SOLEIL needs one. The section length is about 4.6 m. To reach a final energy of 50 MeV, the energy gain in the section must be

45 MeV. The latter value implies an electrical field of 12.5 MV/m and an RF power of about 10 MW. However the accelerator should reach higher energies in order to produce X-rays beyond 50 keV. Since the maximum targeted X-ray energy is 90 keV, the linac design should allow a beam energy of 70 MeV, corresponding to an RF power of 20 MW. Thus, taking into account the RF system efficiency, the specification for the total RF power is set at 35 MW.

This specification lead us to choose a klystron producing 35 MW in a 4.5 μ s. pulse. To feed the klystron, a modulator is needed that provides high voltage pulses of typically 240 kV, through a high voltage transformer soaking in an oil tank. The two technologies which can be used for this component are discussed in detail below.

For the electron beam steering, two coils and two magnetic correctors are required. The coils are placed around the gun. Opposite sign currents circulate in these coils (-310 A; 336 A) so that the magnetic field vanishes at the cathode location. Its amplitude is 0.23 T roughly 7 cm downstream from the cathode. Concerning the magnetic horizontal/vertical correctors, once a good mechanical alignment is achieved, experience has shown that beam trajectory errors are not larger than a few mm between the gun and the acceleration section. Hence the correctors must produce a beam deflection of up to 10 mrad. For the model operating at LAL [2.2], two bipolar power supplies of 10 A per corrector are adequate.

For the diagnostics, three different instruments will be installed between the RF gun and the acceleration section. An Integrated Current Transformer (ICT) will measure the charge per bunch. Beyond this device a beam position monitor (BPM) will measure the transverse positions (x, y) of the electron beam. We will use a BPM based on striplines which was designed for SOLEIL. The third item comprises a vacuum chamber equipped with an arm which can be translated by compressed air in order to introduce a YAG screen to intercept the beam. The YAG crystal fluoresces when ionized by the e^- beam. The emitted light shows the beam transverse shape. A short optical transport line and a CCD camera allow the measurement of the transverse dimensions. LAL designed and constructed the diagnostics chamber. It has already been successfully tested in the PHIL facility. A drawing showing the linac layout is shown in Fig. 2.1.

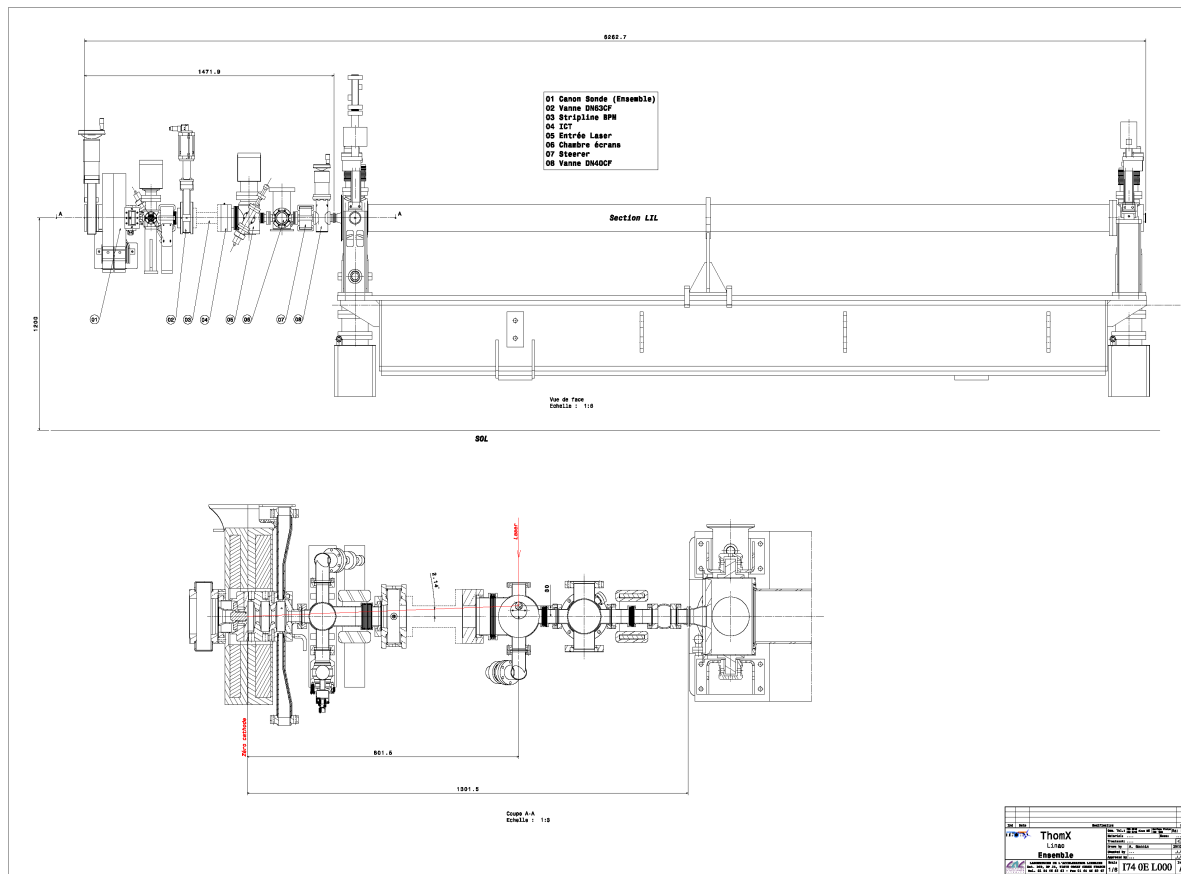


Figure 2.1. Linac layout. In the upper figure the different components of the LINAC are illustrated starting from the gun and subsequently passing through the stripline, the ICT for current measurements, the laser introduction chamber, the diagnostics station, the steerers and the accelerating section

2.2 Technical description of the linac components

2.2.1 Photo-injector

It is a copy of a gun built by LAL for the CLIC Test Facility 3 of CERN, the so-called ‘probe beam gun’[2.2]. Simulations have shown that the performances of this gun fulfill the ThomX specifications. We are thus benefiting from all the technical drawings which already exist and all the fabrication processes are mastered by LAL, from the machining to the brazing. This RF gun is comprised of 2 1/2 cells. The output cell is magnetically coupled and the other end is short-circuited. The main parameters are given in Table 2.2.

Frequency	2998.55	MHz
R _s	50	MΩ/m
Q	14500	
β	1	
E	80	MV/m
PRF	5	MW

Table 2.2. RF characteristics of the photo-injector, at 30°C in vacuum.

The photo-cathode will be made of magnesium. It has the big advantage of producing the specified charge without requiring an in-situ photo-cathode preparation chamber which is a heavy and expensive

installation. Preliminary tests performed at LAL have demonstrated the possibility to obtain good quantum efficiency with such cathodes.

The main difficulty expected in operating this device is the laser cleaning of the photocathode surface when polluted by an exposure to air. To perform this cleaning, a laser intensity of $160 \mu\text{J/mm}^2$ is required together with an RF electric field of at least 50 MV/m . The magnesium disk holder is not designed yet; it could be press fitted, screwed or brazed.

2.2.2 Solenoids

The gun is equipped with two solenoids, one is the focusing coil while the other is the bucking coil which cancels the magnetic field at the photo-cathode location. They have been modeled by usning POISSON. A schematic is shown in Fig. 2.2.

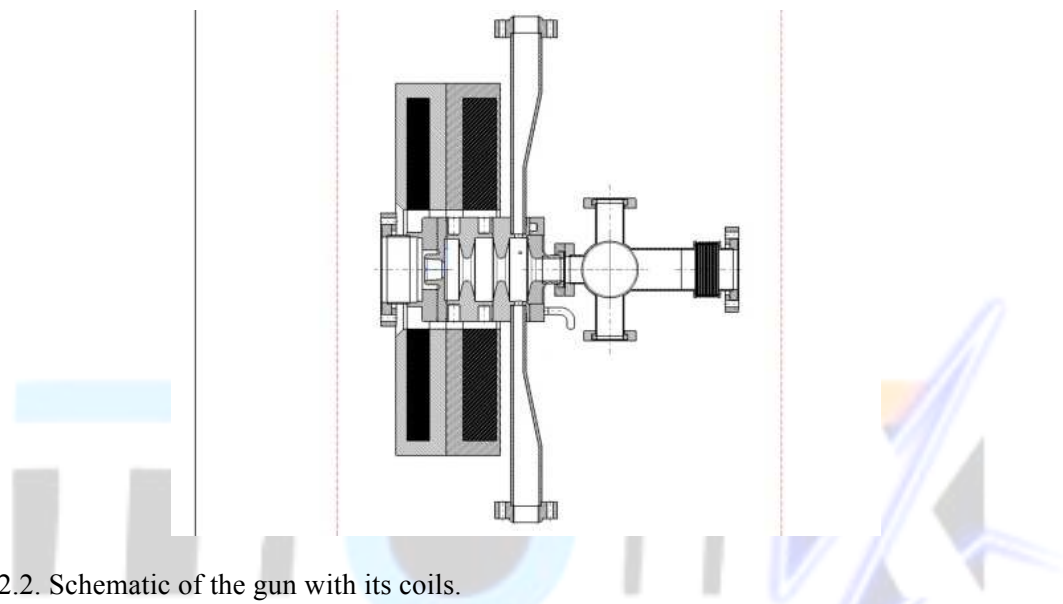


Figure 2.2. Schematic of the gun with its coils.

Dimensions

For both solenoids the inner diameter is 160 mm and the outer one is 500 mm. The copper part is 30 mm long for the bucking coil, and 56 mm for the focusing coil.

The conductor used for these magnets is a standard one with a $6 \times 6 \text{ mm}^2$ square shape. It is cooled by water circulating in a 4 mm diameter channel. One can easily calculate the current, the resistance, the dissipated power and the temperature rise assuming that the cooling water is supplied at 20°C and 8 bars. Values are provided for each ‘pancake’ since the conductors are wound by columns of two. The bucking coil, B_{bc} , has two pancakes and the focusing coil, B_{foc} , four.

	B_{bc}	B_{foc}	units
Number of coils	84	168	MHz
Number of pancakes	2	4	
Current	-274	326	A
P	2.3	3.3	kW
R	30.6	31	mΩ
Flow	1.64	1.64	l/mn
ΔT	+20	+28	°C

Table 2.3. Solenoid electric and cooling parameters. ‘Number of coils’ refers to one pancake.

Two power supplies are required: one for B_{bc} (400A, 30 V) and one for B_{foc} (400A, 60 V).

2.2.3 Laser

The laser extracts a bunch of electrons from the photo-cathode surface by photo-electric effect. Table 2.4 specifies its characteristics.

Parameter	value	unit
I	260-270	nm
Emax	100 ± 0.5	μJ
Beam transverse quality M2	$M2 < 1.1$	
Gaussian Pulse width	5	ps
Transverse profile	square	
Pointing stability	10% of beam diameter	
Oscillator frequency	74.963750, externally triggered with jitter < 1 ps	MHz
Amplifier repletion rate	50, externally triggered	Hz

Table 2.4. Laser specifications for the RF gun photocathode.

The laser architecture is shown in Figure 2.3.

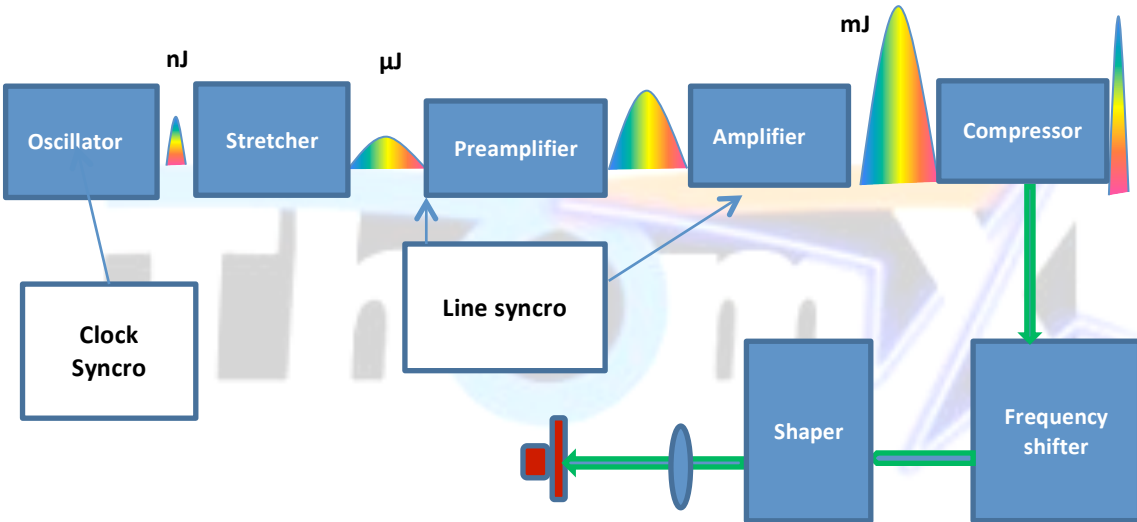


Figure 2.3. Architecture of the laser proposed by industry.

An oscillator provides a signal at the specified frequency. It can be either a fiber or a Ti:Saphire laser. Then the pulse is stretched, amplified (with one or two amplifiers), recompressed and converted in the UV range.

The laser will be installed on an optical table in a hutch whose temperature and hygrometry will be regulated.

2.2.4 Laser injection chamber

The laser injection chamber is located at a distance of 801.1 mm downstream of the photo-cathode. It contains a metallic aluminum mirror placed 30 mm away from the accelerator axis. It provides an 80 % reflectivity. The angle of incidence of the laser beam on the photocathode is 2.14° . This mirror is fixed. To adjust the laser beam position on the photo-cathode and its incident angle, we will use a motorized mirror with a remote control placed on an optical table just beside the laser injection chamber.

The size of this optical table will be $1 \times 1 \text{ m}^2$. On it, there will be

- 2 dielectric mirrors,
- 2 beam splitters,
- 1 UV photo-diode to monitor the laser intensity,
- 1 CCD camera to observe the laser spot on a screen (in paper or lanex) facing the photo-cathode,
- An optical beam expander to adjust the laser spot size on the photo-cathode.

This is the minimum number of optical items that will be put on the table; some changes may be made depending on the very final geometry of the accelerator and laser transport lines. The set-up design can be finalized during the last stage of the accelerator construction since it involves standard components only.

2.2.5 Beam steering coils

The e^- beam trajectory will be adjusted by sets of two steering coils which produce dipolar magnetic fields over short distances along the X and the Y axes. One such device will be located at the gun exit and the other about 800 mm downstream. Only very small position and angle errors must be corrected. Figure 2.4 shows the LAL design for such a coil. Experience with the PHIL photo-injector at LAL [2.2] showed that an integral of $B \cdot dl$ of 5.2 G m is sufficient. The latter figure has been validated by calculations made by a private company. With a current of 5 A, a $B \cdot dl$ of 5.8 G m was obtained that results in a 100 mrad deviation of a 5 MeV beam. Thus a 100 mm lateral displacement of the beam can be produced at the entrance of the acceleration section.

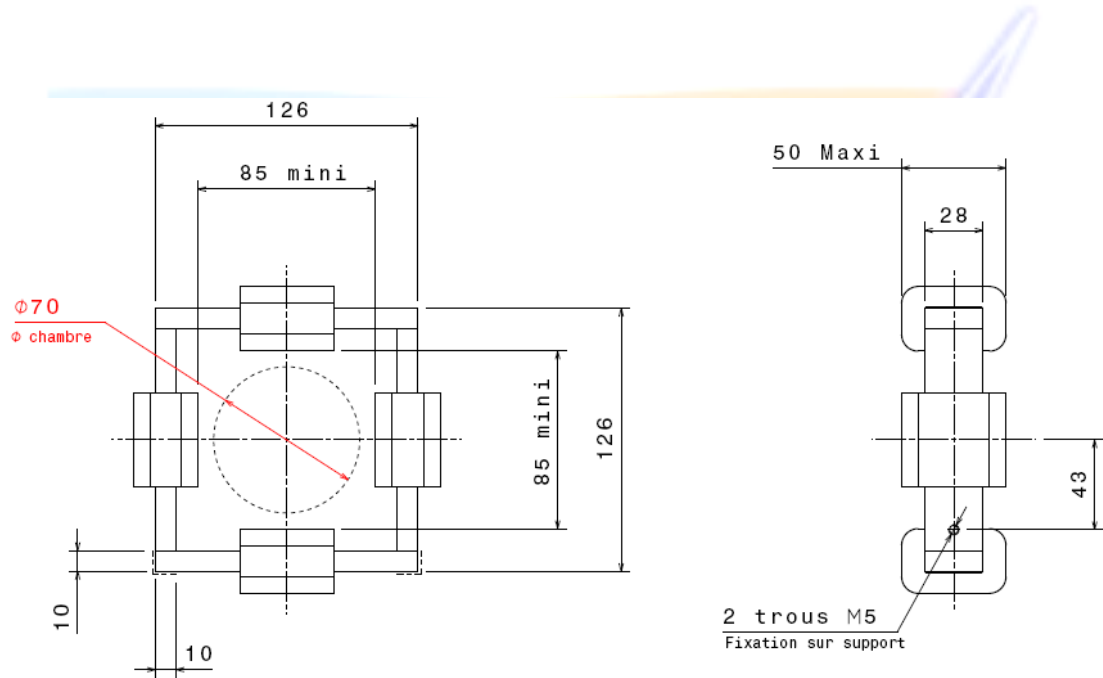


Figure 2.4. Schematic of the beam steering coils. Dimensions are in mm.

All together, the steering coils need 4 bipolar DC power supplies. Their maximum current is 10 A.

2.3 Acceleration section

The acceleration section is shown in Fig. 2.5. Its characteristics are given in Table 2.5.



Figure 2.5. Picture of the SOLEIL LIL acceleration section.

Length	4.5	m
Number of cells, mode	135, $2\pi/3$	
Frequency	2998.55 at 30°C	MHz
R_s	63÷74	MΩ
Q	14800	
Attenuation	7.4	dB
Energy gain @ 15 MW	60	MeV
τ	1.35	μs
Ez max.	18.2	MV/m

Table 2.5. Characteristics of the acceleration section.

In a second stage of the ThomX project, a call of tender will be issued for a new acceleration section that should be shorter in order to make the machine more compact.

2.3.1 The RF source

Figure 2.6 shows the RF source schematic.

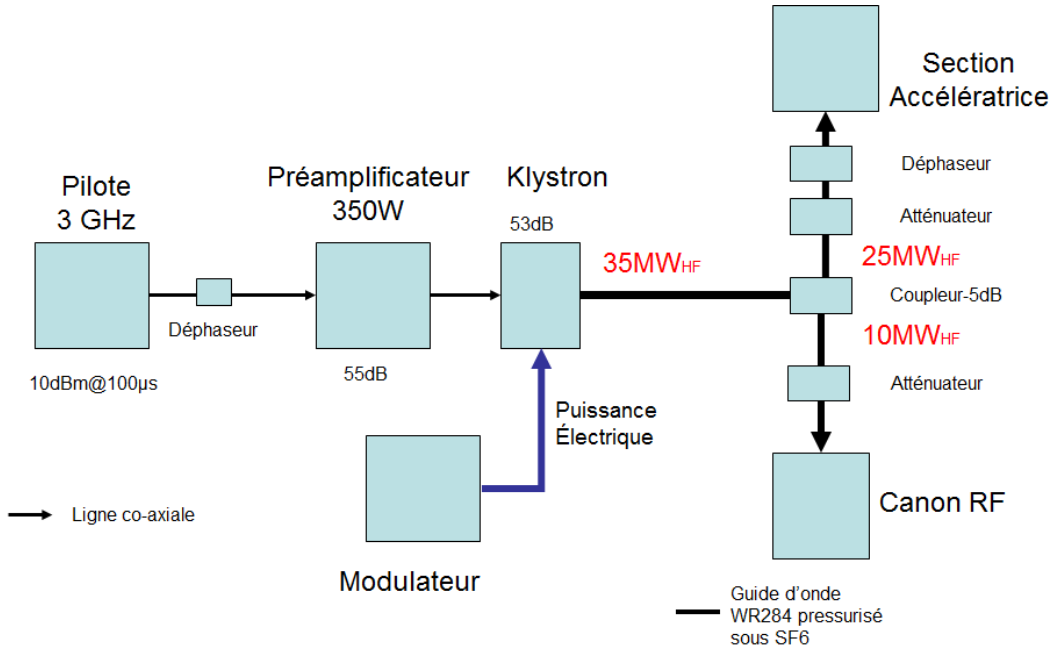


Figure 2.6. Schematic of the RF source.

The RF timing and its synchronization are described in chapter 5. A clock signal is sent to the linac which uses it to trigger a 3 GHz synthesizer. Its output is fed to a preamplifier which brings its power to 350 W. The preamplifier is triggered at 50 Hz. Then the 3 GHz signal is amplified by a klystron whose gain can reach 53 dB to produce a 35 MW wave as required by ThomX. This power is distributed via a waveguide network which is described below.

To drive the klystron, one needs a modulator delivering a pulsed high voltage (HV) whose specifications are given in Table 2.6. The klystron cathode must be heated by a power supply that provides a current rising slowly from 0 to 25 A and a voltage rising from 0 to 30 A in 20 minutes. A precision of 1% on the current value is required. The klystron is generally equipped with focusing coils and their power supply whose standard parameters are 40 A, 120 V.

Repetition rate	50	Hz
Plateau length @ 99 %	> 3	μs
Plateau ripples	< ± 0.5	%
Pulse duration at 50 %	6	μs
Rise time 10 %÷90 %	< 0.5	μs
Fall time 90 %÷10 %	< 1	μs
Pulse to pulse stability	< 0.5 %	%
Voltage range	0÷300	kV
Peak current @ 285 kV	300	Hz

Table 2.6. Modulator specifications.

The classical and well-proven modulator technology relies on the high voltage (40 kV) loading of a delay line made of inductances and capacitances. The delay line is switched by a thyratron. A new technology is presently emerging based on solid-state amplifiers. Each amplifier produces a 100 V

pulse. Thus to produce a 40 kV pulse, roughly 400 amplifiers are put in a rack and their output pulses are added. The performances of both technologies are similar.

2.3.2 RF network

The RF power is transported and distributed to the electron gun and the acceleration section by a waveguide network shown in Fig. 2.7.

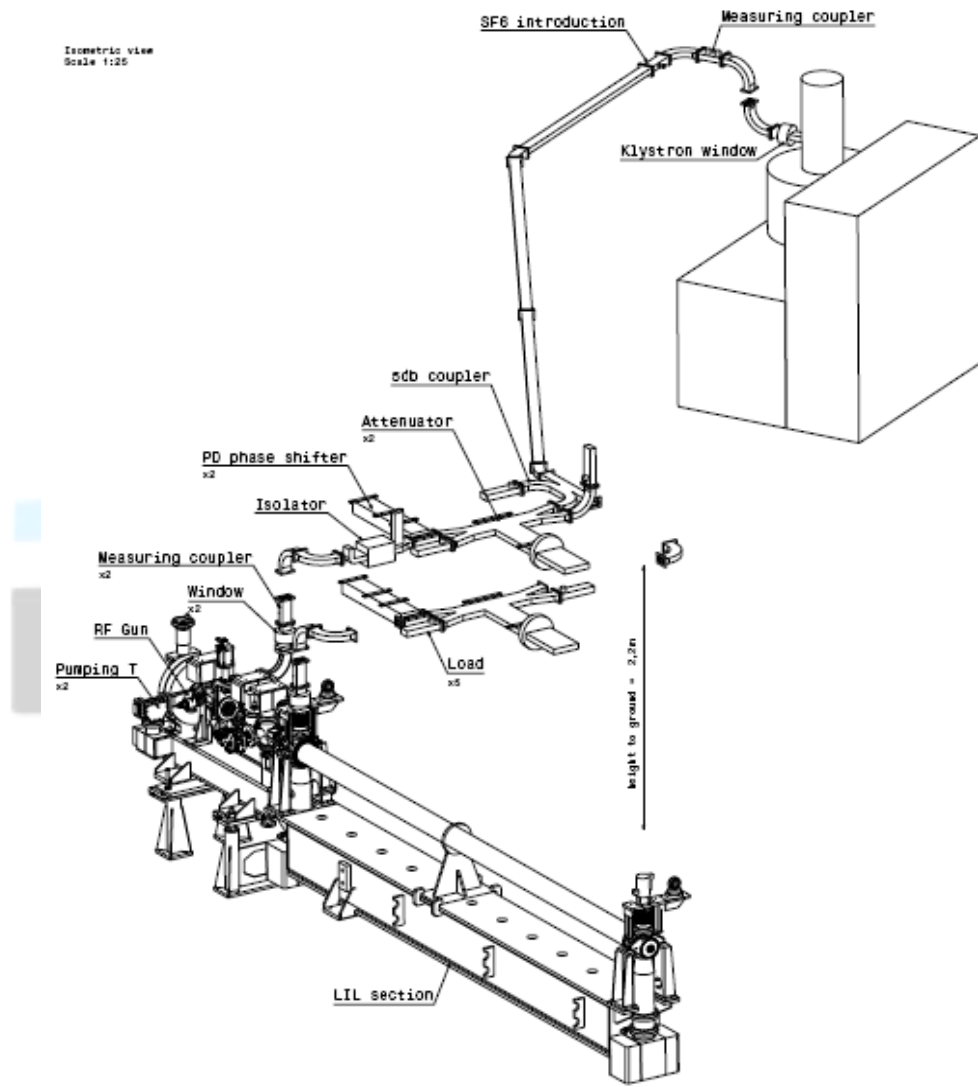


Figure 2.7. Schematic of the RF waveguide network.

The WR 284 waveguide network is pressurized at two bars with SF6 between ceramic windows at the klystron output and at the acceleration structure entrance. A 5 dB bidirectional coupler splits the power in two channels. In the branch which runs toward the electron gun, there is a 10 dB attenuator and a circulator to protect the klystron from the RF power reflected by the electron gun. In the branch running toward the acceleration structure, there is a 10 dB attenuator and a phase shifter to adjust the relative phase between the gun and the acceleration section. Various RF loads (five in total) ensure the system safety by absorbing of RF power of the reflected waves.

The network also includes three couplers to measure the incident and the reflected RF power. One is placed at the klystron power exit, one is placed at the gun entrance, and the last one is placed at the acceleration section entrance. The RF gun is equipped with a loop that measures the stored RF energy. All of these loops used for measurements are weakly coupled, at -70 dB. The signals are measured with crystals or C boxes.

2.4 Beam dynamics

2.4.1 Nominal operation

The beam dynamics was simulated with the PAMELA tracking code for the ThomX nominal parameters, *i.e.* a bunch charge of 1 nC at 50 MeV. The 50 MeV can be obtained with an electric field of 80 MV/m in the RF gun and 12.5 MV/m in the acceleration section. It is clear that a different set of field values can lead to the total of 50 MeV. In particular, one may wish to operate the gun at a higher field in order to improve the beam quality. We will operate the linac with this possible improvement in view.

The beam will be accelerated on crest. Thus the coil magnetic fields are the only parameters savable to minimize the transverses and the longitudinal emittances. Simulations have shown that for precise magnetic field values (see Table 2.7) the e^- beam emittances are optimized as illustrated in Fig. 2.8

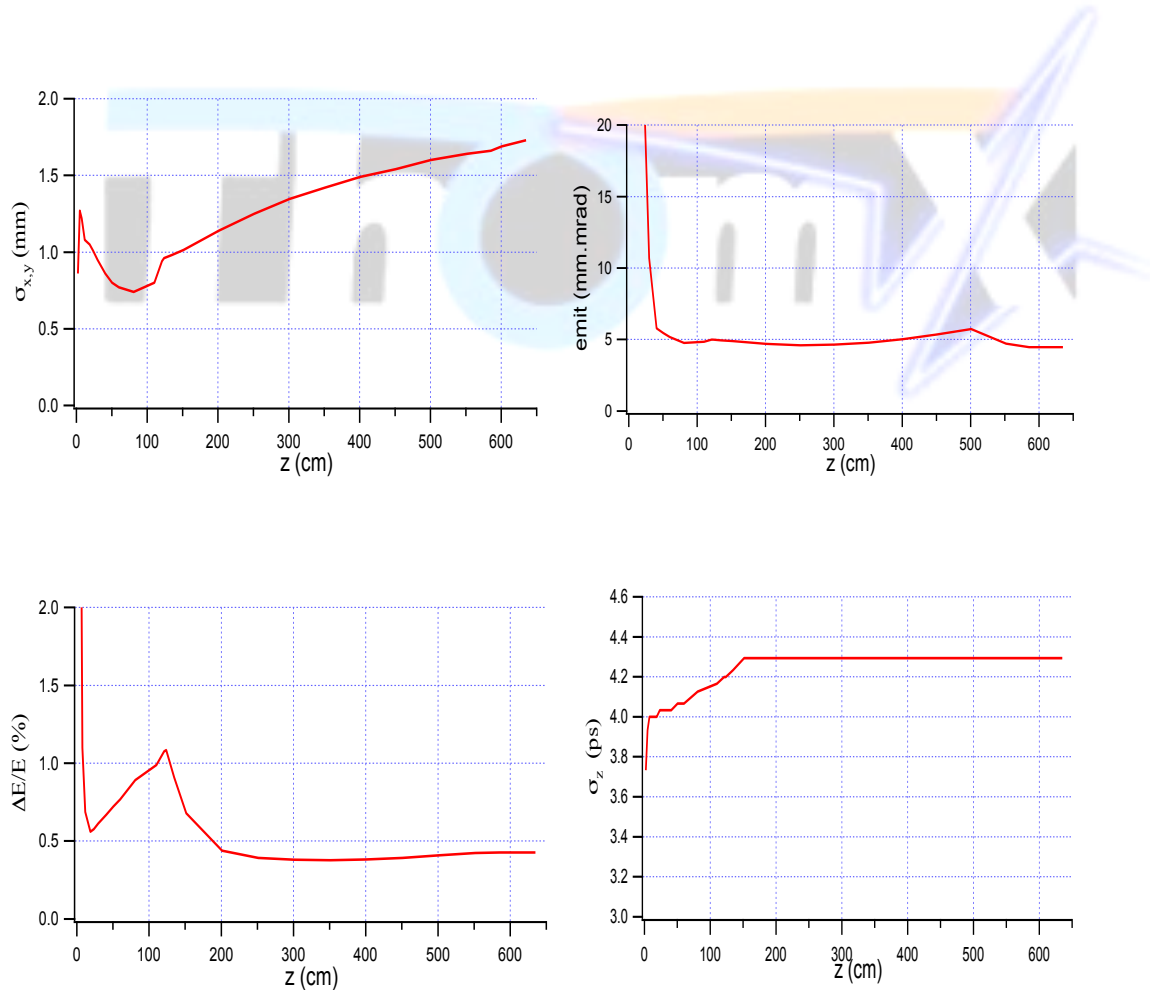


Figure 2.8. Beam characteristics (rms values) as a function of the distance along the accelerator (z coordinate). Upper left panel: Transverse size; upper right panel: normalized emittance; lower left panel: Energy spread; lower right panel: Bunch length.

The beam parameter values at the linac end are given in Table 2.7.

Beam parameters	value	unit
Energy	50	MeV
Beam size	1.7	mm
Normalised Emittance	4.4	$\pi \text{ mm mrad}$
Energy spread	0.4	%
Bunch length	4.3	ps

Table 2.7. Beam parameter rms values at the linac end.

The accelerator parameters which should ensure the above beam characteristics are given in Table 2.8.

RF structure parameters	value	unit
E_z in the gun	80	MV/m
P_{RF} in the gun	5	MW
E_z in the section	14.2	MV/m
P_{RF} in the section	14	MW

Solenoid parameters	value	unit
B_z max	2500	G
I_{bc}	-274	A
I_{foc}	326	A

Laser parameters	value	unit
Energy impinging on a Mg photocathode	10	μJ
Square transverse profile, diameter	2	mm
Variation of the intensity from axis to border	1.4	%

Table 2.8. Summary of the linac parameters.

2.4.2 Alternative operation modes

Concerning the injector, other operation modes can be envisaged. One, at least, will occur, namely an operation at 70 MeV in order to extend the X-ray energy range up to 90 keV. Such an option has attractive applications. In this mode, the electron beam performances should remain exactly the same as the ones prevailing at 50 MeV (cf. Table 2.7). For the accelerator parameters, the only change is the RF power required for the acceleration section: it must reach 19.5 MW, instead of 14 MW at 50 MeV.

The operator can also be tempted to change the RF phase. The one used in the simulations gives the minimum emittance. A phase shift of -10° of the RF gun with respect to the laser could lead to an energy spread reduction by a factor 2 at the expense of an emittance degradation. Whatever the goals, the linac operator must be aware of the high sensitivity of the beam parameters to the RF phase. This is illustrated in Fig. 2.9. An error of 5° in the acceleration section phase results in almost a doubling of the energy spread.

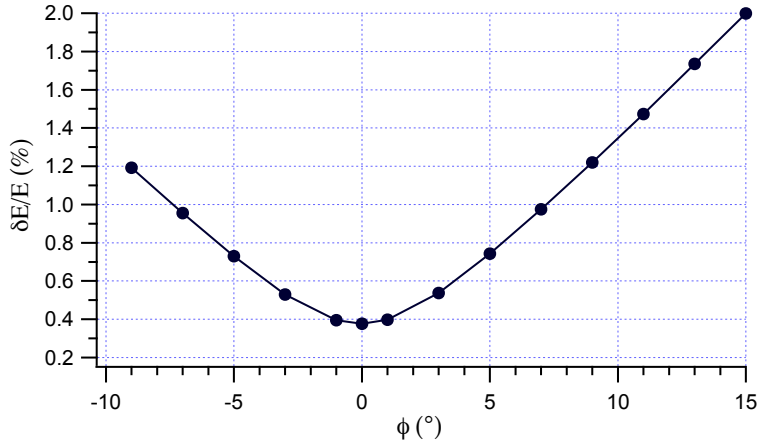


Figure 2.9. Energy spread at the linac end as a function of the RF phase in the acceleration section, all other parameters keeping their nominal values.

The RF electrical field in the gun also plays an important role in the beam performances. The results of simulations of the emittance variation as a function of the gun electric field are presented in Fig. 2.10. If this field reaches 120 MV/m, the emittance is reduced by 20 % with respect to the 80 MV/m case. However, the possibility to operate the gun at such a high gradient can only be assessed experimentally.

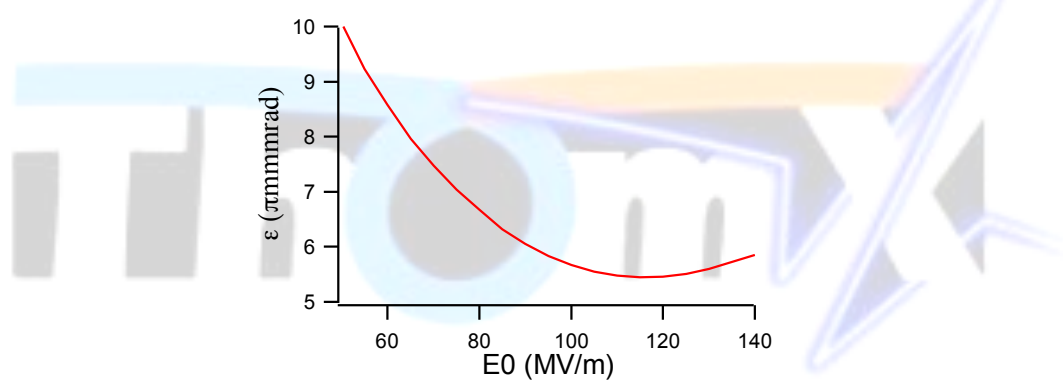


Figure 2.10. Injector beam emittance as a function of the electric field in the electron gun (Gaussian laser beam, 1 nC e⁻ bunches).

The injector performances as a function of the bunch charge are summarized in Table 2.9. Three modes will be available in order to reduce the effect of collective instabilities at injection.

Parameters	Mode 1	Mode 2	Mode 3	Unit
Q	1	0.5	0.1	nC
$\sigma_{x,y}$	1.65	1.5	0.8	mm
$\epsilon_{x,y}$	4.7	3.3	1.1	$\pi \cdot \text{mm} \cdot \text{mrad}$
σ_z	4.4	4	3.3	ps
σ_E/E	0.4	0.3	0.2	%

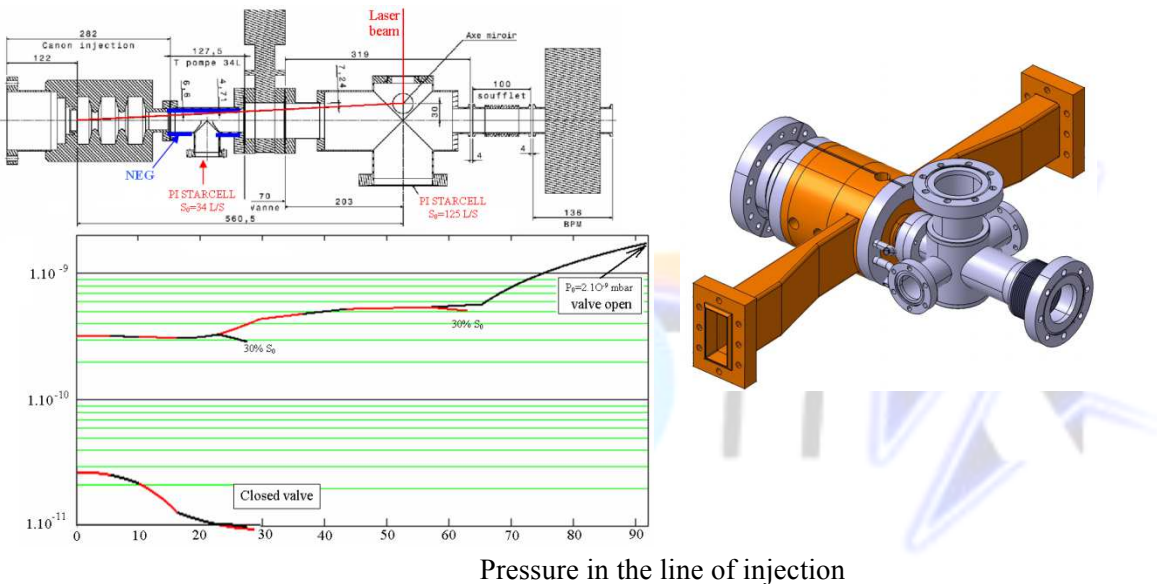
Table 2.9. Linac beam performances (rms values) as a function of the bunch electric charge.

As one can see in the above Table, reducing the bunch charge by a factor 10 leads to an emittance reduction by a factor 4. Although the X-ray flux is reduced, the source brightness, *i.e.* the ratio of the flux to the divergence, is improved by a factor 16. As a consequence, a higher number of X-rays can be

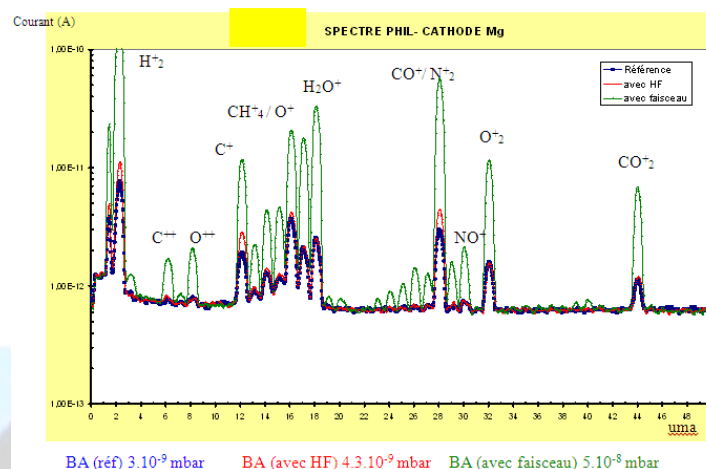
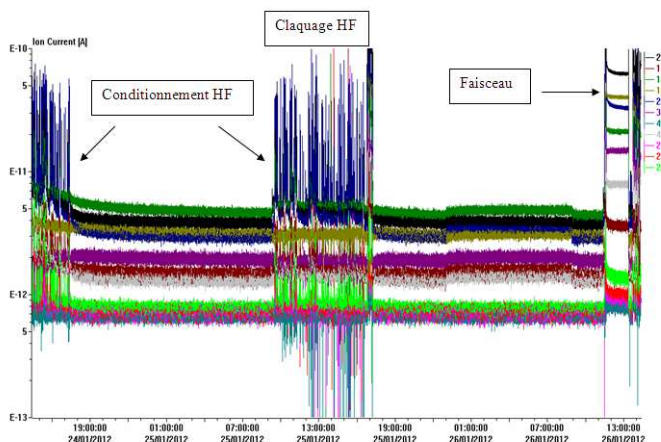
transported to a sample (number per unit area). Whatever the eventual benefits to the X-ray production, the advantage for the accelerator to operate at a lower charge per bunch is clear: the reliability of the accelerator is much enhanced, the laser energy requirement is reduced, and it becomes also possible to use a copper photo-cathode instead of a magnesium one, easier to handle. But the main advantage lies in the ring operation. Indeed, a 1 nC bunch whose length is only 4 ps induce a strong wakefield stemming from the interaction between the beam and the vacuum pipe. Such a wakefield perturbs the beam and may cause oscillations of the bunch centroid, possibly instabilities, and thus a reduction of the X-ray production rate.

2.5 Photo-injector and acceleration section vacuum

Simulations of the photo-injector vacuum have been performed assuming a pressure of $3 \cdot 10^{-8}$ Pa at the cathode location and requiring a vacuum time constant (V/S) that ensures an easy gun conditioning. This constraint must be respected to maintain a 10^{-7} Pa pressure at the acceleration section entrance where the system will be baked to obtain an outgassing rate $\tau = 5 \times 10^{-10}$ Pa m s⁻¹(N₂).



The use of a semi-conductor cathode (Cs₂Te) puts severe constraints on the vacuum and requires a preparation and a transfer chamber. To avoid these complications, some tests have been made on a metallic cathode (Mg). The first attempt ran into difficulties (it took 12 h to reach a gradient of ~ 60 MV m⁻¹), we observed pressure rises and sparks. In presence of only the RF power, we observed hydrogen, CO and CH₄ outgassing (as the main components). A slight reduction in the quantity of water and oxygen was noticed due to chemical re-composition. When the laser beam was introduced to extract electrons, a pressure increase by a factor of ten was observed. The 24th, 25th and the 26th peaks also significantly increased for the H_xC_y compounds, but no Mg was measured.



Gas analyzes during the conditioning of cathode Mg

On the basis of simulations and experimental results, we identified the need for the following items:

- 2 ion pumps, 40 l s^{-1} (upstream of the cathode & injector) with their baking systems and power supplies,
- 2 ion pumps, 55 l s^{-1} (for the RF network) with their baking systems and power supplies,
- 1 ion pump, 150 l s^{-1} (for the laser introduction chamber) with its baking system and power supply,
- 1 ion pump, 300 l s^{-1} (for the acceleration section) with its baking systems and power supply,
- 1 gate valve manually actuated DN 100 (injector- upstream) and a baking valve,
- 1 gate valve electro-pneumatically actuated DN 63 (injector - downstream) and a baking valve,
- 1 gate valve electro-pneumatically actuated DN 40 (injector- downstream) and a baking valve,
- 3 Pirani gauges (before the injector ; injector ; laser introduction; acceleration section),
- 3 cold cathode gauges (after the injector; injector ; laser introduction ; acceleration section),
- 2 power supply gauges;
- 1 residual gas analyzer (RGA),
- 1 turbo pump (DN 63 $\sim 80 \text{ l s}^{-1}$),
- 1 rotary vane pump ($\sim 12 \text{ m}^3 \text{ h}^{-1}$),
- 4 angle valves manually actuated for pre-pumping DN 63,
- 2 T with RF grids.

Chapter 3. TRANSFER LINE and RING

3.1 Transfer line

The transfer line (TL) has to transport the beam from the linac to the ring and to match the optics of these two devices. In addition, a set of beam diagnostics needed for an efficient injection in the ring are localized along the line as sketched in Fig. 3.1. The transfer line main characteristics are summarized in Table 3.1.

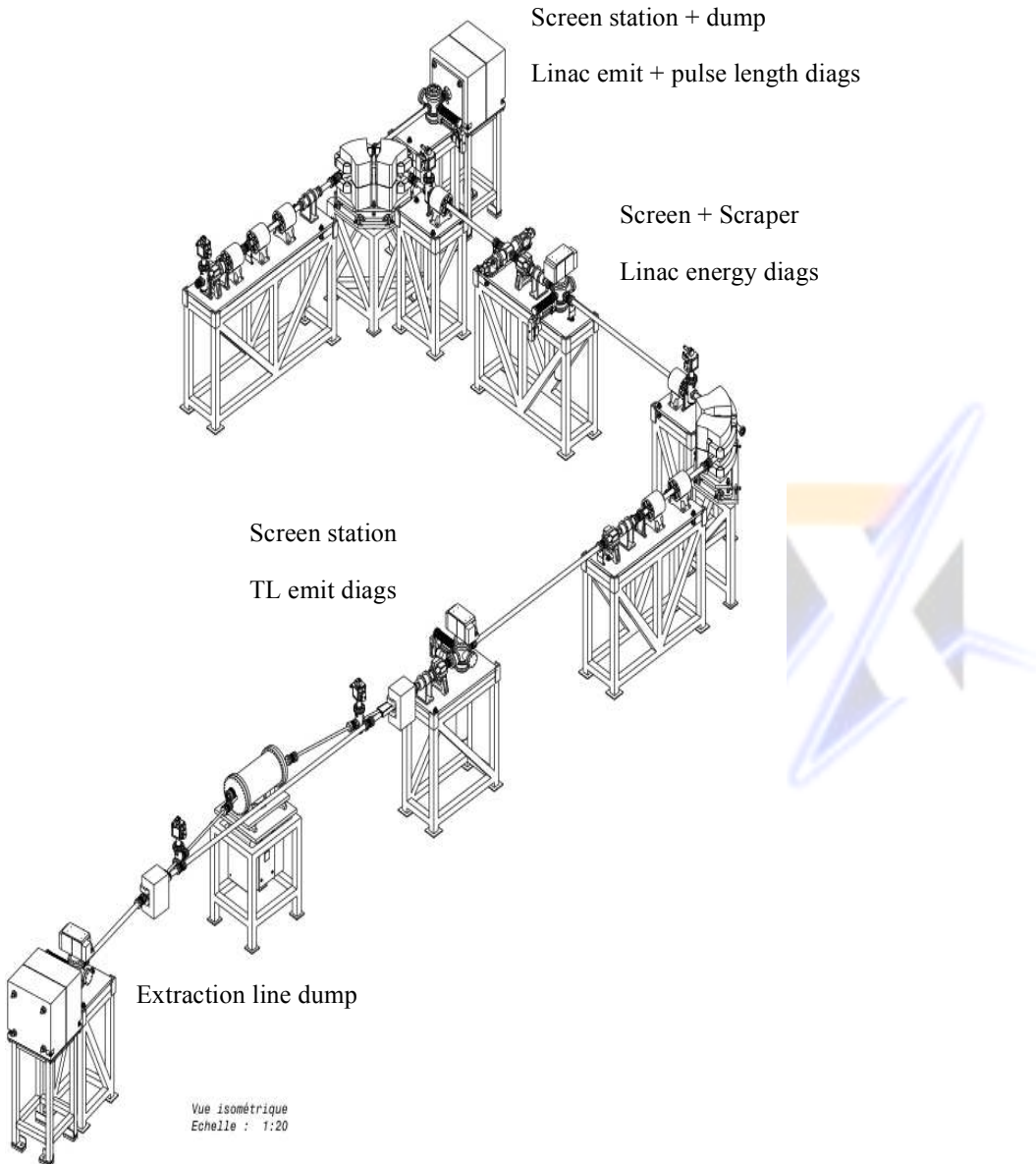


Figure 3.1. Layout of the injection and extraction transfer lines.

A particular attention is paid to ensure a versatile optics that allows the matching of different linac beams to different ring optics. Simulations have been carried out using the BETA code [3.1]. The transfer line optics is optimized in order to accommodate some emittance degradation which may arise from collective effects.

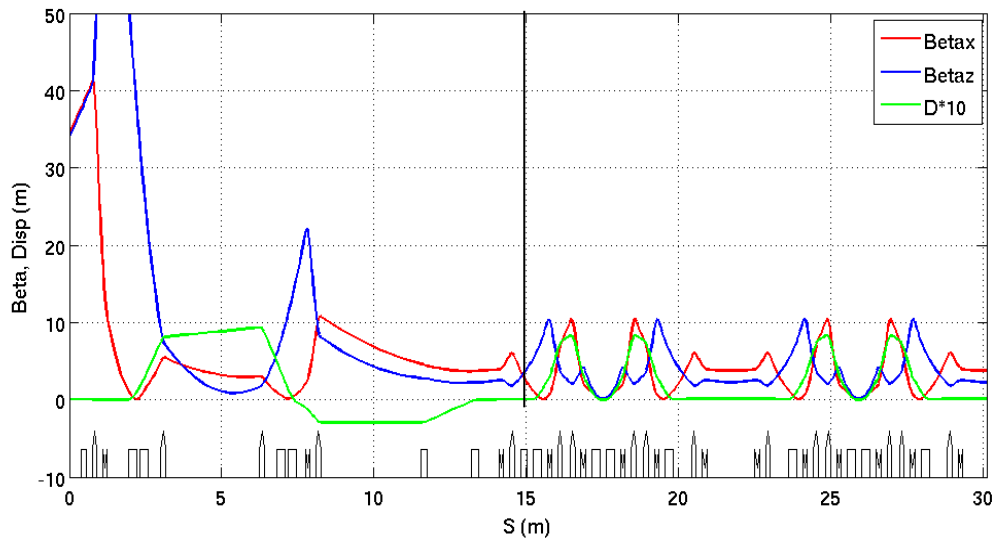


Figure 3.2. Transfer line optics including the ring. The vertical line indicates the ring entrance point.

The nominal transfer line optics is shown in Fig. 3.2, from the linac to the ring, together with the ring. The nominal input bunch Twiss parameters are: $\beta_x = \beta_z = 34$, $\alpha_x = \alpha_z = 4.2$, for $Q = 1$ nC, bunch length = 4 ps (rms) and an optimized normalized emittance of about $5 \pi \text{ mm.mrad}$. The strong bend produced by the four dipoles of the transfer line increases the risk of emittance degradation under collective effects, but simulations show that the emittance increase is only of about 20%, including coherent synchrotron radiation (CSR [2]) and 3D space charge effects (see Fig. 3.3).

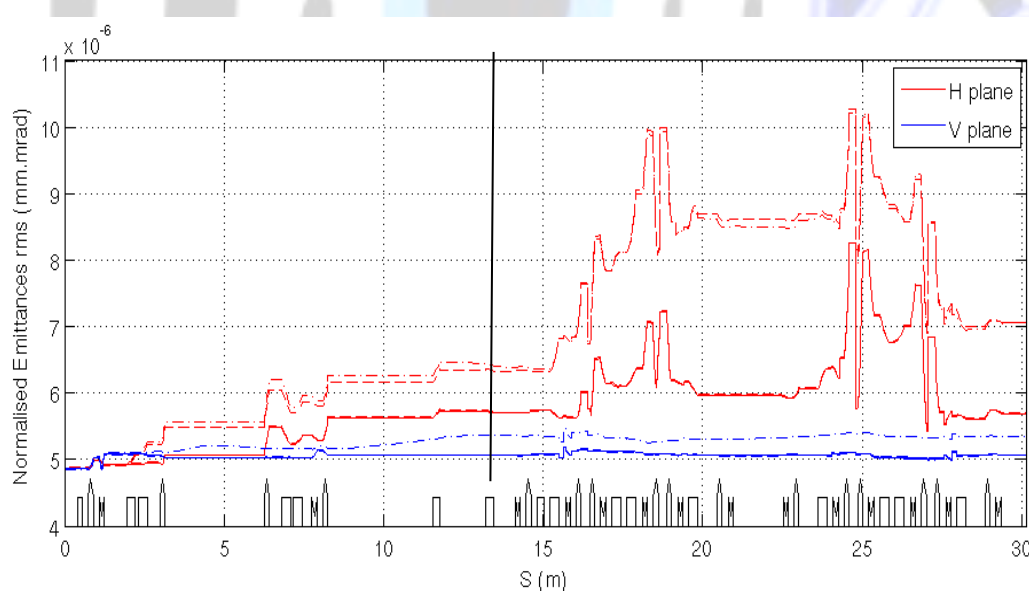


Figure 3.3. Emittance increase due to chromatic (cont. lines), CSR (dashed) and space charge (dot dashed) effects for 1 nC and 4 ps (rms) bunches at 50 MeV along the TL and the first revolution in the ring.

The magnetic elements are identical to those of the ring.

Parameter	value	unit
Length	14	m
Nominal energy	50	MeV
Beta max x, z	70 / 40	m
Maximum dispersion	1	m
Dipole number/family	4 / 1	
Quadrupole number	7	
Biplane corrector number	5	

Table 3.1. Transfer line parameters and components.

Besides ensuring the matching between the linac and the ring, the transfer line must provide the measurement of the beam emittances, the beam energy and the energy spread. Care has been taken to locate the diagnostic stations in a way that ensures accurate measurements of these important parameters.

The emittance measurements will be done by means of the ‘three-gradient’ scheme. (The pepper-pots alternative is also foreseen.) For instance, with an adequate refocusing that produces a double waist (vertical and horizontal) at the screen, it is possible to scan both planes at the same time by varying only one quadrupole gradient (see Fig. 3.4). Other scan variations are also possible. The following figures show the optics retuning as well as the beam spot size variation at the screens of both stations, the one at the linac end and the one downstream of the U-turn.

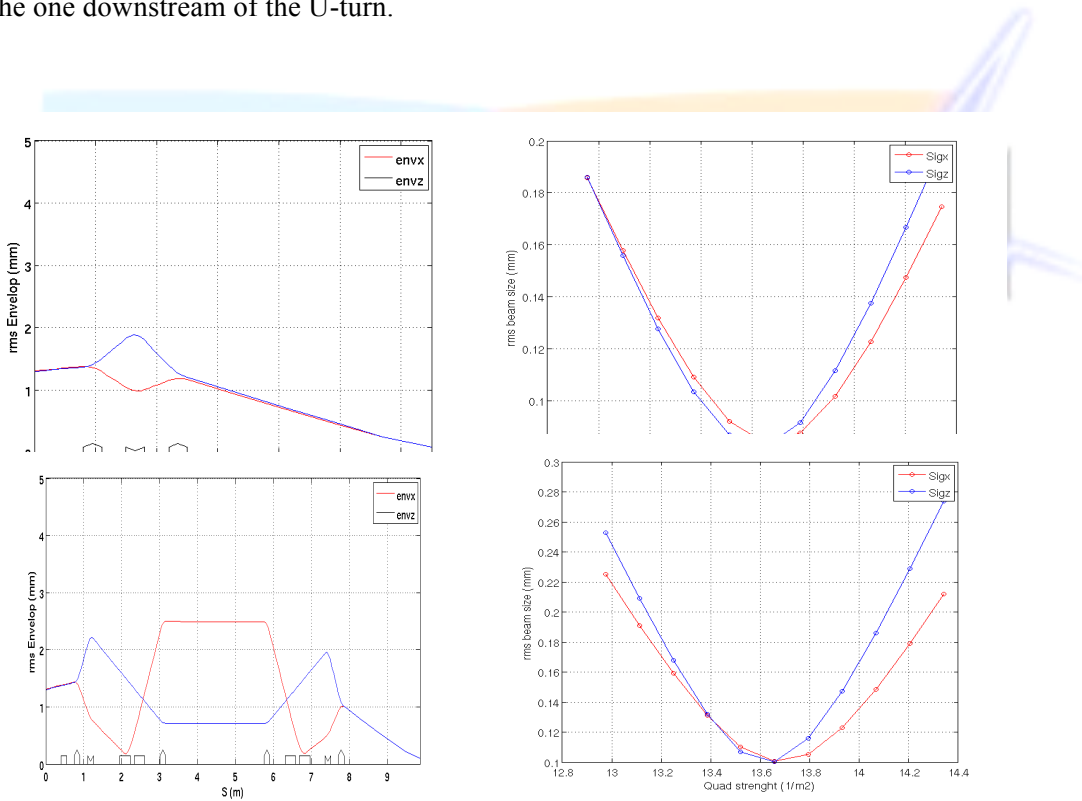


Figure 3.4. Optics retuning and beam spot size scan as observed on the screen (simulation).

The electron energy and its spread are measured in between the dipoles by a dedicated optics. Note that it is also possible to retrieve the bunch length by measuring the energy spread as a function of the linac phase (three-phase scheme).

3.2 Extraction line

To dump the residual beam at the end of the storage time (typically from 20 to 50 ms), an extraction line composed of one small dipole and two quadrupoles is also foreseen. This line will allow the measurement of the beam properties after it has circulated in the ring. The injection/extraction devices are symmetrically implemented in the ring injection section.

3.3 Storage ring

3.3.1 Optics and lattice

Thom-X must produce a high X-ray flux of $10^{11}\div10^{13}$ ph/s, in a stable way. The flux depends on the characteristics of the electron bunch and of the laser pulse. Assuming a 1 nC electron bunch charge at 50 MeV and a 20 to 30 mJ laser pulse (@ 1.24 μm) the optics constraints at the interaction point (IP) are as follows:

- an rms size of the electron beam less than or equal to 70 μm in the transverse plane requiring low beta functions of 0.1 m with an rms geometric emittance of 50 nm.rad injected from the linac (5 mm.mrad normalized),
- a vanishing dispersion at the interaction point in order to avoid a beam size increase resulting from an e- energy spread increase, as well as to avoid potential synchro-betatron coupling resonances,
- a bunch length less than 20-30 ps to ensure a good overlap with the laser pulse (the crossing angle will be 2°), and long enough to reduce collective effects stemming from the pipe impedance, CSR, bunch internal scattering, etc.

Besides these specific IP constraints, there are two general layout constraints, namely

- a ring circumference as short as possible with enough straight sections to accommodate the interaction region, the RF, the injection and possible other equipment as RF and transverse feedback systems,
- the need for some flexibility as far as the optics and the working point are concerned.

The ring layout and its optics are based on a two-fold symmetric lattice with four achromatic arcs and four straight sections: two short ones (0.2 m) and two long ones (1.6 m). This layout preserves the ring compactness and provides an adequate interaction region in one of the two straight sections, between two adjacent dipoles (cf. Fig. 3.5). The main ring characteristics are summarized in Tables 3.2 and 3.3.

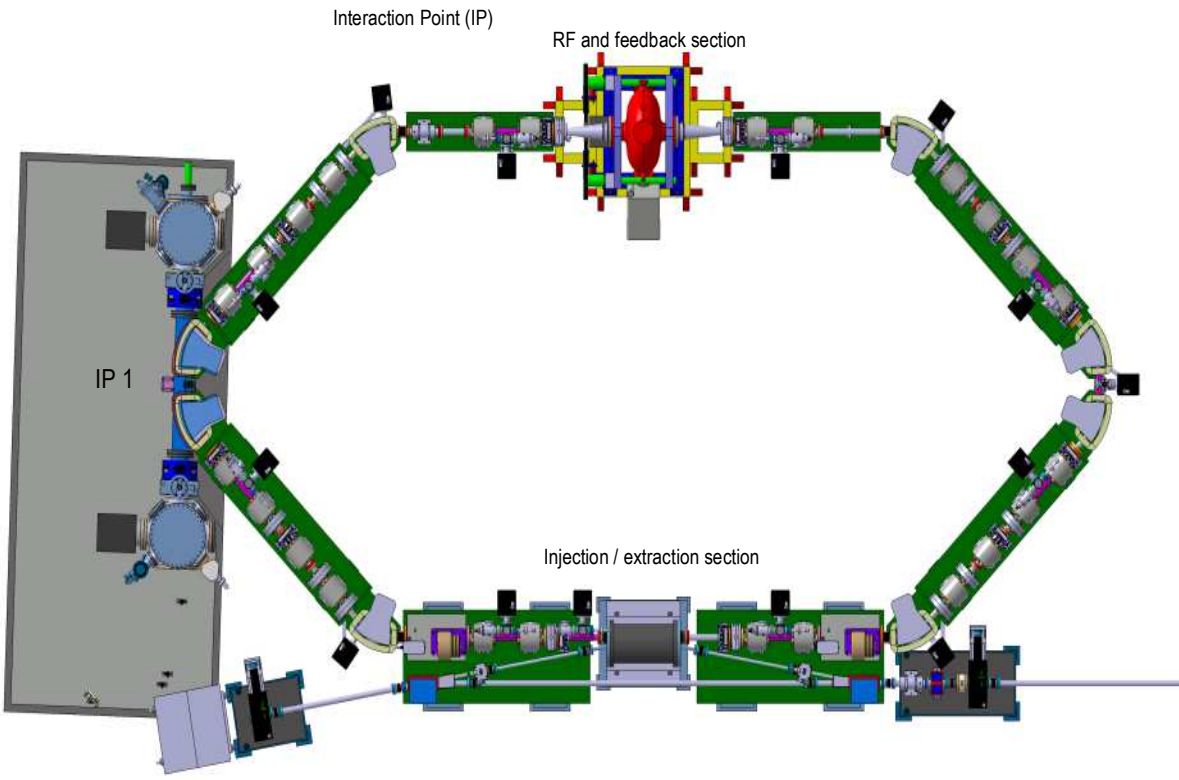


Figure 3.5. Ring layout.

The laser pulse frequency is the harmonic 2 of the e^- bunch revolution frequency in the ring, *i.e.* 35.7 MHz. This leaves open the possibility of storing two bunches in the ring in order to increase the Compton flux, but at present this operation mode is not taken into account because of injection constraints. The optical cavity mirrors are located outside the ring vacuum chamber, thus enabling a mirror substitution without affecting the ring. In addition, the extraction of the X-rays can be performed closer to their source than in the case where the optical cavity is inserted in a long straight section.

The two long free straight sections accommodate the injection/extraction devices for one, and the RF and feedbacks for the other.

The ring is composed of 8 dipoles, 24 quadrupoles and 12 sextupoles. Its circumference is 16.8 m long; the revolution frequency is 17.85 MHz. The RF frequency is set at 500 MHz, *i.e.* at the 28th harmonic of the ring revolution frequency. The nominal optical functions have been optimized with the BETA code [3.1]. They are plotted in Fig. 3.6. The dispersion vanishes in the long and in the short straight sections (RF, injection and interaction regions). The beta functions decrease down to 0.1 m at the IP to provide a 70 μ m focus, assuming that the injected beam has an emittance of 50 nm.rad (5 mm.mrad normalized) in both the vertical and the horizontal planes.

Ring parameters	value	unit
Circumference	16.80	m
Nominal energy	50	MeV
Betatron tunes n_x, n_z	3.17 / 1.74	
Beta max x, z	11 / 11	m
Dispersion max	0.8	m
Beta x/z, dispersion @ IP	0.1 / 0.1 / 0	m
Momentum Compaction Factor	0.014	
RF frequency	500	MHz
RF harmonic	28	
RF voltage	300	kV
Synchrotron frequency	360	kHz
Period / Revolution frequency	56 / 17.84	ns/MHz
Natural chromaticities	-3.2 / -8.2	
Dipole nb, family	8 / 1	
Quadrupole nb, families	24 / 6	
Sextupole nb, families	12 / 3	
Corrector nb, families	12 / 12	

Table 3.2. Ring parameters.

	Max field @ 70 MeV	Bore length	Gap / Diameter
Dipole	0.7 T	276.5 mm (R=352 mm)	40 mm
Quadrupole	5 T/m	150 mm	41 mm
Sextupole	15 T/m ²	60 mm	42 mm
Correctors	$5 \cdot 10^{-4}$ T.m		

Table 3.3. Main magnet characteristics.

Taking into account the constraints imposed by the optical functions, the chromaticity and the dynamic aperture, the operating point was chosen with tunes: $\nu_x=3.17$ and $\nu_z=1.74$. There is still enough flexibility to vary these tunes by ± 0.2 without spoiling the main ring performances. The momentum compaction factor can also be changed over a large range in order to scan the best working point regarding the beam dynamics and the X-ray flux.

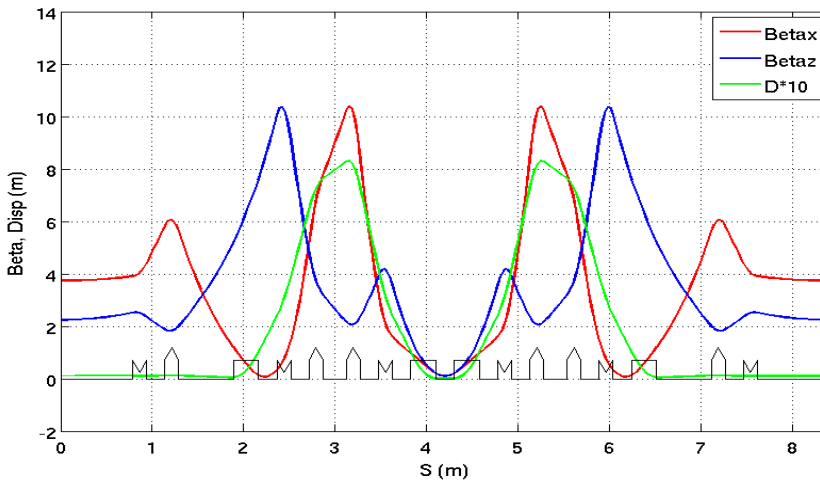


Figure 3.6. Nominal beta functions and dispersion over one super-period.

The RF acceptance for the nominal momentum compaction factor (MCF) and a larger one including the non-linear MCF and the vacuum pipe limit are plotted in Fig. 3.7.

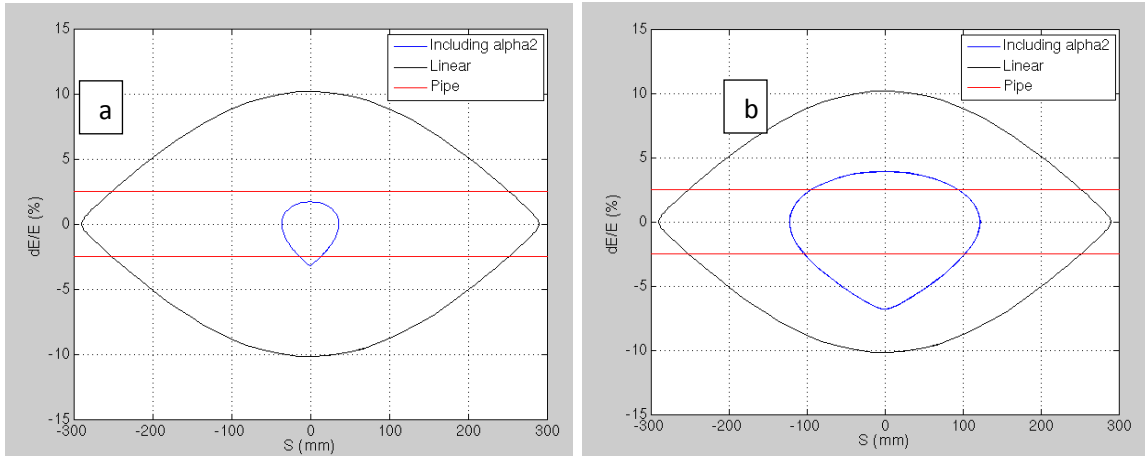


Figure 3.7. RF acceptance. Left panel: nominal lattice. Right panel: for a MCF twice as large as the nominal one. $V_{RF} = 300$ kV.

RF acceptance	nominal	r56 = - 0.2 m	r56 = - 0.4 m
Linear (RF bucket)		10%	10%
Non linear	-3.2 % +1.8 %	-6.8 % +4 %	
Pipe limit	2.5 %	2.5 %	

Table 3.4. RF acceptance for two different values of the momentum compaction factor.

The two following plots (Fig. 3.8) show (i) the vacuum chamber occupation by the beam at injection when the emittance is 50 nm.rad and the energy dispersion is 0.3 %, and (ii) at the end of the storage cycle when the emittance reaches 300 nm.rad and the energy dispersion reaches 0.6 % (see section 4.3.8). The orbit components (misalignment errors) are not included since they are negligible once corrected. The choice of the pipe aperture (40 mm in H by 28 mm in V, full aperture) takes into account several constraints: the beam pipe occupation, the magnet bore radius, the vacuum and the coherent synchrotron shielding [3.2].

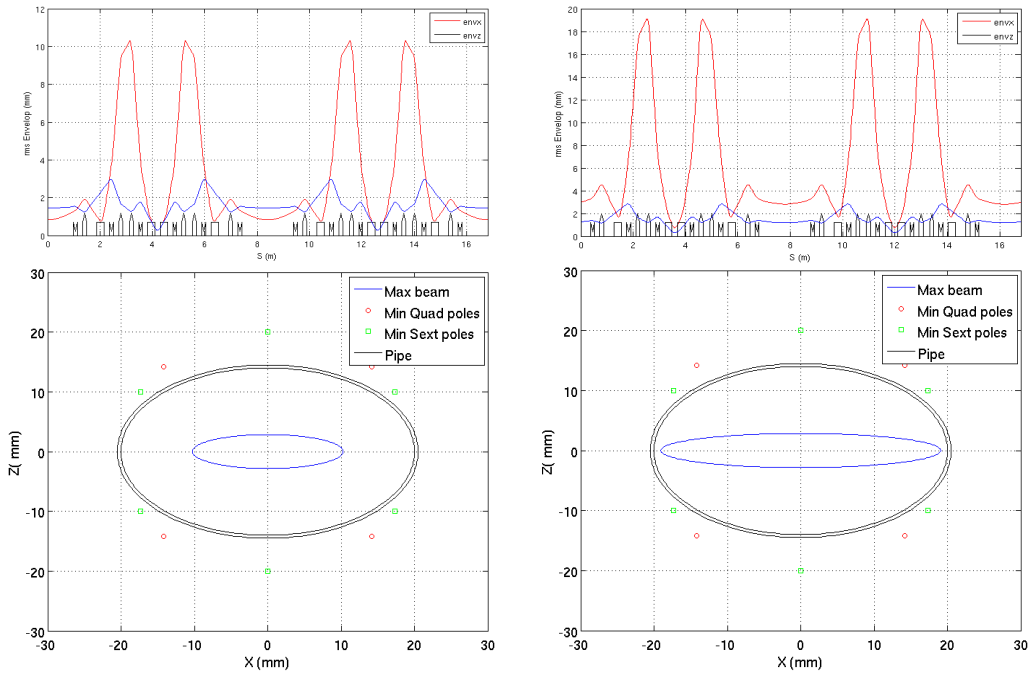


Figure 3.8. Transverse occupation (3 rms) of the vacuum chamber at injection (left) and at the end of the storage cycle (right).

3.3.2 Non-linear dynamics

The natural horizontal and vertical chromaticities are respectively -3.2 and -6.8. Chromaticity corrections are achieved by means of 12 sextupoles (3 families) located in the dispersive sections. Without performing a specific optimization, the dynamic aperture is large enough, about 50 times the rms transverse size of the injected beam (see Fig. 3.9), the quadrupole fringe fields being taken into account. Furthermore, this dynamic aperture remains about the same for off-momentum particles (up to $\pm 3\%$) compared to particles having the nominal energy. The fringe field of the dipole magnets introduces high order non-linear components. Since the Thom-X dipoles are short, with a large gap, their magnetic design (see section 3.4) has been carefully worked out in order to maintain the dynamic aperture.

Pole number	6	8	10	12	18	20	28	30
Inner dipoles	+10	0	+3					
Outer dipoles	-16	-1	-6					
Quadrupoles				+10		+5		-5
Sextupoles					+10			-10

Table 3.4. List of multipole tolerances for each kind of magnets expressed in 10^{-4} relative field variation at 18 mm radial position.

Figures 3.9 and 3.10 show the change of the dynamic aperture with and without considering the multipole (the fringe field of the quadrupoles is also taken into account in these plots). These Dynamical Apertures (DA) have been calculated with two different codes BETA and TRACYIII. They

both give very similar results. In addition the TRACYIII code, dedicated to long symplectic tracking, performs Frequency Map Analysis (FMA) giving more detailed information concerning the particle diffusion process.

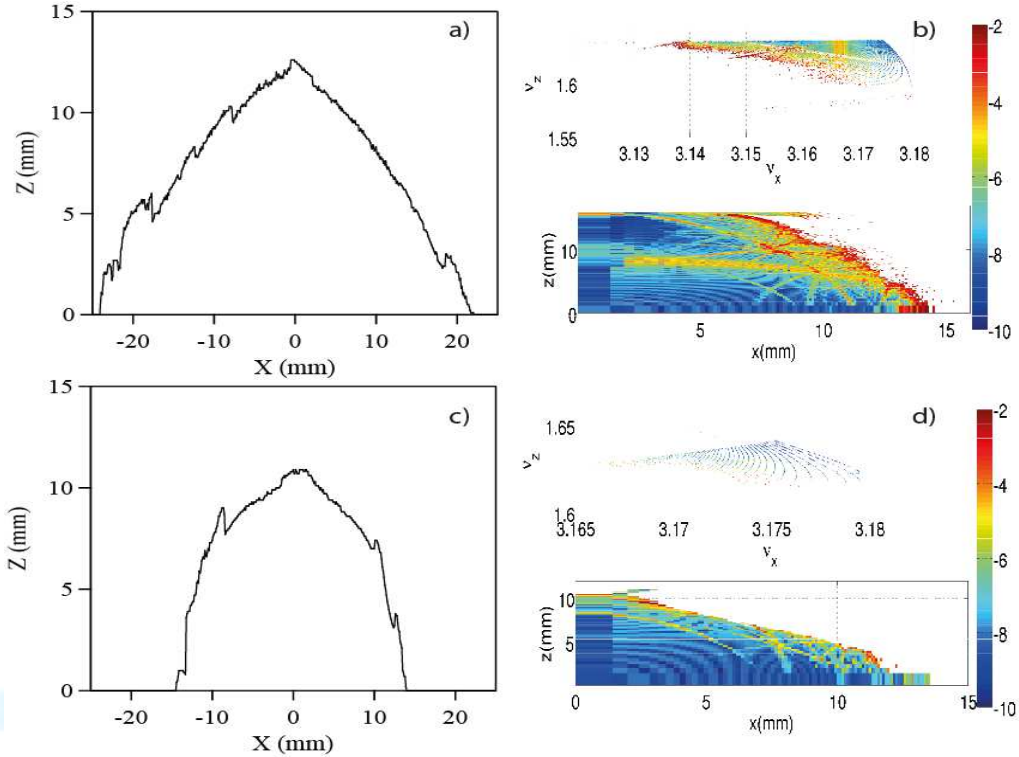


Figure 3.9. On-momentum DA and FMA for the nominal ThomX lattice. Beta code left and TracyIII code (right), sextupoles only (top) and including magnet multipole tolerances (bottom).

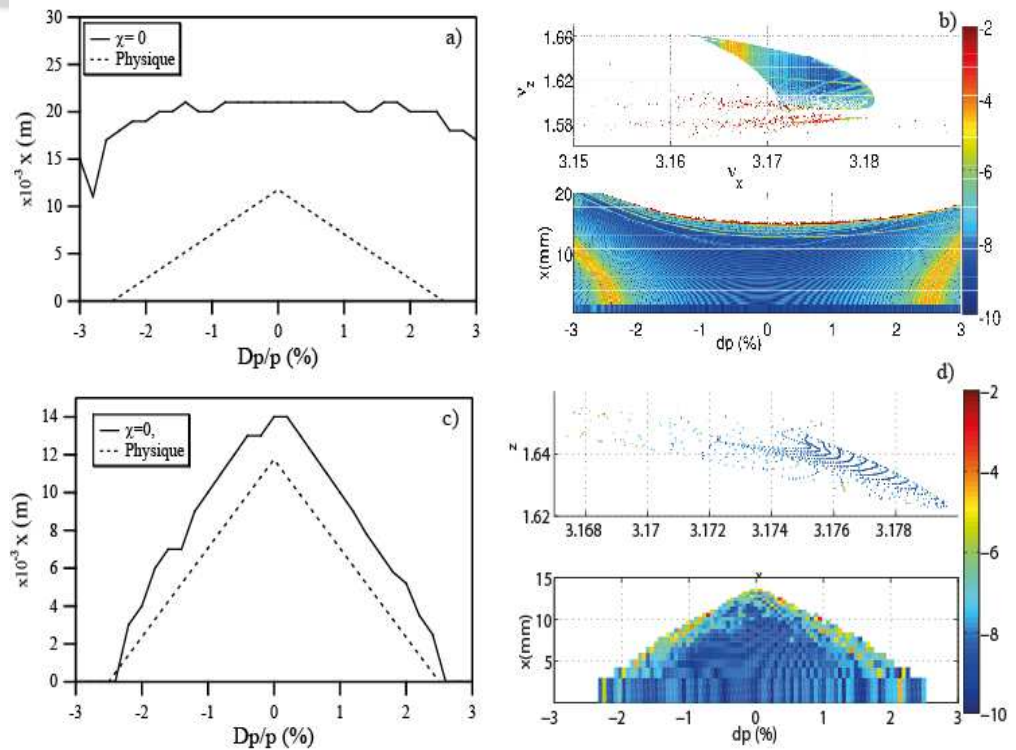


Figure 3.10. Off-momentum DA and FMA for the nominal ThomX parameters. Beta code left and TracyIII code (right), sextupoles only (top) and including magnet multipole tolerances (bottom).

3.3.3 Collective effects, feedbacks

At low energy and thus low beam rigidity, the electron bunch is sensitive to electromagnetic self-perturbations that act revolution after revolution in the ring. Several instability sources can be identified:

- Interaction with surrounding metallic items, such as the resistive walls (RW), the RF cavity and various discontinuities such as bellows, BPMs and flanges, HOMs etc,
- Space charge forces,
- Coherent synchrotron radiation (CSR).

These interactions affect the bunch energy and the bunch longitudinal time-profile leading to distortions, emittance growth, bunch oscillations or even, above some threshold, instabilities and beam losses. Similar interactions may also affect the transverse beam dynamics, but to a lower extent. The two relevant parameters for the instability threshold are the bunch charge and its length. The strength of the interaction is proportional to the bunch charge and varies inversely with the bunch length.

The two plots in Fig. 3.11 show the longitudinal wakefield over one revolution at 50 MeV generated by a 1 nC Gaussian bunch with an rms length of 1.2 and 6 mm (4 and 20 ps). Five different contributions are compared in this figure:

- the shielded CSR following the Murphy and Skrinsky [3.2] formulation with a beam pipe full height of 40 mm, a dipole field of 0.5 T and a curvature of 0.352 m,
- the longitudinal space charge (LSC),
- the resistive wall (RW) following the K Banes and M. Sands formulation [3.3] with a full beam pipe height of 40 mm and an electrical conductivity of $1.4 \cdot 10^6$,
- the vacuum vessel broadband component including 12 BPM, 12 flanges and 12 bellows based on the synchrotron SOLEIL type. This potential has been calculated by means of the HFSS finite elements code [3.4],
- the 500 MHz ELETTRA type cavity broadband component. This potential has been calculated by using the HFSS finite element code.

They exhibit a very strong CSR wake field (up to few per mil) with the shorter bunch case.

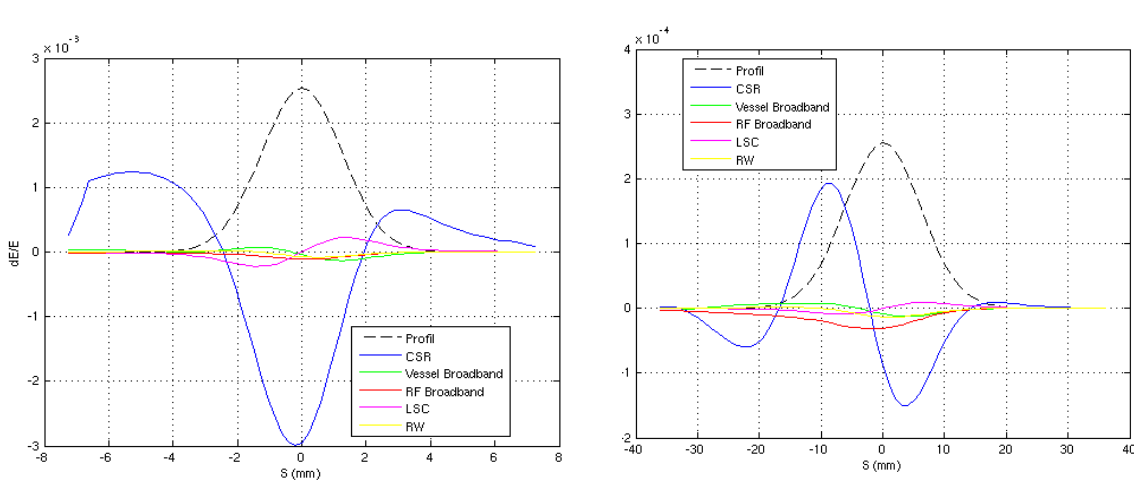


Figure 3.11. Longitudinal wakefield over one revolution.

turn generated by a 1 nC Gaussian bunch at 50 MeV for a bunch length of 4 ps (left panel) and 20 ps (right panel).

The ThomX low energy operation (50 MeV) practically suppresses the natural damping effect of the synchrotron radiation and complicates the bunch stabilization. Each kind of perturbation grows irreversibly, implying that feedback systems in the three planes are essential to cope with the induced oscillations of the bunch center-of-mass. In addition to these collective effects, the unavoidable injection jitters have also to be taken into account. To calculate these effects, 6D tracking simulations that include the longitudinal impedance as well as the large mismatch between the linac and the ring optics in the longitudinal phase space have been performed (see Fig. 3.12).

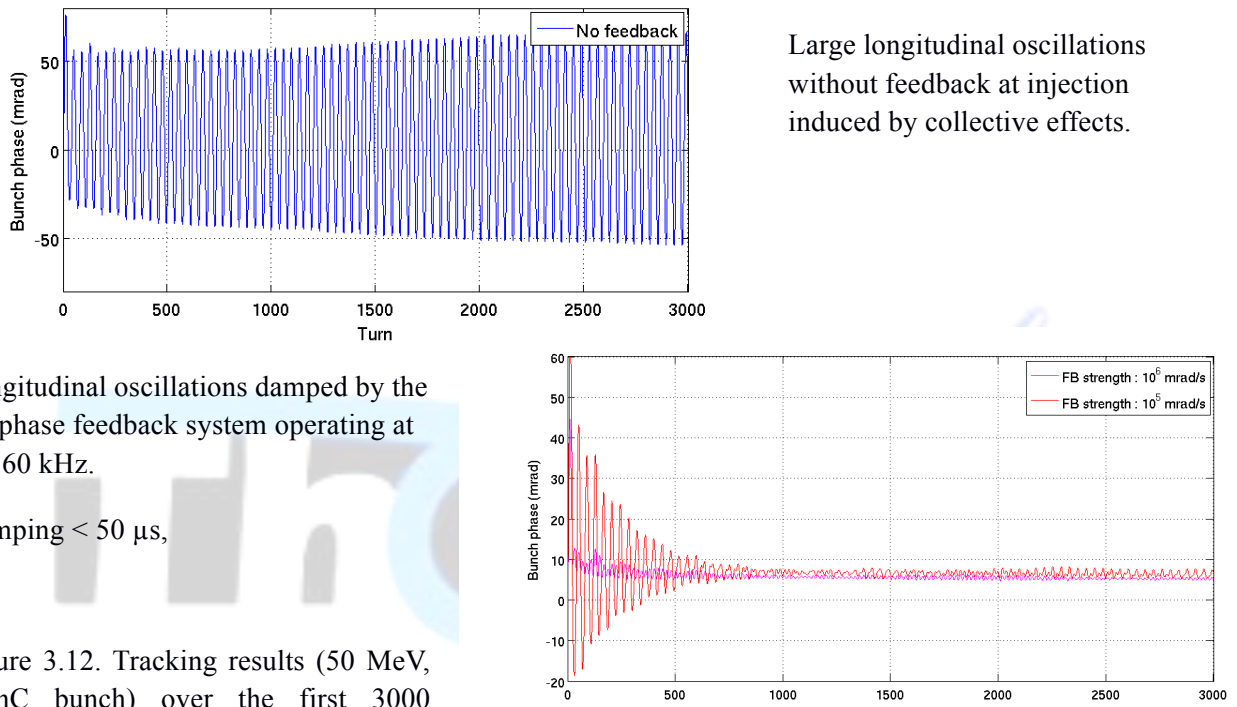


Figure 3.12. Tracking results (50 MeV, 1 nC bunch) over the first 3000 revolutions just after injection, without and with the RF phase feedback system ($V_{RF} = 300$ kV).

Large oscillations start very quickly after injection when the bunch is still short (4 ps) and are of the same order of magnitude as the ones induced by the energy-phase jitter that affect the linac injection. This effect is the one to address in the design of the longitudinal feedback. As far as the transverse plane is concerned, the growth times characterizing various instability sources are listed in Table 3.5. The revolution-by-revolution feedback strength indicated for each instability source is the one needed to suppress the oscillations.

Source	Type	Growth time	Revolution-by-revolution kicker strength
Beam pipe geometry	TMCI Head-Tail	- 160 μ s	>10 nrad
Resistive Wall		600 μ s	> 2 nrad
Ions		< 100 μ s	>20 nrad

Table 3.5. Transverse instability growth time and feedback kicker strength for a 1 nC bunch at 50 MeV.

In contrast with what prevails in the longitudinal phase space, the main transverse oscillation source is the injection position jitter. Since the non-linear sextupole components are large, this jitter may produce a large emittance increase as a consequence of the phase space painting process (see Fig. 3.13).

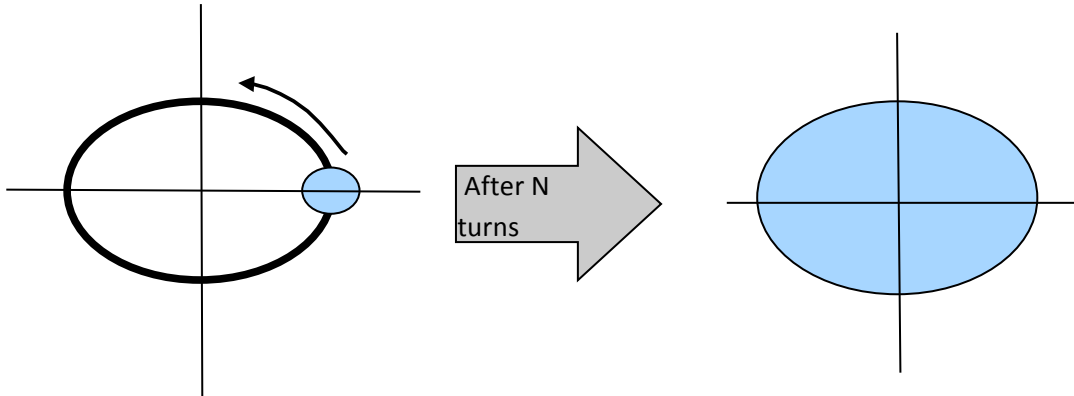


Figure 3.13. Sketch of the transverse phase space painting process.

Simulations show that a very fast increase of the transverse emittance can result from steering errors at injection, in about 500 revolutions or 25 μ s. To overcome this effect, a fast transverse feedback is needed; it has to damp the oscillation in about 100 revolutions or \sim 5 μ s. The strength of the revolution-by-revolution feedback has to be on the order of 2 μ rad. This strength is far larger than the ones estimated to cope with the transverse instabilities. For this transverse feedback, a dedicated strip-line acting in both planes is foreseen in the RF section (see Fig. 3.14).

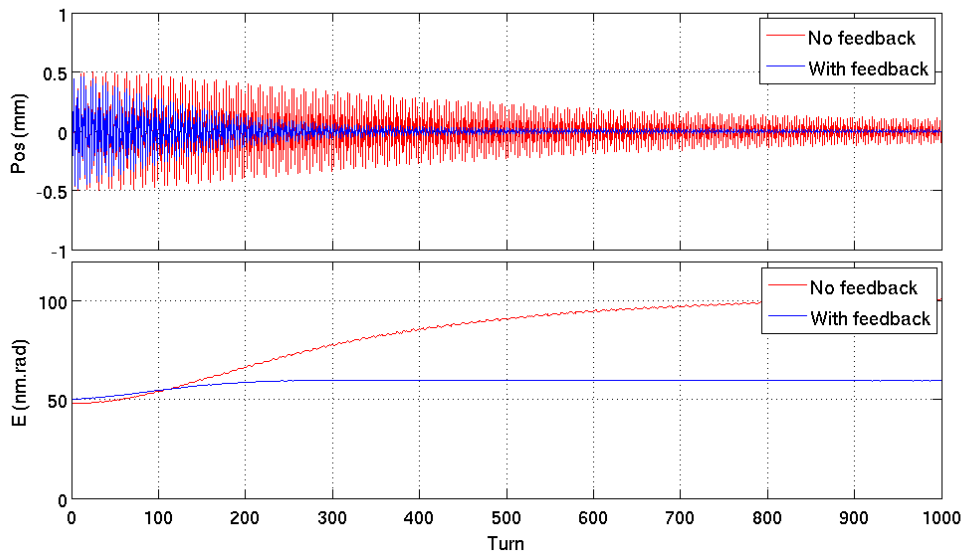


Figure 3.14. Simulated transverse emittance increase induced by a 0.5 mm injection jitter, with and without feedback

Phase space	Specifications	Device
Horizontal & vertical	Frequency = 17.8 MHz (F0) Strength = 2 μ rads	Dedicated strip-line for both planes
Longitudinal	Frequency = 360 kHz (Fs) Strength = 10^5 rad/s	Main RF phase loop

Table 3.6. Summary of the feedback specifications.

Other collective effects, such as the intra-beam scattering (IBS) which is important at low energy or the Compton recoil effect, play an important role during the 20 ms storage time. Their dynamics differ from an instability dynamics, but they also increase the electron energy spread and the bunch emittance — and thus reduce the X-ray flux.

To summarize, three different contributions to the e^- bunch dynamics must be dealt with:

- at injection, jitters which may affect either the injected bunch energy or its trajectory or the precise timing of its injection in the ring generate oscillations which may be large and which must be quickly damped by feedbacks in all three dimensions (x, y, z),
- during a transition period corresponding to the first \sim 1000 revolutions, strong collective effects enhanced by a possible synchronization error between the linac and the ring may lead to a complex turbulent regime in the longitudinal plane prior to ring matching (elliptical phase space density profil).
- during the 20 ms storage period, IBS and CBS produce a progressive increase of the bunch size in all three directions. This evolution cannot be stopped by a feedback system. In contrast, RF HOMs and other perturbations may generate instabilities that should be controlled by feedbacks.

To take into account collective effects, a dedicated code has been developed including a collection of wake field as well as non-linear dynamics. It is based on a 6D multi-particle symplectic tracking restricted to perfect hard edge drift, quadrupoles and dipoles of finite length. Other higher order elements, as sextupoles, are treated in the thin length approximation. The RF cavity is simply treated as a longitudinal cosine kick. The mapping through elements is given by the exact Hamiltonian solution [3.4] for the drift sections and the dipoles (including their small curvature and dipole edge effects). The quadrupole mapping is restricted to small radial angles. It has been compared to various codes (TRACYIII, ELEGANT, BETA and MADX) by performing simulations of the SOLEIL and the ThomX rings with special care given to the dipole edge effects [3.5].

The transverse beam size at IP and the bunch length are plotted in Fig. 3.15 over the first 10 000 revolutions or 0.56 ms with a 1 nC bunch charge. This study shows that a small positive chromaticity in the horizontal plane is necessary to stabilize the horizontal emittance. During the very first revolutions the tune dependent emittance behavior has not been fully investigated nor understood. It appears that this behavior follows from the bunch length mismatch between the linac and the ring. The fact that the linac produces very short bunches of 4-5 ps (rms) leads to a complex turbulent dynamics (see Fig. 3.16). The effect of this mismatch disappears progressively over the first 1000 revolutions; then the bunch length reaches 20-25 ps (rms).

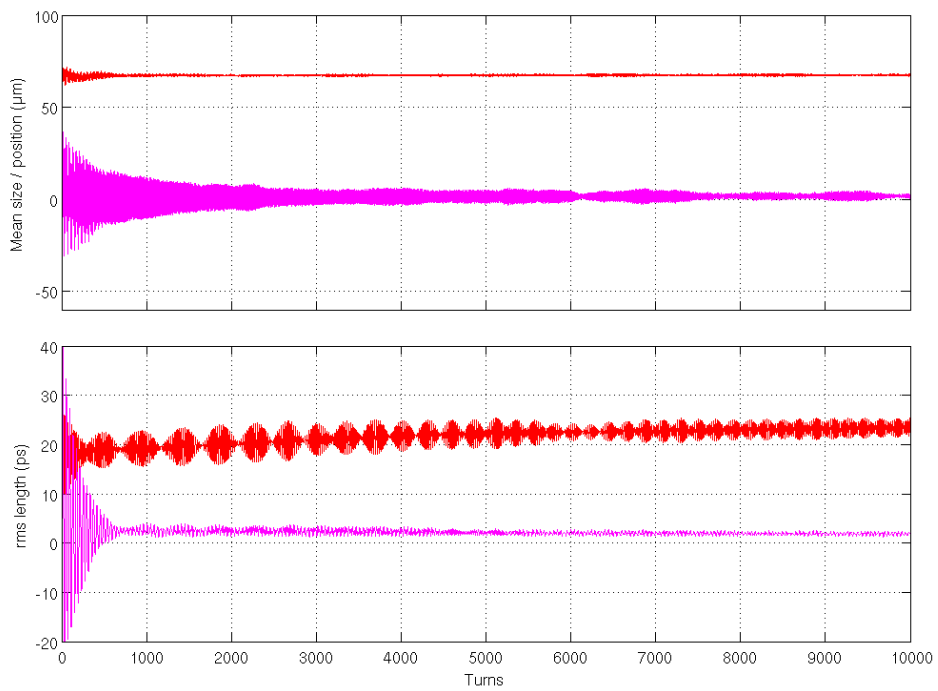


Figure 3.15. Red: RMS beam size and bunch length at IP. Magenta: bunch centroid position over the first 10 000 revolutions (0.56 ms) for a 1 nC bunch. The beam energy is 50 MeV.

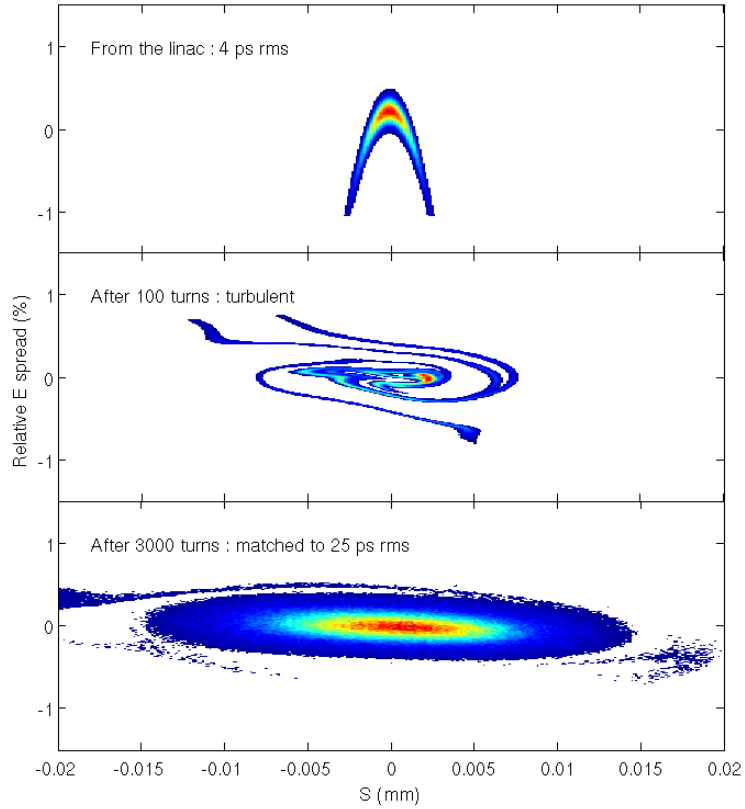


Figure 3.16. Turbulent dynamics in the longitudinal phase space that us taking place just at injection. These plots show the phase space density after 100 and 3000 turns.

3.3.4 CBS and IBS effects

The electron beam dynamics that prevails in a ring where Compton back-scattering is taking place is similar to the one resulting from synchrotron radiation (SR) in a synchrotron light source. CBS gives rise to random excitation in the transverse and the longitudinal planes. In the transverse plane, the emittance turns out to remain close to the one at injection [3.7]. In contrast, the CBS excitation strongly affects the dynamics in the longitudinal phase space. It leads to a substantial energy spread increase over 50 ms storage time* (see Fig. 3.17a), resulting in a significant bunch lengthening.

Based on the lattice parameters, the calculation of the Touschek lifetime leads to a value on the order of 10 s; this effect can thus be neglected.

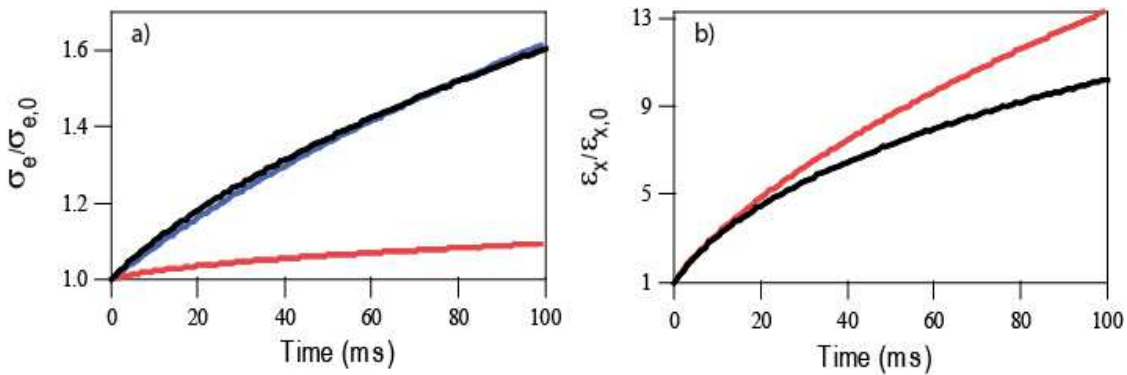


Figure 3.17. a) Energy spread increase, and b) Radial (x, x') relative emittance increase during a 100 ms storage time. Blue curves: CBS effect only; red curves: IBS effect only; black curves (almost on top of the blue ones): CBS and IBS combined effect. The IBS calculation is based on the Mttingwa formalism [3.8].

In contrast, the multiple Touschek effect ('IBS') plays a significant role in the radial phase space (x, x') as shown in Fig. 3.17b. After 20 ms, this horizontal emittance is increased by a factor ~ 4 , from 50 to 200 nm.rad, and the relative energy spread by $\sim 20\%$, from 0.3 to 0.36 %, as can be seen in Fig. 3.17a. Figure 3.17 shows that the Compton back-scattering process plays a role by far more important than the IBS does. It also shows that, because of the large emittance increase produced by the CBS, the bunch density decreases by a large amount, making the IBS much less effective (see Fig. 3.17b where the curve showing the *combined* effects lies *below* the curve illustrating the IBS effect by itself).

When the electron beam energy is increased up to 70 MeV, the IBS effect on the horizontal emittance becomes less important. During a 20 ms storage cycle, this effect is reduced by a factor 2. On the other hand, the energy spread degradation increases by more than a factor two compared to the 50 MeV case. This change is due to the higher energy of the back-scattered photons. In contrast, if the electron beam energy is decreased down to 25 MeV, the energy spread is reduced by a factor two while the horizontal emittance increases by a factor seven compared to the 50 MeV case.

Assuming an optimal overlap between the e^- bunch and the laser pulse in the interaction region, and neglecting the e^- bunch size variation across this region (the 'hourglass' effect) as well as the variation of the laser beam envelope near its waist (characterized by the Rayleigh length), the X-ray flux is given by the following formula (see Eq. 1.1):

* The nominal storage time is 20 ms only.

$$N_x = \frac{\sigma_{th} N_e N_\gamma \cos\varphi f / 2\pi}{\sqrt{\sigma_{y,e}^2 + \sigma_{y,\gamma}^2} \sqrt{(\sigma_{x,e}^2 + \sigma_{x,\gamma}^2) \cos^2 \varphi + (\sigma_{z,e}^2 + \sigma_{z,\gamma}^2) \sin^2 \varphi}}$$

where σ_{th} is the Thomson cross section, N_x is the number of photons per laser pulse, f is the e^- bunch revolution frequency, φ is half the collision angle, $\sigma_{x,y,z,e}$, $\sigma_{x,y,z,\gamma}$ are respectively the three dimensional bunch rms sizes for the electron (e subscript) and for the laser pulse (γ subscript). In fact, because of the increase of the e^- bunch size during the storage time, the flux is reduced by roughly a factor two at the end of a cycle as shown in Fig. 3.18.

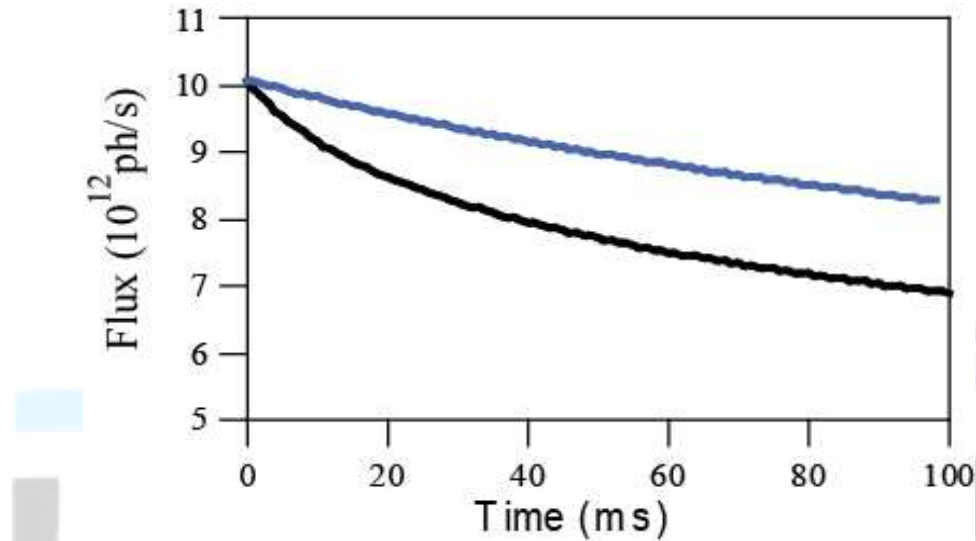


Figure 3.18. X-ray flux as a function of the storage time. These results take into account the energy spread increase and the emittance degradation due to IBS only (blue curve), and to the combined CBS and IBS effects (black curve).

To calculate more precisely the X-ray flux produced by Thom-X, the code CAIN [3.9] (cf. § 1.2 above) has been included in the previous 6D tracking code including the non linear effects of the lattice magnets as well as collective effects. The X-rays characteristics are computed at each ring revolution. The intra-beam scattering effect is calculated also at each e^- bunch revolution based on the Bjorken and Mtingwa formalism [3.8]. To reduce the computing time, the code extrapolates the IBS effect whenever there is only a little change from one revolution to the next (this method reduces the computing time by a factor 4). This code runs on linux OS. Using the computer farm of the IN2P3 computing center in Lyon, it takes about 15 days to simulate a full Thom-X cycle (20 ms, *i.e.* 400 000 revolutions) when the e^- bunch is modeled by 500 000 macro-particles.

The way the total X-ray flux decreases during the first 10 000 revolutions is shown in Fig. 3.19. This decrease is due to the e^- beam quality degradation, mainly due to the CBS effect. Also shown in this figure is the X-ray flux evolution as a function of the storage time for three different lower cut-offs in the X-ray energy spectrum. Figure 3.20 shows a typical angular distribution of the X-ray emission.

Figure 3.21 plots the bunch longitudinal phase space for the first revolutions. The macro-particles in green are those which have been hit by photons at the last crossing while those in blue have been hit before, the others are in red.

Cross comparison and benchmarking of this code against other codes developed for ThomX (6D tracking without Compton effect or Compton + IBS without tracking) are in progress and indicate a good agreement between the codes.

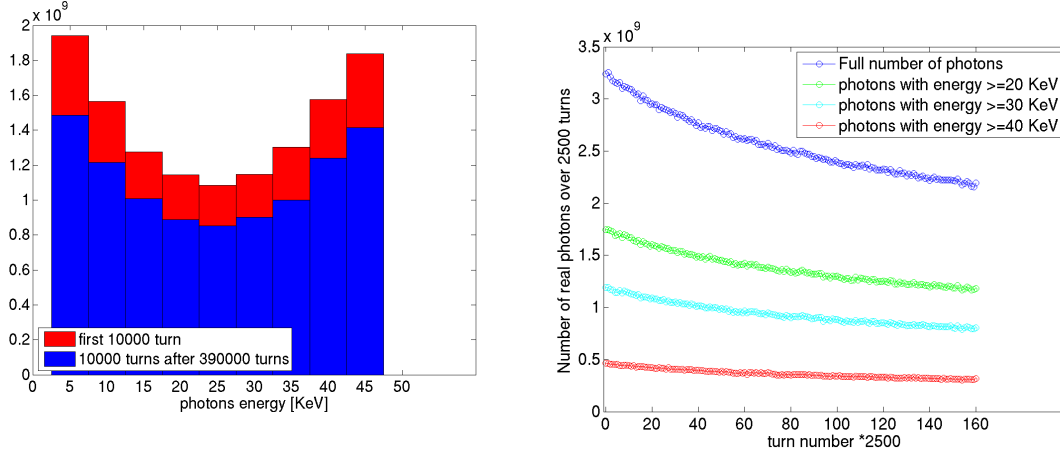


Figure 3.19. Left panel: Number of X-rays produced as a function of the X-ray energy, at the end of the first 10 000 first revolutions (in red), and during the last 10 000 revolutions before extraction (in blue). Right panel: Number of X-rays produced, summed over 2500 revolutions, as a function of the revolution number.

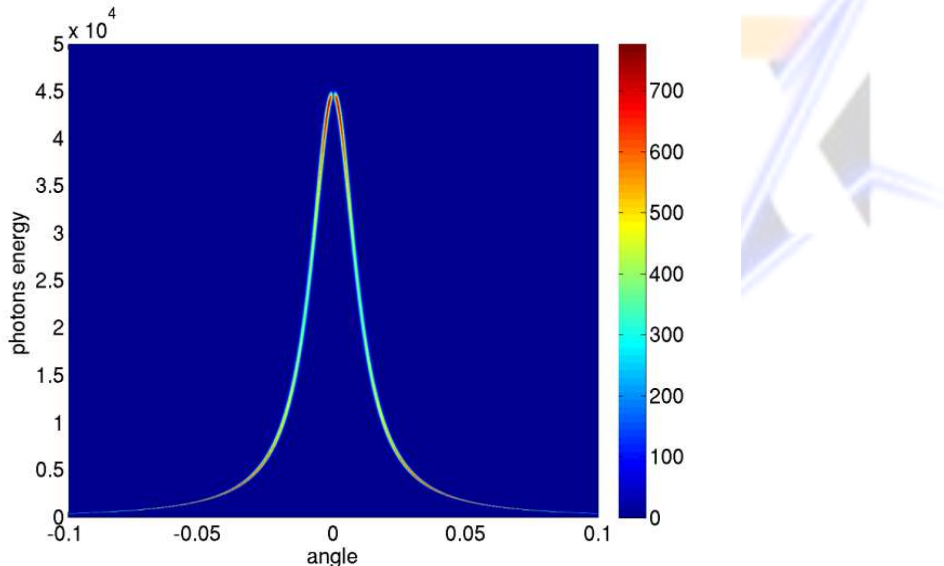


Figure 3.20. X-ray intensity as a function of the emission angle in mrad (horizontal axis) and their energy in eV (vertical axis). The color bar indicates the number of X-rays.

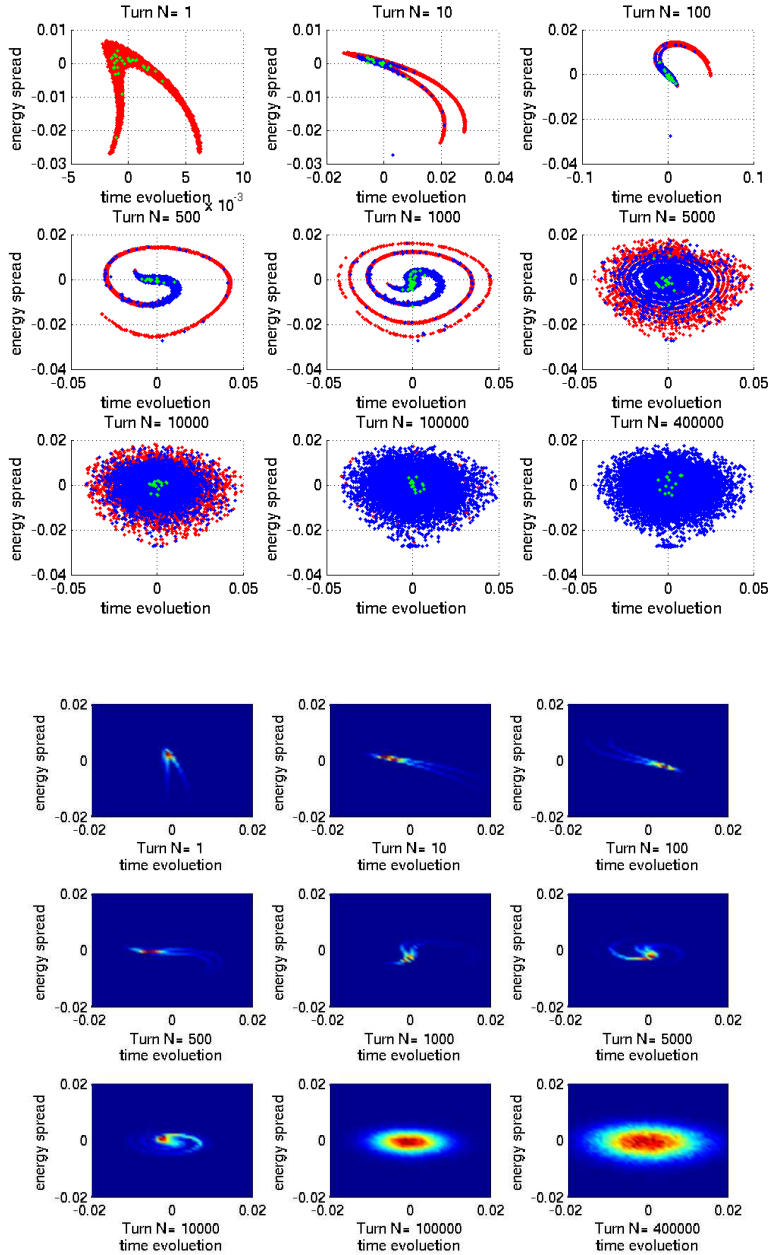


Figure 3.21. Upper nine panels: Evolution of the e^- beam longitudinal phase-space after injection. The macro-particle positions are plotted along the horizontal axis while their energy deviations are plotted along the vertical one. Green: electrons which have collided with photons at the last crossing, blue: electrons which have collided before, red: electrons which have not yet undergone any collision. These plots reveal a turbulent dynamics. Lower nine panels: Time evolution of the beam longitudinal phase space as a result of a turbulent regime, from the initial ‘banana shape’ at injection to a Gaussian distribution after a few ms (colors indicate the electron number-density, red corresponds to the most populated region).

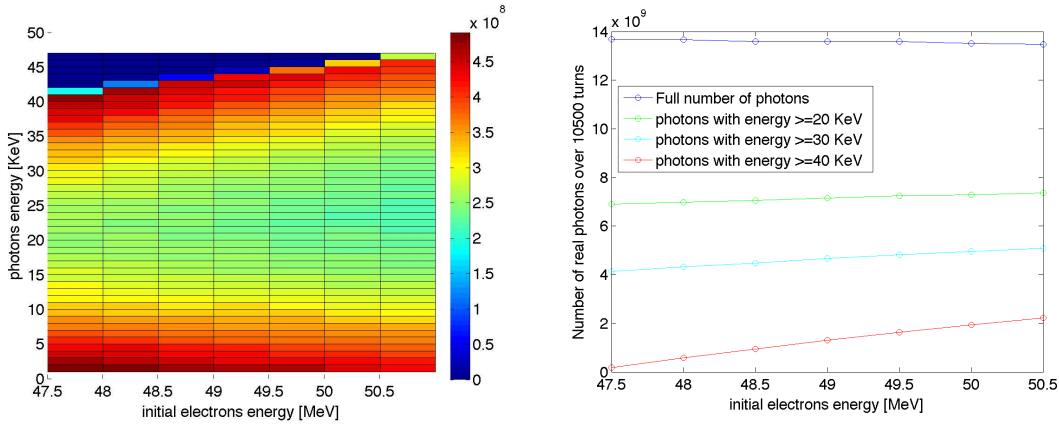


Figure 3.22. Evolution of the X-ray energy spectrum when the e^- beam energy is increased from 47.5 to 50.5 MeV. Left panel: The X-ray energy spectrum is plotted vertically for seven e^- beam energies. Colors characterize the X-ray intensity. Right panel: Each curve shows the total number of X-rays above some lower energy cut-off. Green: cut-off set at 20 KeV, blue: cut-off at 30 KeV; red: cut-off at 40 KeV.

3.3.5 Scattering on the residual gas

Coulomb scattering of the electrons on the residual gas molecules induces an increase of the circulating beam emittance. The amplitude of this effect is proportional to the average of the beta functions and to the gas partial pressure. Moreover it varies as the square of the atomic number of the residual gas atoms, and is inversely proportional to the electron energy. With a low beam energy of 50 MeV, it is therefore essential to keep a low pressure to minimize the time-averaged emittance. Fig. 3.23 shows the growth of the transverse emittance during the 20 ms storage time in the nitrogen case and in the hydrogen one. Assuming that one deals with nitrogen at a pressure of $8 \cdot 10^{-7}$ Pa, the emittance increases by a factor of two (see Fig. 3.23), while the degradation is negligible in the dihydrogen case. We conclude that a pressure lower than $3 \cdot 10^{-7}$ Pa must be maintained to keep the emittance growth at an acceptable level.

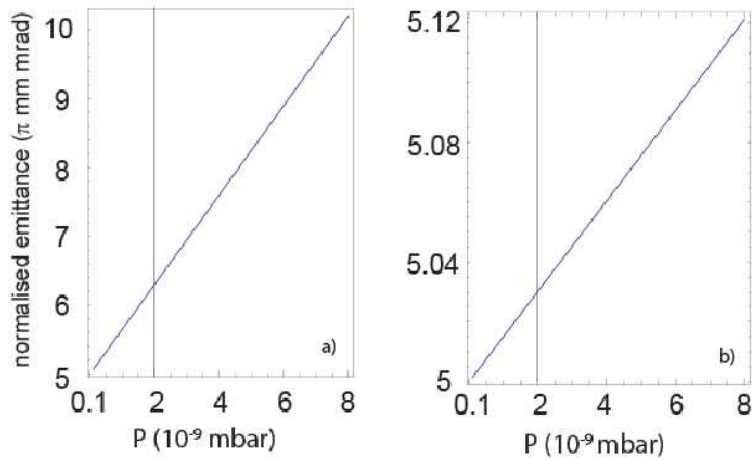


Figure 3.23. Emittance increase due to Coulomb scattering assuming that the residual gas is composed of a) 100% nitrogen, b) 100% dihydrogen.

3.3.6 Ion effects

The beam-ion instability [3.10, 3.9, 3.12] originates in the ionization of the residual gas molecules. Ions can subsequently be trapped by the electron beam electrostatic potential. We recall that the on-axis potential is inversely proportional to the beam size.

When the trapped ion number density reaches some threshold, beam instability is triggered. Besides this effect, trapped ions damage the beam quality by shifting the tunes, increasing the emittance and lowering the beam lifetime since the local pressure is increased.

For the Thom-X ring, the critical mass above which ions are trapped is on the order of one, in units of the proton mass. Thus all ions, whatever their mass, can be trapped in our case.

Once trapped, ions oscillate transversally in the potential well. Their oscillation frequency depends on the electron beam size and on the ion species (see Fig. 3.24 1c). Because of the e^- beam bunching, when the ion oscillation frequency becomes larger than the beam betatron frequency, a ‘fast ion instability’ may develop: the e^- bunch is submitted to the electric field of the oscillating ions, eventually resulting in an exponential growth of the oscillations of all particles (electrons and ions). This instability arises above some value of the neutralization factor* which depends on the lattice.

The neutralization factor and the growth time of either the vertical or the horizontal oscillations are shown in Fig. 3.24 as a function of the horizontal beam size, for several ion species. For a horizontal beam size averaged over the ring of 0.5 to 1 mm (which is about what is expected), the growth time is very short (less than one μs) but for this would happen for a neutralization factor much larger than one: obviously this is excluded. To keep under control the other ion harmful effects mentioned above, one may prevent ion accumulation over many storage cycles by introducing gaps between short series of injections, or by clearing the ions by an electrostatic potential that cancels out the potential well produced by the e^- beam. A simple solution consists in polarizing the beam position monitors (BPMs), thus avoiding the insertion of electrodes along the ring. This scheme should be effective since ions will drift longitudinally as the kicks they receive at each e^- bunch revolution has a longitudinal component. The amplitude of these kicks along the z direction is shown in Fig. 3.25 where the BPMs are represented by circles. They are placed near accumulation points, where the longitudinal kick vanishes, *i.e.* where ions will converge. A difficulty may arise at $s = 12.5$ m. This point is opposite to the IP in the lattice; at this point the e^- beam has small transverse dimensions and a vacuum pump is placed. Indeed, with a small beam size, the neutralization factor threshold is very low (10^{-3}) and the growth time constant is on the order of one μs . This potential difficulty can be overcome by adding an electrode in the short section between the two dipoles to clear the ions at this accumulation point.

Ion clearing with polarized BPMs or gaps introduced in the injection sequence should keep other ion effects at an acceptable level (more work is needed to quantify this statement).

* Defined as the total number of ions divided by the total number of electrons.

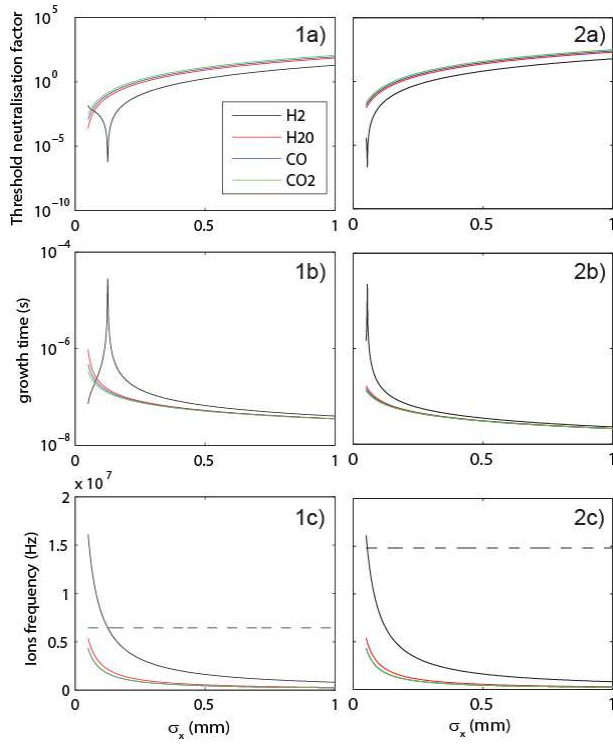


Figure 3.24. a) Threshold neutralization factor, b) growth time, and c) ion oscillation frequency for the following fractional b  tatron tunes: 1) 0.64 and 2) 0.17, for different ion species. The dashed lines show the e^- bunch betatron frequency. σ_x is the *mean* beam size.

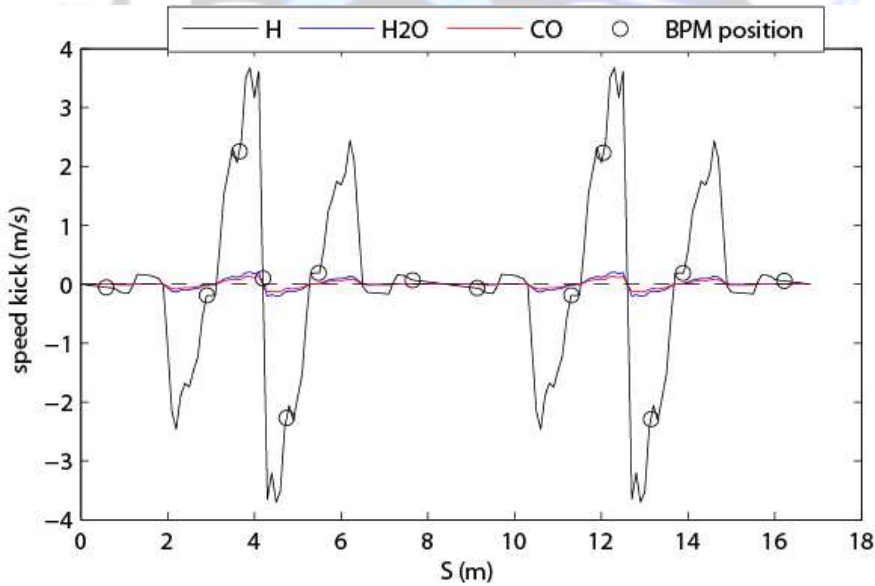


Figure 3.25. Longitudinal kick given to on-axis ions at each e^- bunch revolution.

3.3.7 Electron beam injection and extraction

Originally, the linac beam was injected in the ring by using only a septum followed by a fast kicker. Given the high repetition rate (50 Hz), radiation safety issues and a possible noise in the X-ray experimentation area lead to set up an e^- beam extraction line. The symmetric septum magnet located in

the middle of one of the long straight sections is used in a double pass mode, for injection and extraction. It is flanked by two identical kickers, one downstream for the injection and one upstream for the extraction (Fig. 3.26).

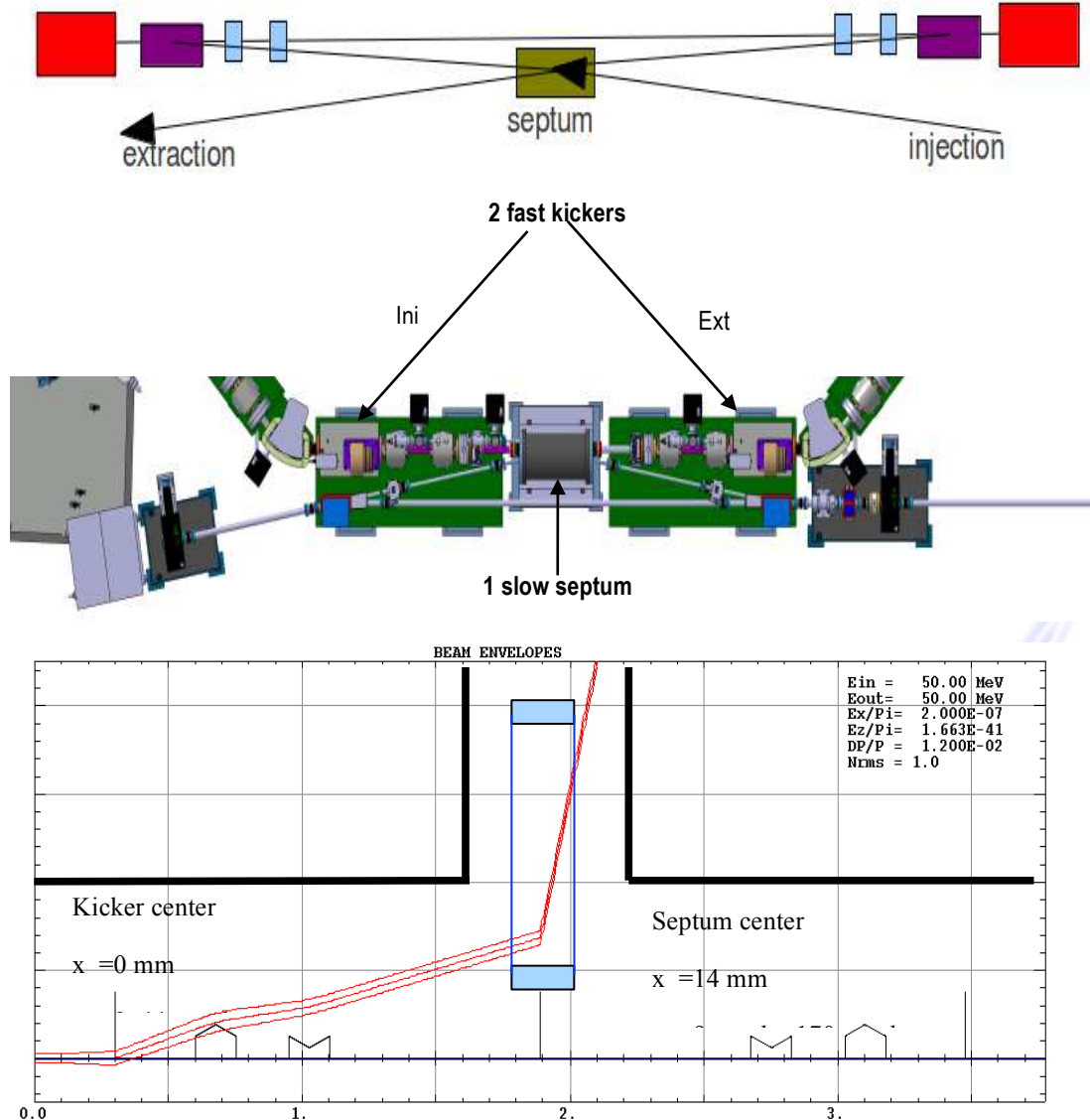


Figure 3.26. Sketch (top panel), implementation (middle panel) and simulation (lower panel) of the injection/extraction process.

The main characteristics of the septum and the kicker magnets are listed in Table 3.7. Since in both processes the beam runs through quadrupoles, some margins with respect to the nominal deflection values must be provided to cope with the fact that quadrupole fields are not uniform.

	Kicker	Septum
Deflection	5 mrad max (11 nominal)	170 mrad (40 mT.m @ 70 MeV)
Pulse duration	< 56 ns half sine	130 μs full sine
Effective length	200 mm	250 mm
Overall length	450 mm	500 mm

Table 3.7. Main characteristics of the pulsed devices.

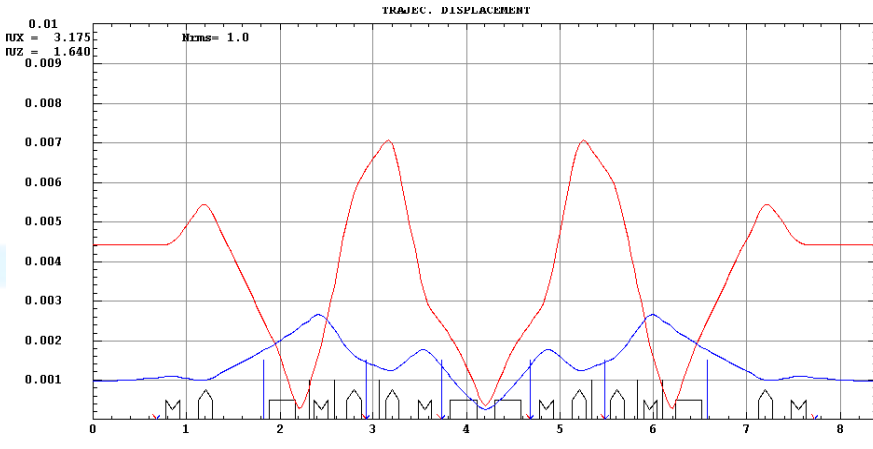
3.3.8 Orbit corrections

A set of 12 beam position monitors (BPMs) and 12 correctors in both planes are implemented along the lattice in order to control and correct the orbit. An additional BPM, located at the IP, is fixed on the table that supports the laser cavity. The main error sources are listed below. Uncorrected and corrected orbits are illustrated in Fig. 3.27.

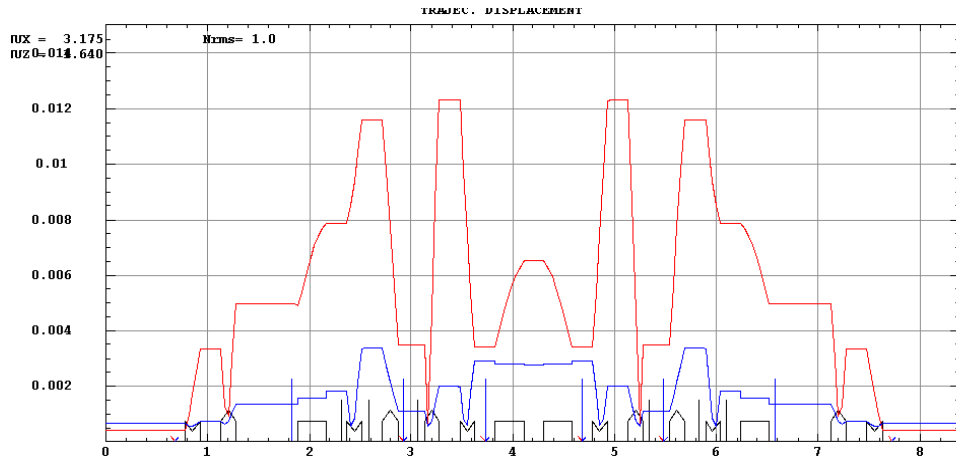
rms value	dB/B	dL	dX, dZ	dS	tilt
Dipoles	10^{-4}	0.1 mm	0.2 mm	0.1 mm	0.2 mrad
Quadrupoles	-	-	0.2 mm	-	-
Dipoles	10^{-4}	0.1 mm	0.2 mm	0.1 mm	0.2 mrad
Quadrupoles	-	-	0.2 mm	-	-

Table 3.8. Main magnet misalignment errors.

Uncorrected orbit with typical magnet alignment errors:

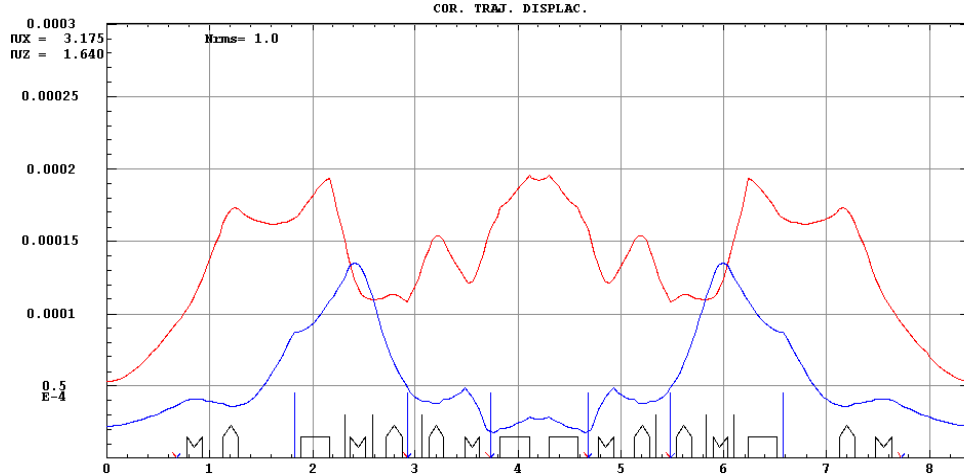


rms value	x_{max} (mm)	z_{max} (mm)
Max	7	3
IP	0.5	0.3

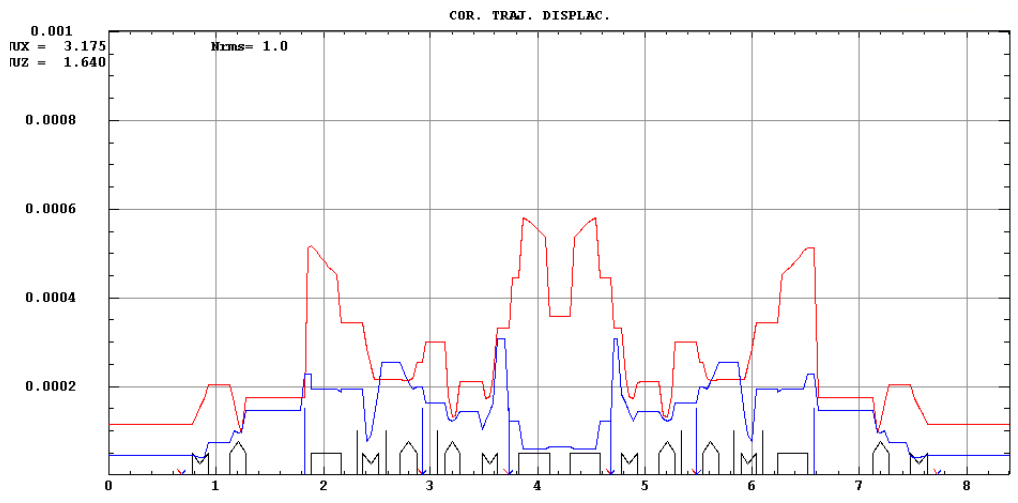


rms value	x'_{max} (mrad)	z'_{max} (mrad)
Max	12	4
IP	6	3

Corrected orbit :



rms value	x_{\max} (μm)	z_{\max} (μm)
Max	200	140
IP	200	30



rms value	x'_{\max} (μrad)	z'_{\max} (μrad)
Max	600	300
IP	350	60

Figure 3.27. Uncorrected and corrected closed orbits. Red lines: horizontal projection, blue lines: vertical projection.

Quadrupoles and sextupoles are fixed on girders with a maximum error of 50 μm . The magnetic field center error relative to the magnet yoke being of the same order, the expected total alignment errors are $\sim 100 \mu\text{m}$ in each plane. The girders supporting all the elements will be aligned as solid blocks. Since

dipole misalignments have a large effect on the orbit, dedicated additional support tools will allow the readjusting of the dipole positions relative to the girder.

One needs a maximum corrector strength of 0.5 mrad when this strength is computed by assuming just one sigma alignment errors; to cope with alignment errors which would be twice as large, corrector strengths of 1 mrad are thus necessary.

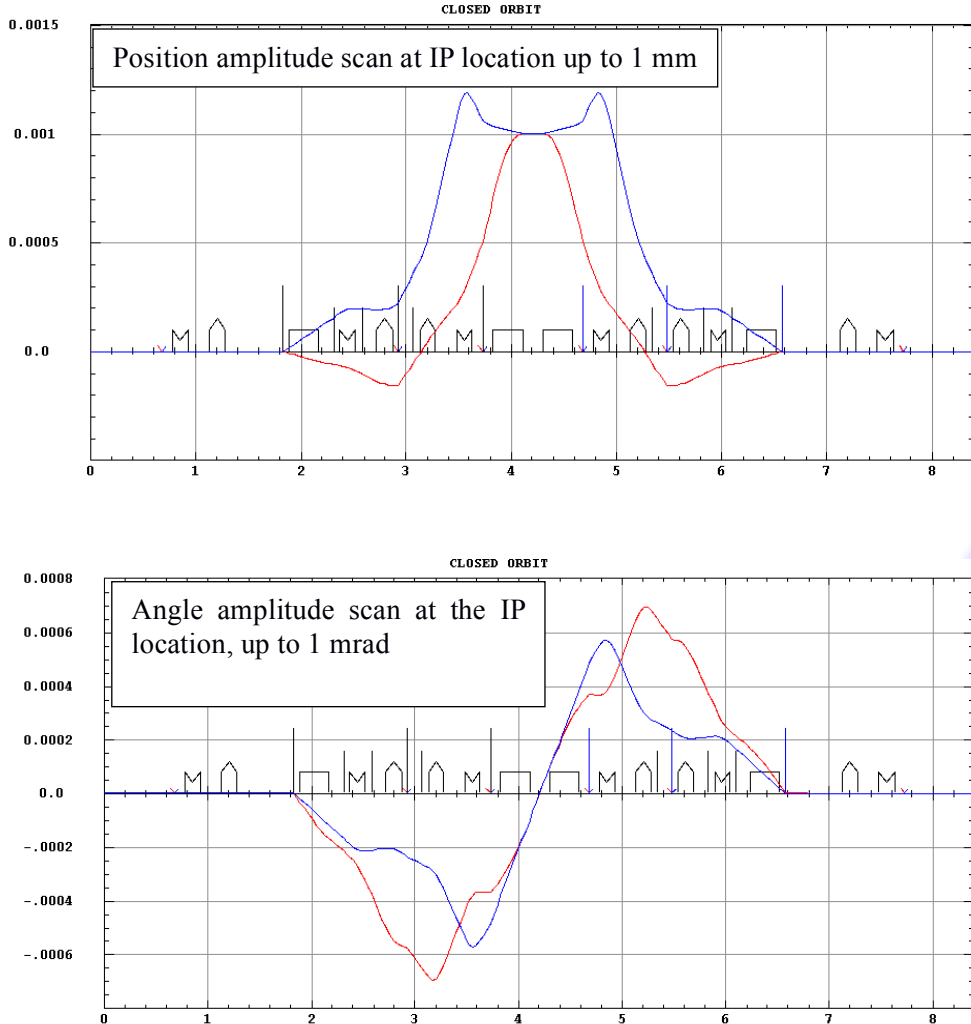


Figure 3.28. Orbit bumps (red: horizontal, blue: vertical) that can be produced at the IP.

In addition to this standard orbit correction procedure, a dedicated orbit scan at the IP will be very useful to ensure an optimal overlap between the e^- bunch and the laser pulse in the interaction region (see Fig. 3.28). To provide a scan range of up to 1 mm or 1 mrad, the corrector strength must be further increased by 1 mrad. Thus, the corrector maximum strength will be 2 mrad.

The orbit correction will be performed by a slow feedback operating around 0.1. The correctors are in the sextupoles magnets (combined magnets). The orbit feedback correction will also control the RF frequency in order to keep the orbit length at the ring design value. A specific synchronization scheme that ensures the proper injection timing and that maximizes the electron-photon collision rate is described in chapter 5.

3.4 Magnets

Table 3.9 describes the magnets that will equip the transfer line, the ring and the extraction line.

Magnet type	Dipoles	Dipoles for inj.	Quad	Sext	Corr
Number	4+8+2	2	7+24+2	12	4+12+1
PS number	3	2	33	3	34
Strength	0.180 T m		5 T/m	40 T/m ²	0.5 mTm
Length	276.5 mm		150 mm	60 mm	30 mm

Table 3.9. ThomX magnet parameters.

3.4.1 Dipole magnetic design

The dipole bending angle is 45°. A magnetic field of 0.5 T is needed at 50 MeV. Since their radius of curvature is very small (0.352 m), special attention has been paid to the field profile between the magnet poles and to the pole edge shape where large multipole components are present. Lateral shims and pole edge specific profiles have been optimized with the TOSCA3D code to minimize the impact of the multipoles on the beam dynamics.

Characteristics	unit	value
Gap	mm	40
Field at centre	T	0.63
Overall dimension	mm ³	350 x 400 x 400
Current	A	263
Voltage	V	17.7
Pole width	mm	100
Pole height	mm	100
Yoke length	mm	276.5
NI	A.turns	13000
Coil area	mm ²	67x40
Current density	A/mm ²	11.6
Number of turns	turns	48
Transverse size of the conductor	mm ²	6x6
Cooling channel	mm	4
Water pressure drop	bar	7
Temperature increase	°C	4.7
Flow rate (per dipole)	l/mn	8.6
Electric power (per dipole)	W	3100

Table 3.10. ThomX dipole parameters.

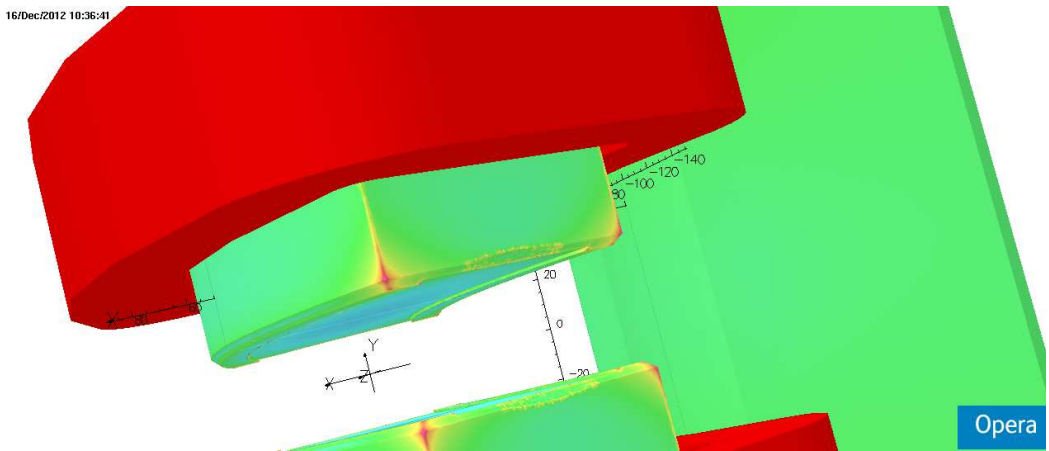


Figure 3.29. Drawing of a ThomX dipole.

3.4.2 Quadrupole magnetic design

The quadrupole design (see Fig 3.30) was also performed with the TOSCA software. The magnetic field is produced by four coils carrying a DC current. The conductor is wrapped around four poles which concentrate and define the quadrupole magnetic field map.

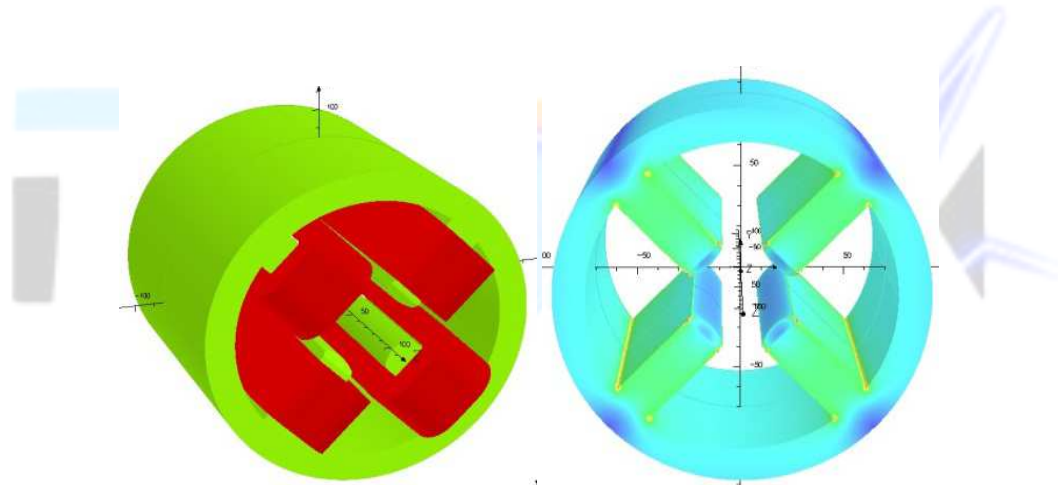


Figure 3.30. Quadrupole magnetic design.

A quadrupole can be manufactured in four identical parts, each one comprising one pole and one quarter of the yoke, or the yoke and the four poles can be manufactured separately. The quadrupole will be equipped with special shims which will be adjusted during the magnetic measurement to ensure a good alignment of the magnetic axis and low harmonic components. The ThomX quadrupoles are air-cooled to reduce the infrastructure cost. This is possible since the maximum current density is 1.5 A/mm^2 . Figure 3.31 shows the magnetic field intensity versus the radial distance from the quadrupole axis. The maximum gradient is 5 T/m . Figure 3.32 shows the magnetic field intensity at a distance of -20 mm from the magnet axis versus the longitudinal coordinate z . The maximum magnetic field is 0.1 T .

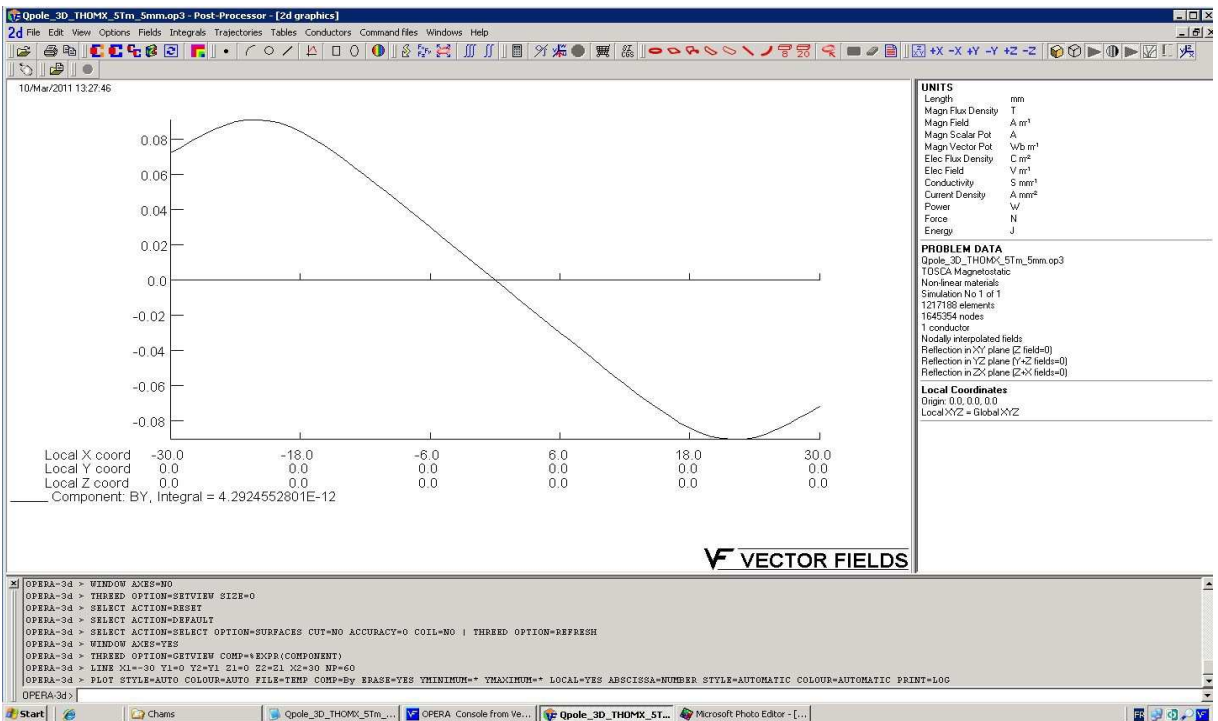


Figure 3.31. Magnetic field (in T) versus the distance (in mm to the magnet axis).

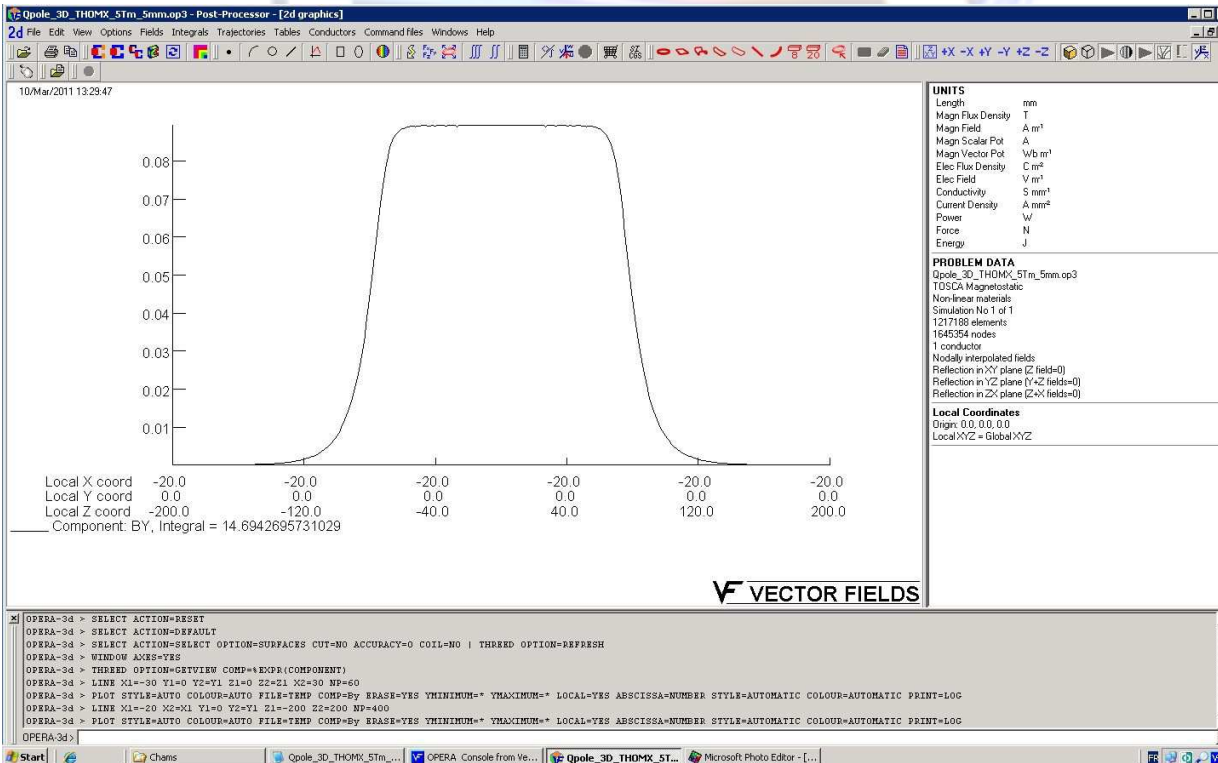


Figure 3.32. Magnetic field intensity (in T) versus z (the longitudinal coordinate in mm).

The main parameters of the ThomX quadrupoles are given in Table 3.11. Each quadrupole is powered by a 10 A, 3.2 V DC power supply; thus the released heat power remains below 32 W. A dedicated magnetic bench equipped with a rotating coil will be used for the quadrupole magnetic measurements. This bench has been developed for the magnetic measurements of the SOLEIL storage ring quadrupoles.

Parameters	unit	value
Bore	mm	41
Gradient	T/m	5
Current density	A/mm ²	1.5
Overall dimensions	cm ³	19x19x18
Current	A	10
Voltage	V	3.5
NI	A.turns	810
Pole width	mm	20
Pole height	mm	50
Coil dimensions	mm ²	15x36
Number of turns	turns	81
Wire dimensions	mm ²	5x1.25
Yoke length	mm	150
Yoke thickness	mm	20
Chamfer	mm	5 (not optimised yet)

Table 3.11. Main parameters of the ThomX quadrupoles.

3.4.3 Sextupole magnetic design

The ThomX sextupole design (see Fig. 3.33) was also performed with the TOSCA software. The magnetic field is produced by six coils that carry a DC current. The coils are wrapped around six iron poles which concentrate the field and define the sextupole field map. These magnets are combined function and are also equipped with additional coils to produce the corrector dipole fields.

17/Dec/2012 14:42:33

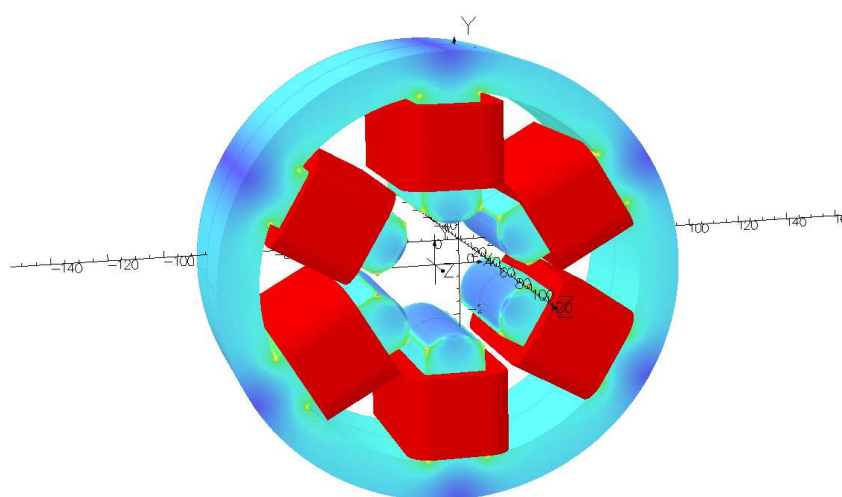


Figure 3.33. Sextupole magnetic design.

Each sextupole yoke is manufactured as a single piece and the six poles are screwed on this yoke. Then a coil is wound around each pole. During the design phase, a chamfer was calculated with TOSCA to guaranty a low harmonic content. The sextupoles will be air-cooled to reduce the infrastructure cost. The maximum current density is 1.5 A/mm².

The magnetic field intensity versus the distance to the magnet axis is shown in Fig. 3.34. The maximum sextupolar strength is 40 T/m².

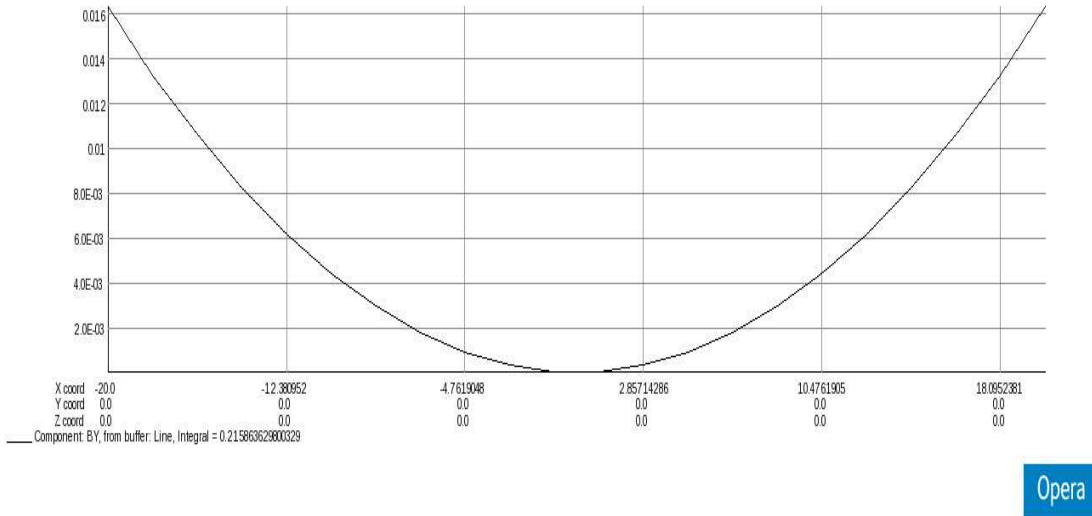


Figure 3.34. The ThomX sextupole magnetic field versus the distance to the magnet axis.

Fig. 3.35 shows the variation of the magnetic field at a distance of -20 mm from the sextupole axis versus the longitudinal coordinate z. The maximum magnetic field is 0.016 T.

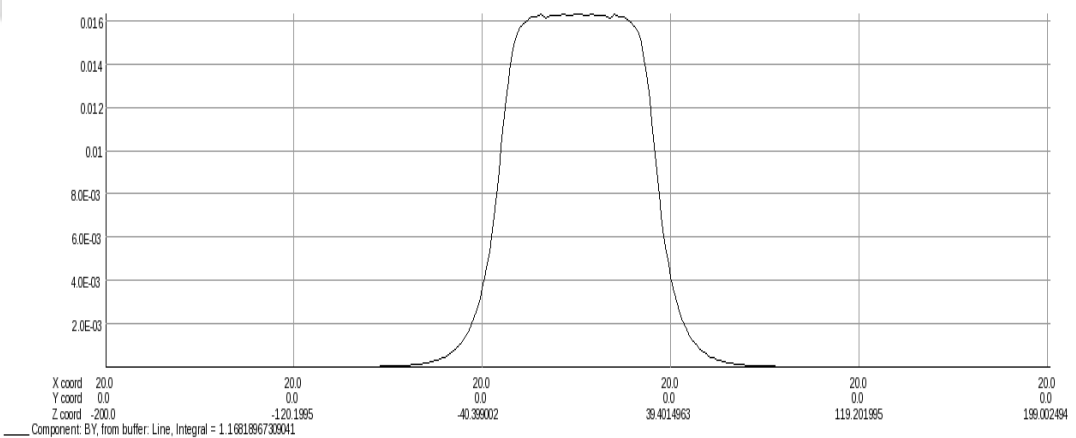


Figure 3.35. ThomX sextupole magnetic field versus z (the longitudinal coordinate).

Table 3.12 gives the main parameters of the ThomX sextupoles. They will be powered by a 10 A, 0.5 V DC power supply.

Parameters	unit	value
Bore diameter	mm	42
Sextupolar Strength	T/m ²	40
Field @ 20 mm	T	0.016
Current density	A/mm ²	2.5
Overall dimension	cm ³	19x19x8
Current	A	10
Tension	V	0.5
Ampere.Turn	A.t	100
Pole width	mm	20
Pole height	mm	40
Coil dimension	mm ²	6x40
Number of turns	Tours	10
Conductor dimension	mm ²	2x2
Yoke length	mm	60
Yoke thickness	mm	20
Chamfer	mm	1.5

Table 3.12. Main characteristics of the ThomX sextupoles.

A dedicated bench equipped with a rotating coil will be used for the magnetic measurements of the sextupoles. This bench has been developed for the magnetic measurements of the SOLEIL storage ring sextupoles.

3.4.4 Corrector magnetic design

Simple window frame correctors based on an already existing SOLEIL design will be used for the orbit corrections of the two transfer line.

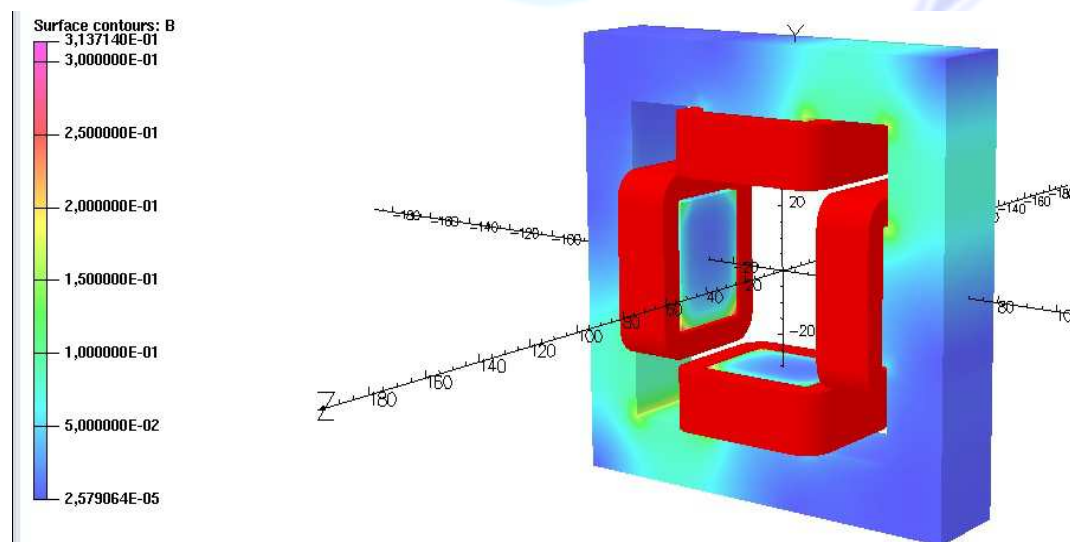


Figure 3.36. Magnetic design of the window frame correctors.

3.4.5 Injection dipole

The two injection/extraction dipoles compensate the septum deflection with a 170 mrad deflection (cf. § 3.3.7, see Fig 3.26). They are also air-cooled. Their design and their technical characteristics are illustrated in Fig 3.36 and Table 3.13.

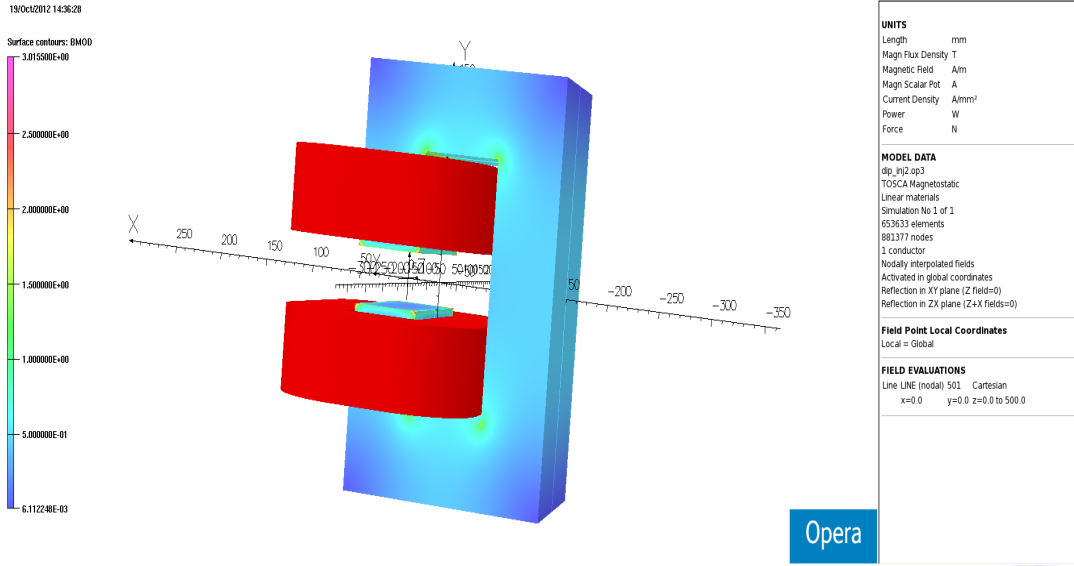


Figure 3.36. Magnetic design of the injection dipole.

Parameters	unit	value
Gap	mm	40
Field at the magnet centre	T	0.224
Current	A	10
Voltage	V	6
Pole width	mm	60
Pole height	mm	70
Yoke length	mm	150
AI (per coil)	A.t	3600
Coil cross section area	mm ²	60x60
Current density	A/mm ²	0.9
Number of turns	tours	360
Conductor size	mm ²	10 x 1
Pressure drop of the cooling water	bar	NC
Temperature increase	°C	NC
Power (per dipole)	W	120

Table 3.13. Parameters of the injection and extraction dipoles.

3.5 Power supplies

In order to provide a high operation flexibility, ThomX will be equipped with the following power supplies:

- One power supply for the ring dipoles (the latter will be connected in series), one for the TL dipoles and one for the DL,
- Individual power supplies for all the other magnets (quadrupoles, sextupoles and correctors).

All the power supplies will have a 16 bit-resolution and a ± 20 ppm reproducibility/stability over 24 hours. The technology is a switched-mode one, in order to achieve good efficiencies ($> 85\%$).

Magnet	Nb PS	Nb mag	current (A)	voltage (V)	type	load R (mOhm)	load L (mH)
Dip ring	1	8	300	170	Unipol	565	48
Dip TL	1	4	300	85	Unipol	280	24
Dip DL	1	2	300	45	Unipol	150	12
Dip inj	2	1	12	18	Unipol	1330	180
Quad	33	1	12	6	Unipol	500	10
Sext	12	1	12	3	Unipol	250	0.8
Corr ring	24	1	± 12	± 3	Bipol	250	0.8
Corr TL DL	10	1	± 12	± 3	Bipol	250	0.8

Table 3.14. Overview of the ThomX power supply equipment.

3.5.1 Pulsed magnets

3.5.1.1 Layout

As discussed above, the e^- beam injection in the storage ring and its extraction will take place in the same straight section (see Fig. 3.37).

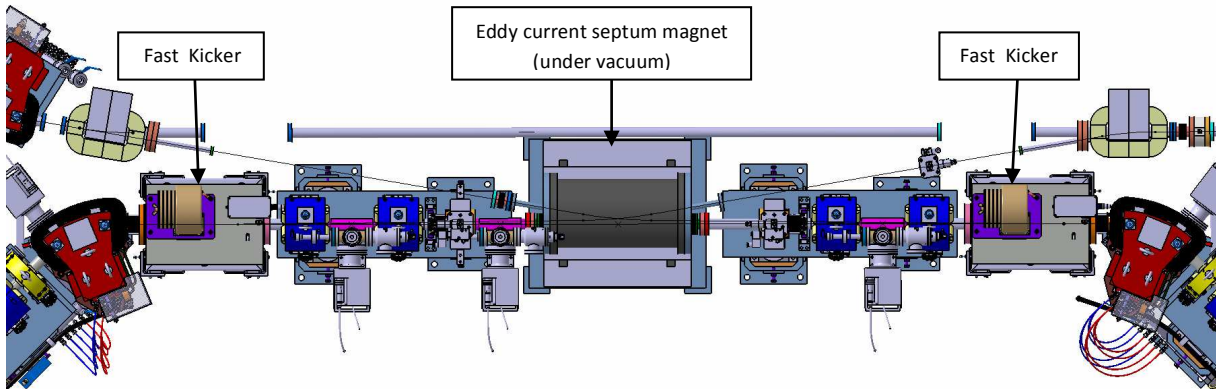


Figure 3.37. Injection/extraction section layout.

The first injection step involves a thin septum magnet. It bends the incoming bunch trajectory to bring it inside the ring vacuum chamber, close to the stored beam orbit. Then a fast kicker compensates for the residual trajectory angle and brings the injected bunch on-axis.

Extraction is realized by another fast kicker, followed by the same septum magnet as the one used for injection. This kicker deflects the bunch trajectory so that it enters into the septum channel; in turn, the thin septum bends the bunch trajectory which enters then into the extraction channel that brings the bunch into a beam dump.

In this configuration, the same thin septum magnet is used for both the bunch injection and the bunch extraction. This requires a symmetrical design, with two flanges, one dedicated to the injection and the other to the extraction. The magnetic gap is wide enough to accommodate the two bent trajectories. When operating at a 50 Hz injection rate, the septum current pulse consists of a slow full sine whose same positive half sine will be used successively for the ‘old bunch’ extraction and the for the ‘new bunch’ injection, with a suitable delay between the two steps.

The two fast kicker magnets are identical; their length has been reduced as much as possible because of the very limited space available. The current pulse in the kickers will have a half-sine shape. One must achieve a rise time (from zero current to peak current) and a decay time (from peak current to zero) each less than a ring revolution period. Thus the current pulse can have a maximum duration of two ring revolution periods. Consequently their charging voltage reaches high values even though most of the deflection is performed by the septum magnet.

The design of these three devices ensures that they can operate with a beam energy of 50 MeV (nominal) or 70 MeV (maximum), and at a 50 Hz repetition rate.

3.5.1.2 Slow septum magnet and its pulsed power supply

The main constraints on the septum design are as follows. This septum must produce a large trajectory deflection (160 mrad nominal peak value; 170 mrad maximum peak value) to bring the injected beam very close to the ring straight section axis, with no significant disturbance of the stored beam. The magnet mechanics should preserve the ring vacuum chamber geometry to keep its impedance as low as possible. Furthermore, its stray field must remain very low within the vacuum chamber where the stored beam circulates, as the septum excitation is done by a full sine pulse whose width (130 μ s) is very long compared to the ring revolution time (56 ns).

An eddy current septum magnet, installed in vacuum, will fulfil these constraints. The effective septum blade thickness can be as small as 3 mm, thus ensuring the closeness of the stored beam orbit and the desired bunch trajectory at the output of the septum yoke. An internal chamber, connected to the magnet yoke, extends the ring vacuum chamber and preserves the impedance budget. The injected bunch, deflected by the septum magnet field, penetrates through a small hole in this internal chamber. Such a septum magnet is very asymmetric in the transverse plane: it is driven by a copper loop that wraps the steel yoke.

In order to contain the magnetic flux, the whole yoke is enclosed in a copper box which carries the eddy current. On the side facing the stored beam orbit, the copper box thickness is reduced so that it constitutes the thin septum blade. As a result of the electric shielding provided by the eddy current circulating in the copper septum, such a structure is very effective to avoid a large magnetic stray field outside the magnet gap. The fact that the excitation pulse is a full sine reduces the duration and the

amplitude of the stray field (the slow delayed stray field tends to be the sum of the two opposite half current arcs ; this feature brings about a reduction of the stray field).

An additional magnetic shielding is required to strongly reduce the residual strayfield. This shield is provided by a 0.5 mm thick sheet of high permeability mumetal that will completely surround and enclose the internal chamber (thus shielding the stored beam orbit from the strayfield).

Such a design that combines an eddy current shield, a full sine pulse excitation and the use of a high permeability magnetic material, reduces the stray field to a very low level (a few 10 ppm of the main pulsed field) [3.13].

Assuming a septum opening of $H \times V = 30 \times 12 \text{ mm}^2$ and an active length of 250 mm (the length was chosen as short as possible because of constraints coming from the septum implementation in the straight section), the septum magnet inductance is estimated to be $1.6 \mu\text{H}$. Connexions and cables increase this inductance up to $2.3 \mu\text{H}$.

This design leads to the following parameters for the septum magnet and its power supply (values for a 70 MeV ring operation):

Septum	deflection	field integral	field	peak current	charging voltage
	170 mrad	40 mT.m	160 mT	1500 A	226 V

Table 3.15. Septum main parameters.

The pulsed power supply will be based on the ‘classical’ resonant discharge circuit scheme, composed of a storage energy capacitor ($190 \mu\text{F}$), a fast high-current thyristor switch, and a transmission line to the magnet comprising a few low impedance coaxial cables.

A 300V-20A power supply is foreseen. It will be connected to the storage energy capacitor through a current-limiting power resistor.

3.5.1.3 Fast kicker magnet and its pulsed power supply

The two fast kicker magnets must be identical. Because of the very limited space available, their length has been reduced as much as possible. The final numbers are 200 mm and 450 mm for the active length and for the overall length respectively. They will be located outside the vacuum vessel, with their ‘window frame’ rectangular ferrite yokes surrounding the ceramic vacuum chamber (see Fig. 3.38).

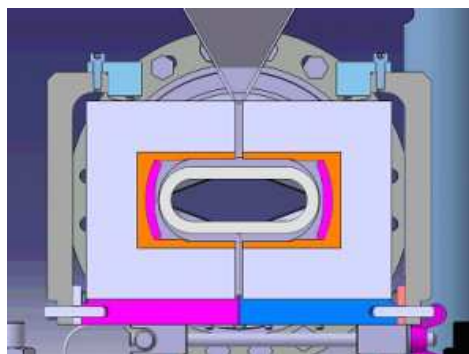


Figure 3.38. Front view of the kickers.

The two ceramic sections of the vacuum chamber will have a flange-to-flange length of 450 mm. Their aperture will be the same as the one in the ring standard sections, but with a racetrack transverse shape. Both extremities of each ceramic chamber include a smooth shape transition and a short bellow that

allows for RF finger contacts. These bellows can accommodate thermal dilatations, especially during bake-out. The ceramic chambers will be coated with a metallic deposit that will carry the bunch mirror current and thus avoid an increase of the chamber impedance. This coating needs to be very thin. It will consist of a titanium layer with a thickness $\leq 0.050 \mu\text{m}$. The thickness has been calculated so as to avoid the deterioration of the fast pulse shape and to avoid the temperature rise due to the mirror current [3.14].

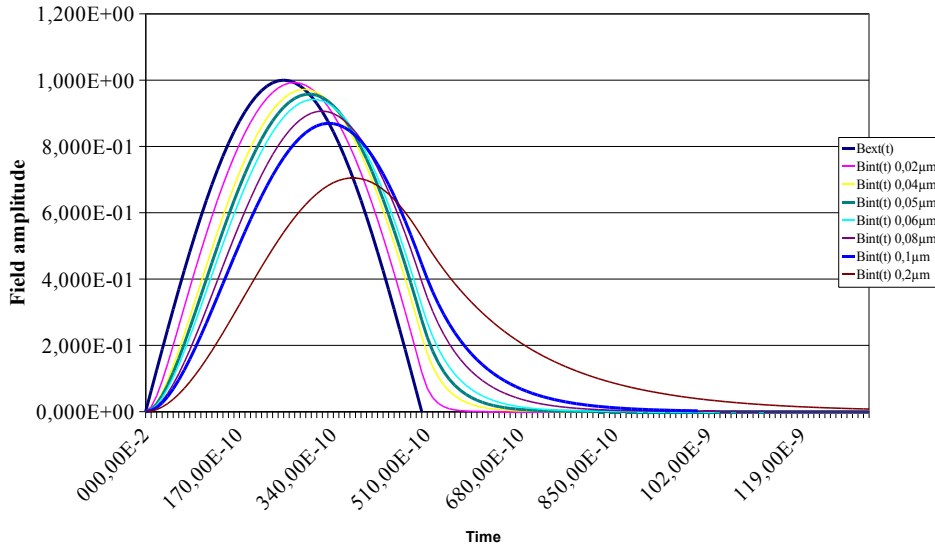


Figure 3.39. Time profile of the kicker pulse versus the titanium layer thickness.

The kicker dimensions follow from

- the aperture needed by the stored beam: $H \times V = 40 \times 28 \text{ mm}^2$,
- the required deflection kick: nominal 11 mrad, maximum 15 mrad,
- the beam energy: nominal 50 MeV, maximum 70 MeV,
- the short revolution period of the stored e^- bunch: $T_{\text{rev}} = 56 \text{ ns}$,
- the very short length of the injected bunch: from 4 to 25 ps (rms).

With a ceramic thickness of 6 mm, the effective magnet aperture must be $H \times V = 55 \times 55 \text{ mm}^2$. These parameters determine the current and voltage pulse characteristics.

The kicker magnets will be powered by a circuit delivering half-sine pulses [3.15]. In fact, because of the e^- bunch short revolution period (56 ns), the field pulse duration has to be less than twice the ring revolution period (less than 112 ns), and thus must have a very fast rise time and decay time (both less than a ring revolution period). On the other hand, with such a very short bunch length (4 or 25 ps (rms)), whether one deals with the incoming bunch or the extracted bunch, one may assume that the pulses do not have to present a marked flat top.

These considerations lead to the following kicker parameters:

Kicker	beam energy	deflection	field integral
Operation at E_{nominal}	50 MeV	15 mrad	2.5 mT.m
Operation at E_{max}	70 MeV	15 mrad	3.5 mT.m

field	peak current	estimated voltage
9.2 mT	406A	10 kV
17.5 mT	771 A	18 kV

A specific R&D program is necessary to guarantee that these constraints will be fulfilled by the power supply and by the magnet. Preliminary studies were based on the standard circuit used for such a pulsed power supply (see Fig. 3.40), involving a high voltage (HV) capacitor to store the energy, in series with a HV switch and a load whose inductance is close to the one of the kicker magnet. In this circuit, the HV switch is a very fast MOSFET switch followed by a HV fast recovery diode module.

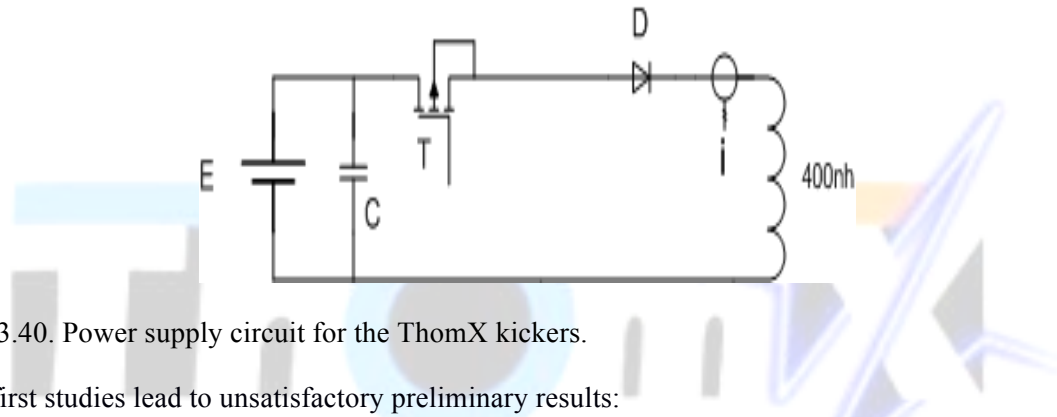
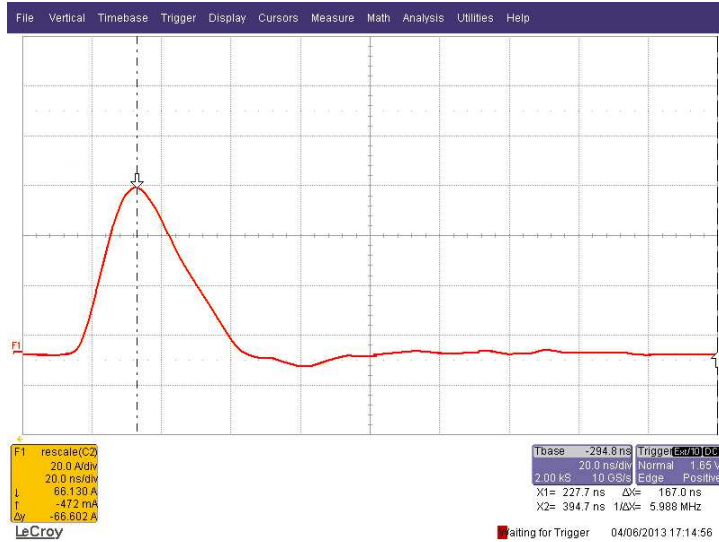


Figure 3.40. Power supply circuit for the ThomX kickers.

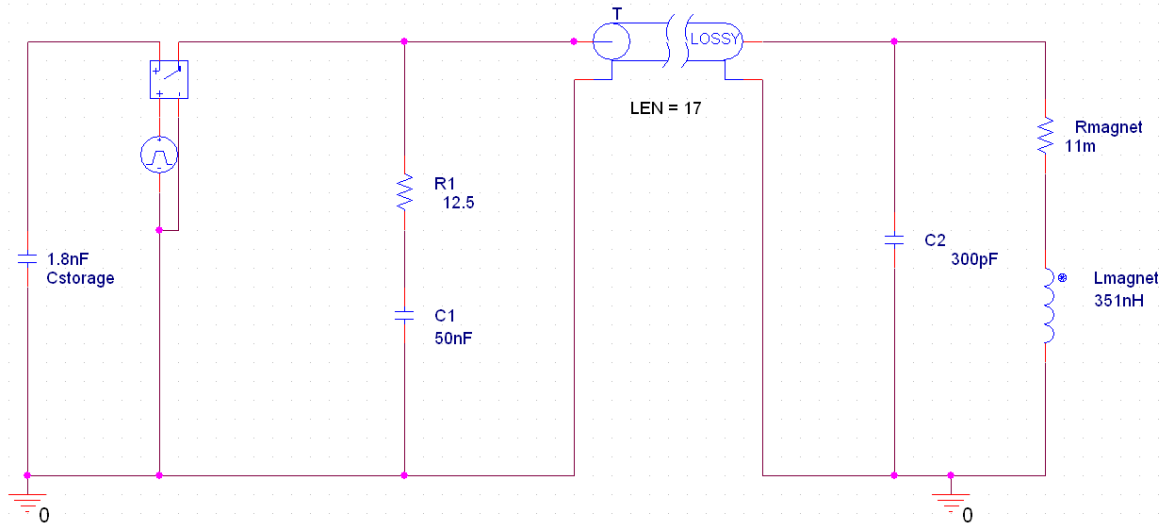
These first studies lead to unsatisfactory preliminary results:

- The BEHLKE Ultra-Fast 17 kV 480 A MOSFET module can switch ON in a very short time, less than 8 ns. Then the pulse shape is normally determined by the passive component parameters in the circuit, provided that the negative current is quickly interrupted, either by HV diodes in series, or by a turn Off control of the HV switch..
- But the different types of HV diodes used are not able to switch OFF the pulsed current quickly enough. Even the ‘fast recovery diodes’ have a reverse recovery time too much long to stop cleanly the pulse at its zero crossing. Thus it was necessary to work on other topologies and to find better suited components.

Further simulations were performed to see how the circuit could be improved. It turned out that controlling the switch both at the closing and at the opening can improves the shape of the current pulse. A prototype using the same Behlke MOSFET modules and including a coaxial transmission line was built and tested. A plot of the current pulse in the kicker coil that was obtained is shown below.



This plot was obtained with the following prototype circuit:



As one can see, more work is still needed to improve the shape of the current in the coil (namely one should reduce the level of reflections, improve the current pulse shape and work on the peak current to meet the 70 MeV requirements). We are also looking for an other supplier who could provide controlled HV switches ensuring both ON and OFF fast operation.

Mechanical and magnetic studies of the kicker magnets are ongoing.

3.6 Storage ring RF system

The choice of 500 MHz for the RF frequency is a compromise between several constraints : the cavity fundamental and high order mode (HOM) impedances, space requirements, the availability of RF power sources and other components. The required accelerating voltage of 500 kV can be provided by only one 500 MHz single-cell cavity, with about 40 kW of RF power. As shown in the following, the choice of the cavity design is mainly dictated by the need for a strong damping of the HOM.

3.6.1 HOM impedance thresholds as regard to beam instabilities

When a cavity mode is excited in resonance, it generates beam oscillations with a rise time approximately given by one of the two following expressions:

$$(1/\tau)_l = I_b \alpha f_m R_l / (2 Q_s E/e) \text{ in the longitudinal case, and}$$

$$(1/\tau)_t = I_b \beta_t f_t R_t / (2 E/e) \text{ in the transverse case,}$$

where f_m is the HOM resonant frequency, $R_l [\Omega]$ and $R_t [\Omega/m]$ are respectively the longitudinal and the transverse HOM impedances, $Q_s = f_s / f_o$ is the synchrotron tune (f_s and f_o are the synchrotron and the revolution frequencies), β_t is the beta function amplitude at the cavity location, α is the momentum compaction factor, I_b is the average beam current and E/e is the beam energy in eV.

Assuming typical values for the cavity HOM impedances ($R_l . f_m = 0.1$ to $1 M\Omega . GHz$, $R_t = 1$ to $10 M\Omega/m$) and the machine parameters listed in Table 3.15, the instability growth time is around $10 \mu s$ in both the longitudinal and the transverse cases.

Orbit length, C	16.8 m
Electron energy, E	50 MeV
RF frequency, f_{RF}	500 MHz
Revolution frequency, f_o	17.86 MHz
Harmonic number, h	28
Momentum compaction factor, α	0.015
β -function amplitude at the cavity location, $\beta_{x,z}$	3 m, 4 m
Relative energy spread, σ_E / E	$4.0 \cdot 10^{-3}$
Peak acceleration voltage, V_{RF}	300 (500) kV
RMS bunch length, σ_s	27 (21) ps
Synchrotron frequency, f_s	358 (462) kHz
Bunch charge, Q_b	1 nC
Number of stored bunches, N_b	1
Maximum current, I_b	17.86 mA

Table 3.15. Ring parameters used to estimate the rise time of the HOM induced instabilities.

In a low energy ring like ThomX, radiation damping is so weak (the damping time is ~ 1 s) that a stationary state is not reached during the beam storage time (20 ms). On the other hand, to ensure a good ring operation, it is sufficient to make all instability rise times much longer than this storage period. This can be achieved by attenuating the HOM impedances very strongly, typically by a factor 10^4 .

3.6.2 Cures to the HOM induced instabilities

There are essentially two ways of coping with such HOM induced instabilities, either by performing a strong de-Qing of the HOM resonances or by tuning their frequencies away from the beam spectral lines in order to prevent resonant excitation.

In practice, HOM de-Qing is achieved by extracting the cavity HOM power and transferring it towards external dissipative loads. But, in this approach, it is difficult to reach attenuation factors higher than 10^2 - 10^3 over a large frequency range and this technique requires heavy and cumbersome equipment close to the cavity (coaxial lines with coupling antennas or ferrite loaded waveguides). The DAMPY

cavity, designed at BESSY [3.16] and which is used in ALBA [3.17] and the PEP II cavity, developed at LBNL [3.18], are two variants of this technique.

The other method, which consists in controlling the HOM frequencies, is better suited to a small circumference machine like ThomX, where the beam spectral lines' spacing (~ 18 MHz) is very large compared to the HOM bandwidth (this bandwidth is of a few tens of kHz for Q_o equal to a few 10^4). As long as the HOM density is not too high and the modes can easily be tuned far enough from the beam spectral lines ($\delta f \gg f_m / Q_o$), it should be possible to reduce their effective impedances (the ones 'seen' by the beam) down to tolerable levels, *i.e.* $R_{\text{eff}} \approx R_s / (2 Q_o \delta f / f_m)^2 \ll R_s$.

We are investigating the potential performance of this technique by applying it to an ELETTRA-type cavity (see Fig. 3.44) [3.19] which combines three frequency tuning means. The HOM frequencies can be precisely controlled by an appropriate choice of the temperature of the water cooling the cavity while the fundamental frequency is maintained constant by a mechanism which deforms the cavity longitudinally. In addition, a movable plunger tuner, also called HOM frequency shifter (HFS), located in the cavity equatorial plane, provides an additional degree of freedom [3.20].

Tables 3.16 a and b list the characteristics of such a cavity fundamental and HOM resonances. They have been calculated with the 3D GdfidL code [3.21]. One finds 18 significant HOM (9 monopoles and 9 dipoles) with resonant frequencies lower than the cavity cut-off frequency. Figures 3.45 a and b represent the corresponding HOM spectra, $f_m \cdot R_l(f)$ and $R_t(f)$, folded over a single base band of 18 MHz. The horizontal dashed line in the graph represents the impedance threshold corresponding to an instability rise time of 20 ms, the beam storage time. Although they remain somewhat critical, these results tend to confirm that it should be possible to find acceptable operating conditions, as long as the HOM frequencies can be shifted by a few MHz by combining temperature and HFS tuning.



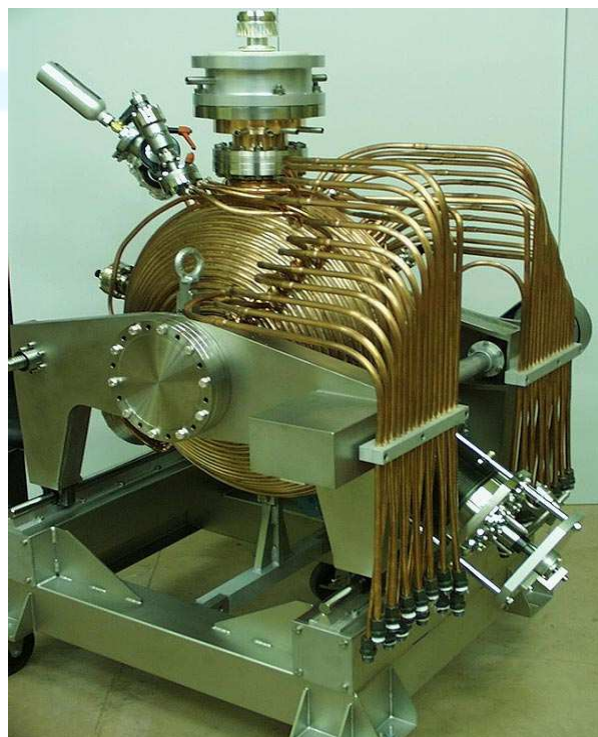
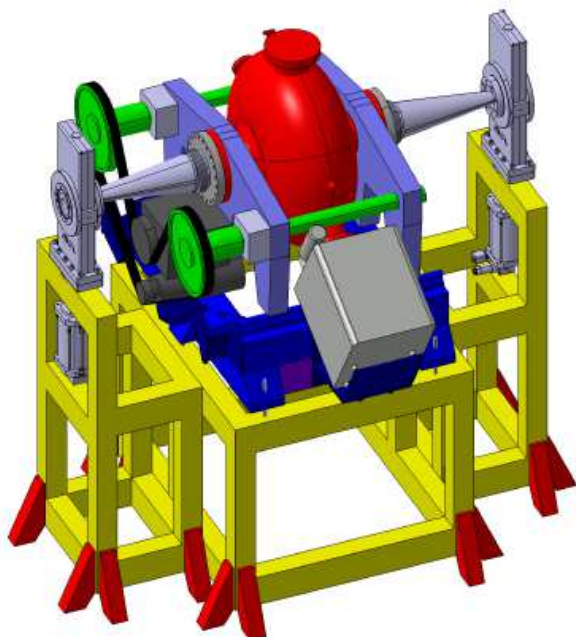


Figure 3.44. Drawing and photo of the ELETTRA cavity.

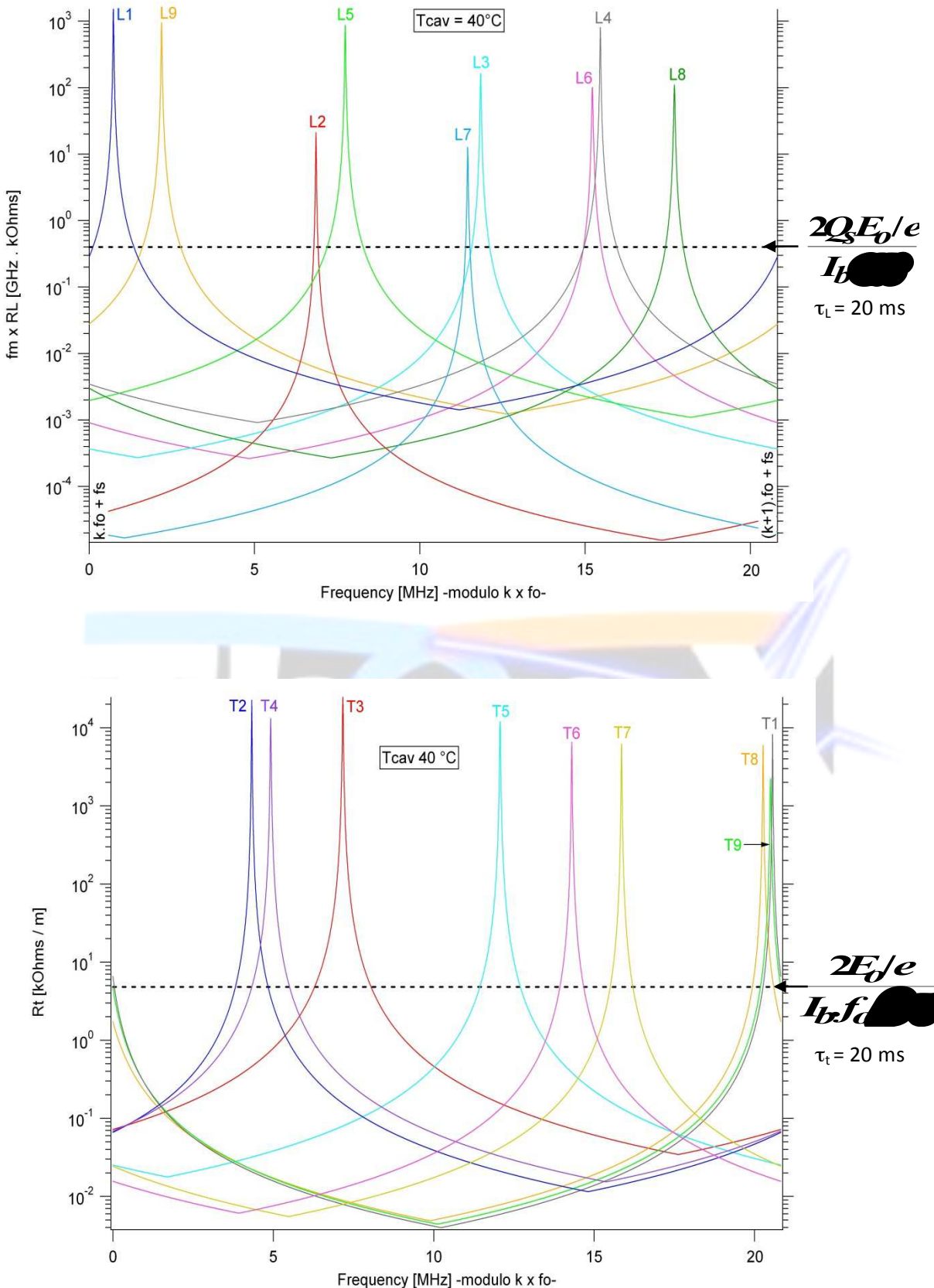


Figure 3.45. (a) Longitudinal and (b) transverse HOM spectra, folded over a single base band of 18 MHz for the ELETTRA-type cavity.

a) Longitudinal modes	fm [MHz]	Q0	Rs / Q0 [Ω]	Δfm (T) [MHz]	Δfm (HFS) [MHz]
L0 (fundamental)	499.132	44164	76.5	0.00	0.00
L1	958.618	48158	33.6	0.37	-1.00
L2	1027.81	57861	0.36	0.80	3.69
L3	1408.7	52562	2.20	1.74	0.21
L4	1515.28	69088	7.83	1.12	0.86
L5	1551.29	66375	8.50	2.40	7.21
L6	1869.12	55785	0.97	1.42	-0.92
L7	1949.5	81752	0.08	1.83	1.43
L8	2039.85	62729	0.86	4.00	?
L9	2068.96	87300	5.30	4.45	6.67

b) Transverse modes	fm MHz]	Q0	Rs _⊥ / Q0 [Ω]	Rs _⊥ [MΩ/m]	Δfm(T)[MHz]	Δfm(HFS) [MHz]
T1	737,01	50267	33,5	25,99	0.4	0.75
T2	746,06	52566	9,2	7,557	1.55	2.85
T3	1152,02	47196	26,4	30,06	0.49	-3.12
T4	1255,65	55386	5,1	7,428	0.68	7.25
T5	1302,49	71674	3,6	7,039	0.97	?
T6	1699,81	69325	10,3	25,42	1.88	?
T7	1736,50	91039	1,65	5,463	> 2	?
T8	1773,37	59409	3,2	7,061	> 2	?
T9	1836,17	77697	5,5	16,43	> 2	?
T10	2061,42	88484	5,9	22,54	> 2	?
T11	2224,75	99092	1,1	5,079	> 2	?
T12	2259,33	56641	1,3	3,484	> 2	?

Table 3.16. Main characteristics of the monopole (a) and dipole (b) modes, computed with GdfidL for an ELETTRA-type cavity. Δf_m (T) and Δf_m (HFS) are the effective temperature and HFS tuning ranges assuming a constant fundamental frequency.

It is worthwhile mentioning that in any event fast longitudinal and transverse feedback systems are required to damp the beam oscillations resulting from injection transients (see section 3.3.3). They will contribute to the HOM damping as well.

3.6.3 RF power source

An RF power of about 40 kW is required to generate the desired voltage of 500 kV in a single 500 MHz ELETTRA-type cavity. For this frequency, there exists a wide choice of power sources, based either on vacuum tubes (klystron, IOT, diacrod) or on solid-state technology. The low operating voltage and high modularity of the solid-state version offer significant advantages compared to vacuum tubes. Experience acquired at SOLEIL after few years of operation has definitely demonstrated all the benefits of this technology [3.22]. Figure 3.46 shows the 35 kW - 352 MHz solid-state amplifier used for the SOLEIL booster synchrotron. It consists of a combination of 147 modules. Each one has a power of 330 W, a gain of 11 dB and an efficiency of 62%. This amplifier was commissioned about 7 years ago. During a running period of more than 35 000 hours it tripped only once and this trip was caused by a human mistake.

This technology has already been extended to 476 MHz in the framework of a SOLEIL-LNLS collaboration aimed at realizing two 50 kW amplifiers for the LNLS storage ring [3.23]. More recently, the SOLEIL team has developed modules which can deliver up to 650 W at 500 MHz with a gain of 17 dB and an efficiency of 62%, while still reducing the thermal stress [3.22]. About a hundred of such modules will be combined to obtain the 50 kW required by ThomX.

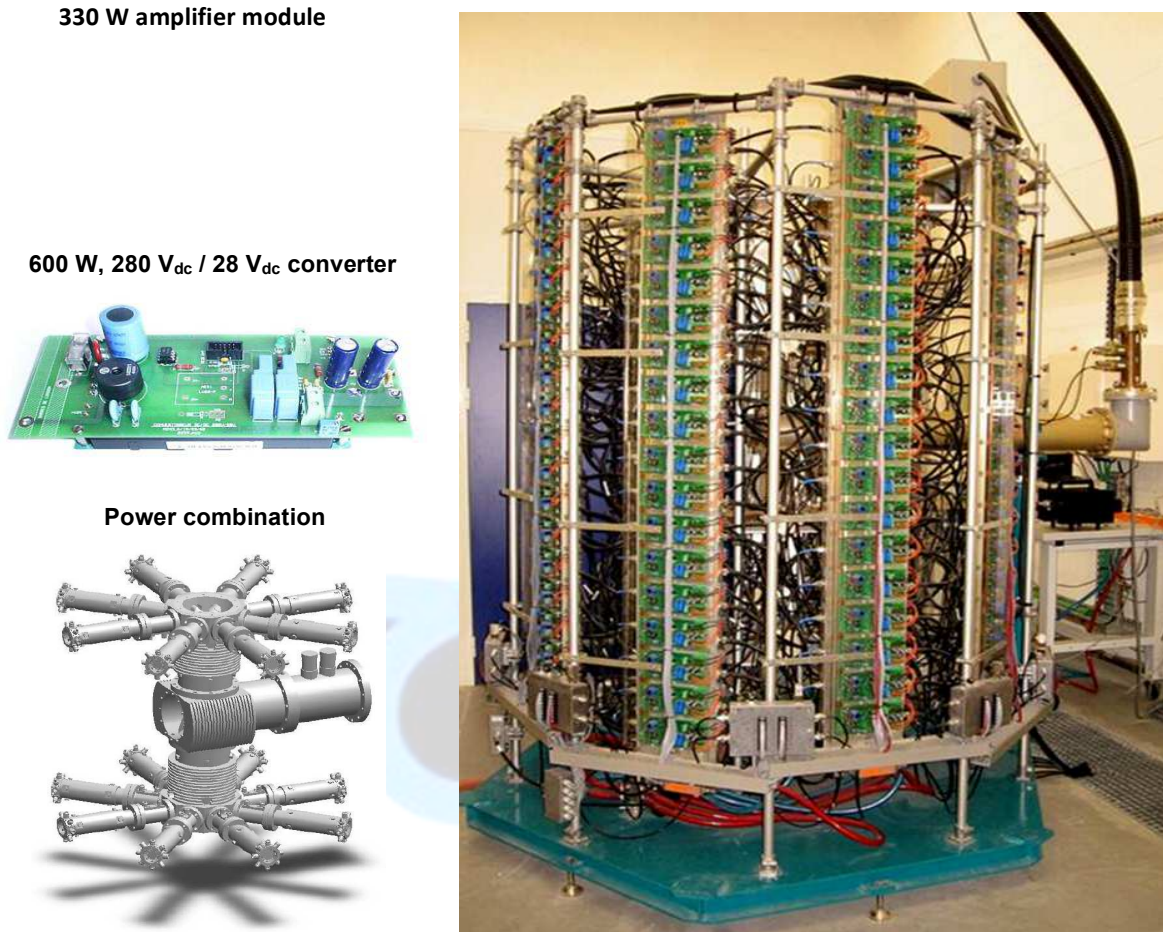


Figure 3.46. 35 kW - 352 MHz solid-state amplifier of the SOLEIL Booster (147 amplifier modules and DC/DC converters, bolted on 8 water-cooled dissipaters).

3.6.4 Low level RF system and longitudinal feedback

The proposed low level RF (LLRF) system is conventional. As shown by the synoptic diagram of Fig. 3.47, it consists of three relatively slow loops (frequency, amplitude and phase) aimed at controlling the cavity voltage with an accuracy of about $\pm 0.2\%$ in amplitude, $\pm 0.2^\circ$ in phase and a response time around 1 ms. This scheme is suitable for compensating the pressure and temperature drifts, as well as the power supply ripples.

Such a system is not fast enough to deal with the beam phase oscillations at the synchrotron frequency, f_s , on the order of 400 kHz, that originate in injection transients. These oscillations can produce an undue emittance blow up and a phase jitter at the interaction point. Beam dynamics simulations show that preserving the beam quality requires a damping of these oscillations within a few tens of a μ s (see section 3.3.3). As the radiation damping is negligible during the storage time, a longitudinal feedback

(LFB) must be implemented. It can be performed by a dedicated broad-band longitudinal kicker that acts on the beam. Since ThomX is operating with a single bunch, we propose to use the main cavity as a longitudinal kicker, despite its narrow bandwidth of $25 \text{ kHz} \ll f_s$. This difficulty can be overcome by making the cavity *effective bandwidth* much larger than this value, in fact larger than f_s . We will use a high gain direct RF feedback (RFFB) that allows the operation of a fast phase feedback (φ FB). Assuming a cavity-to-amplifier distance of about 10 m, the loop delay will be less than 150 ns. Then one expects an RFFB gain, G_o , larger than 50, which leads to an effective bandwidth larger than 1 MHz. Simulations show that a LFB that combines such a RFFB with a φ FB (see Fig. 3.48) can damp injection phase errors of up to 10 degrees within a few μs , *i.e.* faster than the above specification.

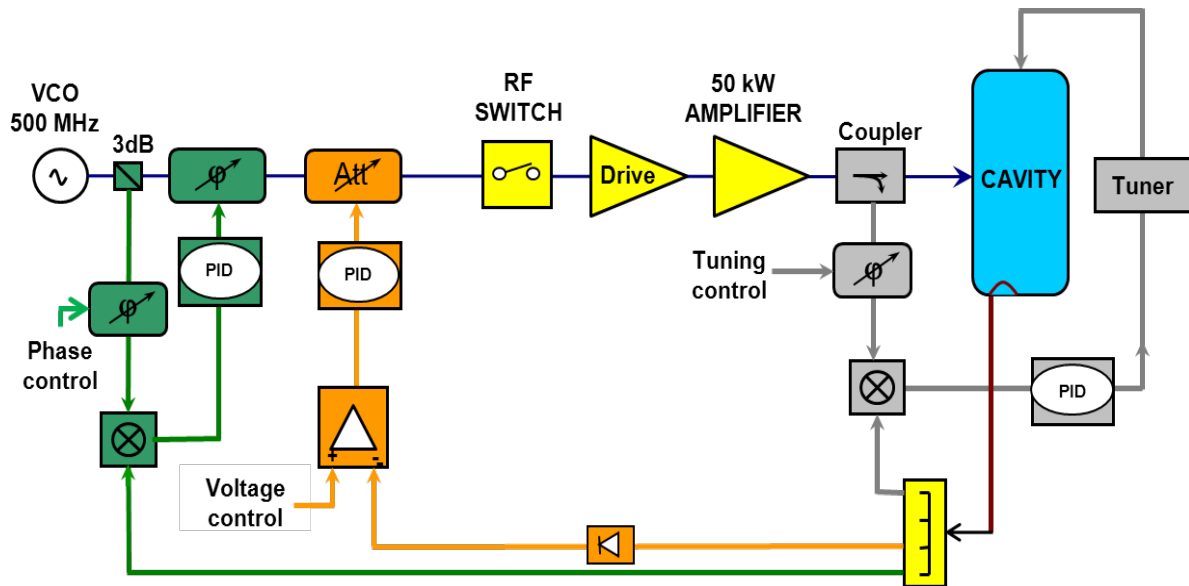


Figure 3.47. Basic LLRF system scheme with ‘slow’ frequency, amplitude and phase loops.

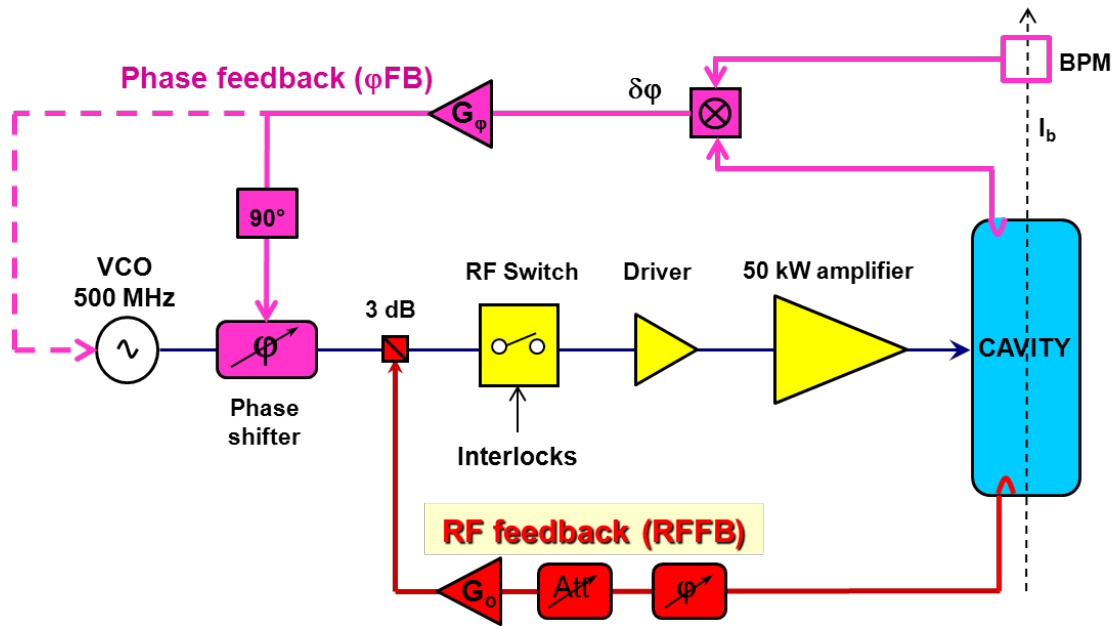


Figure 3.48. Schematics of the longitudinal feedback system combining a phase feedback with a direct RF feedback.

3.6.5 RF equipment status

For the ThomX commissioning, we will use an ELETTRA cavity. The design of all the components of the 50 kW solid-state amplifier (600 W modules, combiners, power supplies...) was validated in 2011. The next two milestones are, first, the validation of a 9 kW unit (combining 16 modules), and secondly the commissioning of the complete amplifier on a dummy load.

Several versions of the LLRF system, including LFB, are under investigation: either fully analogue (see Fig. 3.49) or mixed, analogue for the fast feedback loops, and digital for the slower ones (see Fig. 3.50), or even fully digital, based on the new generation of fast ADC, DAC and FPGA.

3.6.6 RF system: conclusion

For the RF system of the ThomX storage ring, we plan to use a 500 MHz single-cell cavity of the ELETTRA-type. Maintaining at a tolerable level the impact of the RF cavity HOMs on the beam is a challenge. However, this goal should be achievable with a proper control of the HOM frequencies. It can be done by combining three different means of tuning the cavity: temperature control, longitudinal elastic deformation of the cavity and motion of a plunger. The fast longitudinal and transverse feedback systems - which, in any event, are required to damp the beam oscillations resulting from injection transients - will contribute to the damping of the HOM excitations as well.

In order to provide the required accelerating voltage of 500 kV the cavity will be powered by a solid-state amplifier of the ‘SOLEIL’ type, able to deliver a power of up to 50 kW. The cavity voltage will be controlled with an accuracy of $\pm 0.2\%$ and ± 0.2 degree by means of conventional amplitude and phase loops (either analogue or digital) with a few kHz bandwidths. In addition, a fast phase feedback system combined with a high gain direct RF feedback will provide the longitudinal damping which is required to preserve the beam quality

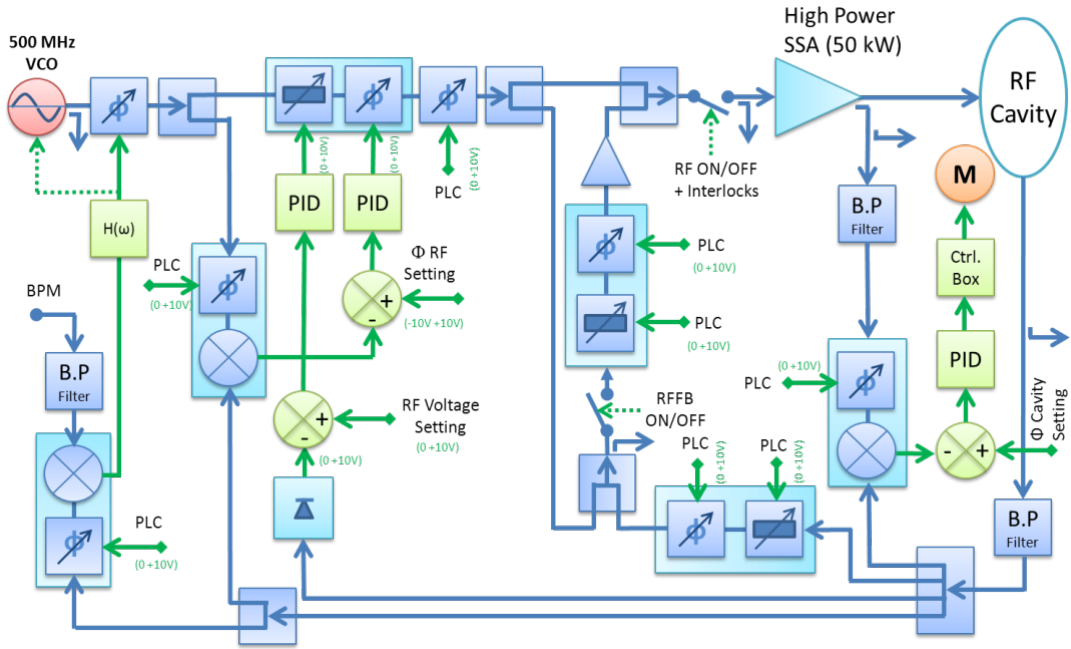


Figure 3.49. Complete LLRF system, longitudinal feedback included (analogue version with phase and amplitude modulation – the option with I/Q modulation is also considered).

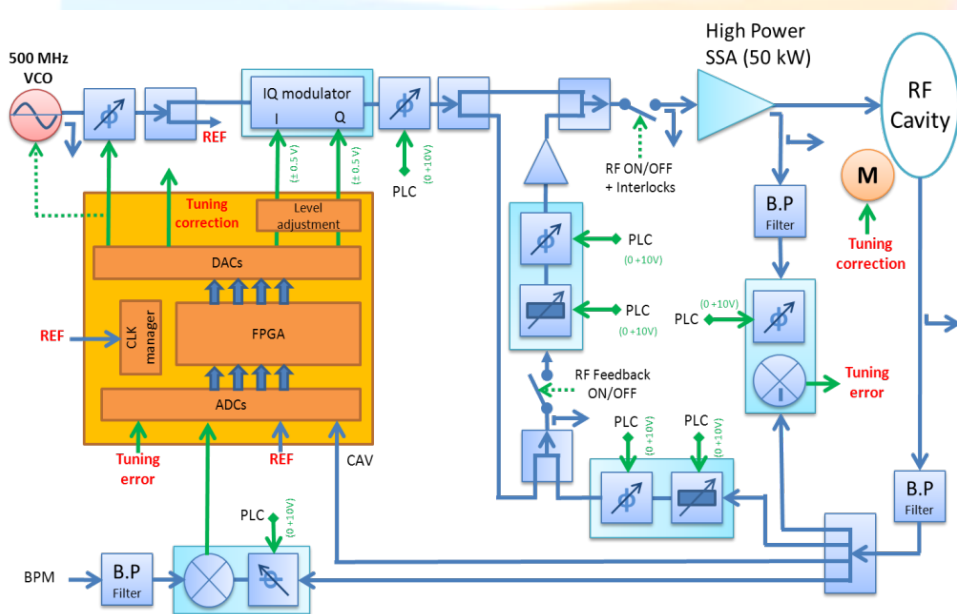


Figure 3.50. Complete LLRF system, longitudinal feedback included (mixed analog/digital version).

3.7 Transverse feedback

3.7.1 Specifications

Table 3.17 summarizes the instability growth time constants and the corresponding kicker strength requirements for the main types of instability. It shows that for Thom-X the betatron oscillations due to the injection jitter in position and angle are the most critical ones. They require a feedback damping time constant of 5 μ s or less (cf. chapter 3).

Source	type	growth time constant	kicker strength
Beam pipe geometry	TMCI Head-Tail	- 160 μ s	>10 nrad
Resistive Wall		600 μ s	>2 nrad
Ions		< 100 μ s	>20 nrad
Injection Jitter		5 μ s	2 μ rad

Table 3.17. Overview of expected instabilities (1 nC, 25 ps rms at 50 MeV).

3.7.2 Electronics

To cope with these instabilities we will use a SPring-8 based high performance digital transverse feedback system which consists of a wideband detector (a BPM), an RF front-end, an FPGA based processor, a power amplifier and a stripline kicker (see Fig. 3.51). This system is capable of detecting a coherent transverse motion and applying a counter kick to damp it, bunch-by-bunch and turn-by-turn, with one or two bunches stored in the ring.

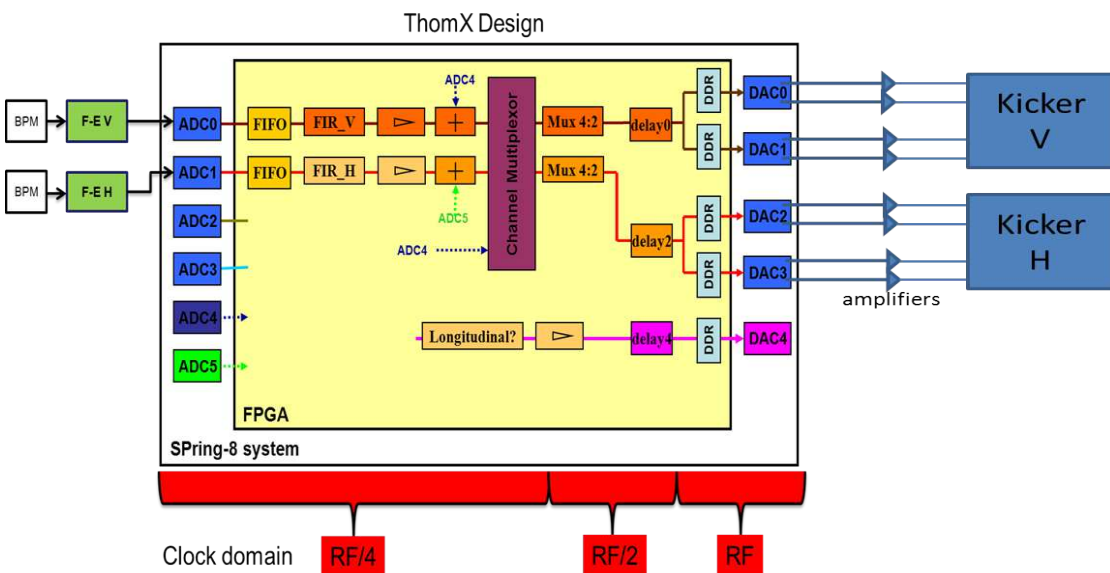


Figure 3.51. Spring-8 based digital feedback system.

Two BPMs (one for each plane) will provide the beam position information. The RF front-end will extract the betatron oscillation information which will be sampled by ADCs. From the sampled data, the FPGA will compute a suitable kick to damp the oscillation. The signal processor output will be amplified by a 10 W wideband amplifiers before being fed to the kicker.

In the RF front-end (see Fig. 3.52) a baseband down-converter will be implemented in order to amplify the beam signal and to minimize the jitter effect; for the same reason, the digital kick will also be extended over four RF periods.

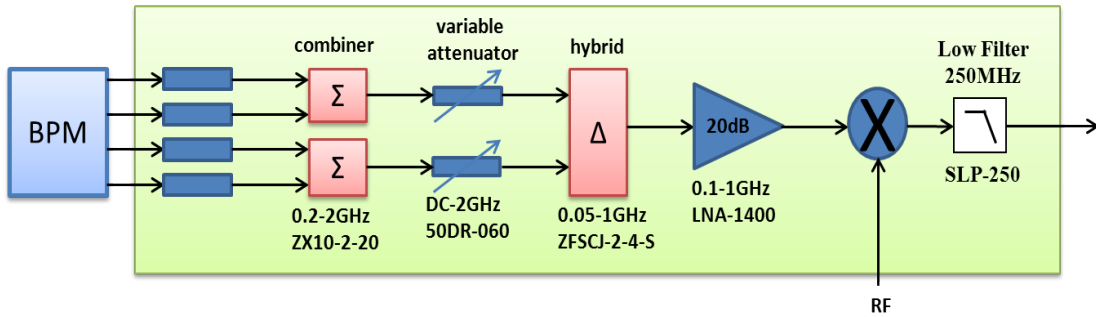


Figure 3.52. Front-end of the Thom-X RF electronics.

For the commissioning phase, a digital system (rather than an analog one) will be used to benefit from the tuning flexibility provided by the digital parameters of the FIR filter. Once the machine tune will be fixed, a more suitable low cost analog system will be installed.

3.7.3 Kicker

The kicker is under development. It consists of a stripline composed of four electrodes connected to vacuum feedthroughs on each side (see Fig. 3.53). The amplifiers will be connected to the downstream ports, whereas upstream ports will be used for signal detection and they will be equipped with $50\ \Omega$ loads. The same kicker will be used to act on the beam in both planes.

Electrode line impedances must be adapted ($50\ \Omega$). Electromagnetic 3-D simulations are being performed to optimize the bandwidth and shunt impedance (*i.e.* to maximize the stripline efficiency) and also to minimize the kicker impedance to wakefields.

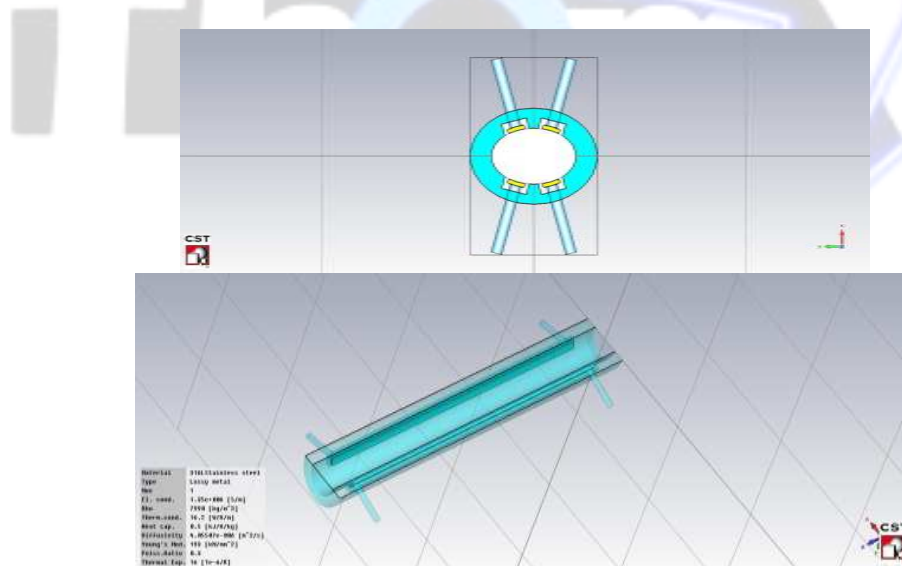


Figure 3.53: Schematics of the Thom-X stripline kicker.

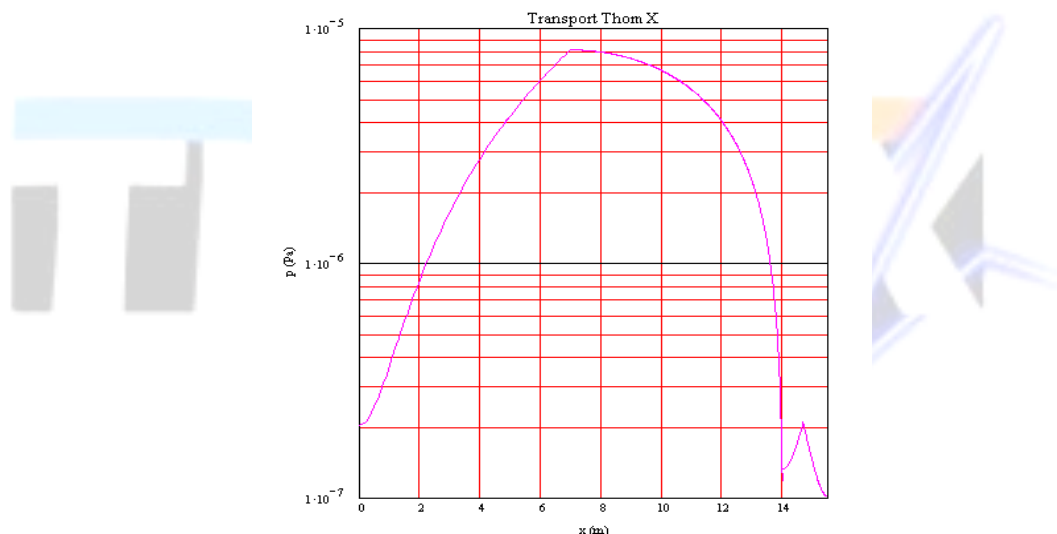
3.8 Vacuum

3.8.1 Transfer line vacuum

Concerning the design of the transfer line vacuum system, three main constraints have been taken into account:

- Pressure of 10^{-7} Pa at the acceleration section output,
- Ion pump operating at 10^{-6} Pa,
- Ring pressure of 10^{-8} Pa.

Simulations have been performed assuming that two $0.3 \text{ m}^3 \text{ s}^{-1}$ triode pumps will be installed, one at the end of the acceleration section and the other at the septum. The vacuum chamber is a DN40. The septum output conductance is $0.18 \text{ m}^3 \text{ s}^{-1}$. Without baking, the outgassing rate would be $\epsilon \tau = 2 \times 10^{-8} \text{ Pa m s}^{-1}$, and the pressure at the ring entrance would be about 10^{-7} Pa. Thus the septum and its environment must be baked to bring τ down to $5 \times 10^{-10} \text{ Pa m s}^{-1}$ and obtain a pressure of 10^{-8} Pa at the ring entrance.



Pressure in the line of transfer

The vacuum equipment envisaged for the transfer line is the following one:

- 3 ion pumps 150 l s^{-1} with their baking systems and power supplies,
- 1 ion pump 500 l s^{-1} with their baking system and power supply,
- 4 Pirani gauges,
- 4 cold cathode gauges,
- 2 power supplies gauges,
- 2 gate valves electro pneumatically actuated DN 40 (acceleration section output ; ring entrance ; beam dump),
- 1 turbo pump (DN 63 $\sim 80 \text{ l s}^{-1}$),
- 1 rotary vane pump ($\sim 12 \text{ m}^3 \text{ h}^{-1}$),
- 4 angle valves manually actuated for pre-pumping DN 63.

3.8.2 Ring vacuum

Concerning the ultra-vacuum to be maintained in the ThomX ring, one must take into account first the pipe relatively low specific conductance $c = 4.52 \times 10^{-3} \text{ m}^3 \text{ m s}^{-1}$, and secondly the pipe specific outgassing rate $\Omega_t = 1.08 \times 10^{-10} \text{ Pa m}^2 \text{ s}^{-1}$. Also, the pumps' effective pumping speed is reduced by the T port with the grid: $S_{\text{eff}} = 1.9 \times 10^{-2} \text{ m}^3 \text{ s}^{-1}$. In a first stage, the ionic pumps chosen for the simulations are $0.040 \text{ m}^3 \text{ s}^{-1}$ diode pumps. This corresponds to $S = 0.030 \text{ m}^3 \text{ s}^{-1}$ at 10^{-8} Pa and, with a grid pumping port whose conductance is $0.0362 \text{ m}^3 \text{ s}^{-1}$, to an effective pumping speed $S_{\text{eff}} = 0.019 \text{ m}^3 \text{ s}^{-1}$. The pressure has been estimated by modeling a quarter of the ring including half of the non-baked optical cavity, *i.e.* in the most unfavorable case.

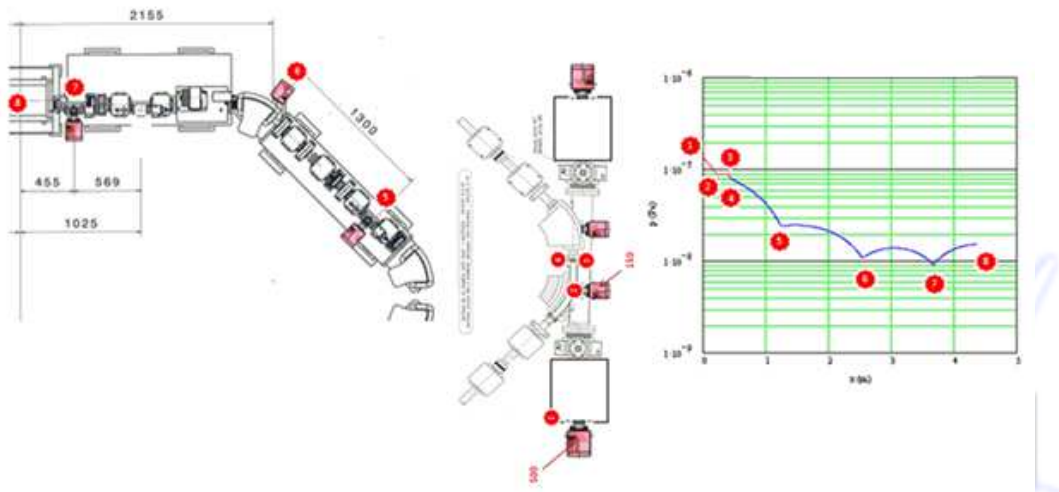


Figure 3.54. Pressure distribution in the vacuum chamber.

The calculated average pressure is $3.06 \times 10^{-8} \text{ Pa}$. It can be improved by increasing the grid pumping port conductance by replacing the DN35 with a DN63. Monte-Carlo simulations show an improvement of $\sim 16\%$ in efficiency:

The entire ring must be baked. Geometrical and temperature constraints (respectively a distance of only 0.7 mm between the magnet coils and the vacuum chamber, a baking temperature of 150°C for the chamber while keeping the coils' temperature below 80°C) are strict. An ultra-thin baking system has been constructed, tested and validated.

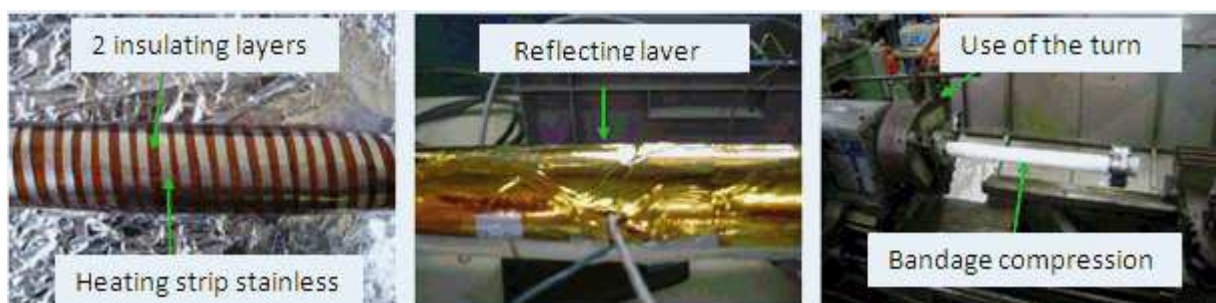


Figure 3.55. The vacuum chamber ultrathin baking set-up.

The following is the vacuum equipment needed for one quarter of the ring:

- 3 ion pumps (40 l s^{-1}) with their baking equipment and their power supplies,
- 1 residual gas analyzer (RGA),
- 2 turbo-pumps (DN 63 $\sim 80 \text{ l s}^{-1}$),
- 2 rotary vane pumps ($\sim 12 \text{ m}^3 \text{ h}^{-1}$),
- 2 Pirani gauges,
- 2 cold cathode gauges,
- 1 gauge power supply,
- 1 DN 63 gate valve electro-pneumatically actuated, with an HF feed-through (one on each side of the RF cavity and similarly for the septum) and the baking equipment,
- the vacuum chamber baking equipment,
- 3 angle valves manually actuated for pre-pumping DN63,
- 3 T with the grid.



Chapter 4. INJECTOR, TRANSFER LINE AND RING DIAGNOSTICS

Several diagnostic devices will be implemented in the ring to measure the electron beam parameters listed in Table 4.1.

Parameter	unit	value
Energy	MeV	50
Average current	mA	17.84
Bunch charge	nC	1
Energy dispersion	%	0.3 at injection to 0.6 at storage end
Emittance x	m.rad	5 e-8 at injection to 30 e-8 at storage end
Normalized emittance x	m.rad	5 e-6 at injection to 30 e-6 at storage end
Emittance y	m.rad	5 e-8
Normalized emittance y	m.rad	5 e-6
Bunch length	ps-rms	revolutions 1 ~ 4 revolutions 100-200 ~ 25 revolutions 200-300000 ~ 50
RF frequency	MHz	500
Revolution frequency	MHz	17.84
Period	ns	56
Injection repetition rate	Hz	50
Ring circumference	m	16.80

(a) Ring parameters

Magnetic field	T	0.5
Radius of curvature	m	0.352
R51	m	0 to -0.25
R52	m	0 to -0.45
R56	m	0.7 to -0.7
Beta x	m	0.6
Beta y	m	6
Eta x	m	0.2 - 0.3
Transverse dimension x	mm (rms)	0.6
Transverse divergence x	mrad	2
Transverse dimension y	mm (rms)	0.54
Transverse divergence y	mrad	2

(b) Parameter values at the location of the bending magnets

Table 4.1. ThomX beam parameters.

4.1 Charge measurement

4.1.1 Current transformers

The beam charge will be measured non-destructively with commercial, in-flange, high resolution current transformers (ICT). Three devices will be installed

- one in the linac (LI/DG/ICT.010), located before the accelerating sections.
- one at the transfer line entrance (TL/DG/ICT.010),

- one at the transfer line exit (TL/DG/ICT.020).

In-flange ICTs are directly mounted in the beam line. They are UHV compatible, can be baked up to 150° C (185° C on request) and they are available for many pipe diameters (also with an elliptical aperture or any other aperture shape). We will use the CF6" model; its internal diameter is 60.4 mm and it is 60 mm long. This device includes a ceramic gap, a shield and a wall current bypass. Bellows are not required.

The signal from each integrating current transformer will be processed by a BCM (beam charge monitor). A built-in calibration generator provides an on-line check of the measurement reliability. An Integrate-Hold-Reset (BCM-IHR) device is suited for pulse repetition rates ranging from 10 kHz down to single pulses and for bunch charges up to 2 nC. The acquisition will be performed by using a 100 kHz, 12 bit ADC.

4.1.2 Faraday cups

Interceptive absolute beam charge measurements will be performed by Faraday cups. There will be two of them, placed inside the two beam dumps (see Fig. 2 of the Introduction). They should provide a better resolution for small electric charges.

4.2 Transverse profile measurements

4.2.1 Diagnostics stations

Five diagnostics stations will be installed to measure the transverse beam profile as shown in Fig. 4.1. Diagnostics station 1 (DS1 – LI/DG/SST.010) will be located after the RF gun at the beginning of the linac. Diagnostics station 2 (DS2 – TL/DG/SST.010) will be located between the end of the linac and the linac beam dump. Diagnostics station 3 (DS3 – TL/DG/SST.020) will be placed in the middle of the transfer line. Diagnostics station 4 (DS4 – TL/DG/SST.030) will be located at the end of the transfer line and Diagnostics station 5 (DS5 – EL/DG/SST.010) will be located before the ring dump.

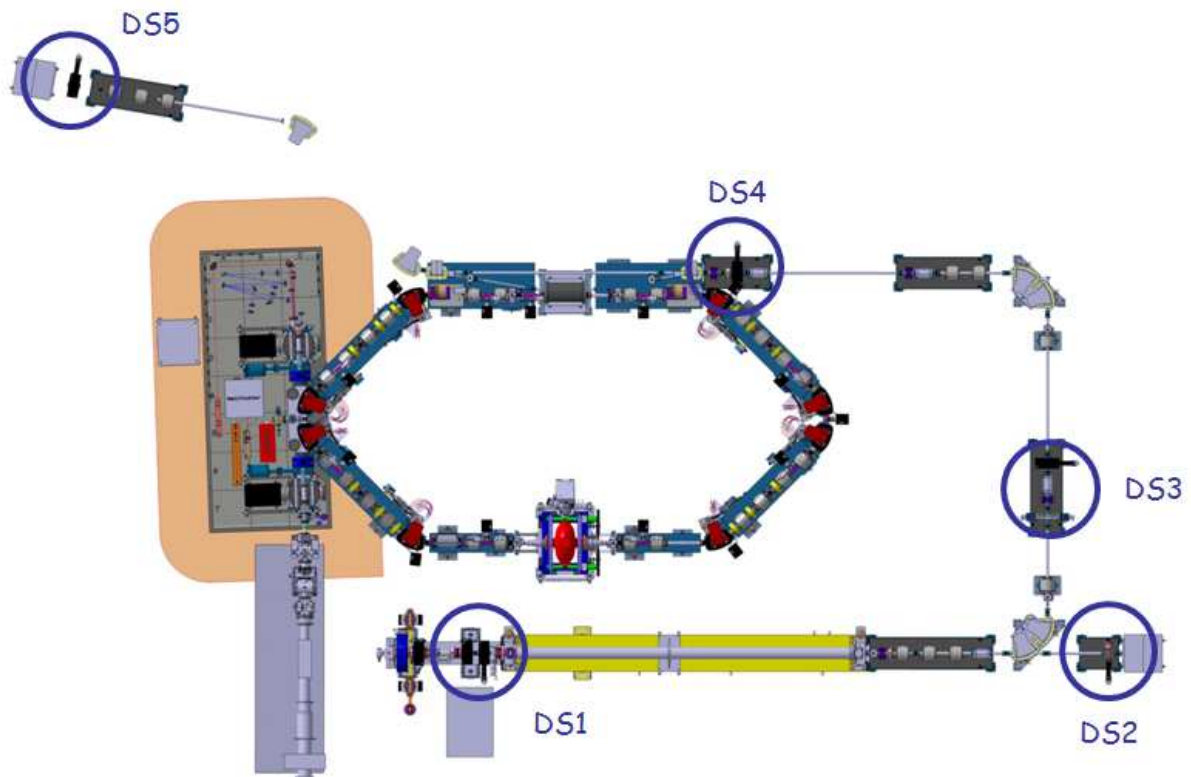


Figure 4.1. Location of the diagnostics stations (see text for the nomenclature).

The ThomX station design draws from the station built by LAL for PITZ (itself drawn from a SOLEIL design). It is illustrated in Fig. 4.2.

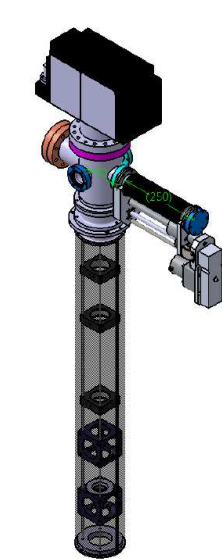


Figure 4.2. 3D view of a ThomX diagnostic station.

Each station will have a motorized arm on which several screens will be mounted. A stepper motor will move this arm and insert the screens laterally. The following screens will be available:

- 1 YAG(Ce) screen in all stations,
- 1 optical transition radiation (OTR) screen in all stations,

- 1 target to allow an online calibration of the camera in all stations,
- one Cerenkov screen for bunch length measurements in station DS2 (described in more detail below).

The YAG(Ce) and OTR screens and the calibration target will be tilted at 45° with respect to the beam axis so that the emitted or reflected light will travel downward and exit the vacuum through a DN60 CF fused silica window. A CCD camera will be located below the station to image the screens. The Cerenkov screen will be titled so that its light exits at the top of the diagnostic station. Shutters will be used to close either the Cerenkov window or the YAG(Ce)/OTR window when not in use to prevent measurement noise due to background photons. Several LEDs located just after the bottom window will be used to illuminate the inside of the chamber when needed.

At the beginning of the Linac, at station DS1 the beam size will be about 0.5-0.7mm (rms) in both planes, at the end of the Linac, at DS2, the beam size will be 1.5 mm (rms) in both planes. In the middle of the transfer line, at DS3, the beam size is expected to reach 2.5 mm (rms) in x and slightly less than 1mm in y. At the end of the transfer line, at DS4, it will be about 1 mm in both planes. After the extraction, at DS5, the beam size will be about 0.5-0.7mm (rms) in both planes. Given these beam sizes, we chose a screen diameter of 25 mm for all stations.

Screen photon yield

The YAG(Ce) screen will be 100 µm thick. Such screens have a light yield of 8 photons per deposited keV [4.1]. The YAG radiation length is 35 mm [4.2]; assuming the usual model for energy deposition in matter [4.3], each electron will deposit about 143 keV in the screen; this corresponds to the emission of ~1100 photons. Thus the total number of photons produced by an e⁻ bunch crossing the screen will be $7.1 \cdot 10^{12}$. We recall that YAG(Ce) emission occurs in all directions.

The second screen will be of the OTR type. The screen support design allows either the use of a 100 µm aluminized silicon wafer or of an ultra-thin aluminized mylar film. The silicon wafer has the advantage of giving a better image quality while the mylar film allows a beam injection through the screen without significantly affecting its quality. The OTR yield within a cone of half-aperture θ for photons whose wavelengths range between λ_1 and λ_2 is given by [4.4]:

$$N_{OTR} = \frac{\alpha}{\pi} \left[\ln(\gamma\theta)^2 - 1 \right] \ln \frac{\lambda_1}{\lambda_2}$$

Thus, for a standard CCD camera whose sensitivity ranges between 400 nm and 800 nm and assuming an acceptance cone of 0.03 radian, this expression gives ~0.002 photon per electron at 50 MeV (station DS2-5). A similar yield is reached at 5 MeV with an acceptance of 0.3 radians (station DS1).

To image the screens, a lens will be located 500 mm away from them. A small telescope made of two lenses will be used to focus the light on the CCD camera. At least one of the telescope lenses will be movable to provide the needed dynamic range. A Gigabit Ethernet camera with at least 600 x 400 pixels will record the images. The camera's square pixels are about $7.4 \times 7.4 \mu\text{m}^2$.

With such a configuration, one expects that a 50 MeV bunch passing through the YAG(Ce) screen will emit 7.1×10^{12} photons and assuming that the CCD chip has an average efficiency of 50%, 10^{10} counts will be recorded by the camera, taking into account the solid angle covered by the lens.

The same bunch passing through the OTR screen will emit $8.2 \cdot 10^7$ photons within the lens acceptance. Thus $3 \cdot 10^6$ counts will be recorded by the camera.

For a 5 MeV bunch (station DS1), the YAG(Ce) screen will emit $2 \cdot 10^{12}$ photons and 10^9 counts will be recorded by the camera. The OTR screen will emit $8.2 \cdot 10^7$ photons within the lens acceptance and $3 \cdot 10^6$ counts will be recorded by the camera.

Assuming a transverse beam size of 1.5 mm, one expects $8 \cdot 10^6$ counts per pixels with a YAG(Ce) screen and $2.5 \cdot 10^5$ counts per pixel with an OTR.

If the 50 MeV beam is defocused (for example during a quadrupole scan) to produce a 5 mm spot size, these numbers become $8 \cdot 10^5$ for the YAG(Ce) screen and $2 \cdot 10^4$ for the OTR.

	Number of OTR photons emitted	Number of OTR photons recorded by the camera	Number of YAG photon emitted	Number of YAG photons recorded
DS1	$8.2 \cdot 10^7$	$3 \cdot 10^6$	$2 \cdot 10^{12}$	10^9
DS2-5	$8.2 \cdot 10^7$	$3 \cdot 10^6$	$7.1 \cdot 10^{12}$	10^{10}

Assuming a YAG Cerium dopant density of 0.18%, we get a Cerium density of $2.5 \cdot 10^{19} \text{ cm}^{-3}$ [4.5] and a 15% scintillation efficiency. It follows that the scintillating site density is $3.7 \cdot 10^{18} \text{ cm}^{-3}$. Therefore the 100 μm YAG(Ce) screen will saturate when the photon density reaches $3.6 \cdot 10^{14} \text{ mm}^{-2}$. This last figure translates into an electron density of $3.2 \cdot 10^{11} \text{ mm}^{-2}$ for an e^- beam energy of 50 MeV. In these conditions the YAG(Ce) screen will saturate if the beam is focussed on a spot smaller than 20 μm . This is five times less than the smallest beam foreseen at ThomX.

Additional targets will be used to calibrate the cameras when necessary. They will be made of stainless steel plates with etched grids. Each square of the grid will be 2 by 2 mm^2 . In some of these squares, smaller lines of known thickness will be etched. Images of these targets will allow one to check the whole optics.

To minimize a possible radiation deterioration of the cameras, lead-glass windows will be inserted between the vacuum windows and the focusing lenses.

4.3 Emittance measurement

The beam emittance will be measured with the quadrupole scan technique. In this technique, a triplet (set of three quadrupoles) is used to find the minimum transverse beam size in each plane. A fit of the beam size variation versus the quadrupole strength enables one to retrieve the projected transverse emittance.

The sets of triplets and the diagnostic stations implemented along the ring allow an emittance measurement at three different locations: at the exit of the linac with DS2, in the transfer line with DS4 and in the ring with DS5 by using the extraction kicker. The beam emittance measurement with DS5

will provide a check of the turn-by-turn emittance growth, thus bringing precious information on the transverse beam dynamics.

Pepper-pot measurements are also foreseen. The advantage of this technique with respect to a quadrupole scan is that it consists in a single shot measurement, independent of machine operation fluctuations.

A pepper-pot set-up comprises a plate with evenly distributed holes. Such a plate is placed in the beam path together with a scintillating screen located downstream and an imaging system. A pepper-pot mounted on a movable arm could be located at the end of the linac, between the last dipole and the diagnostic station DS2, and another one could be located just before station DS5.

At station DS2 the beam size will be about 1.5 mm (rms) and the geometric emittance about $5 \cdot 10^{-8}$ m rad. Therefore the maximum beam divergence will be about 50 μrad . By adjusting the quadrupoles, one may focus the beam down to a 20 μm spot and increase its divergence up to 250 μrad . To measure the transverse emittance, one would have to position this focal point two meters before DS2 (or DS5) and to position a pepper-pot mask with 100 μm holes or slits one meter upstream of DS2 (or DS5).

4.4 Beam position measurement

The beam position will be measured by a set of BPMs placed all along the ring. Their locations are shown in Fig. 4.3.

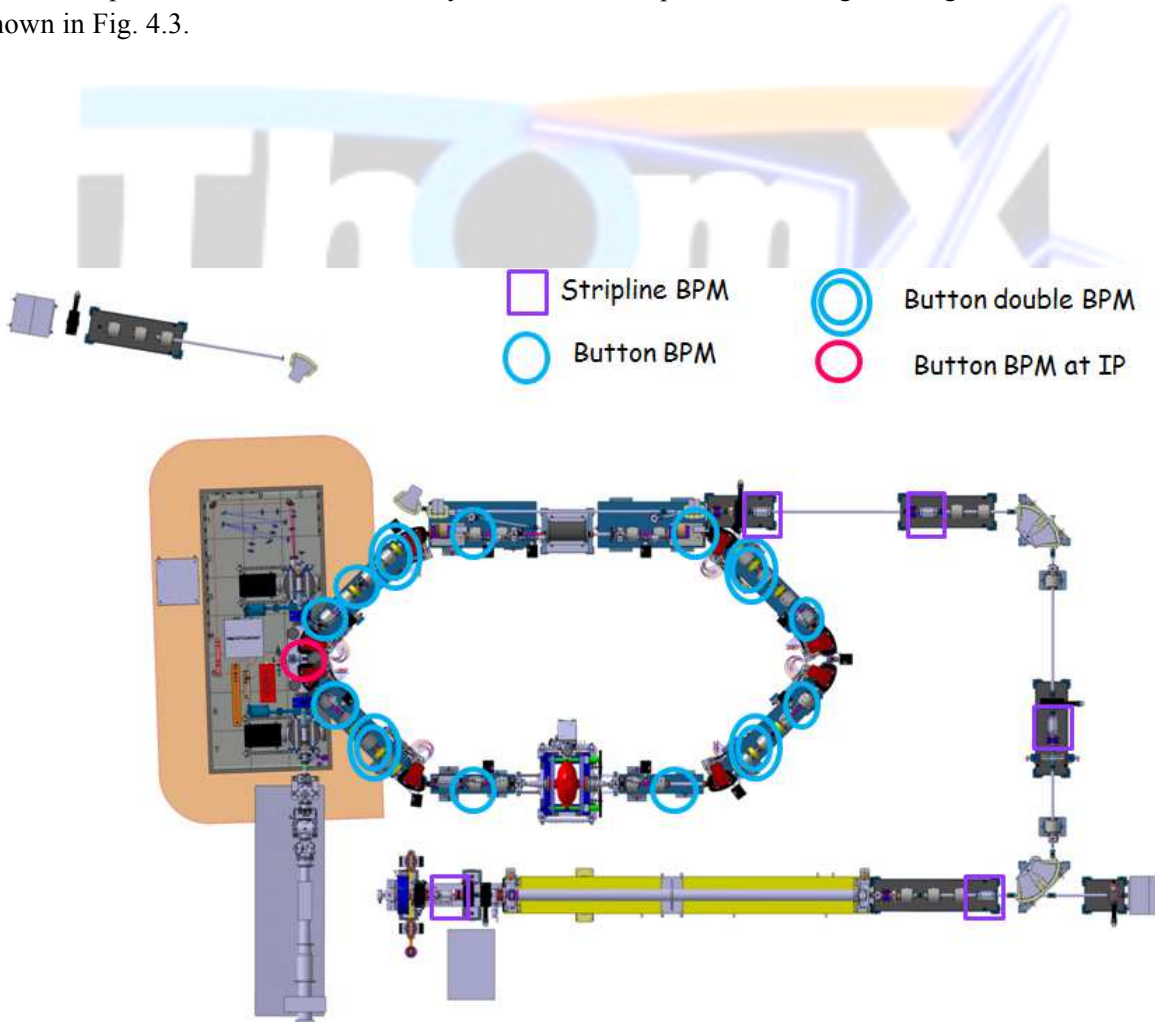


Figure 4.3. Location of the BPMs along the ring (note: the BPM located at the IP has been suppressed since this drawing was made).

4.4.1 Beam Position Monitors (BPM)

Two types of BPMs will be used: short circuited striplines in the linac and the transfer line, and buttons in the storage ring.

Compared to button BPMs, striplines generate a higher signal but need more space and contribute more to the wake-field generating impedance. For these reasons, striplines are preferred for the linac and the transfer line where we need single pass measurements and where wakefield is not an issue. In the storage ring, button BPMs will be chosen for their small size and small contribution to the ring impedance. The lower signal produced by the small electrodes will be compensated by the high repetition rate of the stored beam (averaging is possible).

BPM electronics detection frequency on the storage ring is usually equal to the RF frequency as it is the only common frequency component present in the BPM data whatever the filling pattern is. Even though only one bunch will be stored in ThomX, the same approach is chosen. Therefore, the storage ring BPM electronics detection frequency is 500 MHz.

Since it is more convenient to adopt the same electronics for all the BPMs (linac, transfer line and storage ring), stripline BPMs on the Linac and transfer line are optimized to give a signal with the highest possible component at 500 MHz. Their electrode length is thus adapted to this frequency, which means that it has to be equal to $\lambda/4$ (150 mm @ 500 MHz), where λ is the RF wavelength.

4.4.1.1 BPM for the linac

The linac BPM equipment will be as follows.

- Number of BPM: 1
- Type: short circuited stripline,
- Electrode length: 100 mm,
- Required resolution: 100 μm for a single pass measurement and a 1 nC bunch charge.

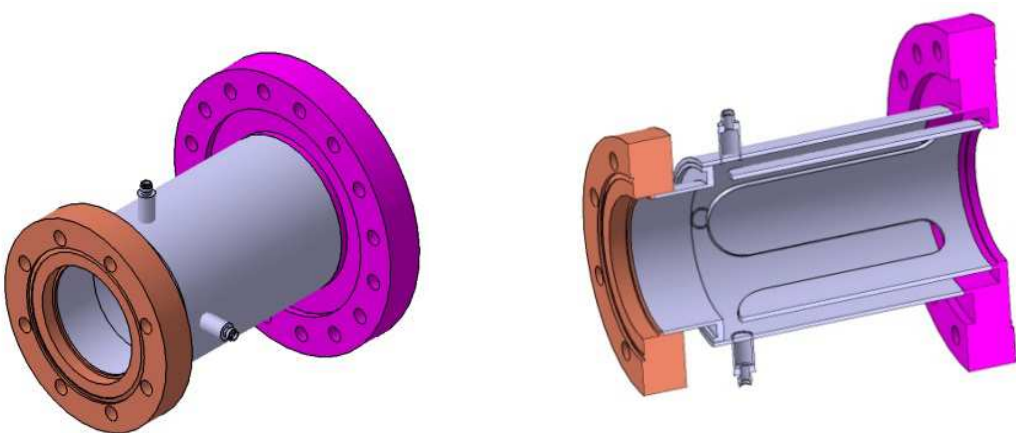


Figure 4.4. Linac BPM.

Due to lack of space in the linac section where a stripline must be installed, the electrode length cannot be 150 mm but must be reduced to 100 mm. Transfer impedance calculations show that at 500 MHz the signal amplitude will be reduced by 13% compared to the optimal length of 150 mm (see Fig. 4.5). This amplitude reduction is acceptable.

Feedthroughs will be soldered on CF16 flanges.

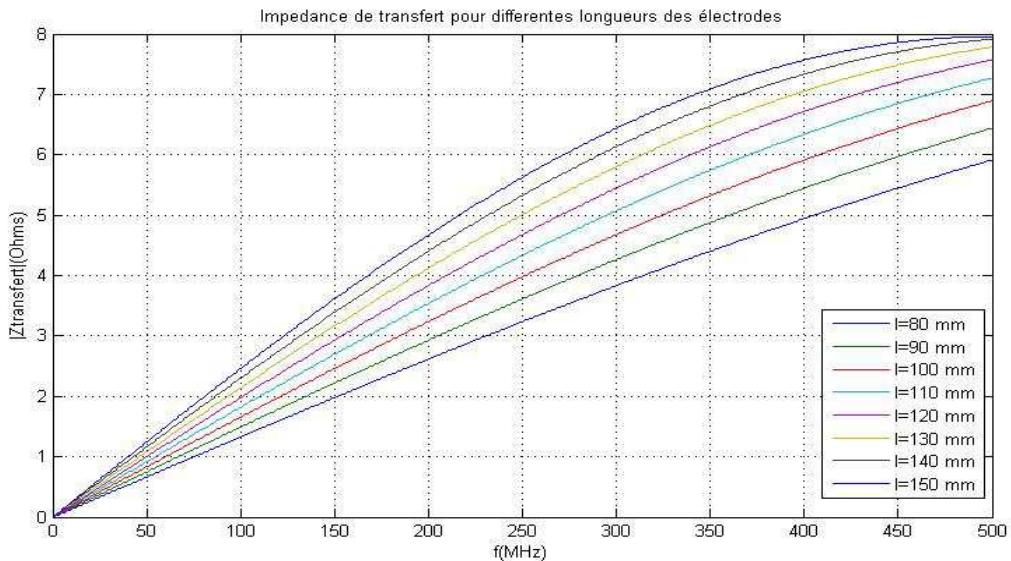


Figure 4.5. Stripline transfer impedance versus frequency for various electrode lengths. With an electrode length of 100 mm, the signal is reduced by 13% compared to its maximum value for a frequency of 500 MHz.

4.4.1.2 BPMs for the transfer line

The transfer line will be equipped as follows:

- Number of BPM: 4,
- Type: short circuited stripline,
- Electrode length: 150 mm,
- Required resolution: 100 μ m for a single pass measurement and a 1 nC bunch charge.

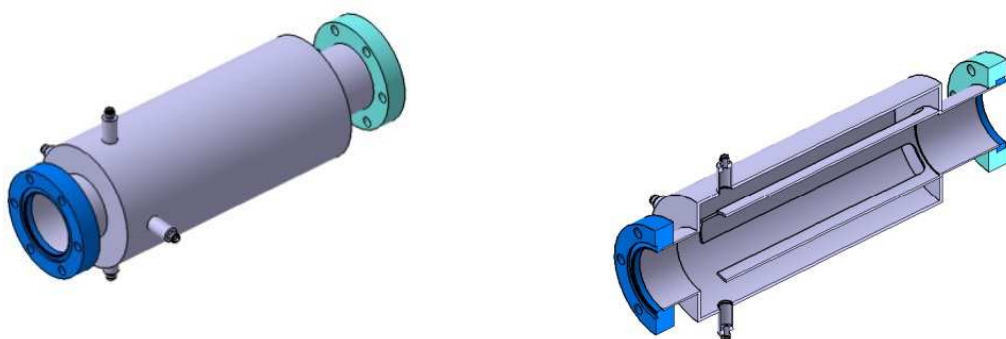


Figure 4.6. Drawing of the BPMs that will equip the electron transfer line.

Feedthroughs will be soldered to CF16 flanges.

4.4.1.3 BPMs for the storage ring

The specifications relevant to the ring BPMs are as follows:

- Number of BPM: 12,
- Type: button,
- Button diameter: 10.7mm,
- Required resolution: $\sim 1 \mu\text{m}$ @ 50 Hz and for a bunch charge of 1 nC,
- Absolute precision: $\pm 250 \mu\text{m}$.

In order to provide additional BPM signals for other applications (see below), 4 BPM blocks will be equipped with a double set of electrodes. In that case only 4 electrodes (among 8) will be used for position monitoring. The button size and the beam pipe size remain unchanged.

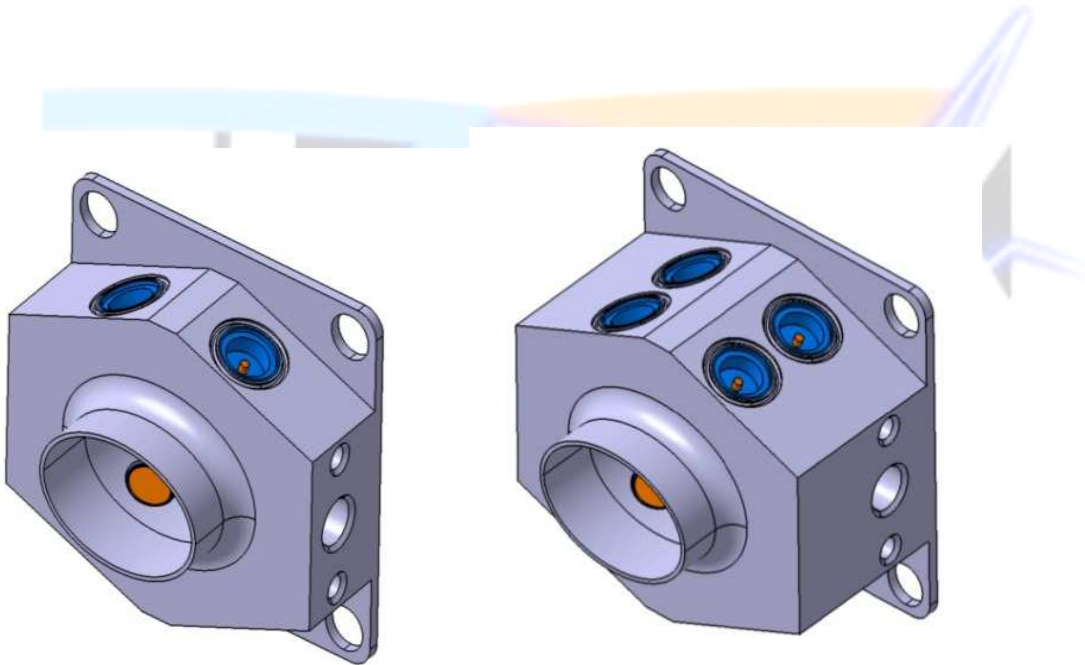


Figure 4.7. Simple and double BPM blocks for the ThomX storage ring.

The button positions and dimensions have been determined by simulations with Poisson Superfish (an electrostatic simulation software). An evaluation of the impedance due to the button discontinuities has shown that their effect will be negligible.

Feedthroughs will be soldered directly to the BPM block. They are bakable. Connectors will be SMA males to prevent any deformation during baking.

Alignment

BPM blocks will have an external mechanical reference. This reference will be used for BPM alignment during the installation phase and to position precisely the block in a calibration bench.

Calibration

Storage ring BPMs will be calibrated by using a dedicated bench. An antenna inside the block will be fed with a 500 MHz wave of constant amplitude. Calibration is done by measuring the signal output by the 4 buttons. A precise position of the antenna is not needed as position errors can be eliminated by repeating the measurement with the BPM block turned by 180°, and averaging the results.

The second halves of the blocks equipped with two sets of buttons will be dedicated to

- longitudinal (beam phase) feedback (one set of BPMs),
- transverse feedback (one set of BPMs),
- ion clearing. To suppress ions which may generate beam instabilities, BPM buttons will be polarized with a high voltage (max ±200V). This electric field will deflect the ion trajectories toward the vacuum chamber.

Electronics

Electronics will be the same for all BPMs (whether equipping the linac, the transfer line or the storage ring).

Data rate

Revolution-by-revolution beam position measurements would be best. But because of the high revolution frequency (17.8 MHz), it might be difficult to get electronic devices that handle the corresponding data rate. Then one may work with averages over two turns. This data will be provided on demand and the acquisition will be triggered. The buffer size should accommodate data collected during at least 20 ms to cover full storage cycles. Revolution-by-revolution data will be used for machine physics studies and tune measurement. The position measurement resolution must be better than 100 µm.

Slow acquisition

Slow data acquisition will be used for slow orbit correction and slow orbit feedback. It will be obtained by averaging the fast data flow with a sampling rate of ~10 Hz. A data rate of 50 Hz would provide just one measurement per storage cycle. The resolution aimed at for this measurement is one micron or better.

Acquisition must be synchronous with the machine revolution frequency. Moreover, modules must be synchronized together.

Connections and cables

The four cables that carry the signals of each BPM should be put together in a strand. Their electrical lengths will be matched so that phase differences are kept below 13° @ 500 MHz. The cable attenuation should not differ much from one BPM to another. If the cable lengths cannot be the same for all BPMs, cable sections will be chosen in order to ensure the same attenuation for all cables. To minimize both

attenuation and cost, cable lengths below will be kept below 30 m. The LMR240 cable is an example of what could be used; its attenuation is ~6 dBm @ 500 MHz over a distance of 33 m.

As radiation close to the machine can damage the cable insulator, short (~1 m) pigtails (that can be easily replaced if needed) will be inserted between the BPMs and the long cables.

4.4.2 Orbit feedback system

A feedback system will keep the beam orbit stable within $\pm 1 \mu\text{m}$. It will use the position measurements provided by the 12 ring BPMs. The correction rate will be comprised between 0.1 Hz and 10 Hz. Correction signals will be applied to the 12 correctors located along the ring. The orbit feedback system will be a matlab based application.

4.4.3 Tune measurement and feedback

The tune will be obtained from the revolution-by-revolution data provided by the BPMs. There is no need for any kicker to excite betatron oscillations as the beam transverse position will naturally oscillate after each injection (*i.e.* every 20 ms). If necessary, a tune feedback will be implemented to keep the tunes constant.

4.4.4 Energy measurement

In the middle of the transfer line, *i.e.* downstream of the dipole located at the end of the linac, the dispersive function is non-zero. Therefore, the beam energy and its spread can be deduced from the electron horizontal distribution shown by the YAG screen in DS3. The same measurement will be performed with DS4, using the dispersion induced by the extraction magnet.

4.5 Bunch length measurement

The bunch length will be measured at two different places: at the end of the linac and in the ring. Depending on the observation point, two different physical processes are used to produce visible light pulses which are then transported by dedicated optical lines through the ThomX shielding wall to a double-sweep streak camera located in the experimental hall.

4.5.1 Cerenkov radiation

Cerenkov radiation (CR) produced in a target placed at the end of the linac will be used to measure the e^- bunch length. Cerenkov radiation is emitted when a charged particle passes through a medium at velocity greater than the speed of light in that medium. It is emitted at an angle θ_{cr} – with respect to the particle momentum – determined by $n(\lambda)$, the medium index of refraction, and β , the particle velocity as follows:

$$\cos(\theta_{cr}) = \frac{1}{\beta n(\lambda)}$$

Above 10 MeV, the emission angle is almost independent of the particle velocity. N_{cr} , the number of radiated photons whose wavelengths range between λ_1 and λ_2 , summed over a path of length d along the charged particle trajectory, is

$$N_{cr} = 2\pi\alpha d \left(\frac{1}{\lambda_1} - \frac{1}{\lambda_2} \right) \left(1 - \frac{1}{\beta^2 n^2(\lambda)} \right) N_{cr} = 2\pi\alpha d \left(\frac{1}{\lambda_1} - \frac{1}{\lambda_2} \right) \left(1 - \frac{1}{\beta^2 n^2(\lambda)} \right)$$

where $\alpha=7.3 \cdot 10^{-3}$ is the fine structure constant.

Two types of radiator are usually used to produce Cerenkov radiation: an aerogel or a solid target. Aerogels dramatically spoil the vacuum and therefore have to be mounted in a separate vacuum vessel to maintain ultra-high vacuum conditions. Solid targets are UHV compatible. This is why they are preferred.

At the end of the linac, when the bending magnet is off, the beam goes straight into a beam dump. Before the dump, several types of targets can be inserted in the beam trajectory for diagnostic purposes. For the production of Cerenkov radiation, a sapphire target is adequate. This material's index of refraction is 1.77. With a 50 MeV beam, the Cerenkov angle is $\theta_{cr}=55.63^\circ$. Assuming that the window thickness is 0.25 mm, 16 photons/e⁻ are created with a wavelength ranging between $\lambda_1 = 300$ nm and $\lambda_2 = 800$ nm. Their spectrum is given in Fig. 4.8. For a 1 nC electron bunch, 10^{11} photons are created. The energy deposited in such a target is negligible.

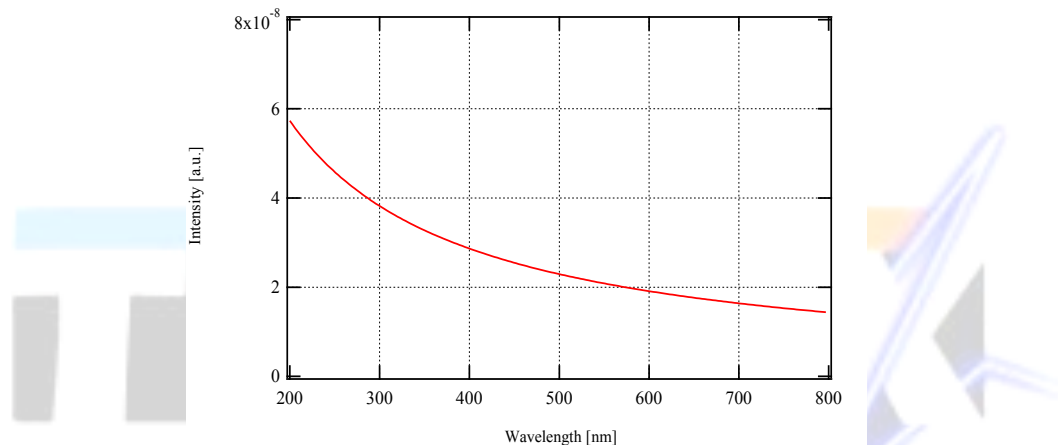


Figure 4.8. Spectrum of the Cerenkov radiation emitted by a 50 MeV e⁻ beam passing through a sapphire window, 0.25 mm thick.

For simplicity, the sapphire target is oriented so that the Cerenkov radiation exits in the vertical direction. For a Cerenkov angle $\theta_{cr} = 55.63^\circ$, the window angle with respect to the beam axis must be $\theta_p = 114.75^\circ$ (see Fig. 4.9).

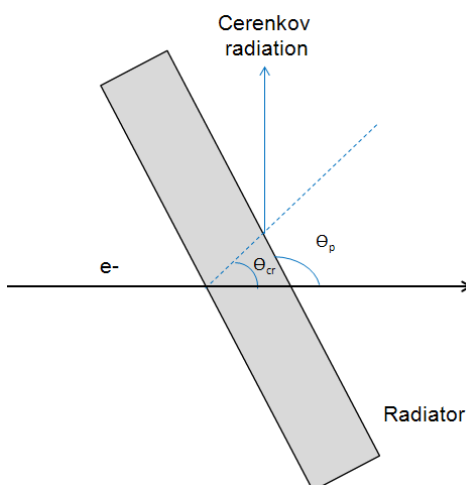


Figure 4.9. Orientation of the sapphire target used to observe the Cerenkov light emitted by the e^- beam at the linac end.

At the target location, the beam dimensions will be $\sigma_{x,y} = 1.4$ mm (rms). It will produce a light spot whose dimensions will be $\sigma_x = 1.4$ mm (rms) and $\sigma_y = 1.54$ mm (rms) in the sapphire. To intercept the whole light beam and to leave some margin for the alignment, we will use a target whose diameter will be equal to $2 \times 6 \times \sigma_y \sim 20$ mm.

The Cerenkov radiation will exit the vacuum chamber via a UHV viewport made of fused silica (FuSi) with a 90% transmission over the 300-800 nm wavelength range. The viewport is mounted on a CF63 flange that provides a 68 mm clear aperture. At the exit of the viewport, a FuSi lens is used to focus the light. This collimated beam is then transported via a set of planar mirrors across the shielded area and then through the ThomX shield to a dedicated hutch in the experimental hall (see § 4.5.3).

4.5.2 Synchrotron radiation

Most of the synchrotron radiation (SR) emitted when the electrons circulate in a bending magnet (BM) will be in the far infrared, but visible light will also be present. The cut-off wavelength of this radiation corresponds to ~ 0.77 eV. Thus the X-ray content is negligible. This last feature makes the extraction of the visible part of the spectrum easy. The spectral flux per unit bandwidth per unit surface Φ_{BM} [Photon/s/0.1%bw/mm²] is shown in Figure 4.10.

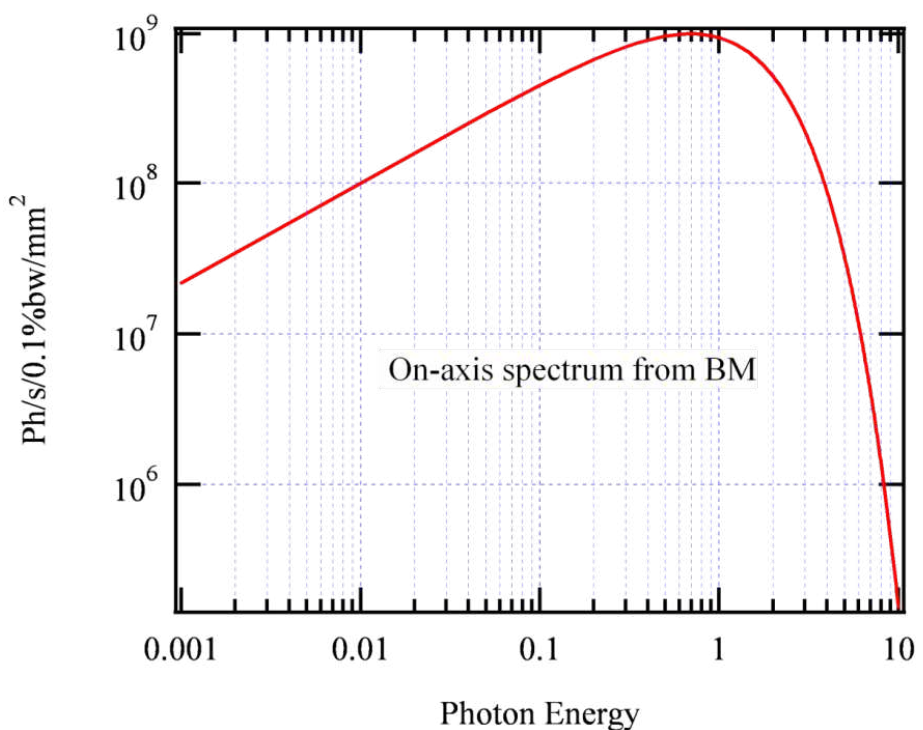


Figure 4.10. On-axis spectral flux, 1 m downstream of a bending magnet. Photon energy in eV. The visible spectral range corresponds to [400 nm - 800 nm] or [1.55 eV - 3.1 eV].

The radiation is extracted at the exit of the BM n°5 through a porthole which provides a 63 mrad x 32 mrad aperture at 15° with respect to the 0° incident angle in the dipole. The maximum power density is

$4 \mu\text{W/mm}^2$ in the horizontal plane of this extraction porthole; thus no dedicated absorber is required. (But for the porthole region, the radiated power will be dissipated in the vacuum chamber wall.) The radiation will exit the vacuum chamber through a UHV viewport made of MgF₂ (this material offers the highest transmission coefficient over the 200-800 nm range). The synchrotron radiation distribution at 5 eV, one meter downstream of the bending magnet, is around 6 mm (FWHM). So the spectral flux integrated over a collecting area of 6 mm x 63 mm is about (around 5 eV):

$$\Phi_e [\text{Ph/s}] = \Phi_{BM} [\text{Ph/s}/0.1\%\text{b.w./mm}^2] \times 6 \text{ mm} \times 63 \text{ mm} \times 1000.$$

Since photons of lower energy thus with a higher divergence will also contribute to the total spectral flux, this value gives a low limit estimate of the real total spectral flux. Figure 4.11 shows the Φ_e spectral flux.

As was the case for the Cerenkov radiation, a FuSi lens will be used at the exit of the viewport to focus the beam. The collimated radiation will then be transported via a set of planar mirrors across the shielded area and then through the ThomX shield to a dedicated hutch in the experimental hall (see next section).

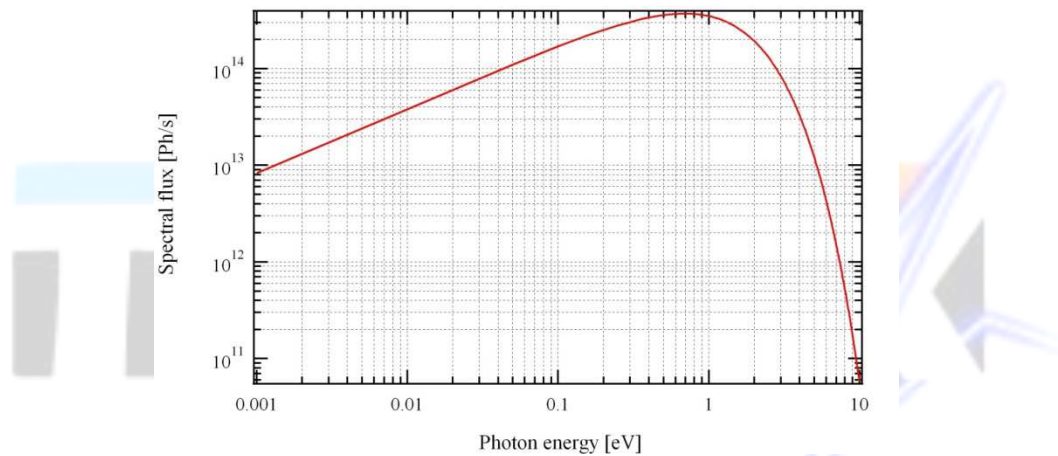


Figure 4.11. Spectral flux Φ_e in a $63 \times 32 \text{ mrad}^2$ aperture, 1 m downstream of a bending magnet.

4.5.3 Transport of the Cerenkov and synchrotron radiations to the diagnostics hutch

Both the Cerenkov light and the synchrotron radiation have to be transported to the diagnostics hutch located in the experimental hall. Starting from different locations, both radiations will be transported via a set of planar mirrors to a ‘meeting point’ inside the shielded area. A flip mirror (*i.e.* a double-orientation mirror) will enable the selection of one of the radiations. The one selected will be further transported, again with a set of planar mirrors, through the shielding wall to the diagnostics hutch.

Inside the diagnostics hutch, the last lens will focus the radiation on the streak camera entrance. The lens aperture and its focal length will be adapted to the selected incoming radiation. All the line components and their parameters are chosen to minimize spatial aberrations and to maximize the number of photons entering the streak camera.

4.5.4 Streak camera for the bunch length measurement

We plan to use a double-sweep streak camera to measure the bunch length and to visualize its evolution over short time scales. Since the bunch length may vary from 4 to 20 ps (rms), a 2 ps (FWHM) resolution streak camera is required.

The time resolution of the bunch length measurement depends on the radiation type (CR or SR) which is used and involves several contributions: the electron transverse beam size at the light emission point, chromatic effects, etc. All these contributions will be minimized as much as possible to maintain the effective resolution as close as possible to the one of the streak camera.

4.6 Bunch imaging using synchrotron radiation

The synchrotron radiation transported to perform the bunch length measurement (see section 4.5) can also be used to image the bunch while it circulates. For this purpose, a beam splitter could be installed at the radiation exit port: the main part of the radiation would be sent to the streak camera while a small fraction would be directed to a CCD camera mounted nearby. A focusing lens placed between the viewport and the CCD would enable the imaging of the stored beam.

In the orbit section where the bunch emits the synchrotron radiation used for the above measurements, the e^- beam transverse size is about 0.5 mm (rms). Since the size of a CCD chip is typically 5 mm, the lens gain should be about 10. Such a set-up would enable one to follow the evolution of the beam size in real time (we will use a CCD whose acquisition rate is about 10 Hz). It would be a non-destructive and cheap diagnostic. Similar setups are currently used on storage rings to measure the electron beam emittance assuming that the beta function is known.

4.7 Beam loss measurement

Particle losses will be measured by using optical fibers [4.6]. When a charged particle crosses a glass fiber, Cerenkov radiation is emitted within the fiber and propagates along the fiber. It can be detected by a photomultiplier that collects the light at the fiber end. The measurement *e.g.* with an oscilloscope of the pulse production (in the fiber) time enables one to recover the particle loss location.

Two fibers will be installed. One will be used to monitor e^- losses along the linac and the transfer line. The second fiber will be used to monitor particle losses along the ring. Each one of these fibers will be connected to a fast photomultiplier (PMT). The PMT time resolution will determine the accuracy with which the losses can be localized.

A fused silica fiber has a yield of 227 photons per cm of a relativistic electron track [4.7, 4.8]. Therefore a 5 mm thick fiber will have a yield of \sim 100 photons per relativistic electron which crosses it. Such a signal should be easily detected by a PMT.

As it may be difficult to place the fiber close to the beam pipe in some parts of the ring, the fiber may have to be located at a distance d away from the beam axis. Then the number of lost particles which will cross the fiber will be reduced by a factor d^2 .

4.8 Beam dumps

The ThomX set-up will include two particle dumps to stop the e^- beam in such conditions that the radioactivity then generated is minimal. The first dump will be located at the linac exit. The second dump will be located downstream of the injection/extraction section. The latter dump can be used to stop the beam either at the exit of the transfer line or after any number of bunch revolutions in the ring.

Both dumps are based on the SOLEIL design and can handle the 3.5 W power deposition (1 nC, 70 MeV, 50 Hz repetition rate).

Chapter 5. SYNCHRONIZATION

5.1 Overall scheme

An ultra-low noise 500 MHz synthesizer will be used as the main clock for ThomX. The 10 MHz output of this synthesizer will be used to drive a second synthesizer (the so-called ‘linac synthesizer’) operating at 3 GHz. The RF output of the latter synthesizer will be used for the linac operation. It will be split in two lines. The first one will be used to synchronize the gun laser oscillator (after appropriate down conversion of the frequency). The second line will be used to drive the gun and the linac RF.

The RF output of the main synthesizer (500 MHz) will be used for the ring RF; it will be split in three lines. The first line will drive the ring RF (after appropriate phase shifting). The frequency of the second line will be divided by 14; this line will synchronize the Compton cavity. As in the MightyLaser experiment [5.1] the laser used to inject power in the Compton cavity will be synchronized with that cavity by using the PDH method. The frequency of the third line will be divided by 28 and will therefore be synchronous with the electron revolution frequency. This line will be used to synchronize programmable delays delivering turn-by-turn triggers and injection/extraction triggers. To ensure that injection is always taking place at a zero crossing of the mains, the programmable delays will also be synchronized with the mains. A counter will reduce the mains frequency to the operations frequency (when lower than 50Hz). The gun trigger will be generated when the mains will be at a zero crossing and the ring RF at a preset phase that takes into account the time it will take for the electrons to travel from the linac gun to the ring accelerating cavity.

To ensure that the e^- bunches will always be injected at a triple zero (50 Hz, 500 MHz and 3 GHz) we need to specify the tolerance on the 50 Hz zero crossing. We may take 1 % (*i.e.* 0.2 ms) for this tolerance; this means that the coincidence between the ring RF (~500 MHz) and the linac RF (~3 GHz) must occur at a frequency greater than 5 kHz. Therefore by choosing a heterodyne frequency (*i.e.* the frequency difference between the linac RF divided by 6 and the ring RF) greater than 5 kHz we ensure that there will always be a common zero crossing between the ring RF and the linac RF within 1% of the mains zero crossing. This sets a constraint on the ring radius of 10^{-5} , *i.e.* 168 micrometres on a 16,8 m long orbit (see Table 2).

The RF bucket must be positioned with an accuracy of 3 ps in the ring RF. Thus the phase noise between the linac RF and the ring RF must be lower than 3 ps when integrated between 50 Hz and 500 MHz. Most good-quality synthesizers achieve such a performance.

The information collected by the ring diagnostics will be used to adjust the exact value of the frequency (around 500 MHz) generated by the main synthesizer so that it matches the exact ring length. This information will also be used to adjust the phase between the injection trigger and the ring.

To reach the correct signal level, each RF line may have to be amplified. An isolator will be added to avoid reflections that may degrade the overall performance of the system.

To ensure long-term low frequency synchronization a Network Time Protocol (NTP) server will be available to allow all computers working at ThomX to synchronize their internal clock.

5.2 Specifications

Synthesizer:

The main synthesizer will be used to generate a 500 MHz adjustable signal. Its phase noise jitter integrated between 50 Hz and 20 MHz must be less than a few picoseconds. It must support a frequency modulation of at least 100 kHz. Typical mid-range synthesizers meet such specifications.

Measurements done at LAL in collaboration with SOLEIL have shown that the addition of an external frequency reference does not necessarily improve the phase noise of these synthesizers in the frequency range of interest.

The linac synthesizer specifications are the same ones, except that it must be able to generate a frequency of 3 GHz.

Programmable delay

Two low jitters units with 8 channels each will be used.

Phase shifter

The phase shifters must be voltage controlled and cover 360° (two 180° units).

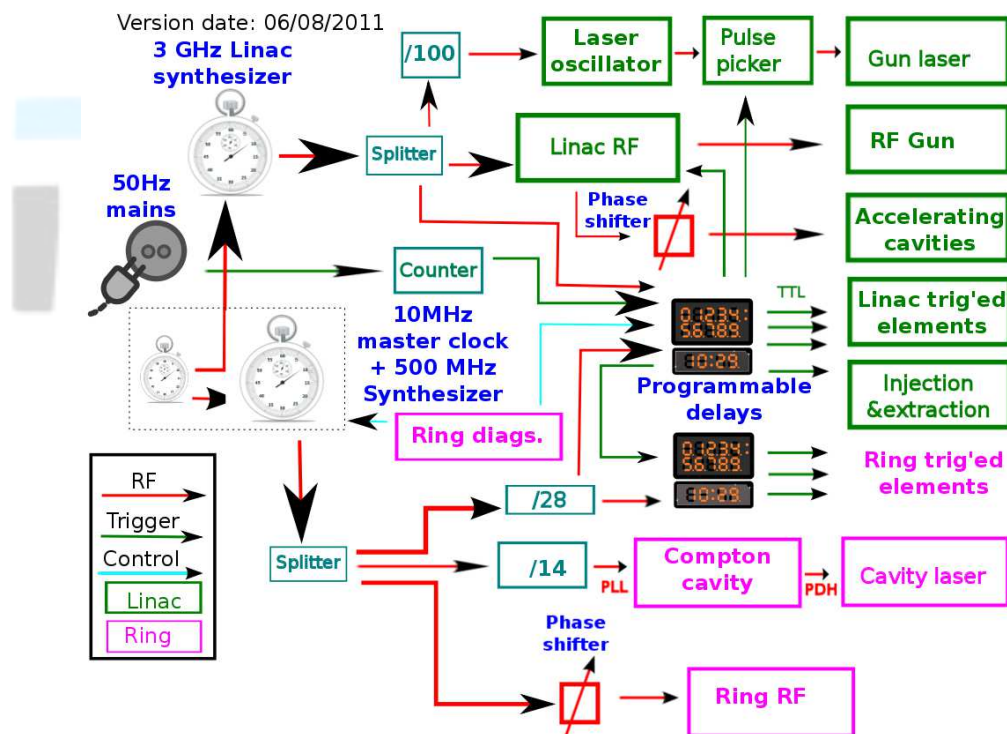


Figure 5.1. Synchronization layout.

Chapter 6. OPTICAL SYSTEM DESIGN

Since the writing of the ThomX CDR, three directions have been pursued: improvement of the feedback system, improvement of the laser amplification and mechanical design of the optical resonator. The results are described in the following three sections.

In the first section, the ThomX feedback system is described. During the past year, a strong R&D program has been developed on the locking of a Ti:Sapph picosecond laser beam on a two-mirror high finesse cavity at Orsay/LAL. Very good results in operating, for the first time, a 30 000 finesse cavity in the picosecond regime were obtained. The feedback techniques used for this task are directly usable for ThomX and are reported in this section. A 3000 finesse four-mirror cavity at KEK was also installed and operated and we succeeded in producing γ rays off the ATF electron bunches (Mightylaser project, [6.1]). Hardware damages were however caused by the Japanese 2011 earthquake. At the time of writing this document, we are recovering all our equipment to reach our final goal: locking a 30000 finesse, four-mirror cavity, to produce a high γ ray flux at ATF. Thanks to a contact with the SYRTE laboratory, we have acquired a new laser oscillator with a 1030 nm wavelength that we are testing and that we plan to use for ThomX. With this oscillator, by embedding an intra-cavity EOM, we are able to increase our feedback bandwidth by more than one order of magnitude.

The second section illustrates the laser amplification developments done at CELIA. First, a non-all-connected fiber amplifier for the Mightylaser project was set up that allows us to extract an average power of 50 W. This amplifier was used to produce γ rays at ATF. A new setup has been designed and built to reach both the reliability and the power level required by ThomX. An important activity is devoted to the construction of a fully all-connected amplification chain. As mentioned above, the new laser oscillator and the new laser amplification chain are being integrated in order to fill a 30000 finesse high finesse cavity to conclude the ANR Mightylaser project.

In the third section, the details of the implementation of the cavity in the electron ring and the cavity vacuum system are described with the opto-mechanical system that will be used for a precise alignment of the cavity mirrors.

6.1 Feedback system and results on a Fabry-Perot cavity locking

To produce a high X-ray flux, the ThomX facility produces high intensity laser pulses and collides them with electrons stored in a ring. Hence, the locking system (see figure below) has a double goal:

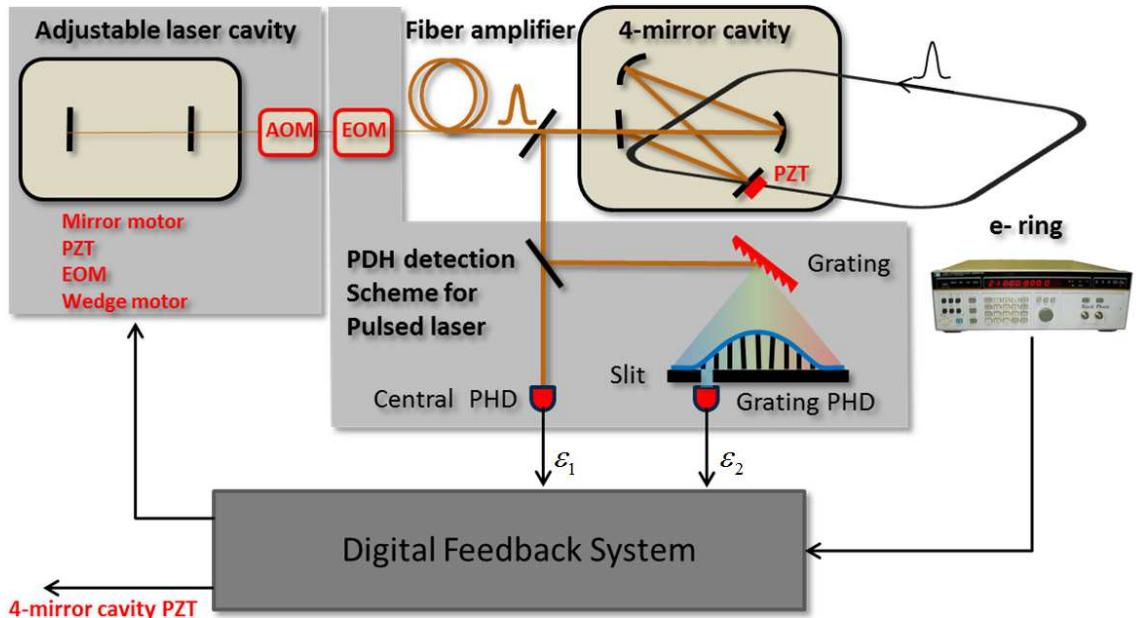
- Stabilize the synchronization of the Fabry-Perot cavity (FPC) photon pulse with the electron bunch,
- Stabilize the synchronization of the laser pulses with the FPC to obtain amplification.

For this last point, as will be seen in section 6.2, firstly the laser beam will be amplified with a CPA technique using optically pumped fibers, and then it will be amplified again by accumulation during many round trips into a high finesse FPC (the target is a gain of 10000 which leads to a finesse of 30000).

This section describes the following topics related to the stabilization of the laser pulses relative to the FPC:

- Parameters to be stabilized: repetition rate and carrier-envelop phase (CEP),
- Error signals: the Pound-Drever-Hall (PDH) measurement technique,

- Actuators: dynamic range and bandwidth,
- Behavior of the digital feedback system (DFS).



General scheme for the locking system. Detection and actuation elements are shown in red.

The results on the locking of a Ti:Sapph laser oscillator on a 30000 finesse cavity will also be illustrated.

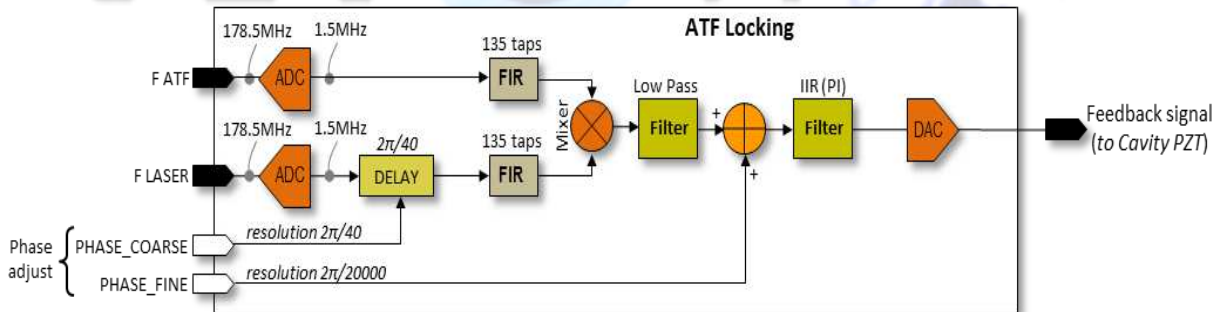


Figure 6.1. Locking scheme for the synchronization of the electron bunch and the FPC pulse for the ATF experiment at KEK.

6.1.1 Electron and FPC pulse synchronization

This kind of stabilization has already been achieved for the MightyLaser experiment at KEK (ATF) @ a 178.5MHz repetition rate. A digital feedback system was used (i) to acquire two clocks, one from the laser and one from the master oscillator of the electron ring, (ii) to perform a digital phase detection, (iii) to build a digital integrator filter to remove phase drifts, and (iv) to react on a PZT inside the FPC to change its length according to the measured phase drift (see Fig. 6.1).

6.1.2 Laser parameters to be stabilized

We will choose a laser with a repetition rate corresponding to twice the e^- bunch revolution frequency in the ring (two laser pulses per electron bunch revolution), around $500\text{MHz}/14 = 35.7\text{ MHz}$. A phase noise measurement on a similar product operating @ 178.5 MHz was already carried out to characterize the repetition rate phase noise and the drift (see Fig. 6.2 and Fig. 6.3).

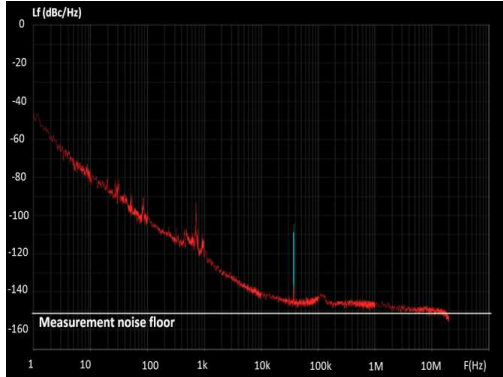


Figure 6.2. Repetition rate phase noise spectrum. X-axis: offset frequency from the carrier in Hz. Y-axis: single side band phase noise power density in dBc/Hz .

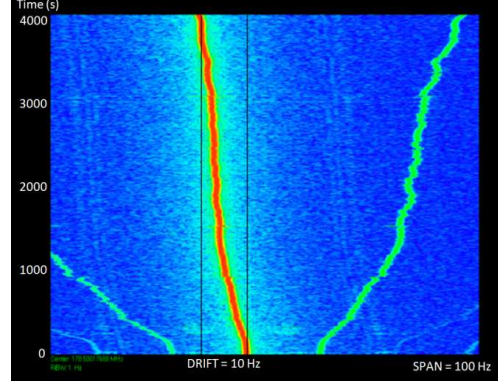


Figure 6.3. Repetition rate drift measured during about one hour. X-axis: repetition rate drift in Hz. Y-axis: time duration in seconds

The global shape of the phase noise in $1/f$ will permit to use three feedback actuators: a high bandwidth /low dynamic one (EOM for repetition rate and AOM or pump current for CEP), a middle bandwidth/middle dynamic one (PZT for repetition rate), and a high dynamic/low bandwidth one (mirror motor and isochronic wedge motor).

$$f_L(m) = m f_{REP} + f_{CE} = \left(m + \frac{\Delta\phi_{CE}}{2\pi} \right) f_{REP}$$

For this kind of laser, the harmonic content (index m) is well known and can be represented either in the time domain or in the spectral domain (see Fig. 6.3 and Fig. 6.4).

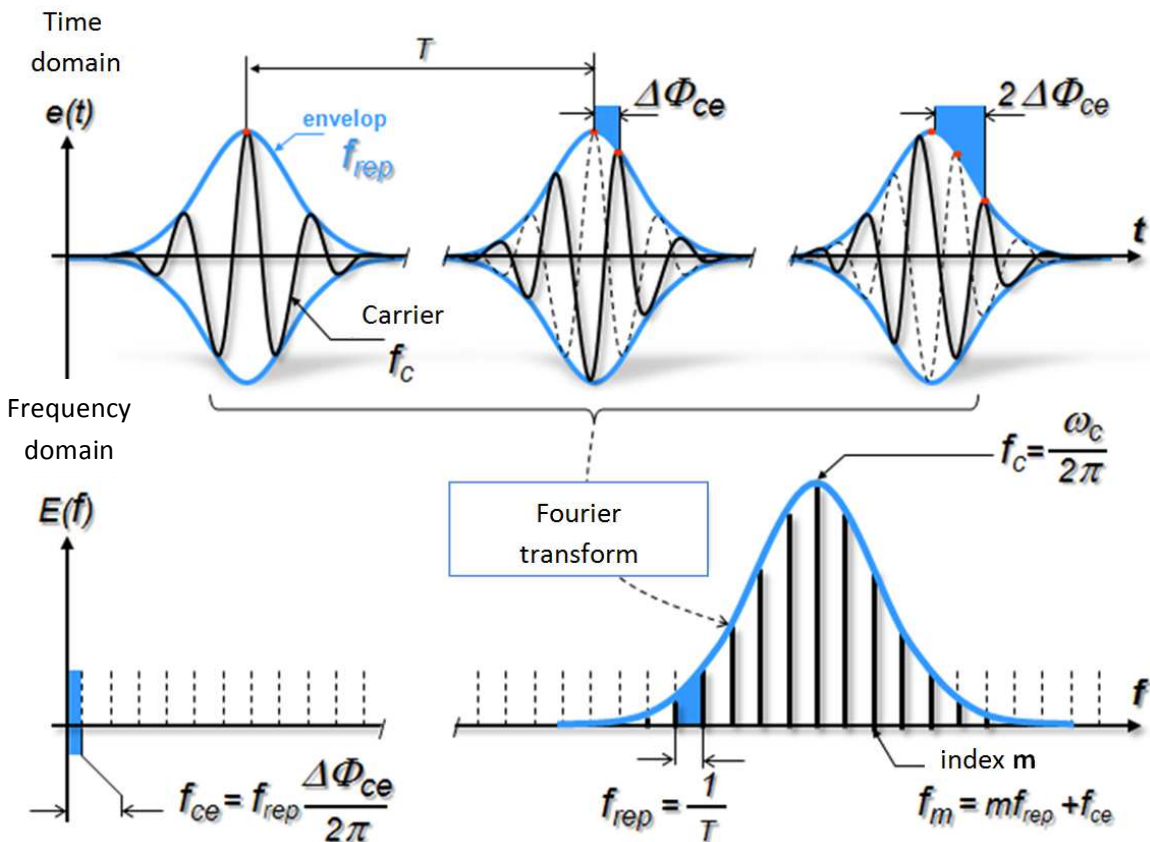


Figure 6.4. Time domain and spectral representation of the laser pulses.

Since one is dealing with two parameters (the repetition rate and the CEP), one needs two different sources of information to measure them. The standard method to measure these two parameters consists in using the Pound-Drever-Hall (PDH) technique [6.2] which gives the position of the laser harmonics relative to the FPC resonances:

$$f_{FPC}(m) = m f_{CAV}$$

One of the parameters is deduced from the whole beam signal using a central photodiode; the second one is derived from a part of the spectrum selected by a grating and a slit and measured by the grating photodiode.

If the repetition rate and the FPC round trip frequency are close enough, the error signal coming from the central photodiode (index m_0) is proportional to the difference between the laser harmonics and the corresponding resonances of the FPC:

$$\varepsilon_1 \propto \left(m_0 + \frac{\Delta\phi_{CE}}{2\pi} \right) f_{REP} - m_0 f_{CAV}$$

As the locking system cancels the error, the central laser harmonic m_0 is perfectly aligned on the FPC resonance but all other laser harmonics ($m=m_0+\Delta m$) are slightly detuned from the corresponding FPC resonances. This introduces a correlation between the CEP and the repetition rate:

$$\varepsilon_1 = 0 \Rightarrow \left(m_0 + \frac{\Delta\phi_{CE}}{2\pi} \right) f_{REP} = m_0 f_{CAV}$$

$$\varepsilon_2 \propto (m - m_0)(f_{REP} - f_{CAV}) = \left(1 - \frac{m}{m_0} \right) f_{REP} \frac{\Delta\phi_{CE}}{2\pi} = \left(1 - \frac{m}{m_0} \right) f_{CE}$$

As a result of these equations, the signal received by the PDH system located after the grating (ε_2) is directly proportional to the offset frequency (f_{CE}) and then to the CEP. Thus, if we change the CEP of the laser, we should clearly see on the grating photodiode PDH signal – which measures the laser-FPC detuning on the border of the spectrum (for an m index far from m_0) – a linear relation between the error signal and the CEP.

This method, well known for femtosecond lasers, has been tested in our laboratory in the picosecond regime. Figure 6.5 shows our results (submitted to Applied Optics) on the locking of a 76MHz Ti:Sapph picosecond laser oscillator on a 30000 finesse cavity.

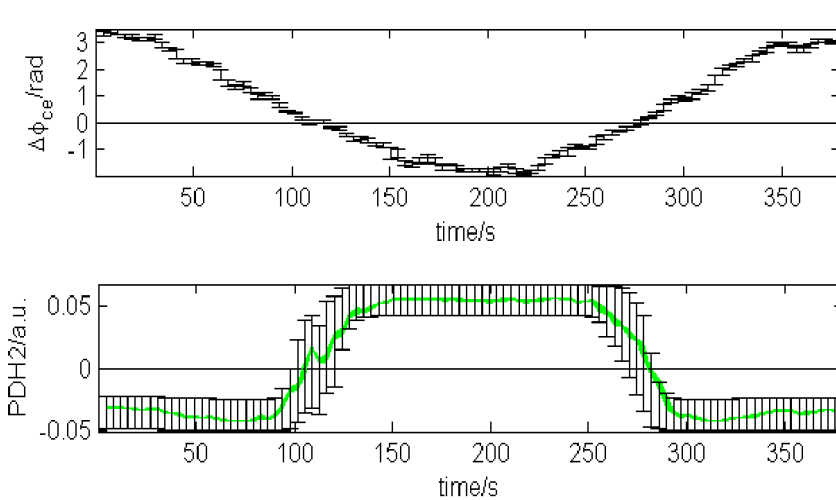


Figure 6.5. Top: experimental measurement of the CEP value of a Ti:Sapph laser oscillator. Bottom: measurement of the corresponding grating photodiode signal.

In Fig. 6.5, one sees that when the CEP is measured close enough to zero, the grating photodiode exhibits a linear relation with the CEP, otherwise the photodiode is saturated (due to the PDH signal saturation). In our experiment, the ratio between the cavity reflected power and the incident beam power was ~20% which leads to a value of 80% for the coupling of the incident beam power to the cavity.

These results demonstrate, for the first time, that a picosecond laser oscillator can be locked to a 30000 finesse cavity (implying a power enhancement factor of 10000) with a power coupling of 80%.

6.1.3 PDH Measurement technique

Having shown that we are able to measure independently both parameters of interest (the repetition rate and the CEP), we will now describe the apparatus to transform these measurements into error signals by

the PDH technique (see Fig. 6.6). Side-bands to the laser optical harmonics are produced by an electro-optic modulator (EOM) modulated by a generator coming from the digital system. Side-bands and laser harmonics are reflected by the FPC, the first ones without acquiring any phase, the second ones shifted in relation with the discrepancy between the laser and the FPC frequencies. All the harmonics and the side-bands of the reflected laser are combined into the photodiodes and the front-end electronics, giving an error signal at the modulation frequency.

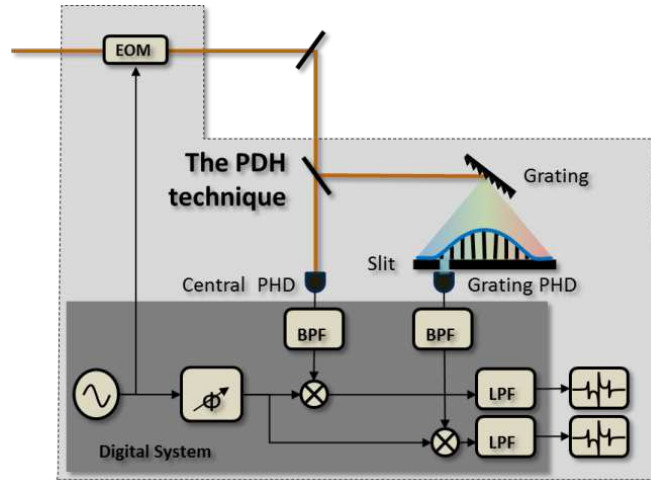


Figure 6.6. Pound-Drever-Hall scheme with digital phase detection.

The photodiode front-end (see Fig. 6.7) amplifies these signals at a level compatible with the digital feedback system (DFS).

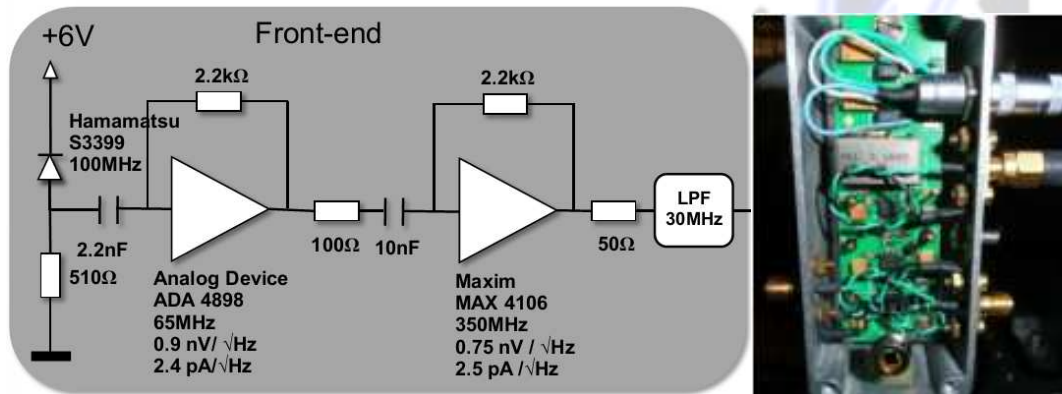


Figure 6.7. Electronic scheme and picture of the PDH front-end.

Inside the DFS, the PDH signals are filtered by a band-pass filter to remove unwanted frequencies, and multiplied by the same modulating signal with a phase shift to allow for the phase detection. A low-pass filter at the end of the chain removes the image signal at twice the modulation frequency. Figure 6.8 shows an example of the input and the output signals.

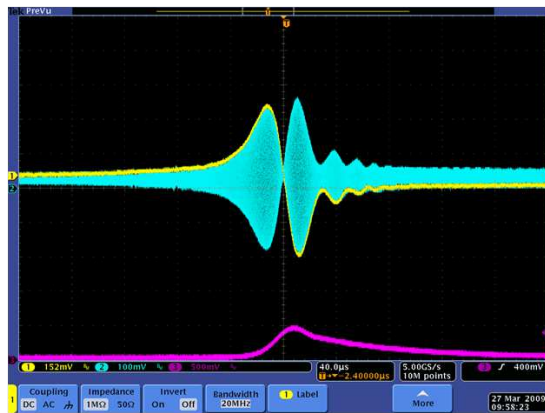


Figure 6.8. Modulated input (blue), error signal (yellow), FPC transmitted signal (pink).

6.1.4 Actuators

In the previous sections we described how the two parameters (the repetition rate and the CEP) of a pulsed laser have to be controlled in order that all the laser harmonics match the FPC resonances, and we also detailed how to measure the variations of these two parameters. We will now describe the devices inside or around the laser on which we need to react to correct the variations of the laser harmonics relative to the FPC resonant frequencies.

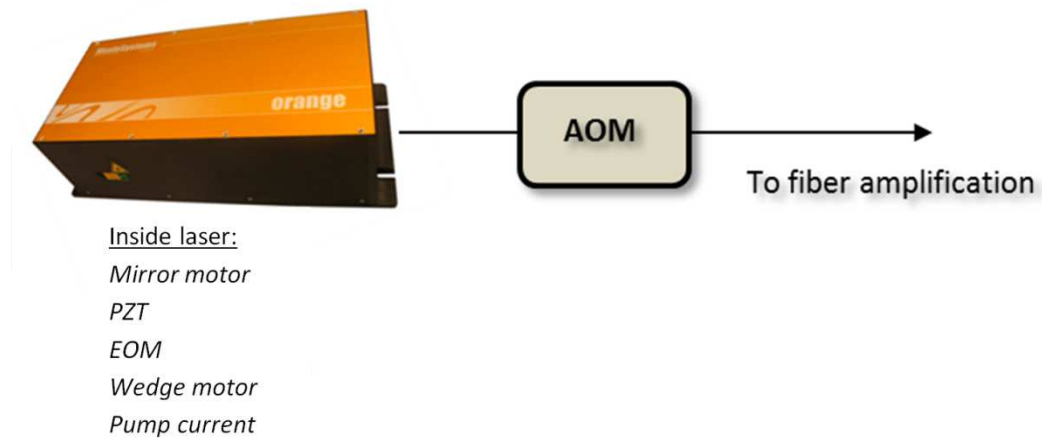


Figure 6.9. Typical scheme of a laser with all its actuators.

The actuators will produce an action on the two parameters to be controlled with different dynamic ranges and different bandwidths (see chart in Fig. 6.10).

	Freq			CEP		
	Mirror Motor	PZT	EOM	Wedge Motor	Pump current	AOM
Dynamic range	Large (mm)	Medium (μm)	Low (nm)	Large (several $\times 2\pi$)	Medium ($\sim 2\pi$)	Low ($2\pi/1000$)
Bandwidth	1 Hz	10 kHz	1-10 MHz	1 Hz	10 kHz	100 kHz

Figure 6.10. Dynamic ranges and bandwidths of the laser actuators.

All of the actuators are located inside the laser, except the AOM (see Fig. 6.10). They are the key items to achieve a good stabilization

All the actuators measurements have been made on the 178.5MHz laser version used at KEK.

- Mirror motor dynamic range, precision and bandwidth

The motor is a step motor with a precision of 140 nm on the round trip variation (equivalent to 15 Hz on Frep). Figure 6.11 shows the linearity and the maximum dynamic range available with the motor stage while Fig. 6.12 shows a step response which indicates the maximum bandwidth we can obtain.

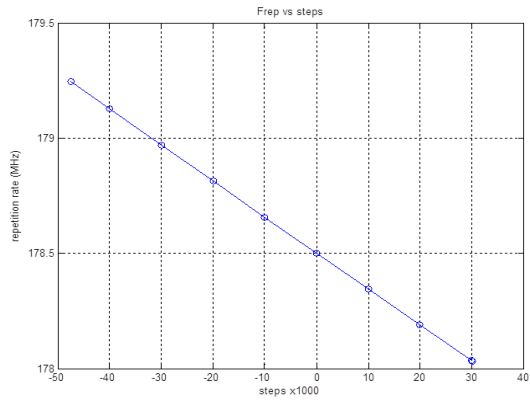


Figure 6.11 Mirror motor range.

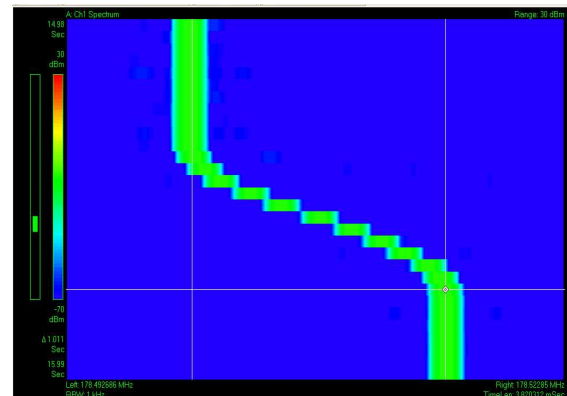


Figure 6.12 Time response of Frep for 1k motor steps. X-axis: repetition rate offset (Hz). Y-axis: repetition rate

The repetition rate range is 178.033 - 179.244 MHz (> 1MHz).

- Piezoelectric sensitivity, dynamic range and bandwidth

The PZT sensitivity is approximately $3\text{Hz} / \text{V} \Leftrightarrow 28 \text{ nm/V}$ (length variation to be compared to the length of a round trip of the FPC pulse).

The PZT can be operated up to 150V, providing a total dynamic range of $4.2 \mu\text{m}$ (round trip length change). Its first peak resonance has been measured and found above 40 kHz.

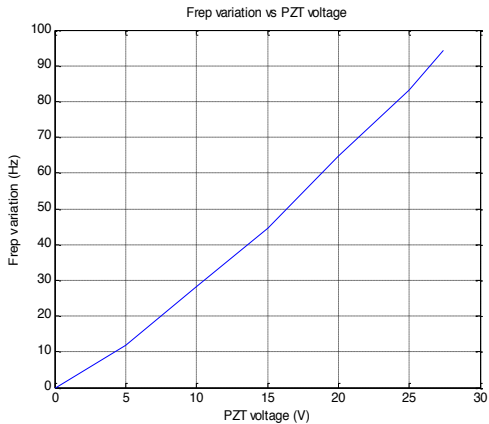


Figure 6.13. Repetition rate change produced by a PZT voltage variation from 0 to 28 V.

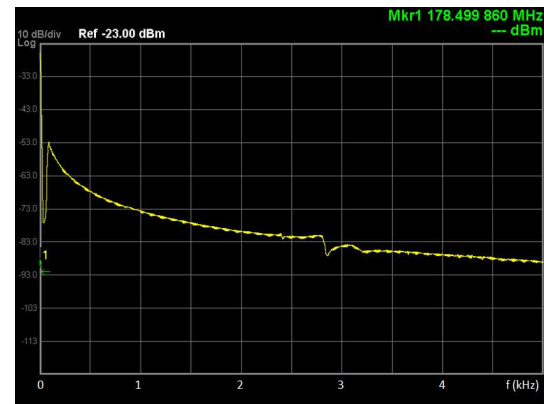


Figure 6.14. PZT frequency response. X-frequency range: 0.1-5 kHz. Y-axis: Attenuation (dB) – arbitrary offset.

Figures 6.13 and 6.14 show the PZT sensitivity and its transfer function.

- EOM sensitivity measurement

Measuring the sensitivity of the EOM is not direct, thus we chose to apply a 10 V amplitude – 10 Hz frequency modulation – to the EOM and to measure the power of the harmonics (see Fig. 6.16). Assuming a pure frequency modulation, the power of the harmonics is a Bessel series that depends on the sensitivity. Thus taking the ratio of two consecutive harmonics gives directly the sensitivity.

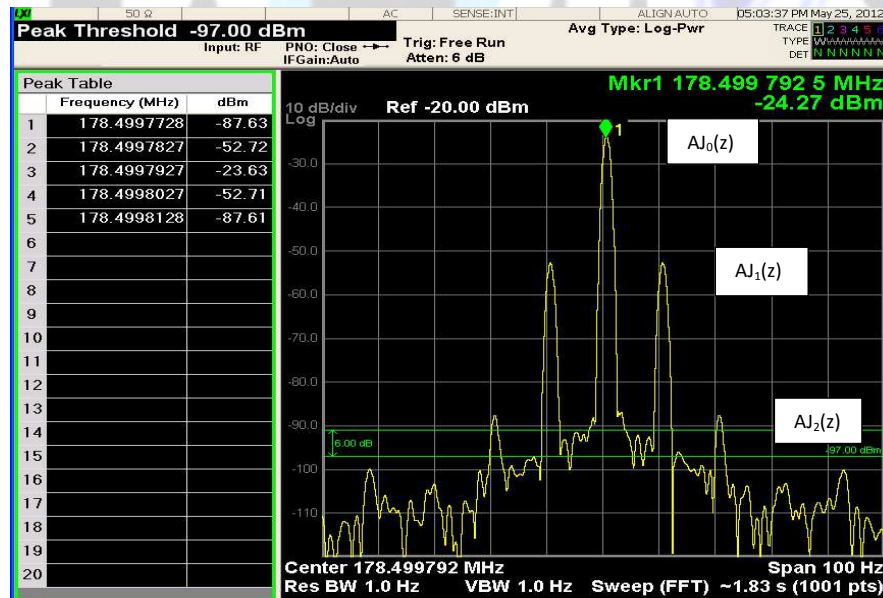


Figure 6.15. EOM modulation spectrum used for sensitivity measurement. X-axis: frequency, centered on the repetition rate. Y-axis: relative optical power around the repetition rate due to the modulation. The table on the left gives the frequency and the power of each harmonic.

We now check that the sensitivity calculated from the ratio of the first harmonic to the fundamental and the one obtained from the ratio of the second harmonic to the fundamental are the same:

$$\frac{A J_1 \left(\frac{f_\Delta}{10} \right)}{A J_0 \left(\frac{f_\Delta}{10} \right)} \sim \frac{1}{2} \frac{f_\Delta}{10} \sim -29.09 \text{ dB} \rightarrow f_\Delta \sim 0.7 \text{ Hz}$$

$$\frac{A J_2 \left(\frac{f_\Delta}{10} \right)}{A J_0 \left(\frac{f_\Delta}{10} \right)} \sim \frac{1}{8} \frac{f_\Delta}{10} \sim -63.98 \text{ dB} \rightarrow f_\Delta \sim 0.7 \text{ Hz}$$

Since the ratio is 0.7 Hz for an applied sinusoidal signal of 10 V, the sensitivity is around 0.07 Hz/V.

- Isochronic wedge

It is made of two glass prisms with different refraction indexes, chosen to maintain a constant group delay in order to avoid repetition rate variation.

We measured that the maximum variation of the repetition rate for a full CEP range (several times 2π) is about 300 Hz for a repetition rate of 178.5 MHz (see Fig. 6.16 which shows the measured repetition rate shift plotted along the X-axis versus the date of the measurement plotted along the Y-axis). Thus the influence of this actuator on the repetition rate is about 2.10^{-6} .

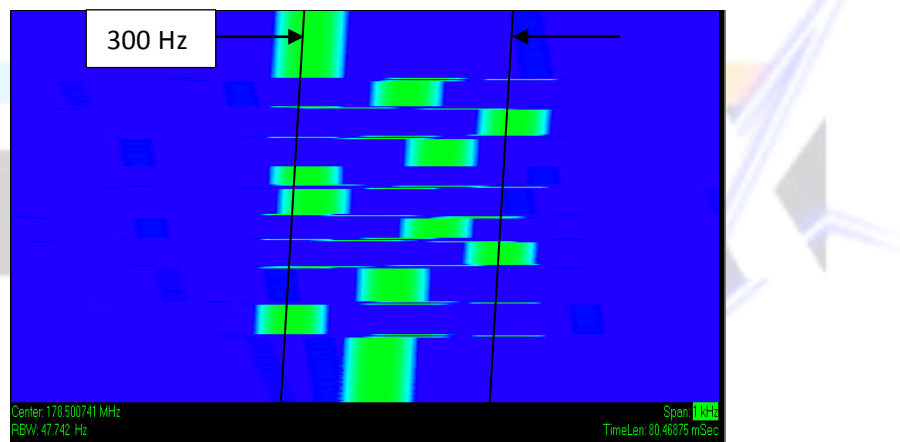


Figure 6.16. Measurement of the influence of wedge displacement on Frep.

- Acousto-Optic Modulator (AOM)

Such an actuator has already been used with a laser which is not the same as the one used for the other actuators, namely a 76 MHz laser locked on a two-mirror FPC.

In Fig. 6.17, we present the closed loop measurement: The lowest frequency part (<10 kHz) is attenuated by the loop gain. If the loop were open, this part of the transfer function would be quite flat. To estimate the AOM bandwidth limits we can use the frequencies where the gain starts to drop significantly: this bandwidth is about 300 kHz.

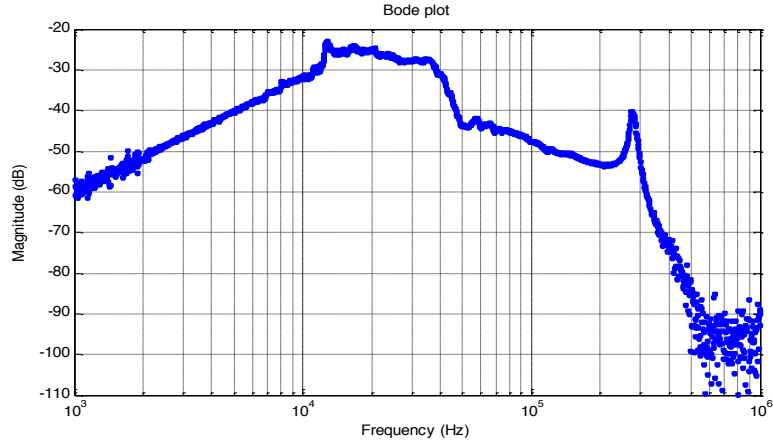


Figure 6.7. Frequency response of the AOM in closed loop.

6.1.5 The digital feedback system

The feedback system will deal with several coupled inputs and outputs. To ensure flexibility, we have chosen a digital system. Since we also want to work with a large bandwidth in closed loop ($> 1\text{MHz}$), a low latency system ($< 100\text{ ns}$) is needed. A digital system featuring such performance does not exist on the shelf. Thus we decided to design and build such a system at LAL (see Fig. 6.18).

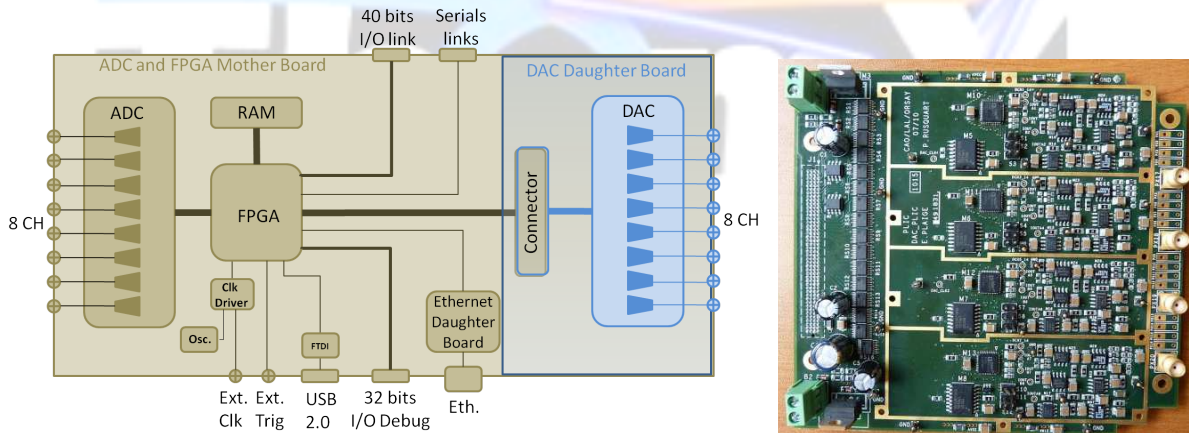


Figure 6.18. Scheme of the DFS and picture of the DAC daughterboard.

This system will perform several functions (see Fig. 6.19):

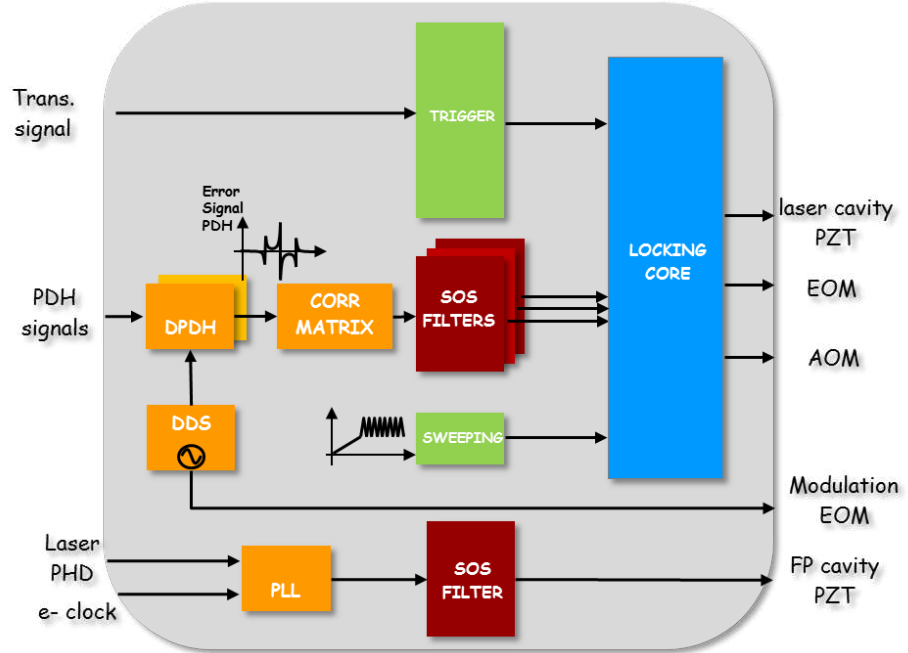


Figure 6.19. Organization of the digital feedback functions.

- The first important function is to produce the error signal from the modulated signal coming from the photodiodes. It is a phase detection block (Digital PDH: DPDH), the main problem being to reduce the latency as much as possible. This will be achieved by optimizing the low-pass filter and the modulation frequency (see Fig. 6.20 for a digital implementation).

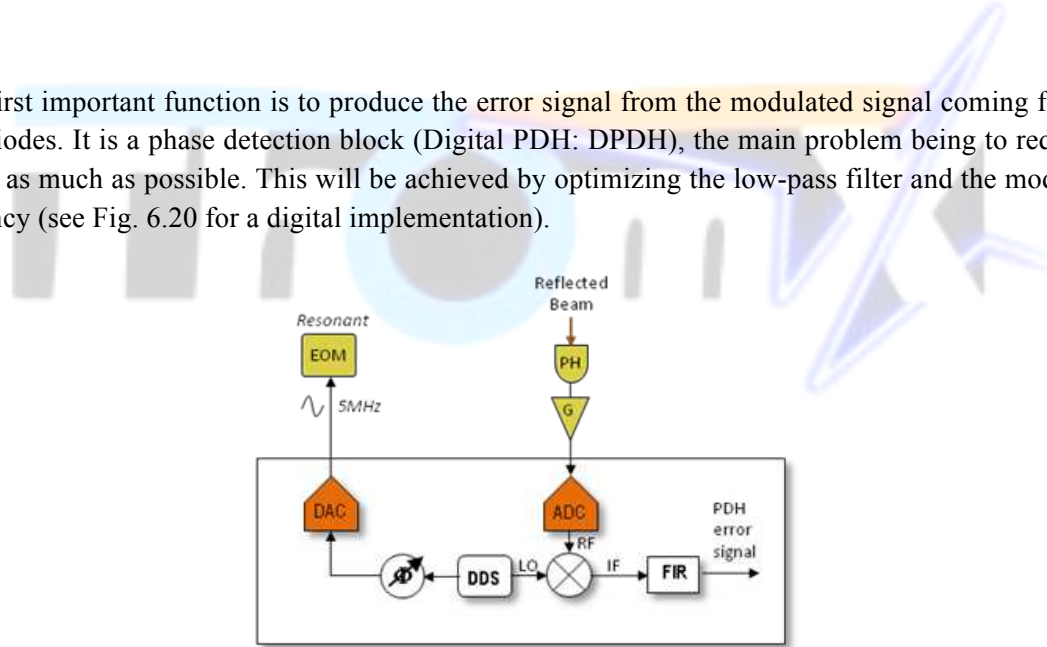


Figure 6.20. Digital phase detection (DPDH) to produce the PDH error signals.

- The second important function is to provide Infinite Impulse Response (IIR) filters to build Proportional-Integrator (PI) filters in order to cancel the system drifts.

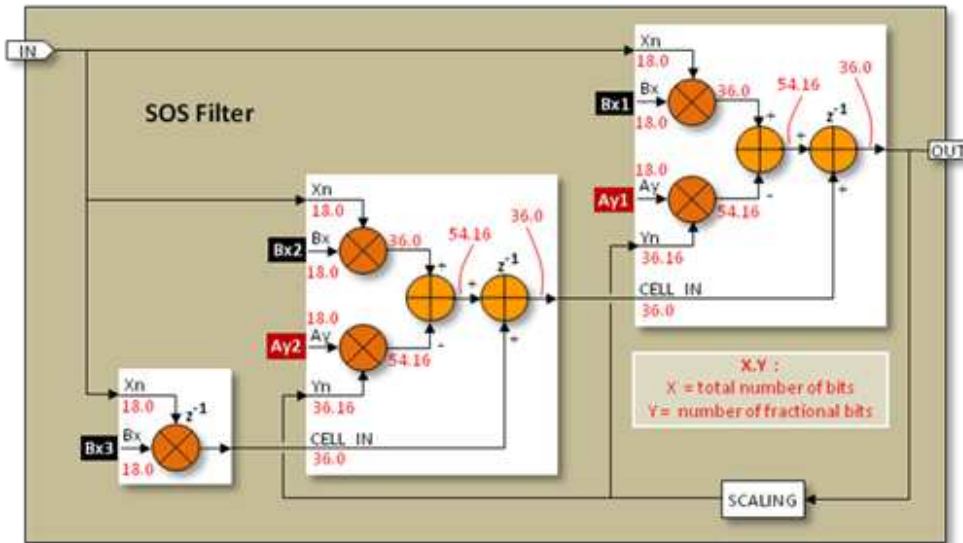


Figure 6.21. Digital IIR filter implementation with adders and multipliers.

These filters can be programmed by the user to change the filter coefficients and it can be cascaded to realize complex filters. They have been cut in Second Order Sections (SOS) to minimize the propagation of fixed precision errors due to quantized data and coefficients (see Fig. 6.21).

- The last important function integrated in the digital system is performed by an identification block which works like a network analyzer by (i) sending a small harmonic signal, (ii) looking at the system response in closed loop at this frequency, and (iii) sweeping this small harmonic signal frequency to cover all the range to be measured (see Fig. 6.22).

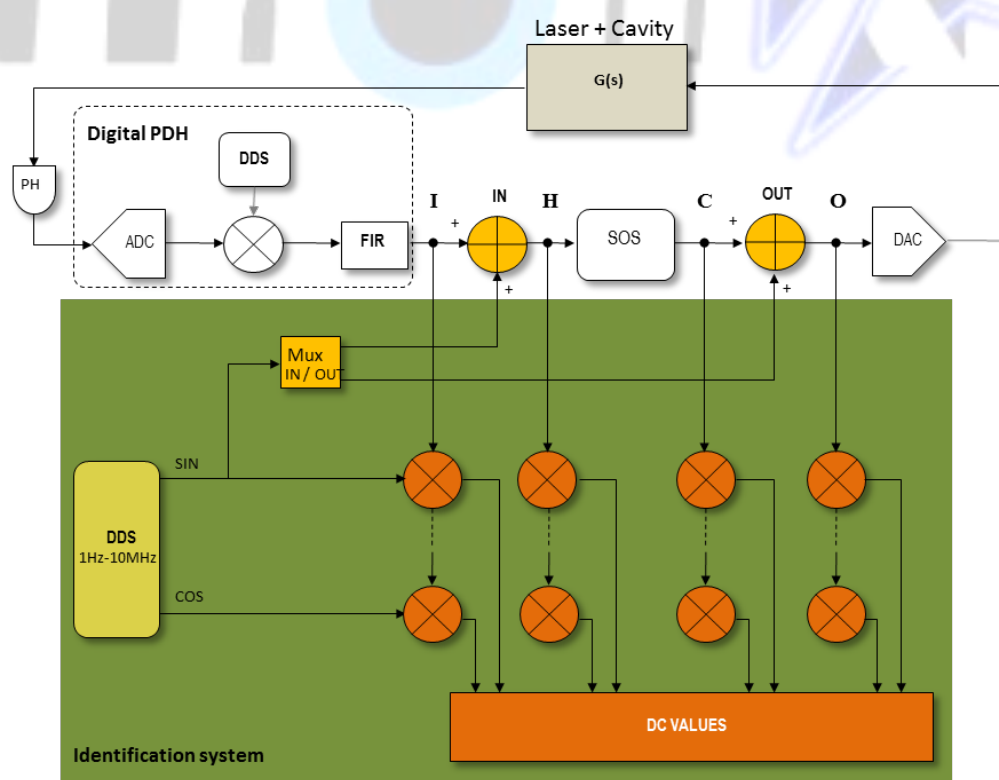


Figure 6.22. Identification system.

This kind of identification system can provide information on (i) the feedback system itself, (ii) the system to be stabilized, or (iii) the open and closed loop transfer functions by producing Bode or Black/Nichols diagrams (see Fig. 6.23). These informations are very useful for system analysis and for tuning or designing the feedback filters.

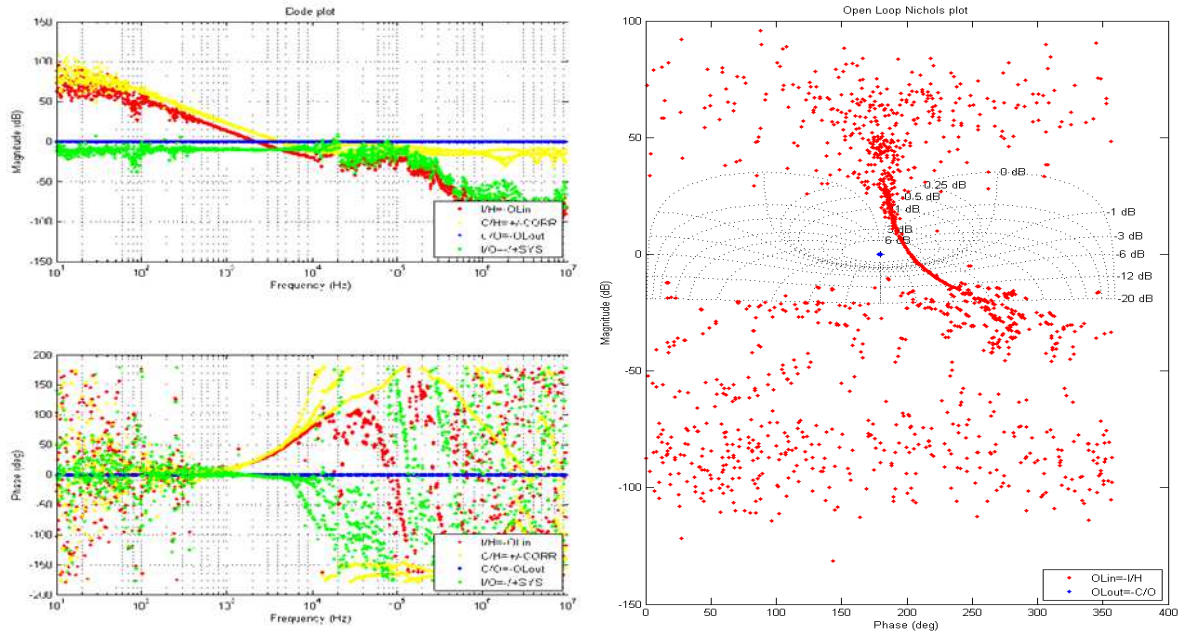


Figure 6.23. Typical Bode (top-left: magnitude, bottom-left: phase) and Black-Nichols (right) diagrams produced by the identification system.

6.2 High average power laser system and its coupling to a high gain FP cavity

The all-fibered laser system will draw from the system developed in the MightyLaser project. It will consist in an oscillator associated with three amplifying stages involving single and double clad Yb-doped fibers (see Fig. 6.25). At present, the amplifiers are based on commercial components to facilitate a potential replacement of damaged parts. The architecture is designed to provide the mandatory diffraction-limited beam. This relatively simple and compact architecture will implement the ‘Chirp Pulse Amplification’ (CPA) scheme. In order to limit non-linearity effects in the fiber, the signal is initially stretched in time, thus reducing its intensity in the waveguide, then amplified in the fiber and finally recompressed to its minimal duration. The difference between the MightyLaser and the ThomX repetition frequencies (respectively 178.5 MHz and \sim 35.7 MHz imposed by the different repetition rates of the two accelerators) requires an adjustment of the laser design.

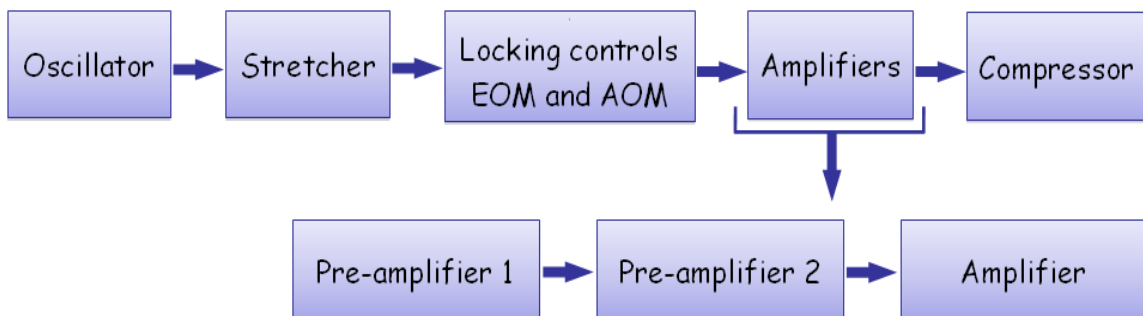


Figure 6.25. Sketch of the all-fiber laser system.

6.2.1 The MightyLaser oscillator

This oscillator is an all-normal dispersion, mode-locked fiber laser based on the nonlinear polarization evolution technique, equipped with a fibered output. It uses an ytterbium doped fiber which allows an emission centered around 1030 nm with a full width at half maximum of 10 nm (see Fig. 6.26). It delivers short pulses at a repetition rate of 178.5 MHz with a low average output power (~10 mW) in order to minimize the noise level (see Fig. 6.28). The main advantage of the all-normal dispersion regime resides in the significant peak power reduction provided by the pulse stretching during the propagation along the cavity. Non-linear effects are thus reduced, allowing a high-energy extraction. The output pulses are naturally chirped with an estimated duration of 2 ps.

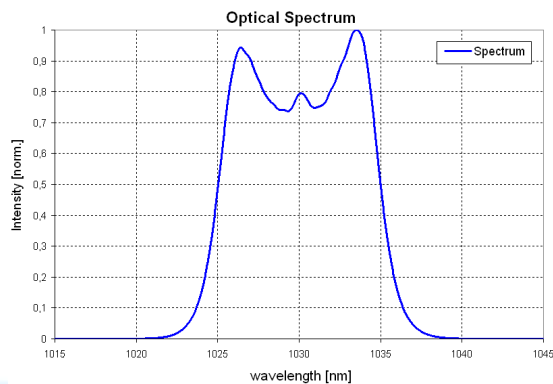


Figure 6.26. Emission spectrum of the oscillator.

The oscillator is passively mode-locked by taking advantage of the non-linear evolution of the polarization. This technique is based on the optical Kerr effect. The polarization of a pulse propagating in a fiber evolves non-linearly as a function of intensity. Thus, by combining polarization controllers and a polarizer, one may generate losses that depend on the intensity (see Fig. 6.27). Beyond the polarizer, all the pulse components are linearly polarized. The wave plates transform the linear polarization into an elliptic one. The latter polarization state then evolves in a non-linear way while it propagates along the fiber. This evolution results from the combined effect of the self-phase and the cross-phase modulations induced on the two polarization components. The polarization rotation of the more intense central part of the pulse is larger than the polarization rotation of the pulse wings. Since the pulse center crosses the analyzer with a reduced loss compared to the wings' loss, the pulse duration is shortened.

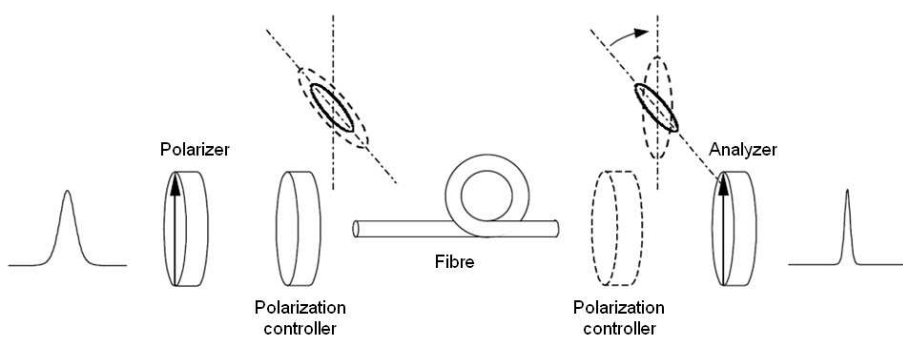


Figure 6.27. Principle of mode locking based on the non-linear polarization evolution.

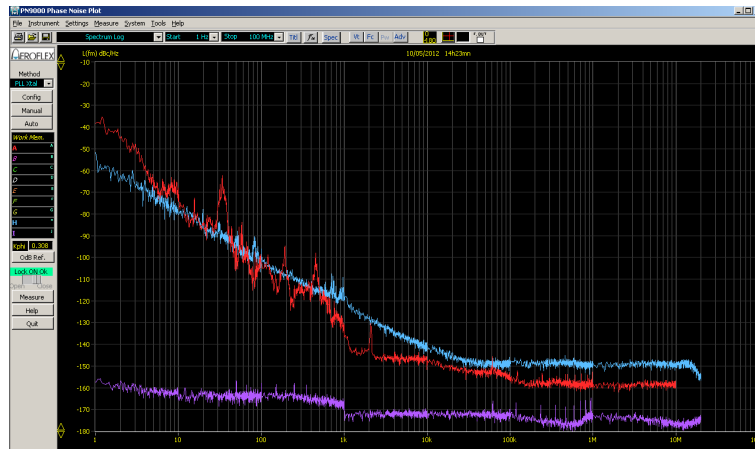


Figure 6.28. Spectrum of the oscillator phase noise: noise level (dBc/Hz) versus offset frequency (Hz).

6.2.2 Amplification stages

The amplification chain is divided in three stages in order to distribute the gain and to saturate the second and the third amplifying stages. The first and the second stages are based on the same architecture. It is an all-fibered amplifier whose central component is a polarization maintaining single mode using an Ytterbium doped fiber with a core diameter of 6 μm and a clad diameter of 125 μm (see Fig. 6.29). A wavelength division multiplexer (WDM) is spliced on the doped fiber to transfer the pump power into the gain medium and to couple the signal of the picosecond oscillator to the amplifier. The first stage is pumped by a single mode diode centered at 976 nm and delivering 200 mW. The second one is pumped at a higher average power, namely 600 mW. The two amplifying stages are separated by an optical isolator to avoid any parasitic feedback from one amplifier to the other.

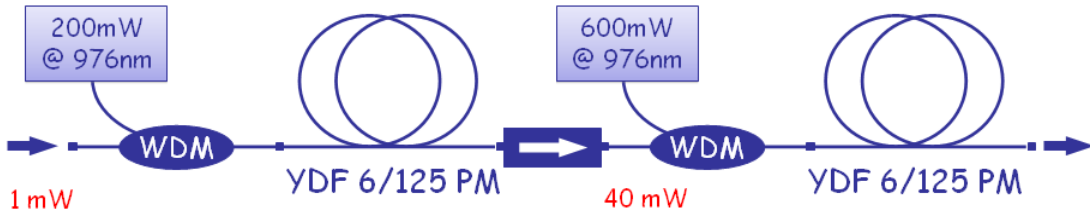


Figure 6.29. Schematic of the first and the second amplification stages.

The average power level at the input of the first amplifying stage is about 1 mW. A limitation is imposed on the output of this stage which should remain below the damage threshold of the isolator fixed at 100 mW. Consequently, we adjust the pump level in order to obtain 80 mW at the output of the ytterbium-doped fiber. The 3 dB losses of the isolator allow one to inject 40 mW into the second amplifying stage. The evolution of the average output power versus the pump level is shown in Fig. 6.30. For the maximum pump level of 600 mW, the second amplifying stage delivers 330 mW.

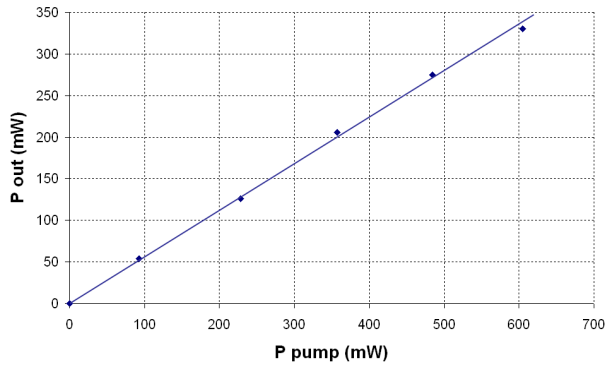


Figure 6.30. Second stage output power plotted versus the pump power.

Beyond the second isolator, the third amplifying stage (see Fig. 6.32) is built by using, as its central component, a polarization maintaining, double-clad, Ytterbium-doped fiber, with a core diameter of 25 μm and a clad diameter of 250 μm . The amplifier is clad-pumped through a special combiner 6+1:1 (see Fig. 6.31). In practice, this component has an input signal fiber 6/125 μm directly spliced to the previous amplification stages, an output signal fiber 25/250 μm spliced to the double-clad Ytterbium doped fiber, and six multimode fibers of 105 μm to couple the pump diodes. Here, only three pump ports are spliced to multimode diodes emitting up to 55 W at 976 nm corresponding to a pump power of at most 165 W. The development of a mode field adapter was necessary to splice the pump combiner to the double-clad Ytterbium-doped fiber because their numerical apertures are different. Losses entailed by this component are compensated by the last amplification stage.

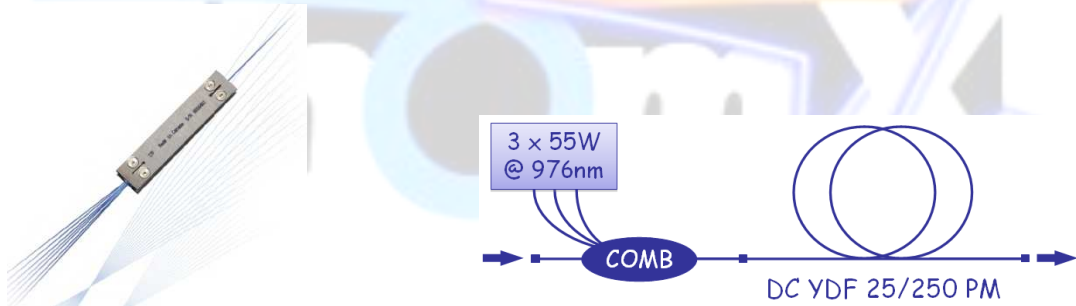


Figure 6.31. Pump combiner.

Figure 6.32. Schematic of the third amplification stage.

Figure 6.33 is a plot of the average output power versus the pump level. For a pump power level of 76W, the last amplification stage delivers 52W. This was the first objective. The fiber laser power stability was measured during 1 1/2 hour at this power level (see Fig. 6.34). The residual pump power, the pump and signal feedbacks into the pump diodes are also plotted in this figure.

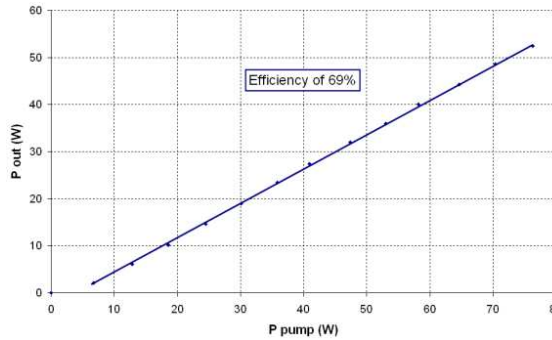


Figure 6.33. Third stage output power versus the pump power.

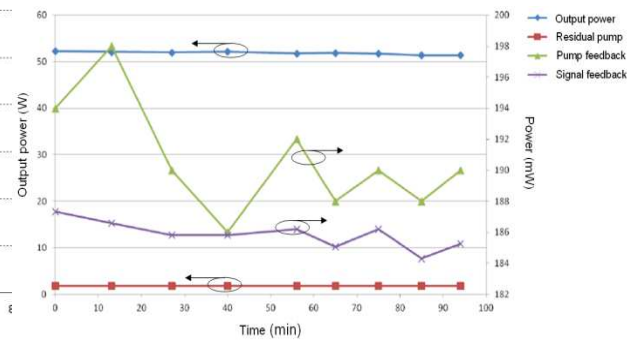


Figure 6.34. Laser stability at 52 W.

New measurements were made after optimizing the central wavelength of the multi-mode pump diodes. The efficiency was increased to reach 78.7% for an output power of 24 W (see Fig. 6.35). The fiber laser power has been tested at this level during two hours (see Fig. 6.36). The observed power variation is less than 0.1%.

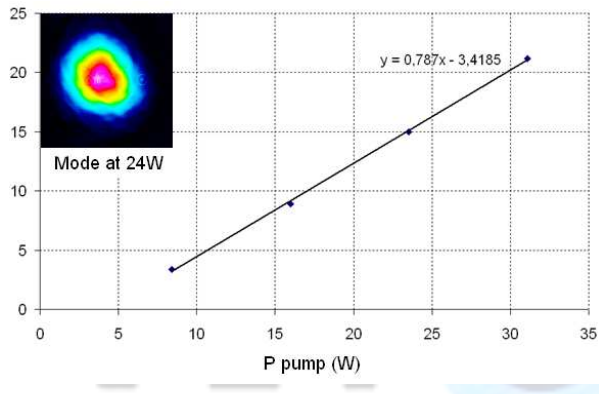


Figure 6.35. Output power versus pump power after wavelength optimization.

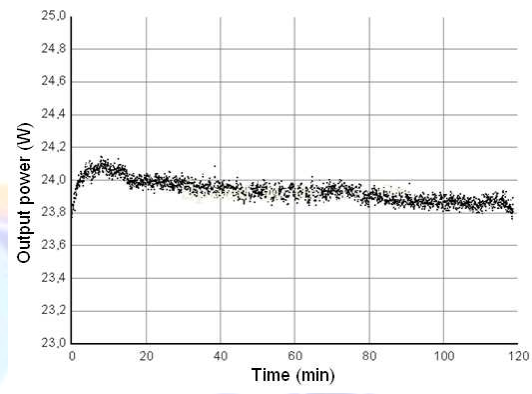


Figure 6.36. Laser stability at 24 W.

The all-fibered amplifier setup has been integrated in a 19'' rack as shown in Fig. 6.37. An FCPC connector placed in the front panel allows the connection of the fibered oscillator to the master amplifier module. Several 95:5 optical fiber couplers have been inserted in our setup at strategic locations to monitor the power level in real time by using photodiodes; they may also signal potential problems. The output fiber comes out of the module through its front panel. The back-side is dedicated to all the electronic controls (diode pump, photodiodes and modulators for noise management described elsewhere).



Figure 6.37. Pictures of the 52 W all-fibered setup integrated in a 19'' rack.

6.2.3 Stretcher and compressor

A chirp volume Bragg grating (CVBG) is used in our setup to stretch and compress the pulse with a very good efficiency of 94%. The CVBG transmission bandwidth is around 2 nm (see Fig. 6.38) leading to a pulse duration ranging from 200 to 250 ps, depending on the grating dispersion. It is possible to recompress the pulse after amplification by using a second CVBG. Then, the pulse length ranges between 20 and 87 ps depending on the second CVBG dispersion (see Fig. 6.39).

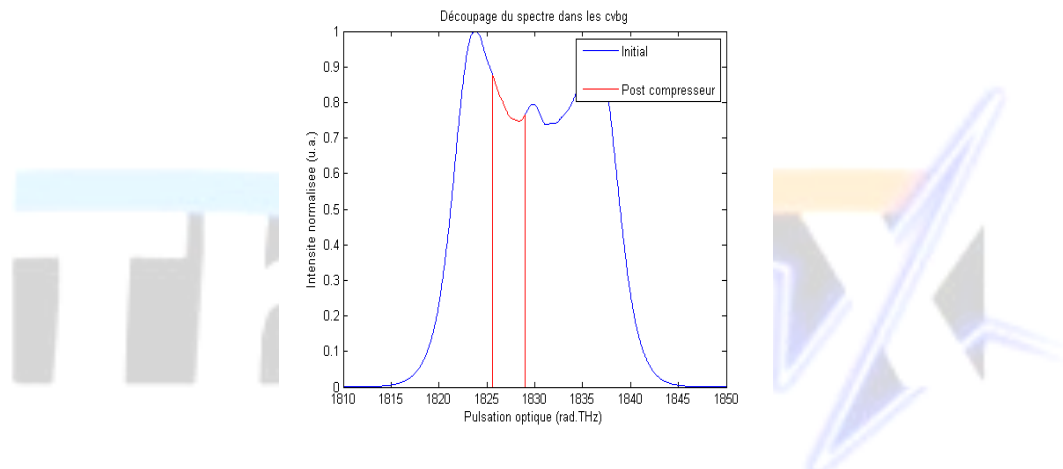


Figure 6.38. Transmission bandwidth of the CVBG.

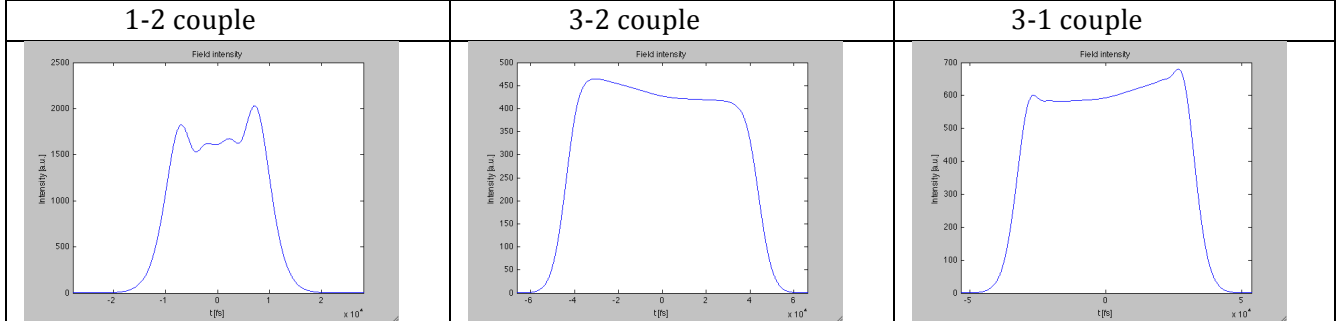


Figure 6.39. Time profile of the recompressed pulses for different grating pairs.

6.2.4 ThomX development

Some changes must be made to the all-fibered ‘Mightylaser’ design in order to use it in the ThomX project. The oscillator repetition rate needs to be scaled down to match the frequency imposed by the accelerator. As far as the laser design is concerned, the stretcher/compressor couple must be modified to limit non-linear effects. The increase of the output power from 50 to 150 W imposes an upgrade of the second amplification stage and eventually of the third one.

6.2.4.1 Oscillator

The oscillator for ThomX will be based on the same principle as the one used for MightyLaser. The only difference is the repetition frequency imposed by the accelerator (35,7 MHz for ThomX). The low average output power, around 5 mW, permits to limit the phase noise. A particular attention will be paid to the noise level of such a long cavity as no commercial products have been tested at this repetition rate.

6.2.4.2 Amplification stages

For the ThomX project, the lower repetition rate and the higher average output power require a change of the second amplification stage architecture in order to limit non-linear effects and to saturate the last amplification stage. Consequently, the second pre-amplifier will be based on a polarization-maintaining double-clad Ytterbium doped fiber with a core diameter of 15 μm and a clad diameter of 130 μm (see Fig. 6.40). The amplifier will be clad-pumped through a special combiner 2+1:1 with an input signal fiber 6/125 μm , directly spliced to the previous amplification stages, an output signal fiber of 15/130 μm , spliced to the double-clad Ytterbium doped fiber, and two multimode fibers of 105 μm to couple the 9 W pump diodes.

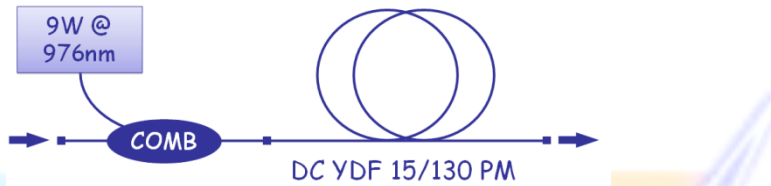


Figure 6.40. Schematic of the second amplification stage of the ThomX laser.

Concerning the final amplification stage, various fibers are available (see below). Micro-structured fibers can be engineered and tailored but suffer from the lack of splicing techniques. Hence their use in an all-fibered setup will require additional developments dedicated to splicing (see Fig. 6.41) and integration. If splicing is not possible, we still have the possibility of proceeding with air propagation and injection. However this approach requires precise mechanics, control and advanced engineering. The ‘coherent beam combining technique’ will also be considered at this point. In such a configuration, amplification would be supported by two parallel amplification stages, dividing by two the energy level in the gain medium. Yet a first version will be developed with commercially spliceable flexible fibers and preliminary tests of cavity locking with high power from these fibers will be performed to validate or invalidate operating with a high level of non-linear effects.

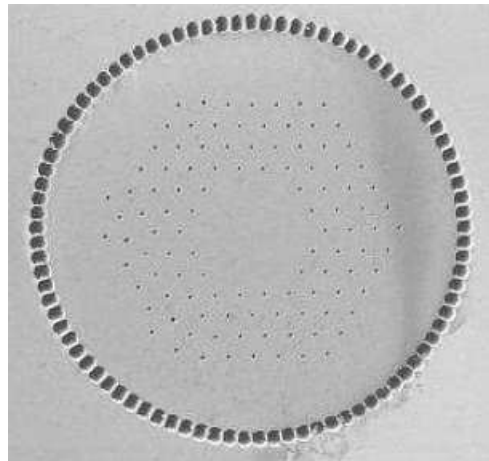


Fig.6.41. A micro-structured fiber.

6.2.4.3 Stretcher and compressor

Because of the high average output power required by ThomX, we must modify the stretcher size. Two techniques can be considered. First, we may continue to use a CVBG which can stretch the pulse up to 450 ps with a maximum size of 2.5 cm (see Fig. 6.42). It would be possible to stretch the pulse up to 900 ps with an efficiency of 88% through a double pass in a CVBG or a single pass in cascaded CVBG. The second way involves a chirp fiber brag grating (CFBG) as depicted in Fig. 6.43. When associated with an optical circulator, it allows a pulse stretching with up to 800 ps in an all-fibered setup. The efficiency is around 70% (92% for the CFBG and 75% for the circulator) in this configuration. This solution is less efficient than the CVBG, but the all-fibered configuration ensures the set-up robustness and stability, and the losses can be easily recovered by the amplifier chain. However, dispersion issues have been reported for these devices and a detailed investigation is needed prior to a definitive integration.

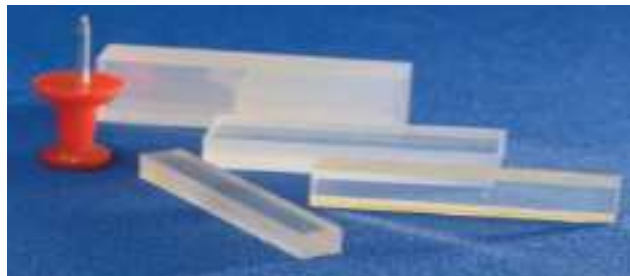


Fig. 6.42. Examples of CVBG.



Fig.6.43. Example of CFBG.

The high output average power forces us to use a CVBG to compress the pulse, one or two units depending on the stretcher configuration. The final pulse duration can be varied between 1 ps and 50 ps, thus leaving the possibility to optimize the X-ray production by adjusting the pulse duration.

We also performed simulations to evaluate the influence of the couple stretching/fiber core diameter on the non-linearity with 3 different fiber cores: 25 μm , 30 μm and 40 μm . Our results are summarized in Table 6.1.

Fiber dimensions	mode field diameter	stretching	B-Integral
25/250	20 µm	250 ps	4,7 rad
25/250	20 µm	500 ps	2,63 rad
25/250	20 µm	1 ns	1,18 rad
30/150	22 µm	1 ns	0,9 rad
40/200	30 µm	1 ns	0,525 rad

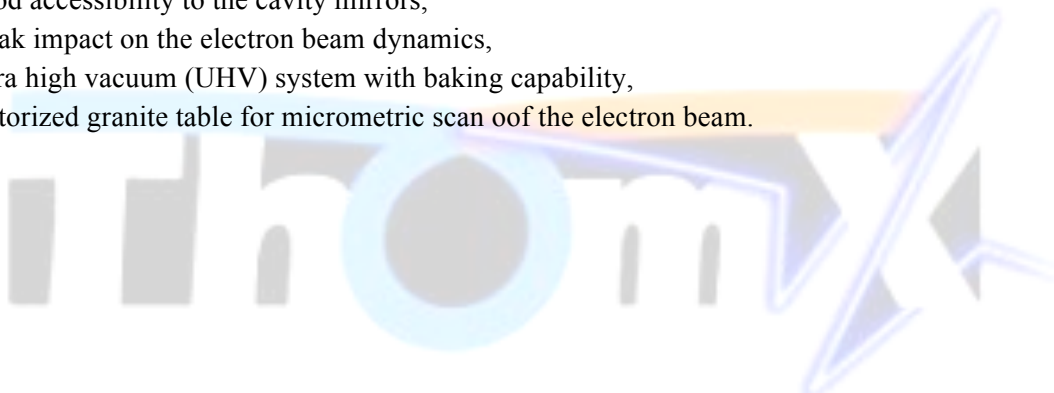
Table 6.1. Pulse stretching as a function of the fiber core diameter (simulations).

A first configuration will be developed with a stretching of 500 ps. If the non-linearity effects remain too high to allow for an efficient locking on the Fabry-Perot cavity, we will modify the setup to induce a larger stretching factor or insert a fiber with a larger core diameter in the last amplification stage, or both.

6.3 Mechanical design

Collisions between the laser pulse and the stored electrons will take place between two dipoles (see Fig. 6.43). The constraints on the optical cavity mechanical design are as follows:

- High stability level (vibrations),
- Good accessibility to the cavity mirrors,
- Weak impact on the electron beam dynamics,
- Ultra high vacuum (UHV) system with baking capability,
- Motorized granite table for micrometric scan of the electron beam.



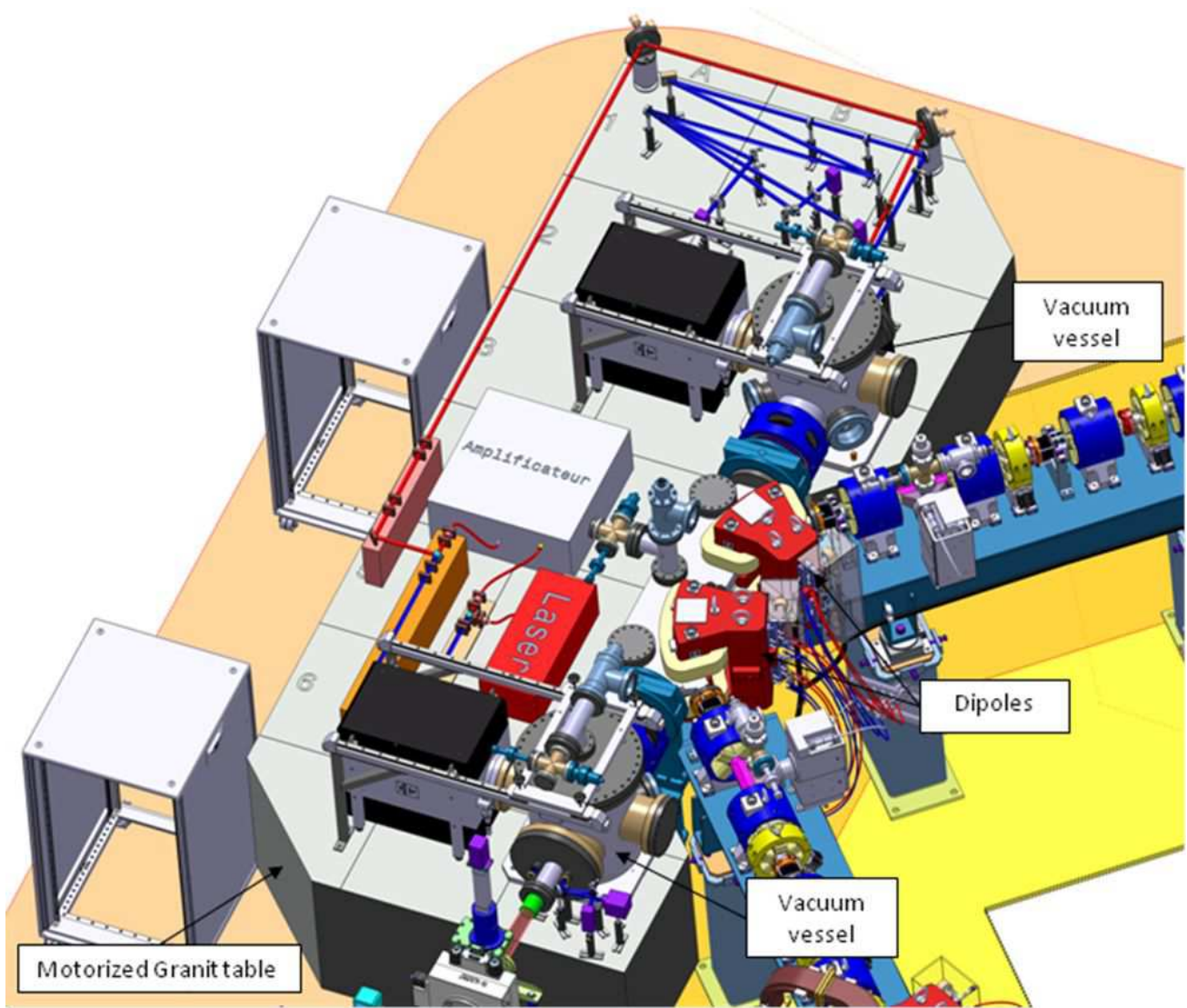


Figure 6.43. Implementation of the cavity in the electron ring.

The cavity mirror system is mounted on a massive granite table which can be driven to perform a micrometric electron beam scan (see Fig. 6.43).

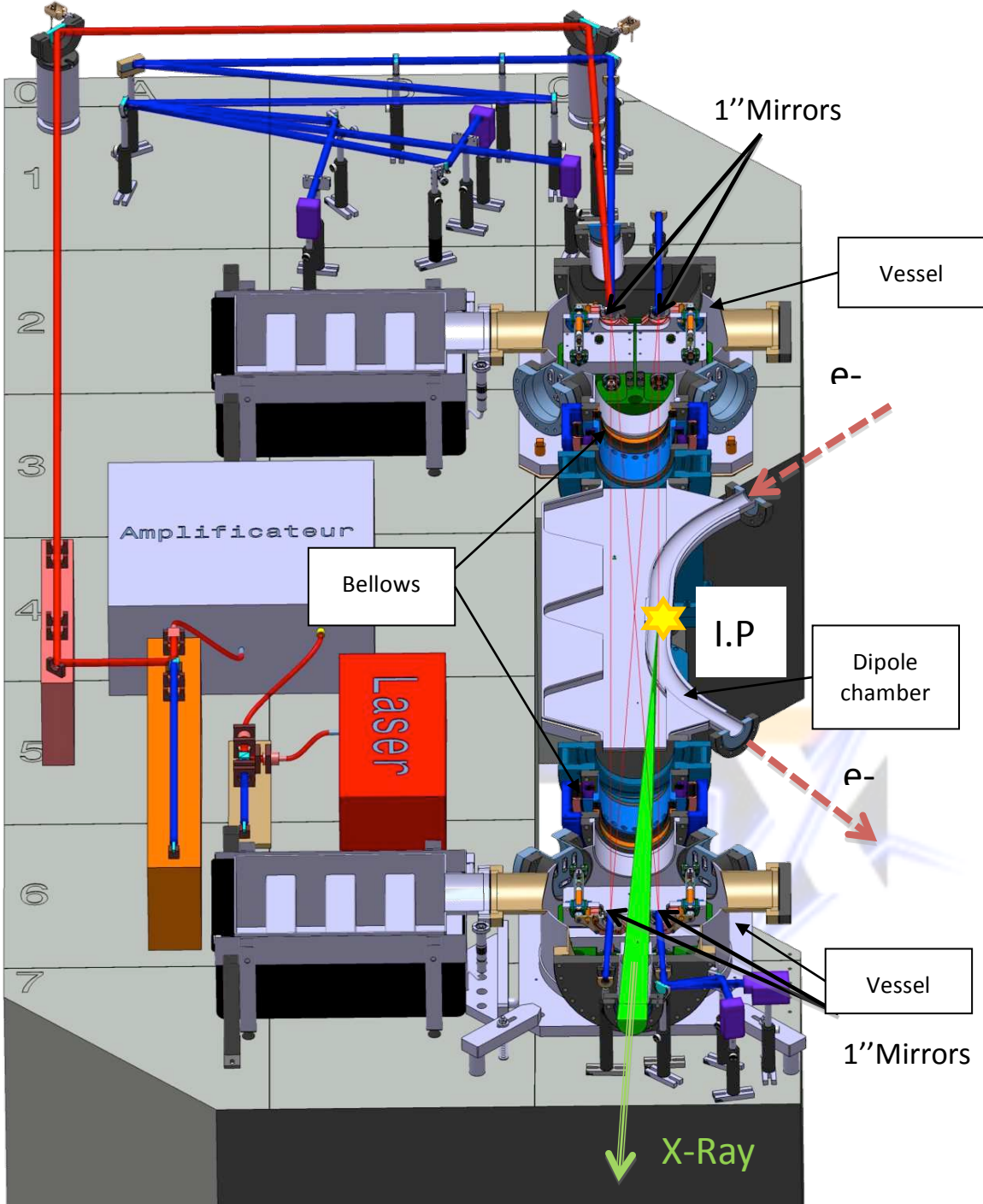


Figure 6.44. Scheme of the Fabry-Perot cavity mounted on the optical table.

The Fabry-Perot cavity is composed of two cylindrical UHV vessels linked by a dipole chamber. Bellows are placed between each element to absorb the dilatation due to the backing (see Fig. 6.44).

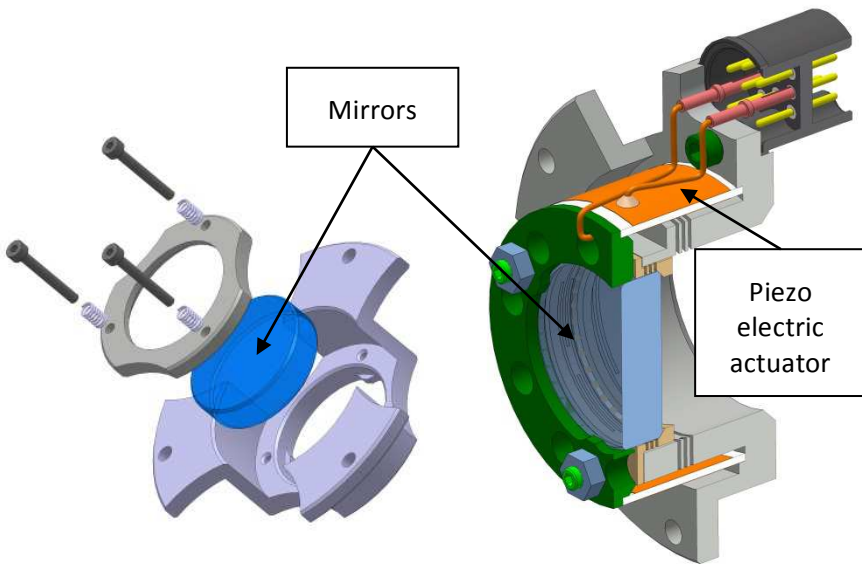


Figure 6.45. On the left: detail of the standard mirror assembly, and on the right: detail of the piezo electric mirror assembly.

The Fabry-Perot cavity is composed of two spherical and one flat mirror mounted in a standard assembly, and one flat mirror mounted on a special assembly with a piezo electric actuator for very small longitudinal displacements (see Fig. 6.45).

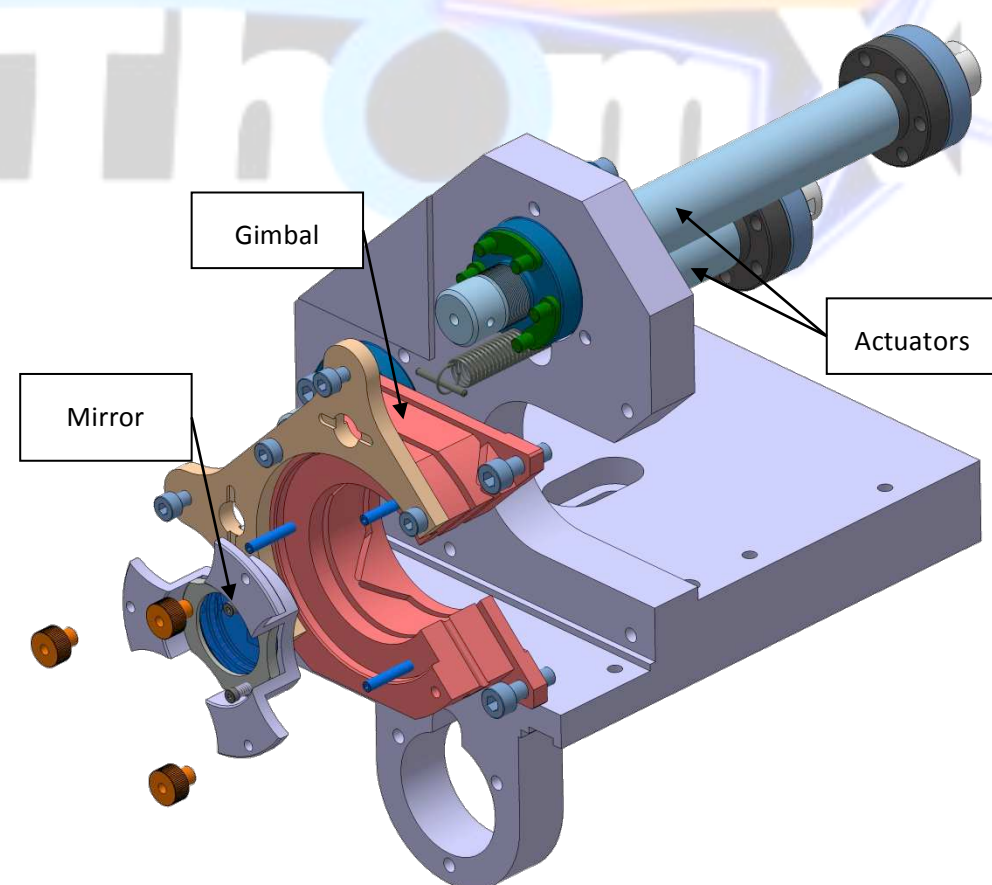


Figure 6.46. Detail of a truck system.

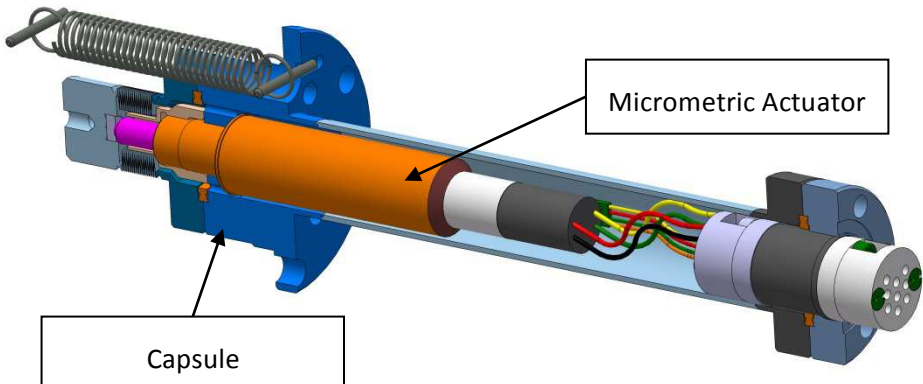


Figure 6.47. Cut of an UHV actuator.

All the mirrors are mounted on a truck system that provides three degrees of freedom (two rotations and one translation) driven by three micrometric actuators. These actuators are specially designed to be compatible with UHV and backing constraints (see Fig. 6.46 and Fig. 6.47).

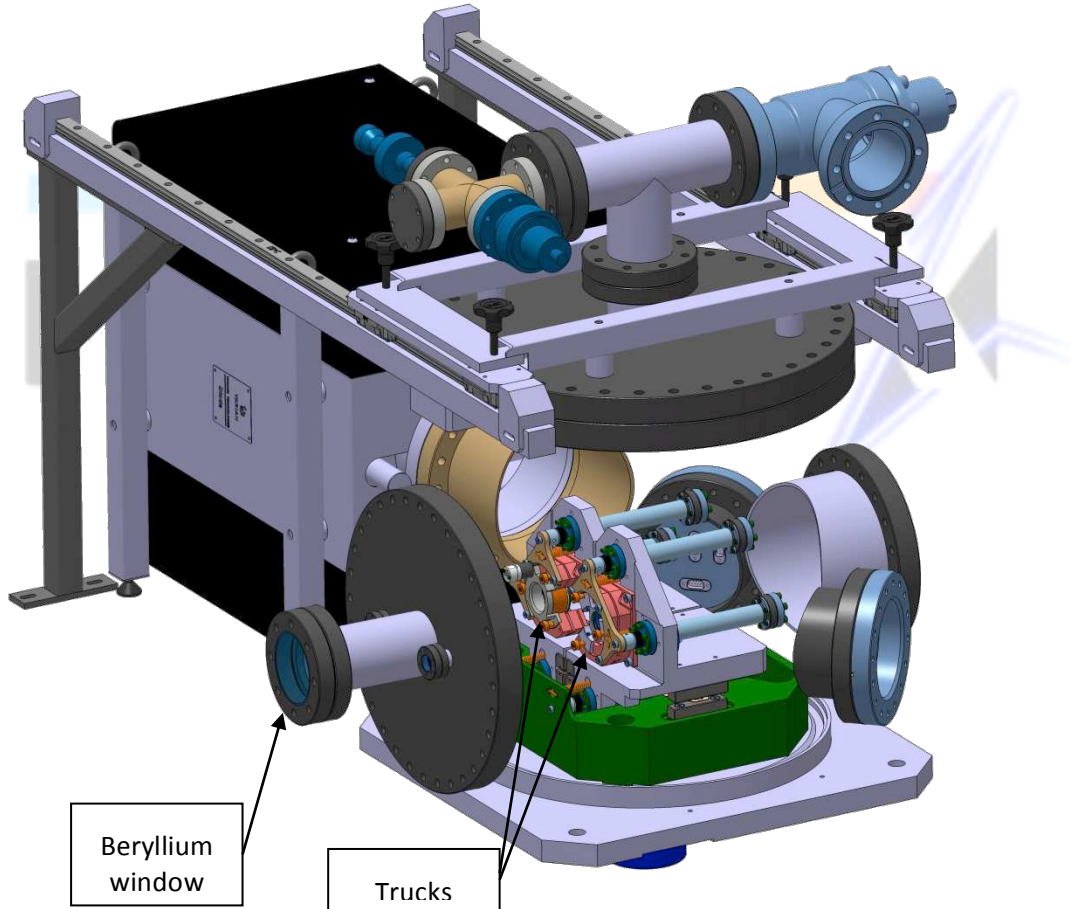


Figure 6.48. Cut of a vacuum vessel.

Trucks (two trucks per vacuum vessel) and plugs with special cables composed of ceramic connectors, oxygen-free copper cables and ceramic pearls and spacers for electrical isolation, are placed in a UHV vacuum vessel. One of the vacuum vessels has a beryllium window to extract the X-ray beam (see Fig. 6.48).

6.3.1 Optical cavity vacuum

A simulation was carried out in the most unfavorable case when the whole optical vacuum chamber is *not* baked. The area of one half of the optical cavity is about 2 m^2 ; the conductance of the rectangular chamber connecting the two cavity halves is $C = 7,08 \cdot 10^{-1} \text{ m}^3 \cdot \text{s}^{-1}$ (value for one half of that rectangular chamber). The conductances of the slits connecting the optical cavity to the ring are respectively $C = 4,52 \cdot 10^{-2} \text{ m}^3 \cdot \text{s}^{-1}$ (9×48) and $C = 1,60 \cdot 10^{-2} \text{ m}^3 \cdot \text{s}^{-1}$ (6×30). The outgassing rate of one optical cavity half, without any baking ($\sigma = 2 \cdot 10^{-8} \text{ Pa} \cdot \text{m} \cdot \text{s}^{-1}$), is $Q = 4 \cdot 10^{-8} \text{ Pa} \cdot \text{m}^3 \cdot \text{s}^{-1}$. The outgassing rate of one rectangular chamber half ($\sigma = 10^{-9} \text{ Pa} \cdot \text{m} \cdot \text{s}^{-1}$) is $Q = 7,6 \cdot 10^{-10} \text{ Pa} \cdot \text{m}^3 \cdot \text{s}^{-1}$. The outgassing rates of the two slits ($\sigma = 10^{-9} \text{ Pa} \cdot \text{m} \cdot \text{s}^{-1}$) are respectively $Q = 2,28 \cdot 10^{-13} \text{ Pa} \cdot \text{m}^3 \cdot \text{s}^{-1}$ (9×48) and $Q = 1,44 \cdot 10^{-13} \text{ Pa} \cdot \text{m}^3 \cdot \text{s}^{-1}$ (6×30). The diode ion pump used for the optical cavity has a pumping speed of $0,5 \text{ m}^3 \cdot \text{s}^{-1}$ DN 150 : $S = 0,320 \text{ m}^3 \cdot \text{s}^{-1}$ at $\sim 10^{-10} \text{ mbar}$. The conductance of the pumping port being $C = 1,36 \text{ m}^3 \cdot \text{s}^{-1}$, the effective pumping speed is $S_{\text{eff}} = 0,278 \text{ m}^3 \cdot \text{s}^{-1}$. The diode ion pump used for one half of the rectangular chamber has a pumping speed of $0,15 \text{ m}^3 \cdot \text{s}^{-1}$ DN 100 : $S = 0,090 \text{ m}^3 \cdot \text{s}^{-1}$ at $\sim 10^{-10} \text{ mbar}$. The conductance of the pumping port being $C = 0,046 \text{ m}^3 \cdot \text{s}^{-1}$, the effective pumping speed is $S_{\text{eff}} = 0,075 \text{ m}^3 \cdot \text{s}^{-1}$.

The outgassing rate of the optical cavity without baking is very high: $2 \times 4 \cdot 10^{-8} \text{ Pa} \cdot \text{m}^3 \cdot \text{s}^{-1}$ (which is approximately 40 times the outgassing rate of the whole ring). With such a rate, one would need a pumping speed of $8 \text{ m}^3 \cdot \text{s}^{-1}$ to reach the required pressure level of 10^{-8} Pa (the present pumping speed is $0,7 \text{ m}^3 \cdot \text{s}^{-1}$). The conductance of the rectangular chamber that connects the two halves of the optical cavity ($7 \cdot 10^{-1} \text{ m}^3 \cdot \text{s}^{-1}$) and the conductance of the two slits between the optical cavity and the ring ($6 \cdot 10^{-2} \text{ m}^3 \cdot \text{s}^{-1}$) are high. These figures do not allow a differential pumping between the cavity and the ring. Simulations of the ring vacuum level show that it is mandatory to bake the whole optical cavity.

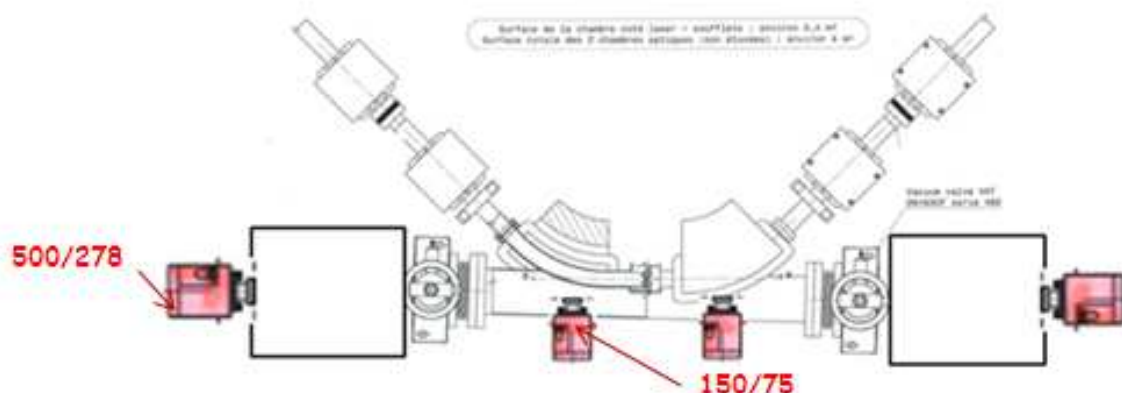


Figure 6.49. Location of the cavity pumps.

The vacuum equipment needed for the optical cavity is as follows:

- 2 ion pumps 150 l s^{-1} with their baking equipment and their power supplies,
- 2 ion pumps 500 l s^{-1} with their baking equipment and their power supplies,
- 2 gate valves manually actuated (pipe diameter DN100) and their baking equipment,
- 4 Pirani gauges,
- 4 cold cathode gauges,
- 2 power supplies for the gauges,
- 4 residual gas analyzers (RGA),
- 1 baking equipment for the vacuum chamber,
- 4 angle valves manually actuated for pre-pumping (pipe diameter DN63).

Chapter 7. X-RAY BEAM LINE AND EXPERIMENTS

Introduction

The equipment of the X-ray beam line should firstly ensure a continuous detection and monitoring of the beam (mainly in the first optical hutch) and, secondly, allow a complete characterization of the beam (in the experimental hutch). This characterization consists in measuring the beam absolute intensity, its total energy range, its spectral and angular distributions, and its degree of transverse coherence. Time analyses of the bunched X-ray beam will also be performed. This line also aims at confirming the ThomX assets in such fields as cultural heritage, biomedical and materials sciences, by performing demonstrative experiments.

7.1 Available extracted X-ray beam

The X-ray beam is extracted through a 50 mm diameter beryllium window as schematized in Fig. 7.1. Because of limitations due to the dimensions and the location of the Fabry-Pérot cavity mirrors, the X-ray beam available for characterization and experimentation is a cone with a half-aperture of 16 mrad.

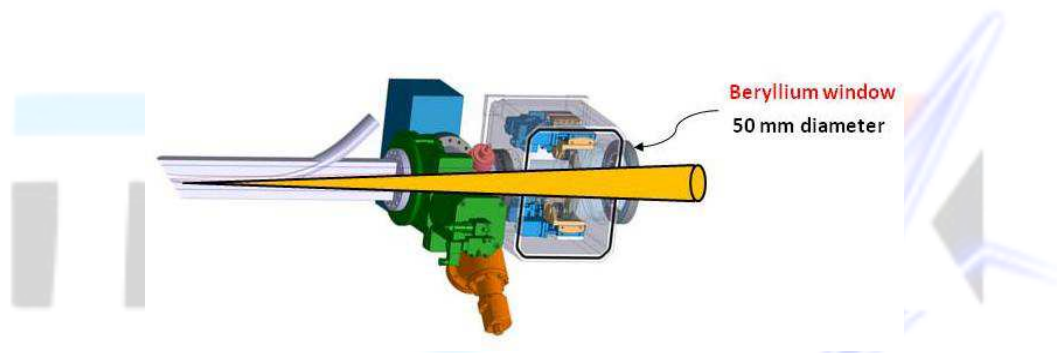


Figure 7.1. The X-ray beam extracted from ThomX through a beryllium window. The beam fills a cone whose total aperture is 2×16 mrad.

In the case of a ‘perfect’ beam (*i.e.* without taking into account the electron beam emittance), the X-ray spectral and energy distributions are shown in Fig. 7.2 as a function of the scattering angle, for two electron beam energies, 50 and 70 MeV, and a laser wavelength of 1.06 μm . In Fig. 7.3, the energy bandwidth and the flux per unit solid angle are shown for on-axis Compton photons produced by either a 50 MeV or a 70 MeV electron beam.

7.2 Global view of the X-ray line

As can be seen in Fig. 7.4, the positioning of the machine in the Igloo imposes the splitting of the X-ray line into two sections: a first optical table ($3 \times 2 \text{ m}^2$) located just after the beryllium exit window, and a second table ($4 \times 2 \text{ m}^2$) located outside the Igloo in hall D1. Along its path and until the optical table # 2, the beam is transported in the primary vacuum inside stainless steel pipes, with the exception of a short upstream section of a few tens of cm between the beryllium window and the optical table: this insulating section will prevent the transmission of harmful vibrations to the Fabry-Pérot cavity. This primary zone is kept oxygen free by a nitrogen flow that prevents ozone production.

The beam diameter at the entry of the first optical table is 4.5 cm. After this first optical table, the beam reaches the second table via a 13 cm diameter beam pipe inserted in a hole which was drilled long ago in the Igloo wall. About 8 mrad beam angular divergence are preserved at the entry of the second optical table where the beam diameter is 13 cm.

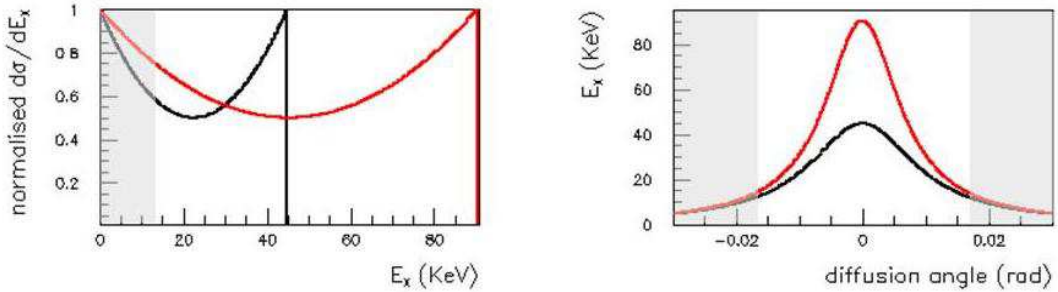


Figure 7.2. X-ray spectral distributions (left panel) and X-ray energy (right panel) versus the scattering angle for an e^- beam of 50 MeV (black) and 70 MeV (red). The laser wavelength is 1.06 μm . Grey areas correspond to emission angles larger than 16 mrad.

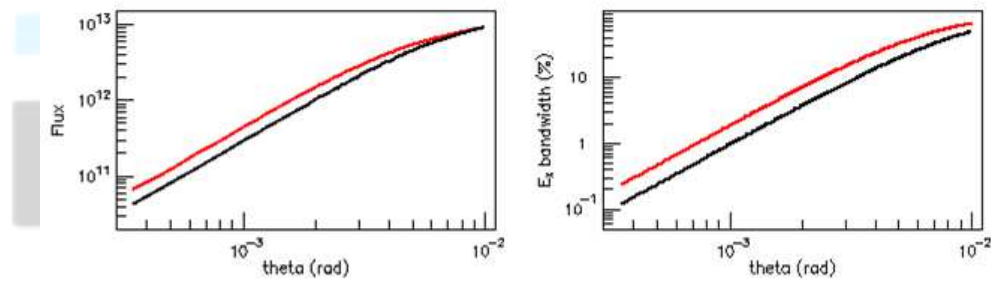


Figure 7.3. X-ray flux (left panel) and X-ray energy bandwidth (right panel) of on-axis photons per unit solid angle versus the emission angle, for an e^- beam of 50 MeV (black) and 70 MeV (red). The laser wavelength is 1.06 μm .

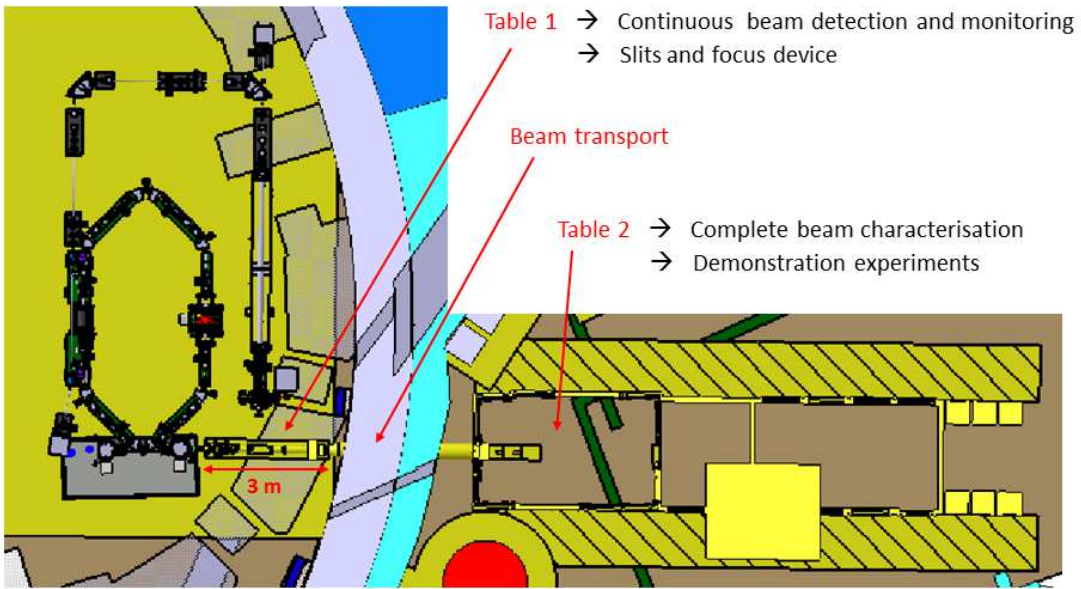


Figure 7.4. Global view of the X-ray line in ThomX.

7.3 Characterization of the X-ray beam

7.3.1 Optical table 1

A global view of the optical table 1 design is presented in Fig. 7.5. Just upstream of this optical table, a 60 mm diameter beam shutter activated when one needs to take background data will allow stopping the beam. A few millimeter thick tungsten is sufficient to stop the full beam (tungsten attenuation mass factor $\mu_{\text{en}} \sim 40.43 \text{ cm}^{-1}$ for 100 KeV photons). This shutter does not have to be cooled since the ThomX radiated power will not exceed 100 mW. A drawing of the shutter mechanical design is shown in Figure 7.6 (a).

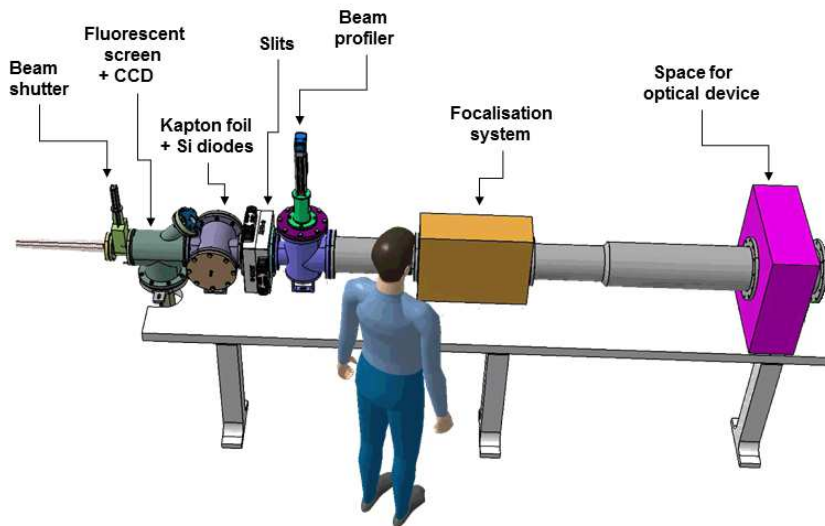


Figure 7.5. Global view of the optical table 1 showing the location of the main devices placed on it.

Beam monitoring

The optical table 1 equipment (see Fig. 7.5) is mainly devoted to the detection and the continuous monitoring of the X-ray beam. The first device monitoring the beam presence is a fluorescent screen mounted on a two-position motor (up or down), as shown in Fig. 7.6 (b). It is inserted in the beam path and viewed by a CCD camera. Its screen absorbs almost the totality of the beam and thus has to be put in the up position when not in use. Downstream of the fluorescent screen, a device composed of two Si PIN diodes measures the beam scattered by a thin Kapton foil inserted in the beam path. This setup, shown in Fig. 7.6 (c), will monitor the beam flux variations and beam position displacements. The Kapton foil is fixed at an inclination angle of about 60° with respect to the beam path. The sum and the difference of the two diode currents will provide a relative measurement of the beam flux and of the beam position respectively. This set-up which is nearly transparent to 20-90 keV radiations is a non-intrusive monitor and can be used continuously. Then, a high precision double slit [7.1] intercepts the X-ray beam and allows one to let through only the desired part of the Compton cone (see Fig. 7.6 (d)). The minimum dimensions of the slit aperture are $10 \mu\text{m}$ in the horizontal and the vertical directions. Beyond the double slit, a wire monitor [7.2] shown in Fig. 7.6 (e) is inserted in the beam. This device consists in two tungsten wires stretched horizontally and spaced by a few tens of a millimeter. This monitor will be driven vertically through the beam. The difference of the two wire signals allows the measurement of the absolute beam position.

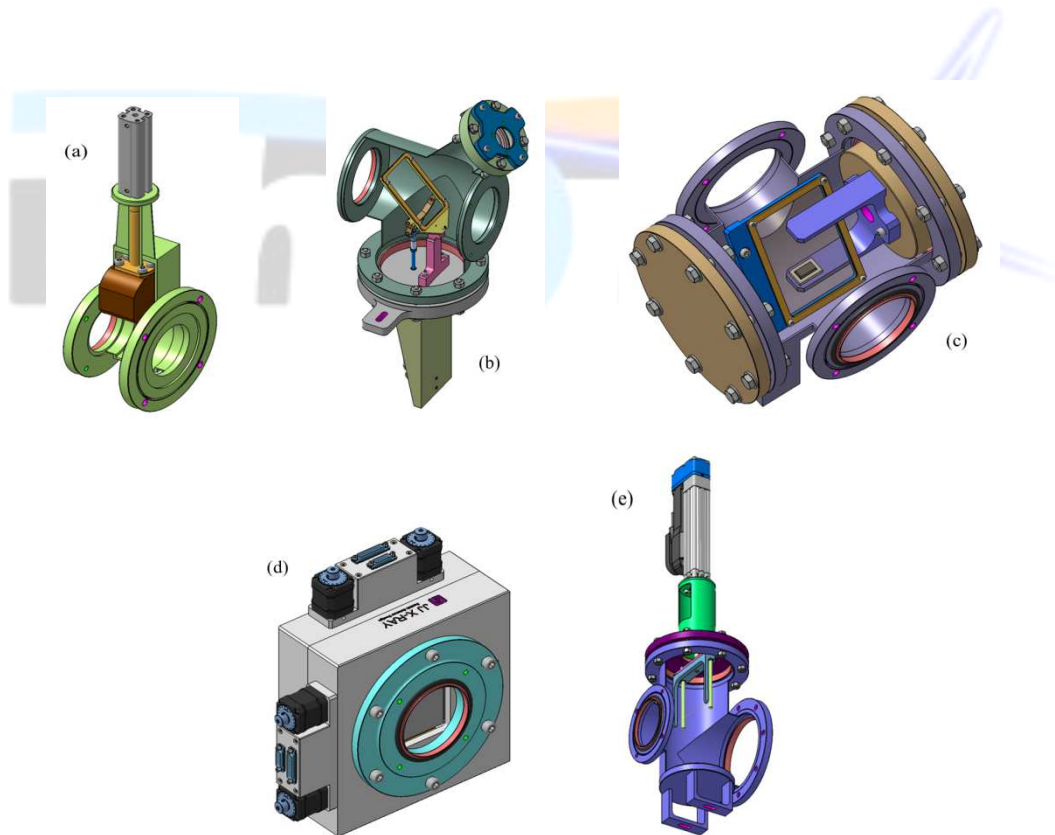


Figure 7.6. Drawings of the X-ray line devices located on the optical table 1: (a) Beam shutter. (b) Motorized two-position fluorescent screen. (c) Kapton foil and Si diodes. (d) Double slit. (e) Wire profiler.

Focusing device

Downstream of the beam monitoring instruments, a focalizing device will be installed (see Fig. 7.5) to make the X-ray beam parallel and/or to focus it on a sample. It can be either a device based on compound refractive lenses [7.3] (a so-called ‘transfocator’) or two bendable mirrors in the Kirkpatrick-Baez configuration (KB Optics), or a capillary optical device. These three techniques will be investigated to evaluate the advantages and disadvantages (aperture, efficiency, focusing strength, etc.) of their eventual implementation in the ThomX facility. Such a focusing apparatus has to be located as close as possible to the X-ray source because of the rapid growth of the beam transverse dimension. Finally, at the end of the optical table 1, some space is kept free for any specific study which might concern optics, detectors or samples.

7.3.2 Beam transport

As shown schematically in Fig. 7.7, beyond the optical table 1 the X-ray beam crosses the Igloo wall inside a beam pipe that runs through a 15 cm diameter hole and reaches the D1 hall where the second optical table is installed in the ‘experimental hutch’. At the entrance of the wall hole, a second beam shutter, in lead, around 15 cm in diameter and 2.5cm thickness is installed. This shutter is connected to an interlock system that ensures radioprotection. It absorbs radiations coming from the electron machine which propagate through the Igloo cylindrical hole, and allows X-ray users to work in the experimental hutch without stopping the electron machine.

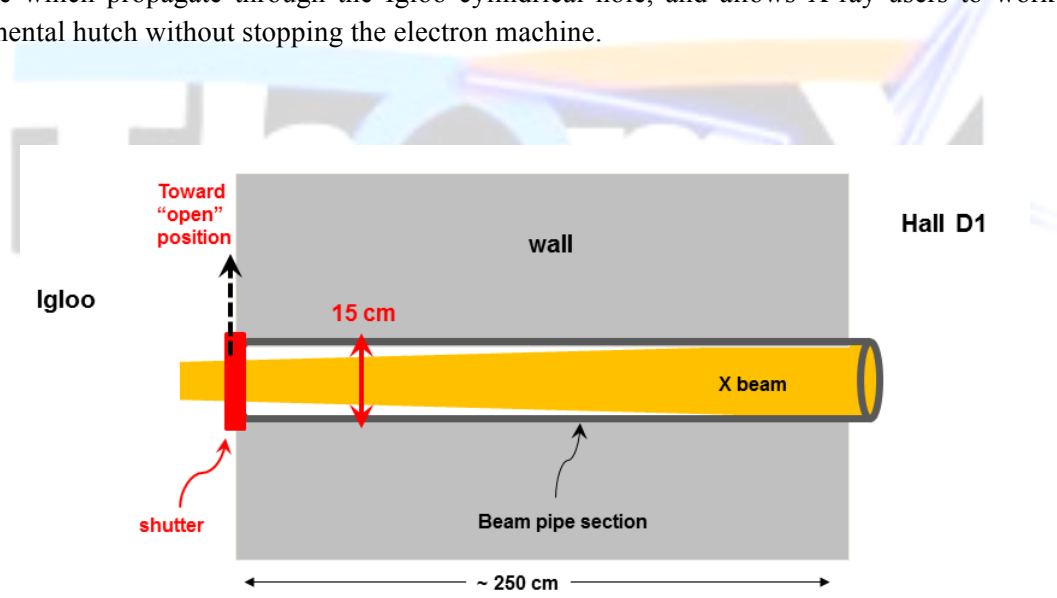


Figure 7.7. Schematic of the X-ray beam transport across the Igloo wall, from the optical table 1 located in the Igloo until the optical table 2 located in the D1 hall.

7.3.3 Optical table 2

Several kinds of instruments will be placed on the optical table 2. The goal is to study in detail the X-ray beam produced by ThomX, firstly to determine how the beam characteristics depend upon the machine operation parameters, and secondly to prepare the demonstration experiments. A global view of the optical and detection instruments placed on that table is provided by Fig. 7.8.

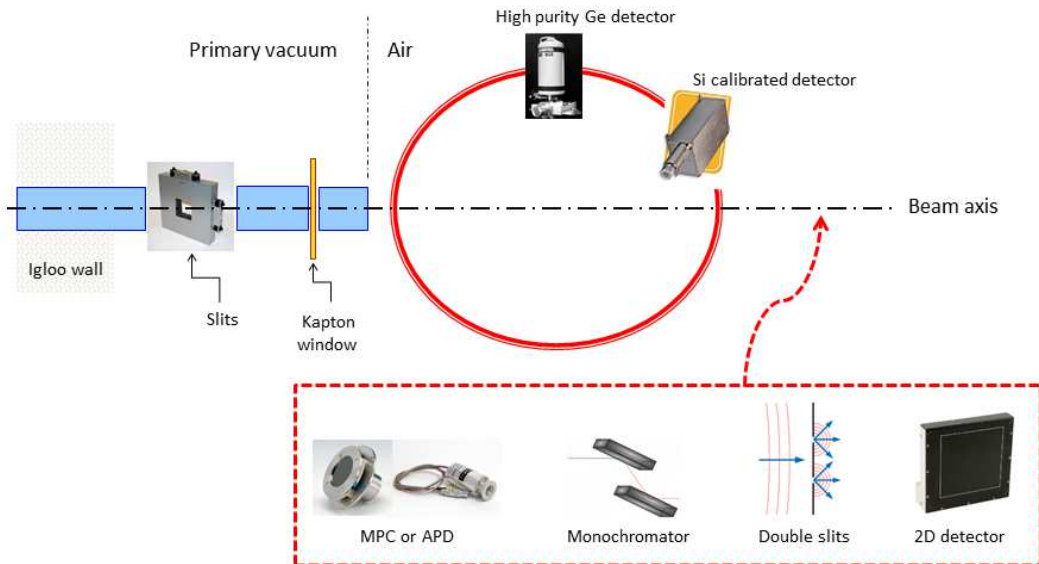


Figure 7.8. Global view of the optical table 2 indicating the main instruments that will be used to characterize the beam.

Absolute and spectral flux measurement

The measurement of the X-ray beam absolute flux and of its energy spectrum will be performed by using two detectors: a calibrated Si diode [7.4] and a cooled high-purity Ge solid-state detector (SSD) [7.5]. The Si diode will be bought already calibrated [7.6]. A ‘good’ Ge SSD has an energy resolution ($\Delta E/E$) around 1% at 20 keV, 0.6% at 45 keV and 0.45% at 90 keV [7.7]. The energy calibration of the Ge SSD will be carried out in the X-ray beam line by using the K_{α} fluorescence lines of reference materials (see Table 7.1).

Element	Ge	Mo	Sn	Cs	Ce
$E_{K\alpha 1}$ (keV)	9.886	17.479	25.271	30.973	34.719
$E_{K\alpha 2}$ (keV)	9.855	17.374	25.044	30.625	34.279
Element	Eu	Er	W	Pt	Pb
$E_{K\alpha 1}$ (keV)	41.542	49.128	59.318	66.832	74.969
$E_{K\alpha 2}$ (keV)	40.902	48.221	75.981	65.112	72.804

Table 7.1. K_{α} fluorescence lines of chemical elements used to calibrate the Ge SSD in the 10-90 keV energy range.

The two detectors will be mounted alternately on a (X, Y) translation stand to measure a large number of points of the emission spectrum:

- the mean emission energy E (Ge SSD),
- the energy spread ΔE (Ge SSD),
- the absolute flux (photon number/s) (Si diode).

These beam characteristics will be measured as a function of the size of the selected X-ray sample, the selection being carried out with a double slit device (see Fig. 7.6 (d)). Our goal is to check

experimentally the theoretical angular/spectral distributions shown in Fig. 1.2 of the Introduction, by measuring the number of Compton photons per second, per mrad², and per 0.1% of energy bandwidth.

Time analysis of the bunch structure

The X-ray source has a time structure which involves two main scales: a 50 ns period which is the interval between two successive collisions between the laser pulse and the electron bunch, and the 20 ms e⁻ storage cycle. To perform a pulse by pulse analysis we will use a high resolution time detector (~1-5 ns) with a high repetition frequency (~10-100 MHz), *e.g.* a micro-channel plate (MPC) detector [7.8] or an avalanche photo-detector (APD). Such time measurements have already been performed at a similar facility by Sakaue et al. [7.9]. MCP Hamamatsu devices can reach a 0.7 ns (FWHM) time resolution which is good enough not only to resolve each one of the collisions between the laser pulse and the electron bunch, but also to measure their relative intensity accurately, from the beginning of the e⁻ storage cycle to the end. These measurements will be performed on the X-ray beam axis. They will have to be synchronized with the ThomX clock.

Transverse coherence of the beam

Some simple diffraction and interference measurements will be performed in order to analyze the source spatial coherence. The diffraction of the X-ray beam by a slit of a known aperture, or the interference effect produced by the insertion of a phase-shifting object in the beam allows one to quantify the transverse coherence of the beam [7.10]. In these experiments, the on-axis photon intensity distribution will be recorded with a 2D high resolution detector (such as, for instance, an XPAD CdTe camera with 130 µm pixels). This measurement will be repeated at several positions along the beam. The pattern analysis will inform us about the degree of coherence of the source. A monochromator will be inserted upstream of the diffractive slit or the phase-shifting object to select a well defined energy. Later on, Young double-slit experiments could also be carried out [7.11] to measure the beam coherence length.

7.4 Demonstration experiments

In parallel with the complete characterization of the ThomX beam described in the previous sections, some simple experiments will be performed in order to demonstrate the potentialities of the ThomX source. In this phase, we will focus on medical and materials science applications. An important aim of the ThomX project is to perform medical and materials imaging, exploiting the high and tunable energy of its beam. A second aim of the ThomX project is to show its capability in the structural investigation of materials using X-ray diffraction/scattering/spectroscopy techniques.

7.4.1 Experiments using the full X-ry beam

Three experiments issued from the expertise of the ESRF-INSERM teams in medical applications of synchrotron radiation have been chosen to be carried out as demonstrators on the ThomX prototype. The goal of setting up such experiments is to demonstrate (i) the suitability of ThomX of performing both imaging and therapy experiments, (ii) the tenability of the source adjustable at energies corresponding to the K edge of high Z elements routinely used in medicine (Gd, I) or of those of new experimental radiotherapy adjuvants (Au, Gd nanoparticles, CisPt), (iii) suitability of the source for phase contrast imaging, (iv) exploitation of the advantage of using a 2D beam with respect to the typical laminar synchrotron X-ray beam. Some imaging and therapy experiments in the biomedical field require a wide 2D beam. Using the natural divergence of the ThomX beam, a sample of a few

centimeters in diameter located at 10-20 meters from the ThomX interaction region can be fully illuminated by the a conic beam, with no need of optical elements. Calculations have been performed in order to show the potential of using the ThomX source in comparison with a hospital X-ray generator (fluoroscopy unit type), as well as in comparison with the beam from the biomedical line ID17 at ESRF. Results of these comparisons are given below for each medical experiment we intend to perform with ThomX.

An imaging experiment

For imaging experiments, the energy range of the beam has to around 60-90 keV. According to Fig. 7.3, the corresponding half-aperture will be 5 mrad, leading to a photon flux of $6 \cdot 10^{12}$ ph/s. When the beam reaches the sample stand placed on Table 2, at 20 m from the ring interaction region, it will have a diameter of 20 cm. This conical beam will then have a cross section of $\sim 300 \text{ cm}^2$ and permit tomographic acquisitions of a full human head using a 2D detector. This wide 2D beam is a major advantage of the ThomX source for biomedical imaging with respect to the laminar synchrotron radiation beam. The dose rate (DR), in Gy/s, can be expressed as:

$$(7.1) \quad DR = 1.6 \cdot 10^{-13} * \Phi [\text{ph/s/cm}^2] * E [\text{keV}] * (\mu_{\text{en}}/\rho) [\text{cm}^2/\text{g}],$$

where Φ is the photon flux per cm^2 , E is the mean energy of the beam and (μ_{en}/ρ) is the mass attenuation coefficient. For an X-ray beam of 75 keV (*i.e.* the average of our 60-90 keV energy range), the mass attenuation coefficient μ_{en}/ρ for soft tissues is $0.028 \text{ cm}^2/\text{g}$, leading to a dose rate of 6.7 mGy/s delivered to a 300 cm^2 area. The corresponding expected ‘dose area product’ (DAP) of the ThomX source for such imaging experiments is $DAP = 2.0 \text{ Gy/s/cm}^2$. For comparison, at the ESRF ID17 line, a dose rate of 800 mGy/s is delivered to an area of $150 \times 2 \text{ mm}^2$ corresponding to a DAP of 2.4 Gy/s/cm^2 . As far as conventional sources are concerned, typical laboratory devices used in 2D fluoroscopy deliver a DAP of 0.6 Gy/s/cm^2 [7.12].

A feasibility experiment will be performed by using a standard human head phantom (see Fig. 7.9) which will be mounted on a rotating stand that allows a 360° rotation. It will be possible to translate this stand in three directions (along the X-ray beam axis and in the two other perpendicular directions) to optimize the sample position in the beam. Acquisition will be performed using the 60-90 keV pink beam before and after the insertion of a high-Z element solution (typically iodine or gadolinium) in a slot available in the phantom head. Several images will be acquired using different concentrations of high-Z element chosen in the range of concentrations that can be typically reached into a tumor (in humans, the high Z element is injected intravenously). The study will also aim at finding, for each high-Z element, the lowest concentration that can be measured with the ThomX imaging system.



Figure 7.9. Typical phantom featuring a human skull, from X-ray absorption point of view.

The detector will be placed downstream of the sample. A typical detector that may be used is a large field of view 2D detector, equipped with Si or CdTe sensors with \sim 100-200 μm pixels, [7.13]. Finally, a standard computed tomography (CT) algorithm will be used to reconstruct the tomography images and to calculate the concentrations (in mg/ml) of the given high Z element in the skull. The results will be compared to previous work done at the ESRF [7.14].

A radiotherapy experiment

For this experiment, the targets will be rats implanted in their right brain hemisphere with rodent brain tumors (F98, 9L) at an appropriate tumor stage (typically at D10 or D14 after implantation). For the irradiation, we need a pink beam with a 10 keV energy bandwidth and a median energy above the K-edge of the high-Z element to be injected as a radiosensitizer (*i.e.* in the 45-80 keV range for both iodine and gadolinium). The beam size will be a few centimeters in diameter. Figure 7.10 shows the X-ray beam energy and beam flux generated by a 69 MeV electron beam versus the photon back-scattering angle. X-rays of energy 80 keV within a 10 keV bandwidth are contained in a cone of half-aperture 2.7 mrad and their flux is $\sim 3 \cdot 10^{12}$ ph/s. At the sample location on optical Table 2, at 9 m from the ring interaction region, the beam has a diameter of 5 cm, *i.e.* a cross section of $\sim 20 \text{ cm}^2$.

The center of the rat's right hemisphere will be placed on the rotation axis of the irradiation system and slits will limit the beam transverse extension in order to define a precise field of irradiation. Assuming an X-ray flux (Φ) of $3 \cdot 10^{12}/20 \text{ ph/s/cm}^2$ with an average energy (E) of 80 keV, a mass attenuation coefficient of $0.025 \text{ cm}^2/\text{g}$ (soft tissue, 80 keV X-rays) Eq. (7.1) leads to a dose rate DR_e of 48 mGy/s close to the tissue region where the X-ray beam penetrates. Before reaching the tumor, the radiation is attenuated by the bone ($\sim 0.2 \text{ cm}$ thickness, $(\mu/\rho)_{\text{att}} = 0.22 \text{ cm}^2/\text{g}$, $\rho = 1.92 \text{ g/cm}^3$) and by the skull healthy tissues ($\sim 1.5 \text{ cm}$ thickness, $(\mu/\rho)_{\text{att}} = 0.18 \text{ cm}^2/\text{g}$, $\rho = 1.0 \text{ g/cm}^3$). Thus, the dose rate DR_t delivered at the tumor is $DR_t = T \cdot DR_e$ (where $T = \exp(-0.22 \cdot 1.92 \cdot 0.2) * \exp(-0.18 \cdot 1.0 \cdot 1.5) = 0.70$) and is expected to be 33.7 mGy/s. The dose will be delivered while the rat undergoes a 360° rotation. The total dose to be delivered to a tumor ranges between 10 to 20 Gy. Therefore, according to the expected rate of 33.7 mGy/s, the irradiation will take typically from 5 to 10 minutes with the big advantage of not having to move the rat. A dosimetry protocol (such as the one used at ID17 [7.15]) will be set to check the homogeneity of the irradiation and to measure the absolute dose with a 2 to 5% uncertainty.

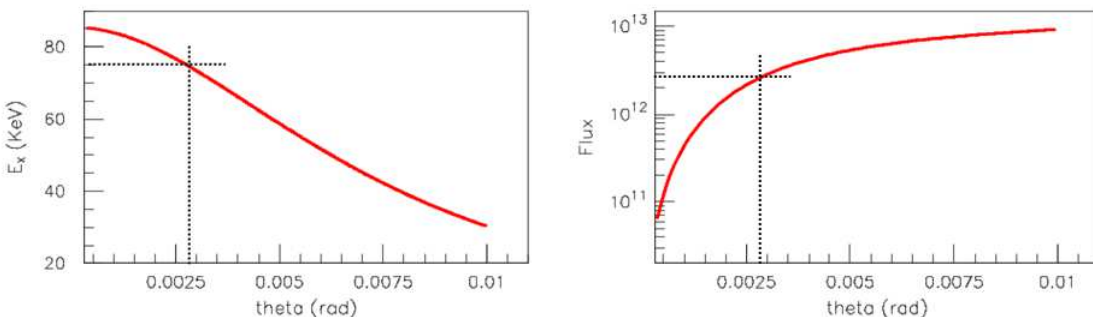


Figure 7.10. X-ray energy (left panel) and X-ray flux (right panel) versus the photon back-scattering angle for stored electrons of 69 MeV. The laser wavelength is 1.06 μm .

For humans, and a tumor placed at 8 cm into the skull, the transmission coefficient becomes $T = 0.19$. Therefore the expected dose rate DR_t delivered by the ThomX source at the tumor is 9.1 mGy/s. One may compare with the ESRF ID17 beam-line where 800 mGy/s can be delivered for irradiation on a

surface of $2 \times 50 \text{ mm}^2$, *i.e.*, with $T=0.19$, a dose rate DR_t of 0.15 Gy/s on 2 mm in height at the tumor, which is equivalent to a rate of 6 mGy/s to cover 5 cm of height with a scanning rate of 50 mm/s . ThomX could therefore deliver doses for human skull irradiation larger than those available at synchrotron radiation facilities, and also perform the irradiation without having to move the irradiated sample. Concerning the conventional hospital devices, they deliver low doses deposited by X-rays whose energy spectrum is broad and, moreover, they are not made to operate continuously for such long time irradiation.

Also, the tunability of the ThomX beam will allow testing several high Z drugs containing iodine, gadolinium, platinum or gold, proven to be promising radiosensitizers [7.16].

Conformal radiotherapy

A final step in this sequence is performing conformal radiotherapy experiments, *i.e.* doing both imaging and therapy at the same time. In fact, one major issue of radiotherapy is to spare as much as possible healthy tissues located around the tumor and at its border. In this regard, it is a key issue to adapt the field of irradiation to tumor geometry, size and positioning by performing first a tomography.

Phase contrast imaging

The absorption medical imaging technique is based on the fact that different parts of a sample absorb X-rays differently. But the fact that X-ray absorption by biological material is weak constitutes also the limitation of this technique. To enhance or replace absorption-based imaging, refraction, diffraction and interference of X-rays can also be used. A better visibility at the edge of different regions of a specimen can therefore be obtained by using the information contained in the phase of an X-ray wave. For this, a spatially coherent X-ray source is required and was available only since the development of modern synchrotron sources. Experimentally, the simplest way to visualize phase-contrast imaging is provided by the propagation-based imaging (PBI) method. In this method, a spatially quasi-coherent radiation illuminates an object which gives rise to a spatially varying phase shift in areas with spatial variations of the refractive index. As the radiation propagates beyond the sample, parts of the wavefront which have experienced different deflections on both sides of an edge of the sample produce a series of fringes due to the classical Fresnel-edge diffraction phenomena [7.17]). This gives rise to a characteristic phase contrast pattern which is then recorded by a 2D detector placed at a proper distance downstream of the object (see Fig. 7.11, left panel). The actual phase-contrast signal is convolved with the detector point spread function which has to be sufficiently narrow to avoid the smearing of the interference pattern. Additionally, the phase contrast signal can be visualized if and only if the transverse coherence is sufficient, *i.e.* if $L_{coh} = \lambda R/s$ is larger than the details to be imaged (here R is the source-sample distance and s is the source size). In contrast, the requirements in terms of longitudinal coherence (monochromaticity) are rather weak: even a beam with a bandwidth of several keV does not lead to a significant smearing of the phase contrast signal [7.17].

Assuming $s = 70 \mu\text{m}$, $R = 15 \text{ m}$, a sample-detector distance of 5 m , and a detector point spread function of $50 \mu\text{m}$, the phase contrast signal expected when the ThomX beam illuminates a nylon wire of $300 \mu\text{m}$ diameter ranges from 10% to 3% when the X-ray energy increases from 20 to 80 keV (see Fig. 7.11, right panel).

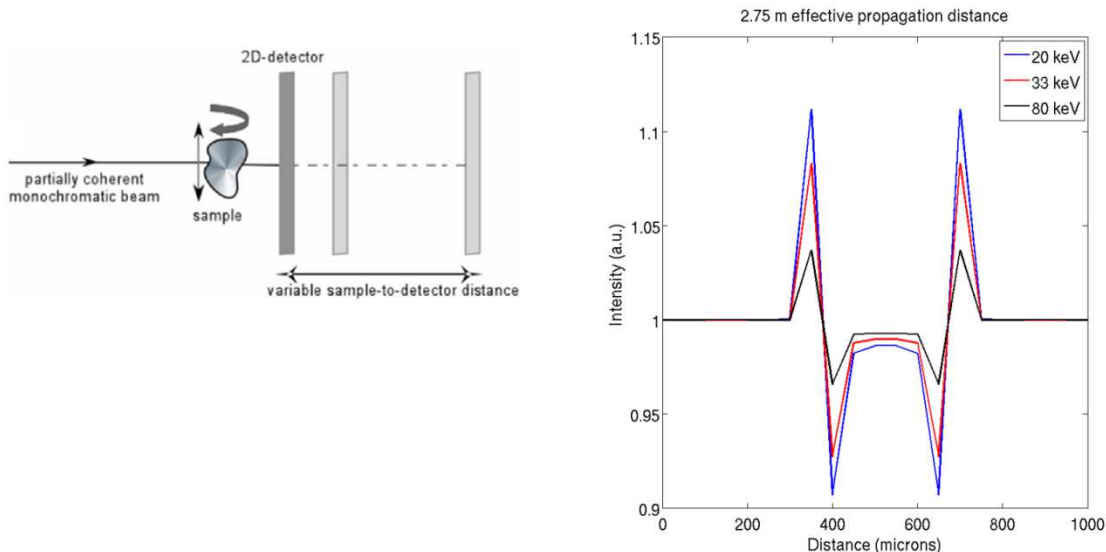


Figure 7.11. Left panel: The set-up for propagation-based phase contrast imaging. Right panel: The simulated signal produced by a nylon wire of 300 μm diameter illuminated by the ThomX source (simulation).

The experiment with ThomX will comprise two parts: a planar radiography and a computed tomography. For the radiography, three kinds of samples will be used: (i) a custom-made phantom composed of nylon wires of different diameters; (ii) the ACR (American College of Radiology) accredited phantom used in mammography quality; (iii) a 4 cm thick formalin-fixed human breast tissue obtained from a hospital bank. The X-ray energy will be chosen in the 20-80 keV range. For each sample and for several energy values, images will be acquired at two different sample-detector distances: in the absorption regime for comparison purposes (the detector will be in contact with the sample) and at 5 m. A silicon detector with 50 μm pixels will be used. Images will be acquired for different doses (measured with a standard PTW dosimeter) in order to obtain the signal-to-noise ratio as a function of the dose. These measurements will allow one to qualify the phase contrast imaging set-up at ThomX.

Computed tomography will be applied to (i) a méthyl polyméthacrylate (PMMA), custom-made, cylindrical phantom containing insets of different compositions and densities (water, ethanol, paraffin etc.); (ii) a formalin-fixed human breast tissue (5 cm in diameter). Images will be acquired using the same parameter values as the ones chosen for the radiography. Samples will be installed on a rotating stand, positioned on a double cradle that will permit an alignment with the beam and with the detector. Images will be taken during the sample rotation over 360 degrees.

The final step will consist in applying standard algorithms to the images in order to calculate the phase and to extract quantitative information about the samples. This data will be compared with equivalent images that will be acquired at the ESRF.

7.4.2 Experiments using the central part of the beam

Most specimens from cultural heritage and functional materials are heterogeneous; these ‘real’ materials often exhibit complex hierarchical structures involving various levels of order and heterogeneity. To understand the properties of such materials better, one needs at least a description of their structure at the atomic scale and at the macroscopic/mesoscopic scale which takes into account weak structural signals (relating to disorder, minor constituents, microstructure, hierarchical order...).

This requires much probing as already demonstrated with synchrotron radiation sources. A major goal of materials science is to link global properties to local atomic features (orientation, strain, structural distortion, grain size...) of some components in relation with neighboring domains, and to deduce from that the macroscopic properties. As the functionalities of these materials often stem from the association of different phases or constituents, or of specific inter-relation between them (microstructure), highly selective structural probes need to be used to characterize them. Also, in the particular domain of cultural heritage, many specimens require non-destructive methods and probes. In order to understand how they were made and to preserve them from degradation over time, their physical and chemical properties must be determined. There is an increasing demand for material probing with complementary techniques. Fluorescence emission techniques excel in revealing the elemental composition of the top-most layers of samples. Diffraction is suited for studying quantitatively the phase composition, the structural details of the constituent phases and the characteristic distribution of sizes and orientations of crystallites. Tomography techniques excel in revealing the 3D mapping of the chemical and/or the density heterogeneities within a sample. This is why the cultural heritage community is today strongly involved in the development of new instruments that may characterize patrimonial artifacts by mapping not only the chemical composition of a variety of samples but also their physical phases.

Experiments described in section 7.4.1 require a large 2D beam and exploit the natural divergence of the ThomX beam. In this section, diffraction, scattering and spectroscopy experiments require a focalized or a parallel beam, and it should also be monochromatic or ‘pink’. The optics will therefore select the central part of the beam, *i.e.* its higher energy part. Let us give an order of magnitude: assuming a perfect 50 MeV electron beam, a collimator of 2 mm diameter located at 2 meter from the IP will cut the X-ray conic beam at 0.5 mrad, leading to a flux of $\sim 8 \cdot 10^{10}$ ph/s with an energy of 45 keV and an energy bandwidth $\Delta E/E$ on the order of 10^{-3} (see Fig. 7.3). In practice, this bandwidth will be broadened and will reach a few percent because of the actual e^- beam divergence and energy spread. For experiments requiring a narrower energy bandwidth, an additional selection will be performed with a monochromator. For instance, selecting an energy bandwidth of 10^{-4} would lead to a flux on the order of 10^9 ph/s.

Since the goal of the first series of demonstration experiments is to qualify ThomX as an X-ray source, these experiments will be performed with samples previously characterized with other sources, such as synchrotron radiation sources.

Diffraction and scattering

Diffraction and scattering experiments are major ways of performing materials structural and micro-structural analyses. This concerns highly ordered samples as well as powders or ill-ordered samples. Complete scattering analyses are based not only on Bragg diffraction but also on diffuse scattering in order to look beyond the average structure and to investigate the local structure or short-range order. The crystalline quality of powders depends on the preparation methods. Grain sizes vary from about 10 nm to several hundreds of μm . In the case of nano-materials, Bragg peaks are strongly broadened and X-ray diffraction performed with standard laboratory sources does not provide suitable data for structural investigations. As illustrated by Fig. 7.12, laboratory X-ray sources do not allow the identification of minor phases in a poorly crystallized powder. Figure 7.13 shows an example of a diffraction pattern obtained with an excellent resolution. The sample used for this analysis is an Egyptian cosmetic powder dated to 2000-1200 BC. The patterns were obtained with the ESRF synchrotron source (bottom panel) and with a classical laboratory source (top panel).

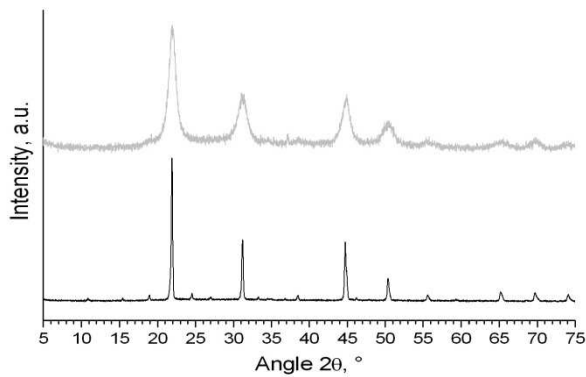


Figure 7.12. Powder X-ray diffraction patterns obtained by using a laboratory X-ray source. Top panel: Poorly crystallized Prussian blue sample. Bottom panel: Prussian blue crystals. From [7.18].

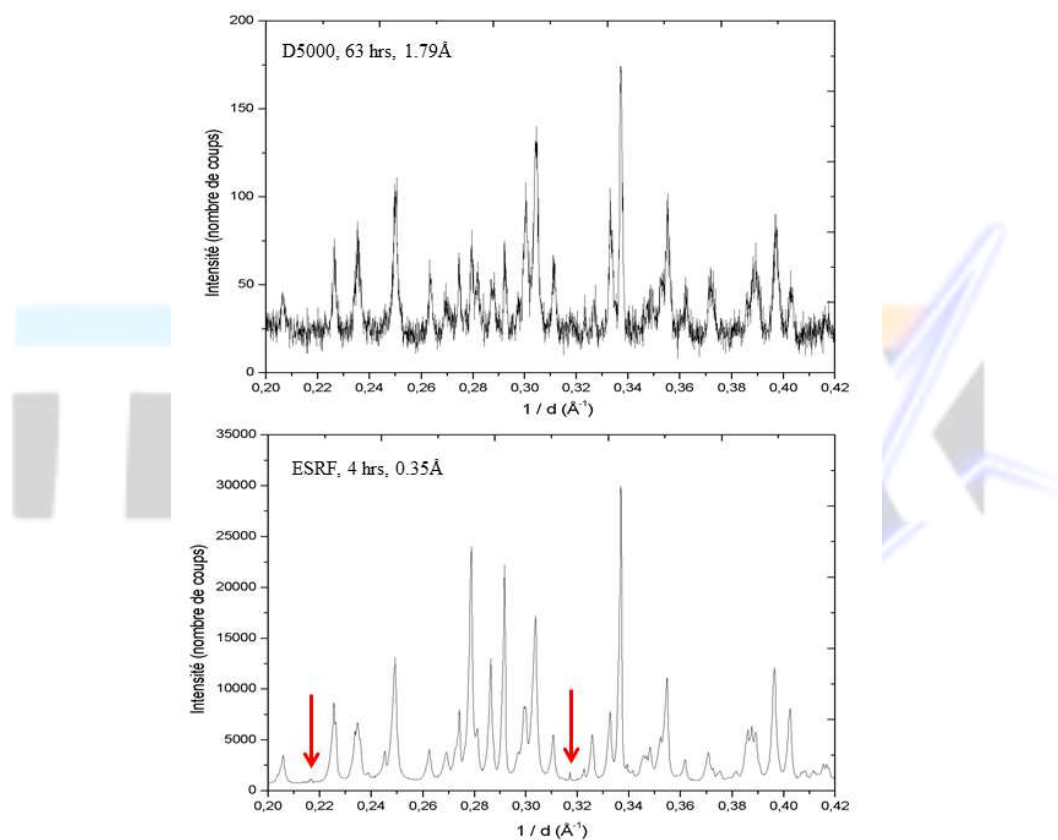


Figure 7.13. Powder X-ray diffraction patterns obtained by using a laboratory X-ray source (top panel) and the ESRF synchrotron source (bottom panel). Arrays indicate minor phases. From [7.19].

We intend to use the ThomX source to record diffraction patterns and scattering plots in order to characterize short-range ordering and identify minor phases in such heterogeneous samples. For the first demonstration diffraction/scattering experiments, we will study ill-ordered Prussian blue and white lead samples. Pigments used for paintings or frescos have various compositions. Since their usage followed a definite chronology, such pigments can sign an era. Pigment characterization can also help the undertaking of a restoration while a thorough knowledge of pigment synthesis through centuries can help to apprehend the degradation mechanisms better.

For ordered samples, diffraction will be performed with a single crystal by using a monochromatic beam but also by using a ‘pink beam’ as done in the Laue method. For ill-ordered samples, the whole scattering pattern will be recorded and analyzed with the Pair Distribution Function (PDF) method. This analysis technique (often called the “total scattering method”) can be used alone or associated with diffraction. For experiments using the ‘pink beam’ Laue method, the beam will be focused directly on the sample (by using convergent refractive lenses (CRLs) or a capillary optic system as mentioned in Section 7.3.1). To determine powder crystalline parameters, diffraction analyses require the monochromatization of the beam in order to reach $\Delta E/E \sim 10^{-4}$. In the optic hutch (optical Table 1), the diverging beam will first be made parallel by the CRLs or the capillary optic method and then monochromatized in the experimental hutch (optical Table 2) by a monochromator. The set-up for these measurements needs a goniometer to align the sample and a low noise 2D-detector sensitive to high energy photons.

Fluorescent spectroscopy

X-ray fluorescence spectroscopy experiments allow one to determine the chemical composition of materials and the mass concentrations of elements. Indeed, depending on the atomic number of a given chemical element, energies of the fluorescence lines emitted after an X-ray excitation are a signature of the element. An illustration of this approach is presented in Figure 7.14 where the fluorescence tomographic images of a *Globorotalia inflata* specimen are shown and compared with a classical radiography image.

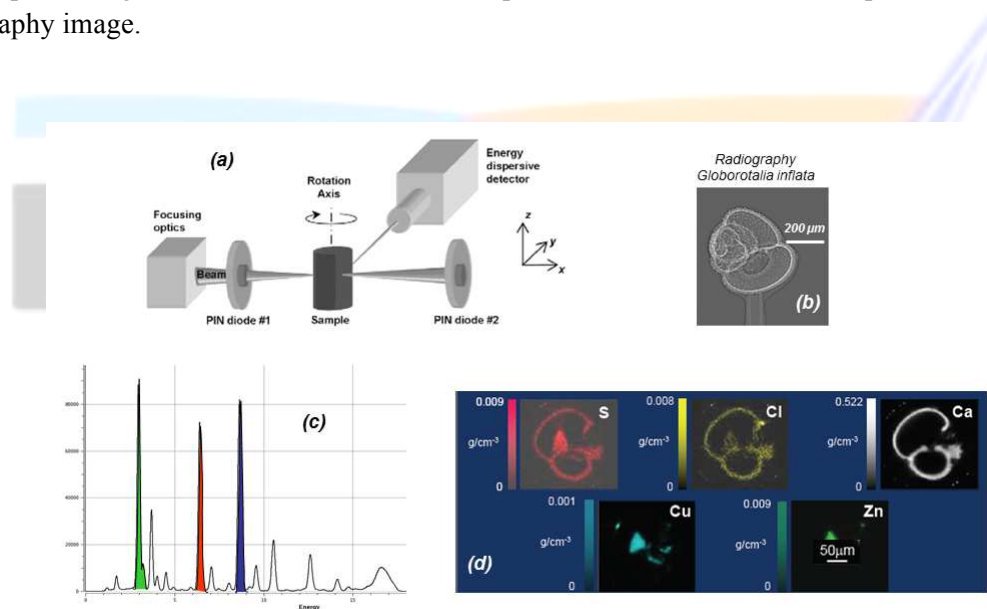


Figure 7.14. Fluorescence tomographic imaging. (a) Set-up. (b) Radiography. (c) Fluorescence spectrum measured at a given angle/position of the sample. (d) 3D tomography reconstruction. From [7.20].

We plan to carry out fluorescence experiments since the energy of the ThomX beam can reach the excitation energy of most chemical elements usually involved in material science for instance, the critical excitation energy of lead, regarded as a heavy element, is 88 keV. For this experiment, the excellent energy resolution of cooled Ge detectors will be an asset to detect the fluorescence light (the detectors will be oriented at 90° with respect to the incident beam).

K-edge and XANES spectroscopy

In K-edge experiments, two images of a given element present in some sample are performed: one at an X-ray energy just below the K edge of the chosen element, and the other at an energy just above. Then they are subtracted (see Fig. 7.15, left panel). The K-edge imaging technique is used in particular in the medical and the cultural heritage domains. In XANES (X-ray Absorption Near Edge Structure), the absorption by a material is measured over an energy range of about 100 eV on both sides of the absorption edge. This technique provides information about the local structure prevailing close to a particular chemical element (see Fig. 7.15, right panel).

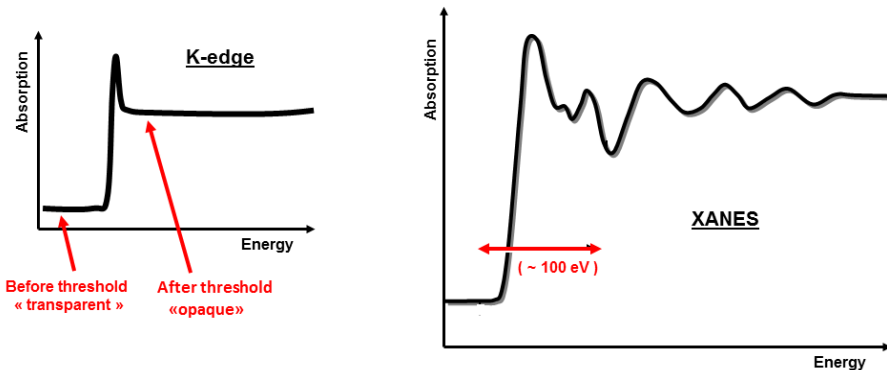


Figure 7.15. Left panel: K-edge subtraction imaging. Right panel: Principle of the XANES method.

The first XANES spectroscopy experiments with ThomX could exploit the K-edge of heavy elements such as W, Pt or Pb. By first selecting the central part of the ThomX beam with an energy spread of a few 10^{-2} , a monochromator could then provide a beam with an energy spread of 10^{-4} . Samples will be aligned by using a goniometer and the transmitted intensity will be collected by a low noise 2D-detector.

Combined diffraction/absorption/fluorescence tomography

A major limitation of diffraction methods comes from the fact that only average properties can be obtained while most ‘real’ materials are heterogeneous and complex. Thus structural studies of such materials are difficult to carry out. A new tool for structure mapping of materials by means of X-ray diffraction/absorption/fluorescence combined with tomography allows one to perform non-destructive 3D structure selective mappings of heterogeneous samples. This way one may identify minor phases and determine crystallite orientation and grain size. Furthermore, the selectivity of the method allows one to separate and locate the origin of the diffuse or diffracted patterns to identify amorphous phases. In archaeology, such complementary micro-structural analyses could shed light on the mechanical history of artifacts.

A recent experiment carried out with a micrometer beam at synchrotron radiation sources have established the validity of such a local probe by analyzing a mixture of chalcedony and iron pigments containing haematite [7.21]. This experiment, illustrated in Fig. 7.16, consists in (i) performing a structure tomography mapping directly from the diffraction data (top panel), (ii) obtaining selective structure patterns of unknown minor phases from these maps (bottom panel). This study was realized by the Néel institute and the C2RMF and was one of the first diffraction tomography experiments performed with a micro-beam.

With the ThomX source, we will use poorly crystallized samples and combine in the same experiment and simultaneously tomography diffraction with fluorescence and absorption measurements. Diffraction

tomography is beam-time consuming; it will be performed to demonstrate its feasibility at ThomX. The experimental set-up will be similar to the one used for multimodal analyses (cf. the top panel of Fig. 7.16). The sample will rotate and this rotation will be combined with a translation to provide a 2Θ scan of 2D diffraction patterns obtained with a 2D detector sensitive to high energy photons. The diffracted 2D fluorescence patterns will be recorded with our Ge detector while the sample absorption will be recorded with our calibrated Si diode.

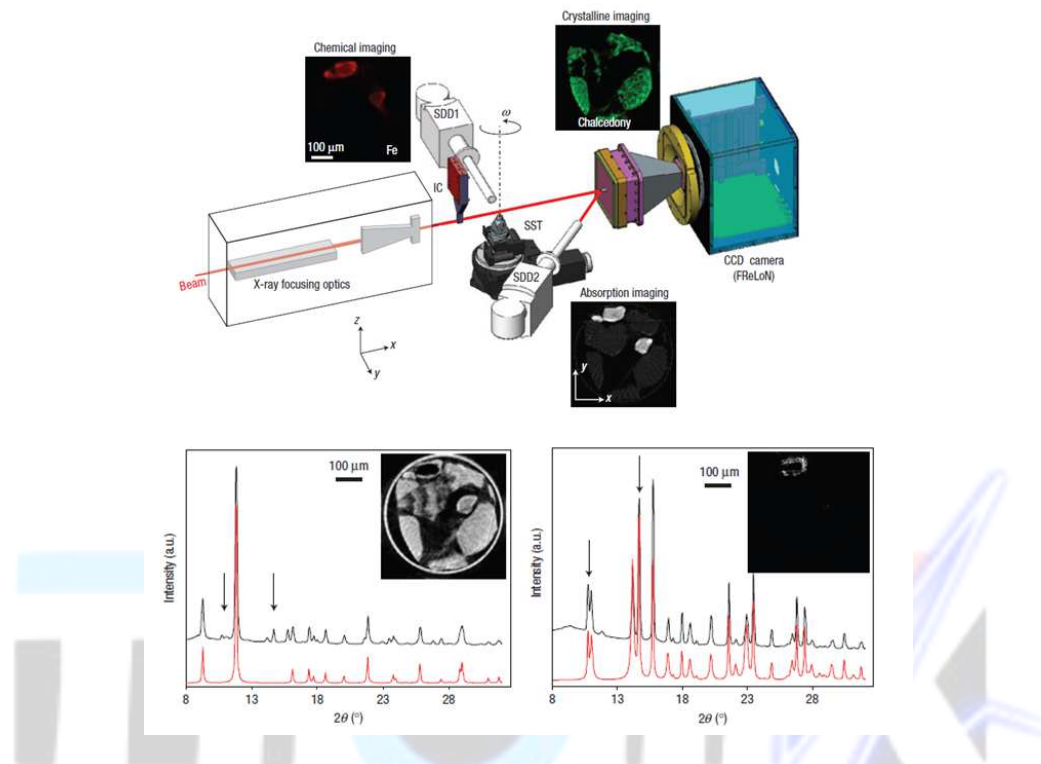


Figure 7.16. Top panel: Experimental set-up for multimodal spectroscopy/diffraction/tomography analysis. Insets: Images of the chalcedony–Fe mixed-pigment sample are reconstructed by combining the various signals: X-ray absorption (bottom), Fe X-ray fluorescence (top left) and chalcedony diffraction (top right). Bottom left panel: Reconstructed diffraction image based on the whole diffraction diagram (black) compared with the calculated pattern for pure chalcedony (red). Bottom right panel: Reconstructed image that only uses the iron pigment scattering contribution (black) compared with the calculated pattern for hematite and siderite grains (red). From [7.21].

7.5 Summary

As shown in this chapter, two types of beams will be available at the ThomX compact X-ray source: (i) wide beams well adapted for imaging (conventional or phase contrast imaging) and therapy in the biomedical field, and (ii) almost monochromatic beams that can be either focused or made parallel for diffraction and spectroscopy experiments in the field of materials science.

The X-ray line is designed

- to ensure a continuous monitoring of the X-ray beam,
- to measure the beam brightness and its transverse coherence,
- to demonstrate the potential of this new type of compact source and identify the benefits it can bring to the currently available X-ray sources.

Chapter 8. CONTROL SYSTEM

Introduction

The ThomX control system combines those hardware and software elements involved in the management of all the facility components. But more than a system dedicated to carrying out operating processes (processes launched from the X-ray beam control room in order to undertake some specific task such as a performing an imaging experiment or a material chemical analysis), it must also be an advanced tool for various studies (data processing, new equipment integration, operating mode evolution...) and scientific experiments which will be performed with the X-ray beam line. Hence, the control system has to be a versatile tool, easily scalable by various users (scientists, operators, IT technicians).

In the following, a ‘Sub-system’ is a physically connected set of hardware items sharing a global logical function. The ThomX sub-systems are as follows: the linac (LINAC), the transfer line (TL), the ring cell #1 (RI-C1), the ring cell #2 (RI-C2), the optical cavity (OC), the extraction line (EL), the section of the X-ray line located in the Igloo (XLI), and the section of the X-ray line located in the X-ray hall (XLH). A ‘Domain’ is a set of hardware items related by a common purpose. The ThomX domains are as follows: alignment/metrology (AM), control-command (CC), diagnostics (DG), infrastructure (IF), magnetic elements (ME)n optics (OP), pulsed elements (PE), power supplies (PS), radio-frequency (RF), safety (SA), synchronization (SY) and vacuum (VA).

8.1 General principles

Some general principles drive the design of such a control system. In broad terms, the following criteria will serve as guidelines:

- Since *monitoring* is a major role of a control system, comprehensive monitoring interfaces must be provided to all users. Moreover the monitoring system must take into account sub-systems specificities: dedicated GUIs must be designed for every need, for instance in synoptic form to give a global system status overview or as charts to show the time evolution of some specific parameters of a particular device (*e.g.* pressure readings on TPG300).
- *Operating processes management*: a control system also aims at the prioritization and sequencing of processes. It has to provide high-level functions in order to remotely launch complex operations (*e.g.* machine start/stop, interlocks...). Computing and data analysis tools which could launch such particular procedures will be integrated or developed to maximize the automation of the machine.
- *Default management*: the facility control system must be able to manage operation defaults. It will be necessary to design graphical tools to quickly identify defaults when they occur. Color display of warnings and errors, according to a criticality-based convention will be implemented in addition to the recording of running process logs.
- *Safety*: for obvious reasons, the ThomX radioprotection and safety system must standalone. It should not use any data generated by the control system. Nevertheless, each end-user must be able to make sure that the ThomX facility does not present any danger whenever the accelerator is running. This information must be available in every control room through a continuous display of all the safety equipment status (radioprotection sensors, door openings...). A full historical record of safety-related

events will be made available for analysis and a procedure of detailed acknowledgement (operator's name, action to close an incident) will be defined in order to guarantee safe operations.

- *Ease of use*: The ThomX control system is intended for various usages, therefore it will concern various users, including operators who are not familiar with software development. Hence, it is crucial to make it modular, through relevant to sub-systems GUIs with various visualization interfaces, control buttons, graphs, sub-system overviews in synopsis or detailed display of subset status. The definition of new interfaces will be possible through visual development frameworks to fit new needs.

8.2 Technical considerations

In order to guarantee a proper accelerator operation, to make its use as easy as possible and to limit costs, some technical points have to be taken into account.

- *Distributed architecture*: an accelerator is a complex structure which results from various designs in different fields. The hardware part of the control system relies on dedicated IT devices (industrial PCs, programmable logic controllers) whose role is to drive sub-systems. Each of these nodes will be fully and remotely controlled by the system software from the control rooms (or from any authorized user terminal in the ThomX network), independently of possible other issues. All of these components must communicate with each other when required by the operation needs. Moreover, the supervision part of the control system must be available in different places (main control room, X-ray line control room, perhaps others). The chosen system must meet these requirements and must run on several terminal types.

- *Standardization* of the hardware items and of the software codes is necessary in order to simplify their integration in the control system (*e.g.* same brand/model for all the stepper motors). Then it will be possible to mutualize high-level controlling tools, whether pre-installed or homemade. Additional benefits of this approach concern the overall maintenance, the deployment of new releases and the replacement of hardware parts.

- *Reliability*: The service continuity of the control system must be guaranteed. A spare strategy must be set up to make sure that the replacement of defective parts will be done on short notice. In particular, storage memory redundancy will guarantee that none of the machine parameters or of the collected data will be lost. Periodic backup of main software systems (device databases...) will be performed right from the start. Uninterruptible power supplies are foreseen to protect major elements of the control system from electrical failures.

- *Upgradability*: Special attention will be paid to communication features when choosing hardware devices. Ethernet is now one of the major protocols and must be preferred when possible. For the PLC driven devices, the fieldbus Profibus [8.1] is recommended since one single master interface can manage more than 100 slave devices without data losses. This product is also valuable as far as cabling cost is concerned.

- *Safety*: Since several users may wish to perform various machine-related tasks (integration, maintenance, measurements...), a policy must be established to control the access to the ThomX network and its control system. The management of these access permissions will be provided. It will take into account the role and the field of expertise of each project member.

8.3 The TANGO control system software

Tango [8.2] is the software chosen to be the backbone of the ThomX control system. It is an open-source software initially developed at the ESRF. It is now used in several Institutes to control huge accelerator facilities like the SOLEIL synchrotron. In fact, the SOLEIL staff is playing a major role in maintaining and developing new Tango features.

8.3.1 Software bus

An accelerator equipment is usually highly heterogeneous. Thus its control system must enable various devices to communicate with each other, even if they use different protocols or communication standards like Ethernet, RS232, USB, PCI DAQ Cards...

The first asset of Tango is the communication standardization that it provides between any type of devices. Tango implements a CORBA-based communication protocol so that a common network is virtually created for the whole hardware. If needed, the parameters of a given device are thus available to every other element of the control system. This is achieved by adding an extra Tango-compliant software layer above the hardware low-level libraries. This layer is specific to a device brand and model and is a simple executable file which can be instantiated as many times as required by the number of devices. This key element of the Tango system is called a ‘Device server’.

8.3.2 A control system for accelerators

For basic reasons, the Tango core and many of the tools developed around this software bus are open source tools. It is therefore an accessible system, fully customizable for specific ThomX needs, and a system which can be maintained. Since Tango is Linux and Windows compliant, issues originating in driver availability for the Linux OS can be avoided while Tango enables the use of scientific applications which are often developed for Linux.

Furthermore, Tango is developed and maintained by a community which involves several accelerator Institutes. Even if Tango is not an accelerator-dedicated tool, a number of developments have been carried out or are being carried out that deal with devices currently used at such facilities. Thus a large Tango library of device servers is presently available to any new user.

Finally, more than a simple tool which provides a network access to a set of devices, Tango is also a framework that provides high level operational services such as: configuration tool, logging, archiving services and alarms, permission management. For developers, specific tools are provided for the generation of codes that fit in the common structure required by all device servers. Other tools allow easy GUI development. As a result, the integration of new devices or the upgrade of control and supervision windows do not need in-depth coding. As far as the compatibility with commercial software is concerned, dedicated bindings can be freely used; *e.g.* applications developed for Matlab or Labview can be used to perform a variety of tasks involving the ThomX devices.

8.4 Control system architecture

8.4.1 Equipment to control

On a complex machine like ThomX, a wide range of devices and control signals must be taken into account: motors, cameras, scopes, diodes or valves will deal with analog and digital inputs/outputs, complex signals transmitted through GPIB, USB, Ethernet or profibus interfaces.

The inventory of devices to be controlled is presented in the following table. Safety equipment is not mentioned as it is a fully standalone sub-system.

	LINAC	TL	Ring	OC	XL
<i>Power Supplies</i>					
Coils	2				
Steerers	2	4	24		2
Dipoles	5	4	8		3
Dipole chicane		1			
Quadrupoles		7	24		3
Sextupoles			12		
<i>Pulsed elements</i>					
Septum			1		
Kickers			2		
<i>Synchronization</i>					
3GHz synthesizer	1				
500 MHz synthesizer	1				
Phase shifter	5				
Programmable delays	2				
Counter	1				
<i>Vacuum</i>					
Ion pump	8	4	17	4	
Gauge	8	8	22	8	1
Valve	4	4	4	2	
Primary pump					1
<i>Diagnostics</i>					
BPM	1	4	12		
Low frequency Signal generator			2		
ICT	1	2			
Stepper motors	1	3			
Camera CCD	2	3	1		
<i>RF</i>					
Klystron coil	1				
Modulator	1				
Amplifier	1				
Canon	1				
Feedback	2				
<i>Source laser</i>					
Photodiode	1				
Camera CCD	1				

Motor	1				
Mirror	2				
Laser – FP cavity					
Camera				4	
CCTV Camera				10	
Motor				16	
Thermal control unit				2	
Laser equipment				3	
Scopes				3	
FPGA				1	
X-ray Line characterisation					
Xpad camera				1	
Si PIN diode				3	
Ge diode				1	
Motor				13	
Stepper motor				25	
Others					
Translation table	1	1			
Slot		1			

Table 8.1. Devices to control (TL=Transfer line, OC = Optical cavity and XL = X-ray line).

8.4.2 Inputs/outputs

All devices listed above communicate with each other by digital inputs/outputs (DI, DO), *i.e.* one bit signals, analog inputs/outputs (AI, AO) or more complex signals, as n-bit digital signals ($n = 8, 12$ or 16). Several communication protocols mentioned in §8.3.2 above will be used.

They are detailed in Table 8.2

	PLC Inputs/Outputs	Bus	Ethernet connections	DAQ (ADC&DAC)
Vacuum	26 DI, 13 DO	26 profibus		
Diagnostics		2 gpib	30	3 x ADC 12 bits 100 kHz
Linac	2 DI, 2 DO, 5 AI		3	ADC 8 bits, 1 GHz
Magnets		35 profibus		
Feedbacks RF (x2)	10 DI, 10 DO, 10 AI, 10 AO	USB		
Ampli RF	64 DI, 8 DO, 32 AI, 16 AO	RS232	2	4 channels ADC 12 bits, 1MHz
Modulator RF	23AI, 4 AO , 69 DI			5 DI, 5 DO, 8 channels ADC 8 bits
Pulsed Elements (x3)	12 DI, 3DO	profibus		ADC 12 bits
Laser – FP cavity		RS232	22	
Timing		2 gpib	14	15 channels DAC 16 bits
X Line	26 DI, 26 DO		7	

Table 8.2. Equipment I/O to control (*not complete at the time of writing*).

8.4.3 Front-end machine architecture: PLCs and industrial PCs

The front-end architecture will comprise equipments individually dedicated to sub-systems. These machines are controlling nodes which will be located in sub-system server racks as close as possible to the equipment to be controlled (when required).

Two kinds of front-end machines will be used:

- *PLCs*: programmable logic controllers are automation OS-based machines able to manage digital and analog I/O and to control processes carried out by devices connected to a field bus (*e.g.* Profibus) or specialized devices. They are reliable devices designed to operate in an industrial environment. A proprietary operating system runs on these machines which are powerful tools (*e.g.* automats) to implement logic appropriate to experimentation. Interconnection with the other Tango network equipment is made through an Ethernet adapter interface.

- *Compact PCIs* (industrial PCs): these crates can embed complex operating systems like a Linux distribution or some Microsoft Windows Operating Systems, hard drives, Ethernet connections and USB adapters. Such crates are based on a PCI bus backplane to interconnect specific cards (DAC, ADC, counters, optoelectronics converters...). cPCI is a standard widely used in an industrial environment; it is compatible with numerous card suppliers. These front-end machines will also allow the running of Tango processes or specific computing tasks locally installed in a sub-system.

The ThomX distributed control system will be build on these controlling nodes. This structure will allow the bandwidth optimization of the network main links and will provide cabling simplifications. The control equipment may be placed in the accelerator hall as well as in the technical rooms where most of the electronics that must be controlled will be clustered in 19" standard server racks.

- Some devices need not be controlled through these front-end machines. They will be directly connected to the control network (*e.g.* ethernet cameras or electronics for motor control). Three ways to interconnect such devices are shown in Fig. 8.1.

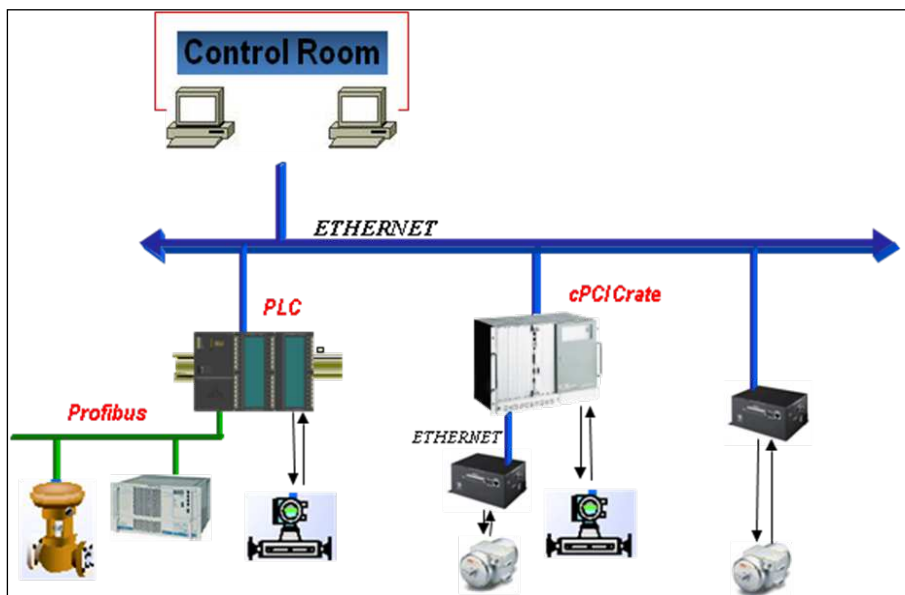


Figure 8.1. Control architecture for one sub-system.

These acquisition and controlling units can be: Profibus, PLC or a cPCI crate. Each driven element will be controlled through one of these acquisition and controlling unit.

The overall control system will be composed of more than 25 front-end machines, as described in Table 8.3.

	PLC	cPCI Crate
Linac (w/out vacuum, diags, modulator, magnets)	2	1
Vacuum	2	
Diagnostics		2
Feedbacks	2	2
RF amplifier/cavity	1	1
RF modulator	1	1
Pulsed elements	3	3
Fabry-Pérot cavity	1	1
X-ray line	1	
Synchronization		1
Magnets		2
Total	13	14

Table 8.3. List of front-end machines (*not complete at the time of writing*).

8.5 IT infrastructure

- *Network*. The ThomX local network will be organized around an IP backbone. It will be based on the Ethernet TCP/IP standard in order to link user terminals, front-end machines, specialized servers etc. Because of the large number of devices and the requirements bearing on the bandwidth (*e.g.* for image storage), 1 Gbits/s compliant equipment will be chosen (LAN adapters, switches...). Depending on the actual number of cameras, an image-dedicated network could be added. On the cabling side, shielded copper cables will be used as interconnection wires to limit electromagnetic interferences as much as possible.

- *Data storage*. During the ThomX commissioning or for the operation monitoring, or for the X-ray experiments, it will be crucial to store a large amount of data. It is foreseen to implement the three storage processes provided by Tango: historical (long term storage at a slow rate), temporary (short term storage at a fast rate) and snapshot (storage of parameters on operator demand or event triggered). It will also be possible to meet the X-ray line needs for the storage of large size images during short periods (at most for several days). This specific storage will not be necessarily on local servers ; it could be convenient to move these data and store them on servers close to the final users, possibly outside the ThomX network..

Two storage-dedicated servers will be installed for analyses, replay of accelerator operation scenarios and for some specific needs of the X-ray line. These storage units will be specific machines which prevent data outages or losses by redundant power supplies, stored data redundancy (RAID), hard disk hot swap, etc. The first of these two storage units will be a 2 To server equipped with a disk array dedicated to the accelerator data management. The second one will have a 10 To capacity; it will be available for the large size images of the X-ray line.

- *Equipment of the control rooms.* Users will work in control rooms on system administration, accelerator control, development and integration (device servers, GUIs, high level computing software, safety analysis tasks). Administration and end-user terminals should be provided in sufficient number (see below).

The main control room will be equipped with

- 5 PCs , 1 for the Tango core system, 2 for operations, 1 for development, 1 for safety (dedicated to visualization, storage and analysis of safety related events),
- 1 server to run high-level applications and device servers,
- 2 screens, one displaying the ThomX status with synopses, and the other one for the safety supervision,
- camera monitors for some direct controls,
- 1 UPS (uninterruptible power supply).

The X-ray line control room equipment will consist of

- 2 PCs for the operation equipment and for macro development,
- 1 server to run high-level applications and device servers,
- 2 screens dedicated to the monitoring of the machine status, to safety synopses and to the display of safety related events.

- Software needs

- Both the Linux and Windows OS must be installed in the control room PCs in order to run Tango and many other operating processes (see the Introduction above), for development purposes, and to use configuration software. Together with the Tango core and specific tools, high-level software will be installed to meet users' needs: Labview and Matlab for science applications, SPEC to control the motors and for the analysis of the X-ray line data,

- Data bases will run on the MySQL open-source database managing system.
- An open-source http server, Apache, will allow the implementation of WEB interfaces for the control system authorized users; this way, these users will be able to remotely visualize experiment data or equipment status.
- Finally, all end-user stations will provide standard office tools.

The following Figure gives an overview of the control room equipment.

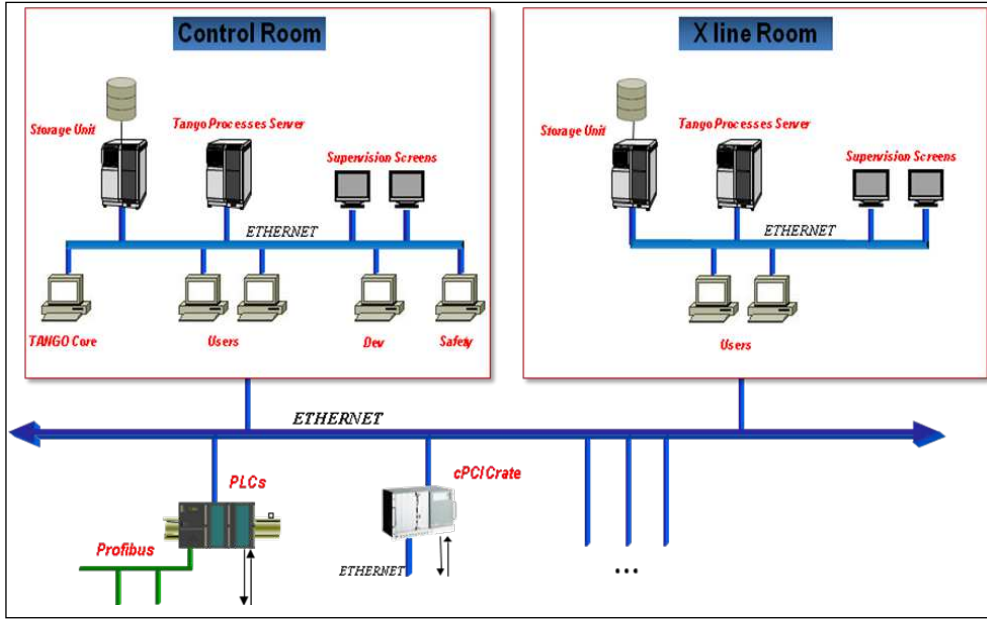


Figure 8.2. Schematics of the equipment foreseen for the main control room and the X-ray line control room.

Overall, the ThomX control system – designed to ensure harmonization and standardization, and based on open source tools – should be cost effective. The investment cost is estimated around 200 k€, including IT small equipment not described in this document: cables, a gateway to provide internet access, extra screens to display the ThomX status in the laboratory, etc.

Chapter 9. SAFETY AND RADIOPROTECTION

9.1 Introduction

The ThomX facility will be sited in an existing building, called ‘Igloo’, where a source of hard X-rays was operated until 2003 by the *Laboratoire pour l’Utilisation du Rayonnement Synchrotron*. The ThomX linear accelerator and storage ring will be built inside this building, while the facility control room and the one of the X-ray line will be located respectively in the D1 and D2 experimental halls. The D4 hall will be devoted to experimental tests.

The ThomX operation will produce high-energy electrons and other particles such as X-rays and neutrons which generate ionizing radiations through their interactions with matter. An adequate protection against these radiations must be ensured for people working at the facility. The safety logic adopted is the so-called ‘positive safety,’ which means that any system dysfunction will immediately cause a complete stop of the accelerator. Furthermore, redundant safety devices will be implemented, allowing various actions that will guarantee the staff safety such as

- Shining the beam into an area shall be submitted to prior people evacuation and to the interlocking of this area’s doorways,
- Access to a sensitive area shall be submitted to the prior stop of the upstream beam by using at least two different means, independent of each other.

Complementary to these two procedures, safety measures will be applied involving hard-wired logic, safety PLCs, shielding, beam dumps, shutters, personnel exclusion interlocks, radiation monitoring of the experimentation areas, staff dosimeters and radiation hazard training of the personnel. In case of dysfunction, radiological monitoring, hard-wired logic or safety PLCs will act through interlocks that will break connections to the mains voltage (Pre-Amplifier, modulator or electron gun, depending on the situation) in order to stop the accelerator.

9.2 PLC safety

The safety hard-wired logic works in association with an automaton PLC system via two completely separate circuits. A Safety Programmable Logic Controller (PLC) is a special purpose machine which is used to provide a critical control and safety applications to automaton users. This controller is an integral part of ‘safety instrumented systems’ (SIS) which are used to detect situations involving potentially dangerous processes. When such a situation occurs, the SIS is programmed to bring the process to a safe state automatically.

A safety PLC is specifically designed to accomplish two important tasks (ensured by a diversitary redundant architecture):

- ‘do not fail but if this cannot be avoided’,
- ‘fail only in a predictable safe way’.

Hard-wired logic is a safety circuit fully independent of automatons. It takes in charge, in particular, the access door interlocking, feedback contacts which provide a large number of checks bearing on the magnetic field, the high voltage, the pre-amplifier status etc., and the running control panel.

The PLC safety level must be as high as the one of a positive safety hard-wired logic. It manages access doors, emergency stop buttons, safety rounds and reports, issue authorizations to operate from a command-control system.

9.3 Radiation monitoring

Concerning the radiation protection, the ThomX facility design satisfies the following principles:

- No one will receive a dose of radiation in excess of the regulatory dose limits as a result of normal operation,
- Professionnal occupation exposures will be kept As Low As Reasonably Achievable (ALARA),
- All practical steps will be taken to prevent accidents with radiological consequences and to minimize the radiological consequences of any accident.

Arrangements will be made for the monitoring of working areas such as the Igloo, the bunker and the Optical hutch. For this purpose, several monitoring modes will be available such as thermo-luminescent dosimeters, measurements made by the qualified person in charge of radiation protection (Competent Radiological Protection Person) and a modular system for continuous monitoring. A continuous monitoring of gamma rays and neutrons will provide radiation dose rates and will manage alarms; its measured values will be transmitted to a central data acquisition unit. Placed in the Compton room, a special treatment unit will also be implemented that will provide a local display of the dose rate, signage and will manage alarms.

9.4 Radiation protection zoning

The D1, D2 and D4 halls are not classified ‘supervised area’; therefore, their access is free to people who satisfy access requirements. In contrast, the Igloo hall is classified ‘supervised area’.

The D1 hall contains the X-ray line and technical equipment.

- The X-ray line is not a classified area with the exception of the Optical hutch,
- The Optical hutch is alternately classified ‘prohibited area’ and ‘not classified’ area, depending on the permission conditions issued by functional elements important to safety (shutter position, permanent radiological level).

The D2 hall contains the ThomX control room and a room which contains the laser equipment.

The D4 hall is devoted to tests and mechanical assembly.

The Igloo hall contains the electron accelerator located inside a bunker. The Igloo is classified ‘supervised area’; therefore only workers subject to individual dosimetry are admitted. However, in exceptional circumstances, public access might be authorized as long as regulations and procedures are respected.

The Igloo bunker on the one hand and, on the other hand, the basement area devoted to the facility are alternately ‘prohibited area’ during the accelerator operation and, respectively, ‘supervised area’ and ‘not classified area’ when the facility operation has stopped.

The accelerator energy is high enough to expect nuclear reactions of photons and neutrons with matter, leading to the activation of structural materials. This is why it is particularly important to use appropriate low activation structural materials or structural materials that are activated for short periods of time only. Furthermore, one must ensure a nuclear waste management which will require a specific room to store and monitor activated materials. This room should be a ‘supervised area’ located in the Igloo.

9.5 Access control

9.5.1 General statement

It is a matter of absolute necessity to have appropriate procedures and devices in place to identify and screen all persons entering the ThomX facility. Consequently the LAL access control should be extended to the D1, D2, and D4 halls and to the Igloo.

9.5.2 Particular requirements concerning the ‘restricted areas’

The validation of door contacts as well as the validation of the position of protective shields and real-time radiation measurement are prerequisites to access the restricted areas (*i.e.* Optical hutch and the accelerator area). As it applies to all functional elements important to safety, signage and door statements (opened/closed/locked/unlocked) from classified areas must be transmitted to the control room. Local indications are displayed alternately with the status messages. The measured values of the dose rate and alarm symbols are shown permanently.

9.5.3 Access to the accelerator area and to the Igloo basement

The accelerator and the storage ring will be located in a concrete enclosure that will provide an efficient shielding to protect people against ionizing radiations inside the igloo, in line with regulations. Prior to the validation, the floor load-bearing capacity must be checked by experts.

The concrete containment structure will have a removable roof made of staggered concrete slabs. Civil engineering will be needed for the anchorage and supports to be used to adapt the bunker concrete blockds to the igloo circular wall which will be part of the enclosure, and to make sure that the roof of the whole ‘prohibited area’ provides a complete shielding. Since doors will be made of standard steel, the bunker access will be indirect, *i.e.* through (short) mazes, to ensure protection against ionizing radiations

Access to the bunker and to the basement area which is part of the ThomX facility will be determined by the equipment that guarantees people’s safety in accordance with the facility operation. As mentioned above, these devices ensure redundancy by using wired logic, safety PLCs and also special safety door locks which are simple but effective devices. A mechanical system called ‘trapped key lock’ will be implemented: the key is trapped in the lock when the door is open and it can be recovered only once the door is properly locked. Turning on the beam in ‘prohibited areas’ is allowed only if the safety systems have been unlocked, which implies that the collection of access keys is complete, as will be checked by the control board. To meet the safety requirements, new access doors must be installed and some existing doors must be modified. .

9.5.4 Access to the X-ray line and to the Compton room

The D1 hall will not be a ‘classified area’ and will be open to authorized people. The X-ray line sections will be in open access during normal operation with the exception of the Optical hutch. To meet the radiation protection requirements, the Optical hutch partition and its roof will be made of thick metal sheets. A thick lead shield will be installed at the end of the X-ray beam axis.

The Optical hutch will be alternately classified ‘prohibited area’ and ‘no classified’ area (under the worst-case conditions it might become a ‘regulated area’) depending on permission conditions issued by safety functional items. External and internal light-signaling warning will indicate the zoning status. Thus access to the Optical hutch is firstly subordinated to the removable shutter position, and secondly to the local permanent radiological measurement values. The shutter is dimensioned to protect people from high radiation rates effectively. A fail-safe closer device triggers the shutter closing automatically in case of electrical power failure too (compressed air, power supply). When a door is open the shutter command is prohibited.

A local radiation detector located in the Compton room will check he radiation exposure and the dose levels down to as low as reasonably achievable values. Measured high dose rates will automatically shut down the accelerator and activate the evacuation alarm. The validation of these safety devices is mandatory to grant access permission.

9.6 Beam dumps

The ThomX facility will comprise two beam dumps made of concrete that will contain high energy particles. They are very important to ensure an adequate protection of people from the ionizing radiations that would be produced if they were not used. One will be aligned with the linac axis and the other one will equip the extraction area. These shields will be installed as close as possible to the radiation source to absorb – or at least to moderate – as much as possible of the produced radiations. Their size and thickness will be sufficiently large to reduce efficiently all secondary radiation (X-rays and neutrons) produced by the stopping of the e^- beam. They will be made of a lined lead shield designed to moderate back-scattered radiation, placed in a cavity made of concrete blocks or high-density polyethylene. Ne peut-on pas être plus précis : donner des nombres sur les dimensions et préciser les matériaux utilisés avec une figure?

9.7 Interlocks

Depending on the dysfunction origin, the safety system will operate and break command circuits such as the pre-amplifier trigger, the modulator high voltage, the electron gun trigger or its high voltage. Feedback information from the control systems may be gradually requested according to the anomaly.

9.8 Accelerator emergency shutdown

Accelerator Emergency Shutdown (AES) are signal and alarm devices located in specific areas. A sufficient number of AES should be installed in prohibited zones, namely the accelerator area, the bunker basement and the Optical hutch. For the users to spot them easily, AES are devices equipped with flashing lights which are turned on whenever the local zone is closed.

If people are still present in a dangerous zone when a machine run is about to start (*i.e.* when the access is going to be forbidden after a short while) they should signal their presence by pushing an AES. This action prevents the accelerator operation. The system reactivation must follow a specific procedure.

9.9 Control console

Placed in the control room, the control console collects all access keys. The accelerator may be turned on if and only if all keys are inserted in that console.

The safety circuit validation (PLC safety, hard wired logic) allows one to launch the accelerator running procedure and triggers audible warning devices for 30 seconds before operation becomes possible.

9.10 Evacuation of dangerous areas

A specific procedure must be followed for the evacuation of the bunker and its basement. Operators should be trained in methodical evacuations with the validation of all checkpoints (roundsman function). Non compliance with the procedure will lead to the non validation of the facility operation.

A sufficient number of roundsman functions should be located in the accelerator area. Also, an exit path should be marked, leading to those areas that provide a possibility to regress.

9.11 Audio system and horns

Loud-speakers and horns will be installed in the Igloo basement (in the so-called ‘rotunda’) and pits, and inside the bunker. The sound system must be of good quality, speeches and broadcast messages must be intelligible. Horns must be loud enough, 80 dBA at least.

9.12 Safety notices

Local notices: Posters should be put up in ‘supervised’ and ‘controlled areas’ to remind people of the regulation requirements. Such posts maintain the worker’s awareness whenever they are in a radiological environment. Access doors to zones with multiple classifications should be equipped with highly visible luminous warning panels. Also, measured radiation levels and messages could be flashed regularly. Regarding the radiation measured level in the Optical hutch, an alarm symbol must be permanently displayed that informs of this level.

Signal boards at zone entrances and within the zones will specify the real-time safety conditions, display warnings (such as: presence of live voltage, ongoing operation mode etc.) and the access permissions (such as: open access, prohibited zone etc.).

9.13 Radiological monitoring

The control of the radiological environment will comply with the ALARA principle*. It will be performed by

- using bimonthly exposure dosimeters based on radio-photo-luminescence (RPL) and neutron sensitive dosimeters,
- PCR controls with live measurements,
- a centralized modular system which will continuously monitor exposures, feeding a data acquisition system that can handle up to 10 sensors.

This centralized system will perform dose rate and integrated dose measurements, manage alarms, test measurement channels, check settings and calibrations. It will allow a special device placed in the Optical hutch to display, in real time, local safety information.

*The ALARA principle is a commitment to keep radiation exposures and doses at a level as low as reasonably achievable (social and economic factors being taken into account).

Chapter 10. MANAGEMENT OF THE THOMX PROJECT

Introduction

The management of the ThomX project will have a simple structure that takes into account the three project phases 1) The construction 2) The exploitation 3) The technology transfer Three boards will govern the ThomX activity, covering all project aspects: the machine design, the purchasing and the assembly, the commissioning, the users' access, the communication and the relationships with the industries. This management board will comprise

- 1) A *steering committee* that will supervise the project activity and define the collaboration scientific policy.
- 2) A *scientific committee* composed of the scientific coordinators of the collaboration partners. It will assess the users' projects and prioritize the beam-time allocation. This committee must also define the scientific policy of the machine exploitation and R&D of the ThomX project.
- 3) A *partnership and valorisation office*. This body will evaluate the cultural and the economic potential of the ThomX innovations. It will stimulate transfer initiatives and check their outcome. It will work in close contact with the steering and the scientific committees.

The composition of these three bodies is given in Fig 10.1.

Steering Committee	Scientific Committee	Partnership office
LAL Orsay: Achille Stocchi	Alessandro Variola LAL Orsay	Alessandro Variola LAL Orsay
CELIA Bordeaux: Philippe Balcou	Alberto Bravin ESRF	Pierre Bordet Institut Neel
UMPC: Philippe Walter	Geraldine Le Duc ESRF	Philippe Debly Synchrotron SOLEIL
Institut Neel: Alain Schuhl	Jean-Louis Hazemann Institut Neel	Yves Trinquet THALES
INSERM Grenoble: François Esteve	Philippe Walter UMPC	Annabelle Alves CNRS DR4
Synchrotron SOLEIL: Amor Nadji	Alexandre Loulergue Synchrotron SOLEIL	Edward Mitchell ESRF
ESRF: Jean Susini	François Esteve INSERM Grenoble	Fabian Zomer LAL Orsay
THALES: Yves Trinquet	Eric Cormier CELIA Bordeaux	

Figure 10.1. The ThomX project committees.

In parallel, the communication group (see Table 10.1) will be in charge of all activity concerning communication and reach-out in the ThomX project. It will organise events, realise the publications relating to the project status and progress' and coordinate the official announcements of the collaboration.

The project management is organized according to a matrix structure. The ThomX facility has been divided in five sub-systems: Linac, Ring and transfer lines, X-ray line, Laser and Fabry-Pérot cavity. There is a coordinator responsible for the design, installation and operation of each sub-system. All these sub-systems involve various technologies which have been grouped in expertise domains: Mechanics and integration, RF systems, Magnets, Diagnostics, Power supplies and Pulsed elements, Vacuum, Synchronisation, Controls, Beam Physics, Alignment, Cabling, Nomenclature and Infrastructures. There is a coordinator for each one of these domains. These coordinators will be in charge of the activity harmonization within each technical field and of the maintenance during the facility exploitation (or “scientific phase”).

The project leader, his deputy and a project engineer are responsible for the project overall coordination. Fig. 10.2 describes the project structure.

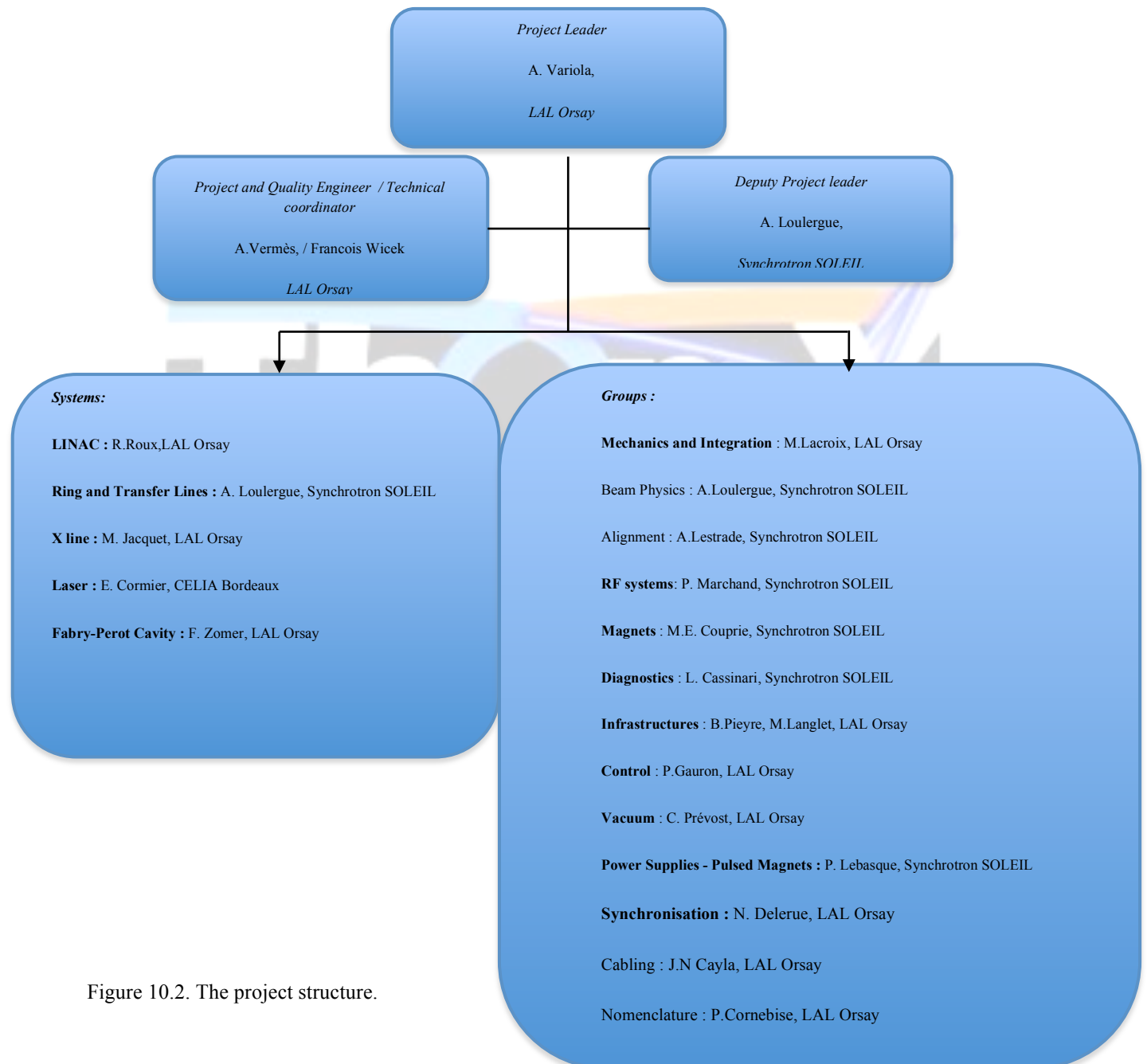


Figure 10.2. The project structure.

In the following Table the support structures are presented.

Support Structures		
Administration	Communication	Quality
<i>Administration : Brigitte Renard, LAL Orsay</i> <i>Procurements : Anngaelle Mardam Beck, LAL Orsay</i> <i>EDMS Support: Agnes Vermes, LAL Orsay</i> <i>Secretary : Chloe Sevestre,LAL Orsay</i> <i>DR04 Support: Edouard Dorion</i>	<i>Dominique Bony, LAL Orsay</i> <i>Marie-Pauline Gacoin, Synchrotron SOLEIL</i> <i>Claus Habfast, ESRF</i>	<i>Sandrine Agnes Vermes, LAL Orsay</i>

Table 10.1.

The ThomX collaboration needs an important support from all administrative services. For this an administrative cell has been set up which is headed by the person responsible for the administration, the purchasing office, the project database management, the secretariat and the contact with the regional CNRS delegation support. Last but not least, a quality engineer plays a major role in the project.

10.1 Partners' complementarity

The ThomX project requires a multidisciplinary environment given the complexity of the facility and of the set-up operation. Each partner contributes its competences to reach the final goal. The ThomX collaboration was organized so as to meet the requirements of a multicultural scientific environment where different communities are called upon to share their know-how and their knowledge to develop a common scientific program. This was already the case – and still is the case – for the MightyLaser project. In this project, LAL and CELIA teams have developed a fully integrated set-up composed of a fibre laser and a high gain optical resonator which is presently installed at ATF (KEK, Japan). There the complementarity between the two teams was crucial: LAL has a solid experience in developing optical resonators in an accelerator environment while CELIA is among the leading laboratories in fibre amplification technology. This program aims at a progressive increase of the light beam power stored in an optical cavity, in order to maximize the Compton back-scattering rate. The final goal of this R&D is to demonstrate the feasibility of a γ factory based on Compton backscattering. It started as a demonstrator for Compton-based polarized positron sources needed for the next generation linear colliders. The interest shown by other scientific communities in this technology made it clear that a low energy Compton source would be very useful in various research fields. This conclusion led to the launch of the ThomX collaboration.

The ThomX CDR has already been published and the present TDR is about to be widely circulated. For the TDR writing, it was mandatory to develop close connections between the various communities

participating in the ThomX project in order to merge technological developments and users' requirements in a single document. All partners have contributed to the scientific case elaboration, the study of the facility feasibility and the definition of its main components:

- LAL and SOLEIL contributed the description of the Compton backscattering characteristics and carried out the study of the accelerators and the Fabry-Pérot resonator,
- CELIA Bordeaux Lyon provided their expertise for the laser dimensioning,
- THALES provided its experience in industrial components and sub-systems,
- UMPC and ESRF enriched the scientific case.

This task sharing results from the multidisciplinary approach to the ThomX project where half a dozen institutes play an important role.

The writing of this TDR provided a unique opportunity of collaborating for laboratories that belong to different fields: LAL specialized in fundamental high energy physics, SOLEIL and CELIA in advanced technology in laser and accelerators, LC2RMF in social sciences and compact detectors, ESRF in medical sciences. In the future, the diversity of this set of teams will still increase with the participation of the Neel Institute and the GIN-INSERM in Grenoble.

After a prototyping phase, ThomX will operate as a mini-synchrotron whose beam line can be accessed not only by the facility partners, but also by other communities. Moreover, the aim of the industrialization phase is to provide the high technology scientific and industrial with compact and reliable sources that can be operated with little or no accelerator and laser expertise. This should open the way to a large community of CBS source users that would benefit from the complementarity between techniques developed at synchrotron sources and Compton back-scattering facilities. Imaging techniques, biological tests on cells and animals, metallurgy, fast chemistry, lithography are examples of future possible applications of these unique instruments.

10.2 ThomX larger framework

ThomX is one of the EQUIPEX projects submitted for approval to the French government by the P2IO. Consortium (Physique des deux Infinis et des Origines) of the Paris-Saclay Campus. This Consortium is composed of eight laboratories or institutes (CSNSM, IAS, IMNC, IPNO, IRFU, LAL, LLR, LPT), some of which are among the largest French laboratories. All together their staffs comprise 2000 scientists, engineers and technicians working in particle physics, nuclear physics, accelerator science, astroparticle physics, astrophysics and their interfaces. P2IO represents between 20% and 90% of the national potential in the various sub-domains. Although obviously not all of the eight laboratories participate in each EQUIPEX project, each project – including ThomX – is fully supported by P2IO and will contribute to the very ambitious common technological platform that P2IO wants to create in the coming years in the framework of the Paris-Saclay Campus initiative. Once equipped with these EQUIPEX facilities, this campus will represent a unique opportunity for French researchers and students.

References

- 1.1 Geoffrey A. Krafft, Gerd Priebe Compton Sources of Electromagnetic Radiation*Reviews of Accelerator Science and Technology Vol. 3 (2010) 147–163
- 1.2 V.Besson et al, NIMA 608 (2009), S75-S77
- 1.3 T Akagi et al, 2012 JINST 7 P01021
- 1.4 CDR ThomX LAL RT 09/28, SOLEIL/SOU-RA-2678 editors A.Variola, F.Zomer, A.Louergue
- 1.5 P.Russbueldt et al, Optics Express, Vol. 17 Issue 15, pp.12230-12245 (2009)
- 1.6 I.Pupeza et al, OPTICS LETTERS / Vol. 35, No. 12 / June 15, 2010
- 1.7 M. Y. Shverdin et al, 2009 OSA/IPNRA/NLO/SL 2009
- 1.8 C.Vaccarezza et al, IPAC Conference proceedings. New Orleans U.S.A.2012, TUOBB01
- 1.9 A.Variola, IPAC Conference proceedings. San Sebastian, Spain 2011, WEOAA01 1903-1905
- 2.1 S. Döbert, “Integration of the PHIN RF Gun into the CLIC Test Facility”. Proceedings of EPAC 2006, Edinburgh, Scotland 2006, MOPLS129
- 2.2 R. Roux, S. Cavalier, M. Bernard, G. Bienvenu, M.Joré,B.Leblond,B.Mercier, B.Mouton,C.Prevost, A. Variola “PHIL: a Test Beamline at LAL” Proceedings of EPAC08, Genoa Italy 2008, WEPP078
- 3.1 J. Payet, Beta Code, CEA, SACLAY
- 3.2 J.B. Murphy et al., Longitudinal Wakefield for an Electron Moving on a Circular Orbit, Vol. 57, Part. Acc. 1997.
- 3.3 K. Bane, M. Sand, The Short-Range Resistive Wall Wakefields, SLAC-PUB, 95-7074.
- 3.4 E. Forest, Phys. Tech. Part. Photon Beam
- 3.5 J. Zang et al, ‘Dipole fringe field effects in the Thom-X ring’, Proc. IPAC13
- 3.6 R. Nagaoka et al., Recent Studies of Geometric impedance At SOLEIL, PAC2006
- 3.7 Z. Huang, R.D. Ruth, Phys. Rev. Lett. 80,976 (1998).
- 3.8 S. K. Mttingwa, African Physical Review 2 (2008) 001.
- 3.9 P. Chen, G. Horton-Smith, T. Ohgaki, A.W. Weidemann, K. Yokoya, Nucl.Instrum.Meth.A355:107-110,1995
- 3.10 K. Ohmi, Phys. Rev. E 55 7550 (1997)
- 3.11 S. Haifets, D. Teytelman, Phys. Rev. Spec. Top. Acc. and beams 8 064402 (2005)
- 3.12 E. Weihreter, Compact synchrotron light sources, Series On Synchrotron Radiation Techniques And Applications - Vol. 3, World Scientific.
- 3.13 P. Lebasque, et al., Synchrotron SOLEIL, ‘Eddy current septum magnets for booster injection and extraction, and storage ring injection at Synchrotron SOLEIL’, EPAC 2006, Edinburgh, Scotland.
- 3.14 P. Lebasque, et al., Synchrotron SOLEIL, ‘Optimisation of the coating thickness on the ceramic vacuum chambers of SOLEIL storage ring’, EPAC 2006, Edinburgh, Scotland.
- 3.15 P. Lebasque, et al., Synchrotron SOLEIL, ‘Four matched kicker systems for the SOLEIL storage ring injection, a full solid-state solution of pulsed power supplies working at high current’, EPAC 2006, Edinburgh, Scotland.
- 3.16 F. Marhauser, E. Weihreter (BESSY), “Impedance Measurements of the HOM-Damped 500 MHz Metrology Light Source Cavity”, BESSY GmbH, Germany, 08 January 2007.
- 3.17 M. Langlois, P. Sanchez, M. Cornelis, F. Perez (ALBA), “Measurements on the RF cavity for the ALBA storage ring”, Proceedings of EPAC08, Genoa, Italy.
- 3.18 R. A. Rimmer (Lawrence Bekeley Lab.) et al., “Development of a high-power RF cavity for the PEP-II B factory”, DE-AC03-76SF00098 (LBL).

- 3.19 P. Fernandes, R. Massarino, R. Parodi, A. Tarditi (INFN, Italy), A. Massarotti (Sincrotrone Trieste, Italy), "The Design of the R.F Cavities for ELETTRA", IEEE, 1989.
- 3.20 M. Svandrlik, A. Fabris, C. Pasotti (Sincrotrone Trieste), "Improvements in curing coupled bunch instabilities at ELETTRA by mode shifting after the installation of the adjustable higher order mode frequency shifter (HOMFS)", IEEE 1998.
- 3.21 W. Bruns, web site: <http://www.gdfidl.de>
- 3.22 P. Marchand et al, Development of high RF power solid state amplifiers at SOLEIL, Proceedings of the IPAC2011, San Sebastian, Spain, p. 376.
- 3.23 C. Pardine et al, Status of the 476 MHz 50 kW solid state amplifier, Proceedings of the IPAC2010, Kyoto, Japan, p. 3972.
- 4.1 YAG(CE) data sheet, Saint Gobain Crystals <http://www.detectors.saint-gobain.com/YAG%28Ce%29.aspx>
- 4.2 SPI Supplies® YAG/YAP Comparison Table
http://www.2spi.com/catalog/scintillator_properties_comparison_table.html
- 4.3 K. Nakamura et al. (Particle Data Group), J. Phys. G 37, 075021 (2010).
- 4.4 Wartski et al., Detection of optical transition radiation and its application to beam diagnostics., IEEE Trans.Nucl.Sci.20:544-548,1973.
- 4.5]Saturation of YAG Beam Profile Monitors Measured at ATF, A. Murokh, J. Rosenzweig, V. Yakimenko, X. J. Wang.
- 4.6 Radiation Detection by Cerenkov Emission in Optical Fibers at TTF; E. Janata, M. Körfer, Tesla-Report 2000-27.
- 4.7 CERN-2009-005, p273.
- 4.8 CERN-2009-005, p272.
- 5.1 J Bonis et al 2012 JINST 7 P01017 [doi:10.1088/1748-0221/7/01/P01017](https://doi.org/10.1088/1748-0221/7/01/P01017)
- 6.1 J. Bonis et al. Non-planar four-mirror optical cavity for high intensity g ray flux production by pulsed laser beam Compton scattering off GeV-electrons. JINST SISSA Vol. 7, January 2012
- 6.2 R. V. Pound, "Electronic Frequency Stabilization of Microwave Oscillators," Rev. Sci. Instrum. 17, 490–505 (1946)
- 7.1 <http://www.jjxray.dk/home>.
- 7.2 R.W. Alkire *et al.*, Nucl. Inst. and Meth. A 350 (1994) 13-16.
- 7.3 B. Lengeler *et al.*, J. Synchrotron Rad. 6 (1999) 1153-1167.
- 7.4 R.L. Owen *et al.* J. Synchrotron Rad. 16 (2009) 143-151.
- 7.5 M.S. Nogueira *et al.*, Radiation Protection Dosimetry 111 (2004) 105-110.
- 7.6 M. Krumrey *et al.*, AIP Conf. Proc. 705 (2004) 861-865.
- M. Gerlach *et al.*, Metrologia 45 (2008) 577-585.
- 7.7 <http://www.canberra.com/pdf/Products/Ultra-LEG-SS-M3843.pdf>
- 7.8 K. Sakaue *et al.*, Rev. Sci. Instrum. 80 (2009) 123304.
- 7.9 http://sales.hamamatsu.com/assets/pdf/parts_F/F9892-31_-32_TMCP1039E03.pdf.
- 7.10 O. Chubar *et al.*, Proc DIPAC (2001) CT09.
- 7.11 D. Paterson *et al.*, Opt. Com. 195 (2001) 79-84.
- 7.12 M. Mahesh, RadioGraphics 21 (2001) 1033-1045.
- 7.13 K. Medjoubi *et al.*, JINST 6 C01080 (2011)
http://www.varian.com/us/xray/products/digital_radiography/paxscan_products.html
- 7.14 H. Elleaume *et al.*, Physics in Medicine and Biology 47 (2002) 3369-3385.

- 7.15 Y. Prezado *et al.*, Medical Physics 38 (2011) 1709.
- 7.16 I. Martínez-Rovira and Y. Prezadoa, Medical Physics 38 (2011) 4430.
- 7.17 L. Samain, Thesis, Liege university (ULG) 2012.
- 7.18 P. Martinetto, Thesis, Joseph Fourier university (UJF) 2000.
- 7.19 P. Bleuet *et al.*, Analytical Chemistry 29 (2010) 518-527.
- 7.20 P. Bleuet *et al.*, Nature Materials 7 (2008) 468-472.
- 8.1 <http://www.profibus.com/nc/download/specifications-standards/downloads/profibus-standard-dp-specification/display/>
- 8.2 <http://www.tango-controls.org/Documents/tango-kernel>



Table of content

INTRODUCTION	2
1. The ThomX project	2
2. Scheme and options	3
3. General layout of the machine.....	4
4. Machine parameters	6
5. Summary of the TDR main technical points.....	8
Chapter 1. THE THOMX INTERACTION REGION	9
1.1 Electron beam and laser pulse characteristics in the interaction region	9
1.2 Expected flux and its characteristics.....	10
1.3 Position stability	11
1.4 Timing stability	12
1.5 Energy stability	13
Chapter 2. INJECTOR.....	14
2.1 Injector specifications	14
2.2 Technical description of the linac components.....	16
2.2.1 Photo-injector	16
2.2.2 Solenoids	17
2.2.3 Laser	18
2.3 Acceleration section	20
2.3.1 The RF source	21
2.3.2 RF network	22
2.4 Beam dynamics.....	23
2.4.1 Nominal operation	23
2.4.2 Alternative operation modes	24
Chapter 3. TRANSFER LINE and RING	28
3.1 Transfer line	28
3.2 Extraction line	31
3.3 Storage ring	31
3.3.1 Optics and lattice.....	31
3.3.2 Non-linear dynamics	35
3.3.3 Collective effects, feedbacks	37
3.3.4 CBS and IBS effects	42
3.3.5 Scattering on the residual gas	46
3.3.6 Ion effects.....	47
3.3.7 Electron beam injection and extraction	48
3.3.8 Orbit corrections	50
3.4.1 Dipole magnetic design	53
3.4.2 Quadrupole magnetic design	54
3.4.3 Sextupole magnetic design.....	56
3.4.4 Corrector magnetic design	58
3.4.5 Injection dipole.....	59

3.5 Power supplies	60
3.5.1 Pulsed magnets	60
3.6 Storage ring RF system.....	65
3.6.1 HOM impedance thresholds as regard to beam instabilities	66
3.6.2 Cures to the HOM induced instabilities.....	66
3.6.3 RF power source.....	70
3.6.4 Low level RF system and longitudinal feedback.....	71
3.6.5 RF equipment status	73
3.6.6 RF system: conclusion	73
3.7 Transverse feedback	74
3.7.1 Specifications.....	74
3.7.2 Electronics	75
3.7.3 Kicker.....	76
3.8 Vacuum	77
3.8.1 Transfer line vacuum.....	77
3.8.2 Ring vacuum	78
Chapter 4. INJECTOR, TRANSFER LINE AND RING DIAGNOSTICS	80
4.1 Charge measurement	80
4.1.1 Current transformers	80
4.1.2 Faraday cups.....	81
4.2 Transverse profile measurements.....	81
4.2.1 Diagnostics stations.....	81
4.3 Emittance measurement.....	84
4.4 Beam position measurement	85
4.4.1 Beam Position Monitors (BPM)	86
4.4.2 Orbit feedback system	90
4.4.3 Tune measurement and feedback.....	90
4.4.4 Energy measurement	90
4.5 Bunch length measurement.....	90
4.5.1 Cerenkov radiation	90
4.5.2 Synchrotron radiation	92
4.5.3 Transport of the Cerenkov and synchrotron radiations to the diagnostics hutch	93
4.5.4 Streak camera for the bunch length measurement	93
4.6 Bunch imaging using synchrotron radiation	94
4.7 Beam loss measurement.....	94
4.8 Beam dumps.....	94
Chapter 5. SYNCHRONIZATION	95
5.1 Overall scheme	95
5.2 Specifications	96
Chapter 6. OPTICAL SYSTEM DESIGN.....	97
6.1 Feedback system and results on a Fabry-Perot cavity locking.....	97
6.1.1 Electron and FPC pulse synchronization.....	98
6.1.2 Laser parameters to be stabilized.....	99

6.1.3 PDH Measurement technique	101
6.1.4 Actuators	103
6.1.5 The digital feedback system.....	107
6.2 High average power laser system and its coupling to a high gain FP cavity.....	110
6.2.1 The MightyLaser oscillator	111
6.2.3 Stretcher and compressor.....	115
6.2.4 ThomX development.....	115
6.3 Mechanical design	118
6.3.1 Optical cavity vacuum	123
Chapter 7. X-RAY BEAM LINE AND EXPERIMENTS	124
Introduction	124
7.1 Available extracted X-ray beam	124
7.2 Global view of the X-ray lne.....	124
7.3 Chracterization of the X-ray beau	126
7.3.1 Optical table 1	126
7.3.2 Beam transport	128
7.3.3 Optical table 2	128
7.4 Demonstration experiments	130
7.4.1 Experiments using the full X-ry beam.....	130
7.4.2 Experiments using the central part of the beam.....	134
7.5 Summary	139
Chapter 8. CONTROL SYSTEM	140
Introduction	140
8.1 General principles.....	140
8.2 Technical considerations.....	141
8.3 The TANGO control system software	142
8.3.1 Software bus	142
8.3.2 A control system for accelerators	142
8.4 Control system architecture.....	143
8.4.1 Equipment to control	143
8.4.2 Inputs/outputs	144
8.4.3 Front-end machine architecture: PLCs and industrial PCs	145
8.5 IT infrastructure.....	146
Chapter 9. SAFETY AND RADIOPROTECTION	149
9.1 Introduction	149
9.2 PLC safety	149
9.3 Radiation monitoring.....	150
9.4 Radiation protection zoning.....	150
9.5 Access control.....	150
9.5.1 General statement	150
9.5.2 Particular requirements concerning the ‘restricted areas’	151
9.5.3 Access to the accelerator area and to the Igloo basement.....	151
9.5.4 Access to the X-ray line and to the Compton room	151

9.6 Beam dumps.....	152
9.7 Interlocks.....	152
9.8 Accelerator emergency shutdown.....	152
9.9 Control console.....	152
9.10 Evacuation of dangerous areas	152
9.11 Audio system and horns.....	152
9.12 Safety notices	153
9.13 Radiological monitoring	153
Chapter 10. MANAGEMENT OF THE THOMX PROJECT.....	154
Introduction	154
10.1 Partners' complementarity	156
10.2 ThomX larger framework	157

